Lundquist Number Scaling in MST Reversed-Field Pinch Plasmas

by

Stephanie Zofia Kubala

A dissertation submitted in partial fulfillment of the
requirements for the degree of

Doctor of Philosophy

(Physics)

at the

UNIVERSITY OF WISCONSIN - MADISON

2023

Date of final oral examination: 06/07/2023

The dissertation is approved by the following members of the Final Oral Committee:

Cary B. Forest, Professor, Physics

Daniel J. Den Hartog, Research Professor, Physics

John S. Sarff, Professor, Physics

Carl R. Sovinec, Professor, Engineering Physics

Abstract

Nonlinear MHD fluctuations appear in both natural and magnetic confinement settings, such as the solar wind, self-organization dynamics in the RFP and spheromak, and current disruptions in tokamak plasmas. In this thesis, parameter scaling experiments oriented toward nonlinear MHD dynamics in RFP plasmas are presented. Experimental data have been gathered spanning a wide range of parameter space characterized by Lundquist number, $S \sim 10^4$ - 10^7, and density, n_e/n_G, where n_G is the empirical density limit. A new programmable power supply allows low-current, low-S operation, which overlaps with parameters available in numerical modeling. Experimental S scalings of magnetic fluctuation amplitude agree well with those from the nonlinear MHD codes DEBS and NIMROD. A transition from quasi-continuous activity to bursty relaxation having discrete sawtooth events is observed in going from low to high S, with a threshold at around $S \sim 10^5$. The spectral properties of the magnetic fluctuations change at this transition, including a reduction in fluctuation phase velocity that suggests plasma flow and/or flow profile changes. Momentum transport and flattening of the flow profile are known features associated with sawtooth relaxation in RFP plasmas.

Acknowledgements

I am immensely and profoundly grateful to the teams of people who have supported me in the process of completing this thesis. I will never be able to sufficiently express the magnitude of my thanks, but I will do my best to begin to here.

First I'd like to thank my advisor, Daniel Den Hartog, who has spent many hours mentoring me not only through this thesis, but also counseling me through life's challenges. I admire your compassion and expertise and will never be able to thank you enough for all the patience and kindness you have shown me.

Also, to the rest of my committee and co-authors, Cary Forest, Craig Jacobson, Karsten McCollam, John Sarff, and Carl Sovinec. The pandemic was a very isolating experience, particularly while writing a thesis, and I always was reenergized following your thoughts and feedback. Your passion and curiosity toward this work was inspirational. Thank you for sharing that with me.

To the other scientists at MST who have provided feedback, Abdulgadher Amalgri, Jay Anderson, Noah Hurst, Mark Nornberg, Lisa Reusch, and Bill Young. Thank you for your support and input.

To the engineering and technical support staff on MST, namely Don Holly, Paul Wilhite, the late Peter Weix, Alex Squitieri, Mark Thomas, Bill Zimmerman, Andrey Levochkin, Mikhail Reyfman, Mike Borchardt, and David Deicher. You were all so patient and understanding with me when I needed your expertise and I enjoyed and felt so fortunate to have the opportunity to work with you all. Don Holly, thank you for all the help with the Thomson power supply upgrade. I would not have been able to complete that project without your expertise. Mikhail Reyfman, thank you for your help with these power supplies and other Thomson electronics. And thank you for all the Polish candies you left on my desk; they meant a lot to me. Mike Borchardt and Mark Thomas, thank you for all the support you provided making the Thomson system functional. Alex and Paul, thank you so much for putting up with all my questions and the numerous Thomson system issues that cropped up. I would not have finished this thesis without your tireless efforts. Alex, thank you for your outreach efforts and being so willing to connect me to opportunities to help my career. Bill, thank you for stopping me to chat and tell me a joke. It was a simple act that often would often lift my spirits quite a bit. And finally thank you to Peter Weix. He taught me so much and I will always remember and value how kind, competent, and giving he was.

To the many MST and WiPPL graduate students who have been there along the way, most especially, John Boguski, Phil Bonofiglo, James Duff, Lucas Morton, Takashi Nishizawa, Eli Parke, Patrick Van Meter, and Anthony Xing with whom I've shared offices, conversations, and diagnostic responsibilities. When I became one of the two MST graduate students as opposed to one of the twelve I was used to, it really showcased how great of a team MST was. I'll look back on that time fondly.

To the women and gender minorities in physics group (GMaWiP) that provided so much career support. I am proud of the impact we were able to have pushing the culture in the department to welcome students whose experiences are not typically centered in physics.

To the support staff in the physics department who have guided me in taking a leave of absence and successfully returning to the program, particularly Renee Lefkow and Sharon Kahn. I have had a bumpy road and your encouragement and guidance were always welcome. Thank you for advocating for me and encouraging me to persevere.

To the undergraduate hourlies who have help me wrangle cables and have contributed code to the Thomson team, Joey Duff, Paul Gradney, Alex Sainterme, and Sam Smith. I hope you know how invaluable your contributions were. I felt lucky to get to see you all take on the responsibilities given to you and handle them so well.

To the people who contributed so many small and big favors during my hardest days, from helping me move out of state in less than a week, covering abandoned operator days, and most importantly, to those who were willing to witness and share the burden of my grief, checking in on me when I really needed it: Phil Bonofiglo, John Boguski, Ethan Peterson, Stephanie Noel, Emily Lichko, and especially Kyle Bunkers, Will Strickfaden, Erin Middlemas, Briana Van Treeck, Stacy Harper, and Jesi Davis. Your unexpected kindness truly meant the world to me.

And to the family whom I've lost while trying to do this already really hard thing. I never could have made it through this, nor losing you all, without the strength, resilience, and kindness you instilled in me. To my father, for teaching me a stubborn sense of self, to my grandparents, Zofia and Władysław, for showing me how to choose and find joy in simplicity, no matter how hard life has been, and most of all to my mother. You were the best person I have ever met and I am so proud to be your child. Tesknie za toba codzienne i kocham cie zawze.

And to my family still here: my brother Paul, my partner, Will and my late mother's dog, Emma. You've helped me rebuild when everything fell apart. Thank you.

Contents

List of Figures

List of Tables

Chapter 1

Introduction

In this chapter, we will briefly preview the main goals of the thesis and the key results. To start, little to no familiarity with the topic is assumed; so, the description is brief and simplified. We also preview key results the reader may look forward to reading about in the thesis. As we will see in a moment, one of the main applications of the results obtained is to consider what they mean for the RFP as a fusion concept. This motivates a discussion of fusion energy and how it could fit into a climate crisis solution. Finally, we will go over an outline for the rest of the thesis.

1.1 Key Goals and Results

The main goal of this thesis was to assess how magnetic field fluctuation amplitudes scale with Lundquist number in Madison Symmetric Torus (MST) reversed-field pinch (RFP) plasmas. In plasmas, charged particles tend to travel around magnetic field lines. RFP plasmas are magnetically confined in a toroidal shape with the toroidal magnetic field (going the long way around the torus) that is of approximately the same strength as the poloidal (going the short way around) magnetic field. The configuration gets its name because the toroidal magnetic field reverses direction as you move from the center of the device to the edge.

The Lundquist number is the ratio of the resistive diffusion time of a plasma to the Alfven time. RFP plasmas are ohmically driven, so for the purposes of this quick introduction, we can somewhat naively trust the choice of the Lundquist number as the parameter to appropriately characterize the plasmas, with the Alfven time acting as a normalization factor. Stochastic transport is the main transport mechanism by which particles and heat escape the core of today's standard RFP devices. This rapid loss of particles and heat radially out from the core of a device diminishes the performance of the device. The word ”stochastic” refers to the nature of the magnetic field lines within the device, which are largely chaotic due to magnetic field fluctuations leading to neighboring field lines reconnecting via a process called magnetic reconnection. It therefore follows that if the strength of the magnetic field fluctuation amplitudes decrease with Lundquist number, the stochastic transport may cease to be a dominate loss mechanism, improving the RFP's potential as a fusion concept.

Data were collected for a wide range of Lundquist numbers ranging from $10^4 - 10^7$. These data were used to determine the Lundquist number and the magnetic field fluctuation amplitudes. They were then fit to the following expression:

$$\tilde{b} = cS^{-\alpha}, \tag{1.1}$$

where $\tilde{b}$ is the normalized magnetic field amplitude, S is the Lundquist number, and c and α are the fit parameters. This assumption of a power-law dependence implies that we can expect the magnetic field fluctuation amplitudes to decrease more strongly as α becomes more positive. This would be favorable for quickly reducing transport in the

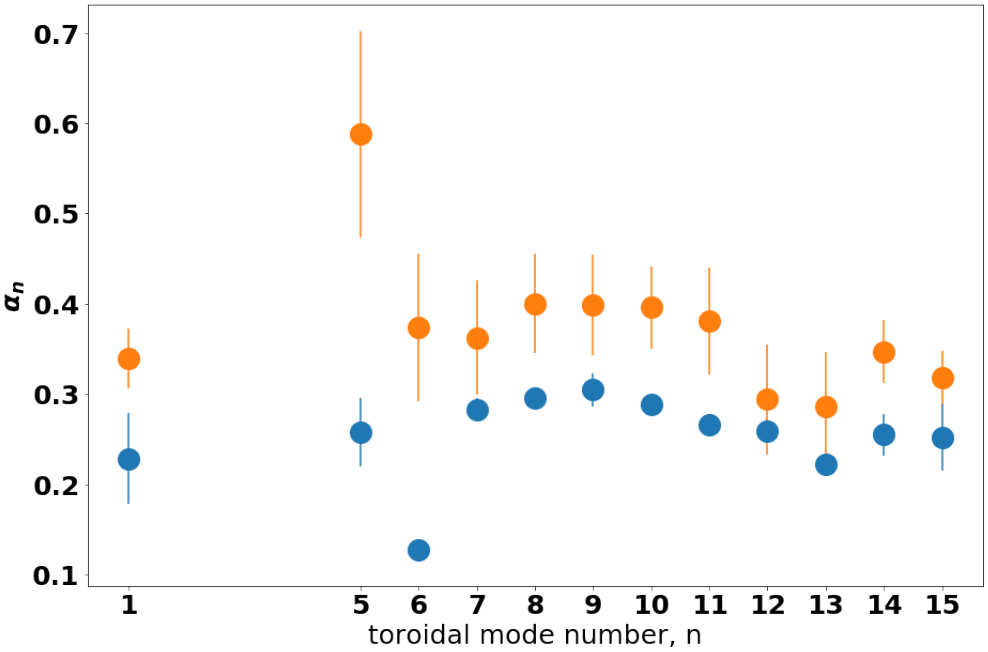

FIGURE 1.1: This figure summarizes the results of fitting the magnetic field fluctuation amplitude scaling data to Eqn. 1.1. The orange points represent data collected at higher electron densities while the blue points represent data collected at lower electron densities. It is one of the key results of this thesis.

RFP caused by stochastic magnetic fields.

The key results from the thesis are shown in Fig. 1.1. We will dive into the details of this plot in the following chapters, but we can see that generally speaking, $\alpha \sim 0.3 - 0.4$. This is a higher value that has been previously expected from MST [1].

1.2 Fusion and the Climate Crisis

Global warming is a crisis that threatens the planet with mass extinction. Fusion is often touted as a near ideal solution to producing carbon-free energy fueled by abundantly available hydrogen isotopes that can be extracted from water. A key application of the work presented herein is to consider the implications of the results for the RFP as a fusion concept. So, let's first provide context for where we are now and how fusion fits into this picture.

Fusion is when two nuclei, or the relatively dense center of atoms containing protons and neutrons, collide and come together into a single nucleus. Recall that Einstein's famous equation states that energy equals mass times the speed of light squared, or, $E = mc^2$. So, if two light nuclei collide, energy will be released in the process because the total mass of the constituent nuclei going into the reaction is greater than the mass of the nucleus at the end of the reaction. The number of protons, or positively-charged particles, in a nucleus defines which element the atom is. For example, all hydrogen atoms contain one proton in their nucleus. The number of neutrons, or particles containing no net charge, in a nucleus can vary amongst nuclei of the same element. The number of neutrons dictates which isotope of an element the atom is. Considering hydrogen again, we have atoms with zero, one, or two neutrons. We call these three isotopes of hydrogen protium, deuterium, and tritium respectively.

Because fusion involves changing the state of a nucleus, it is a type of nuclear reaction. The other type of nuclear reaction, fusion's more infamous and maligned counterpart, is fission, where instead of two nuclei coming together, a single nucleus splits apart into two nuclei, again, releasing energy in the process via the differential between the total mass present before and after the reaction. This can occur with heavier elements. Fission reactions are what fuel today's nuclear reactors. In conducting fusion research, we are interested in developing a blueprint for using fusion reactions to fuel a power plant, supplanting not only nuclear, but also coal power plants. To understand why this is such a tempting avenue of exploration, we will consider the equations for the most relevant examples of each of these two types of nuclear reactions.

Equation 1.2 below shows an example fission reaction where a uranium isotope, U^{235}, is split, via neutron, n, bombardment. This is the main reaction that is used to fuel a nuclear reactor. The advantages to using it for electricity generation are many. No carbon dioxide or other greenhouse gas is produced. Uranium is also energetically denser than fossil fuels: the total volume of rods needed to power the United States in 2019, a country which accounted for four percent of the world's population and 17% of the energy consumed, would fill less than one millionth of a percent of Lake Mendota, whereas the volume of fossil fuels necessary would fill the lake 7 times over [2, 3, 4]. Finally, nuclear reactors are very safe, despite their image to the contrary, causing fewer deaths and injuries than any fossil fuel, particularly when taking into account the deaths that emissions indirectly cause [5]. The downside of fission is that, though it does not produce greenhouse gases or other harmful pollutants, it does produce radioactive elements, the most long-lived of which, if using waste processing strategies, is plutonium, with a half-life of 24,000 years. However, the volume of this waste is small and strategies, such as vitrification and breeder reactors, exist to handle or eliminate the waste, respectively. The remaining radioactive byproducts can decay into a harmless form in around 50 years [2]. Ultimately, these time scales and the geopolitical consequences associated with a nuclear-powered world can be psychologically daunting but may pale in comparison when considering that a good fraction of CO_2 emitted today will linger in the atmosphere for thousands of years, and the consequences of this emission on Earth's climate and populations will be felt for even longer than that [6].

$$ {}_{0}\mathrm{n}^{1} + {}_{92}\mathrm{U}^{235} \longrightarrow {}_{58}\mathrm{Ce}^{140} + {}_{40}\mathrm{Zr}^{94} + 2\,{}_{0}\mathrm{n}^{1} + 6\,\mathrm{e}^{-} + 206\,\mathrm{MeV} \tag{1.2} $$

Now let's consider fusion reactions. Equations 1.3 and 1.4, with equation 1.5, show the reactions that most of the fusion community are aiming to utilize to fulfill their promise to provide a carbon-free, safe, and abundant means of energy production. The reactants are deuterium, D, an isotope of hydrogen that is naturally occurring. The products are helium-3, He, alpha particles (another isotope of helium), α, tritium, T, neutrons, n, and protons, p. Tritium is radioactive with a half-life of 12.26 years, but can be also be consumed as a reactant in the fusion reaction shown in equation 1.5. It can also be bread using Lithium coating on reactor walls [7]. The high-energy neutrons produced in equations 1.3 and 1.5 are the main safety concern. Because they have no electric charge, they cannot be contained and would activate materials in the wall of the reactor, however, the half-life of these materials would be short. Because fusion reactions are not initiated via neutron bombardment, there is no risk of a nuclear meltdown, as occurred with Three Mile Island and Fukushima. Though deuterium only makes up 0.0156% of all hydrogen atoms on Earth, it can be easily extracted and is abundant enough to fuel our planet for 2 billion years at the present rate of energy consumption [2]. Deuterium is remarkably energy dense, even more so than the fuel for nuclear fission. For all these reasons, fusion has captivated generations of scientists and the public interest as a panacea to the energy crisis.

$$\mathrm{D} + \mathrm{D} \longrightarrow \mathrm{He}^3 + \mathrm{n} + 3.27\,\mathrm{MeV} \tag{1.3}$$

$$\mathrm{D} + \mathrm{D} \longrightarrow \mathrm{T} + \mathrm{p} + 4.03\,\mathrm{MeV} \tag{1.4}$$

$$\mathrm{D} + \mathrm{T} \longrightarrow \alpha^{+}\,\mathrm{n} + 17.6\,\mathrm{MeV} \tag{1.5}$$

While we have safe, reliable nuclear fission energy production as an option available today, there are significant challenges that prevent fusion energy production from being readily viable. To begin to understand these hurdles, we will consider a relatively simple equation, Coulomb's law, shown below in Equation 1.6, where F is the force, k_e is Coulomb's constant, $q_{1,2}$ represents the charge of the objects in question, and r is the distance between them. $\hat{r}$ represents a unit vector which points in the direction of the force. This law tells us that electrically-charged objects of the same charge repel each other and that the strength of this repulsion increases as the distance between them shrinks. If we examine this as it pertains to the fusion reactions in equations 1.3 and 1.4, we see that we have two positively charged nuclei that must come together in order for the reaction to occur and that this task becomes exponentially harder as the nuclei get closer together, until nuclear forces can overwhelm Coulomb repulsion, allowing the nuclei to fuse. The amount of energy that this necessitates is at the heart of the challenge of engineering an economically viable, practical, and robust fusion reactor.

$$\overrightarrow{F} = k_e \frac{q_1 q_2}{r^2} \hat{r} \tag{1.6}$$

Energy production is essential for human life. Ultimately, fusion energy is a promising means of energy production. However, given that the most attainable fusion reactions still produce radioactive byproducts, it naturally follows that the comfort with nuclear fission reactors must first also be increased. A usable fusion reactor is many years away. Nuclear fission reactors work today. And it is already past time that drastic measures be taken to cease the emission of greenhouse gases into the Earth's atmosphere. Fusion reactors cannot be a part of the initial solution.

1.3 Thesis Outline

The remainder of the thesis will provide more detail about how the key results were obtained and providing the necessary background to understand the question under investigation and the results. In the next chapter, we will go over the magnetohydrodynamic physics concepts that underlie this investigation. This will motivate the set-up for the data collection and analysis. We will then go over the Madison Symmetric Torus and the diagnostics used to gather the data presented in this thesis. We will discuss how data were collected. The chapter after that will cover the Thomson scattering diagnostic. This tool provided electron temperature measurements which were particularly important for this thesis project. The Lundquist number as a strong dependence on this parameter.

Having by then provided appropriate context, we will go over the results of the scaling study. The study's definition of the relevant parameters and the sensitivity to the selected definition will be discussed there. The scaling results will be presented as well as the scaling of other transport related quantities. We will discuss how consistent the results are with stochastic theory and explore what they mean as the RFP device is scaled to larger sizes. We will also compare the results to computational results.

We will then discuss the results from an extra question that arose while collecting data. It was observed that the nature of the reconnection activity in the RFP changed around $S \sim 10^5$ as the Lundquist number was decreased to values that had not been previously explored. A presentation of this observation and the results of some basic spectral analyses will be given.

We will conclude with a summary of the thesis and suggestions for some future work.

Bibliography

[1] M. R. Stoneking, J. T. Chapman, D. J. Den Hartog, S. C. Prager, and J. S. Sarff, "Experimental scaling of fluctuations and confinement with lundquist number in the reversed-field pinch," *Physics of Plasmas*, vol. 5, no. 4, pp. 1004–1014, 1998. [Online]. Available: https://doi.org/10.1063/1.872670

[2] J. P. Freidberg, *Plasma Physics and Fusion Energy*. New York, NY: Cambridge University Press, 2007.

[3] U. E. I. Administration, “”what is the united states' share of world energy consumption?”,” https://www.eia.gov/tools/faqs/faq.php?id=87&t=1, accessed: 2022-01-11.

[4] U. of Wisconsin Alumni Association, “”what is the volume of lake mendota?”,” https://www.uwalumni.com/news/ask-abe-lake-mendota-volume/, accessed: 2022-01-11.

[5] A. Markandya and P. Wilkinson, "Electricity generation and health," *The Lancet*, vol. 370, no. 9591, pp. 979–990, 2007. [Online]. Available: https://www.sciencedirect.com/science/article/pii/S0140673607612537

[6] J. Goodell, *The Water Will Come: Rising Seas, Sinking Cities and the Remaking of the Civilized World*. New York, NY: Little, Brown and Company, 2017.

[7] J. Freidburg, *Plasma Physics and Fusion Energy*. New York: Cambridge University Press, 2007.

Chapter 2

Nonlinear MHD and Lundquist Number Scaling

The central goal of this thesis was to investigate and characterize how plasma dynamics and behaviors scaled with Lundquist number in reversed-field pinch (RFP) plasmas. This is a basic plasma science question but also has applications in understanding how the RFP might scale as a fusion device. Many of the dynamics of the RFP can be aptly described by resistive magnetohydrodynamics (MHD). The Lundquist number, S, defined as the resistive diffusion time normalized by the Alfvén time, is the constant for one of the main dissipative terms in the resistive MHD equations and has been a traditional choice for the independent parameter in many scaling studies [1, 2, 3]. As such, it was chosen as the independent parameter for this thesis. In this chapter, we will cover the nonlinear MHD model, and some of the most relevant resistive MHD features in MST RFP plasmas. This will frame the motivation for the specific parameter scalings in this thesis.

The experimental data for this project were also collected with an eye toward performing rudimentary comparisons to simulation results and creating a database that could act a basis of comparison for any future validation work. Validation efforts assess the degree to which the physics taking place in the experiment is reflected by computational codes. The ability for computational codes to accurately predict plasma behavior as it scales is particularly important for developing a financially viable fusion reactor, due to the necessary scale, and, therefore, expense such a device would require. The computational codes used for comparison in this thesis, DEBS and NIMROD, will be briefly covered in the second part of this chapter.

2.1 A Physics Background for Lundquist Number Scaling in the RFP

In the 1960s, observations made on the ZETA toroidal pinch device [4] where periods of low magnetic turbulence were associated with the toroidal field reversal near the plasma edge via self-organization[5] inspired the concept of the reversed-field pinch. In linear (ideal) magnetohydrodynamic (MHD) stability analysis, it is found that this field reversal, paired with a sufficiently close-fitting conductive shell, is key for the stability of internal modes[6]. The study of the RFP and the physics of the plasmas it produces is not only useful for understanding the viability of the RFP as a fusion concept, but also has tie-ins to a myriad of other open physics questions. The self-organization process has also been seen in other fusion plasmas [7, 8, 9, 10] and exhibits a great deal of overlap with magnetic reconnection observed in space plasmas [11, 10]. While not every observed process is well understood, many have been successfully described by resistive MHD. In this section, we will review this model as well as the most relevant features of MST RFP plasmas.

2.1.1 Resistive MHD Equations

Magnetohydrodynamics (MHD) is an approximation that can be arrived at systematically by starting with the kinetic equations for ions and electrons. A perhaps more intuitive approach is to consider macroscopic quantities that would appear in the equation of state for any electrically conducting fluid. Through this method of essentially combining the Navier-Stokes (fluid) equations and the Maxwell equations, one can arrive at the ideal, or non-dissipative, MHD equations [12]. So for the RFP, where dissipative effects such as resistivity and viscosity are significant, we must modify this base model to capture relevant physics. To begin, we can add resistivity to Ohm's law and combine it with Faraday's law, then cast the equation in dimensionless form to arrive at the induction equation for resistive MHD,

$$\frac{\partial \boldsymbol{B}}{\partial t} = \boldsymbol{\nabla} \times (\boldsymbol{v} \times \boldsymbol{B}) + \frac{1}{S}\nabla^2 \boldsymbol{B}, \tag{2.1}$$

where $\boldsymbol{B}$ is the normalized magnetic field, t is time, $\boldsymbol{v}$ is the bulk plasma velocity normalized by the Alfvén speed ($v_A = B/\sqrt{\rho\mu_0}$) , and S is the Lundquist number. The Lundquist number is defined as

$$S = \frac{\tau_R}{\tau_A} = \frac{\mu_0 a^2}{\eta(Z_{eff}, n_e, T_e)} \frac{B}{a\sqrt{\mu_0 \rho}} \sim T_e^{3/2} I_p \tag{2.2}$$

where τ_R and τ_A are the resistive diffusion and Alfvén times, a is the typical scale length of the system, μ_0 is the permeability of free space, η is the resistivity of the plasma, Z_{eff} is the effective charge state of the plasma, T_e and n_e are the electron temperature and density, B is the magnetic field amplitude and I_p is the plasma current.

The other resistive MHD equation that captures dissipation and that is coupled to the induction equation is the momentum equation. Cast into a dimensionless form, and assuming negligible plasma pressure and constant mass density, it looks like,

$$\frac{\partial \boldsymbol{v}}{\partial t} + (\boldsymbol{v} \cdot \nabla)\boldsymbol{v} = (\boldsymbol{\nabla} \times \boldsymbol{B}) \times \boldsymbol{B} + \frac{1}{R_e}\nabla^2 \boldsymbol{v}, \tag{2.3}$$

where R_e is the Reynold's-like number defined as,

$$R_e = \frac{\tau_{momentum}}{\tau_A} = \frac{a^2}{\nu}\frac{B}{a\sqrt{\mu_0 \rho}}, \tag{2.4}$$

where $\tau_{momentum}$ is the momentum diffusion time and ν is the viscosity. The magnetic field is normalized to a typical field value and the velocity is normalized to the Alfvén speed [1].

So from equations 2.1 and 2.3, we see that the Lundquist number and the Reynold's number are the key parameters that characterize a dissipative plasma. For this study, the Lundquist number was chosen as the independent parameter along which the scaling analyses were performed. There are many reasons for this:

- It is the traditional choice of several similar and previous studies [1, 2, 3].
- It is an intuitive choice: a relatively large amount of current is injected into MST plasmas which have relatively low density (low viscosity). Therefore resistivity is the more natural parameter on which to focus.
- It was the most feasible option: MST plasmas can be high temperature such that measuring viscosity is a challenge. Additionally viscosity is a highly anisotropic quantity, especially relative to resistivity, in MST.

- Resistivity and collisional viscosity scaling cannot be separated (i.e. $Pm = \nu/\eta$= constant). The perpendicular viscosity scales like $\nu_\perp \sim \beta T_i^{3/2}$. Since $T_i \propto T_e$ and β varies only weakly in MST plasmas, the viscosity therefore scales like the Lundquist number ($S \sim T_e^{3/2}$).

Ultimately, it was just one way to tackle such a study. We will detail which dependent parameters were scaled in Ch. 5. In the next section, we will review the tearing modes of MST and the features they produce.

2.1.2 Tearing Modes and Features of MST RFP Plasmas

One of the most significant consequences of resistivity is the violation of ideal MHD's conservation of local magnetic flux. Breaking this condition leads to changes in field line topology via magnetic reconnection, a process that is still not entirely understood [13]. Due to the RFP's magnetic topology, tearing modes, driven by gradients in the current density profile, are the prevalent MHD modes in the plasma [10, 14]. These modes are resonant inside the plasma and create magnetic islands. A few parameters that are used to quantify the RFP's magnetic topology are the reversal parameter, which characterizes extent of the toroidal magnetic field reversal and is given by,

$$F = \frac{B_{\phi(a)}}{< B_\phi >}, \tag{2.5}$$

the pinch parameter, which is the ratio of poloidal magnetic field at the edge to the average poloidal field and is given by,

$$\Theta = \frac{B_{\theta(a)}}{< B_\theta >}, \tag{2.6}$$

and the safety factor which characterizes the field line pitch in the cylindrical approximation is given by,

$$q = \frac{rB_\phi}{RB_\theta}, \tag{2.7}$$

such that small q represents a tightly wound helix and infinite q represents a straight toroidal field line.

In the above equations B_ϕ are the B_θ are toroidal and poloidal components of the magnetic field, a is the minor radius or edge location, and r and R are the minor and major radial coordinates. For standard MST plasmas, typical values for these parameters are $F \approx -0.2$, $\Theta \approx 1.7$, and $q(r = 0) \approx 0.2$.

The q-profile is of particular significance in understanding tearing modes in MST. The magnetic perturbations that are measured at the edge of MST (see Ch. 3) are resonant inside the plasma volume where a magnetic island can form due to the tearing instability. These islands appear periodically with the same helicity as their associated tearing modes. A condition for resonance of a helical perturbation to the equilibrium magnetic field with a wave vector $\boldsymbol{k} = (m/r)\hat{\theta} - (n/R)\hat{\boldsymbol{\phi}}$ is

$$\boldsymbol{k} \cdot \boldsymbol{B} = 0. \tag{2.8}$$

This expression can be rearranged to obtain the safety factor,

$$q = rB_\phi/RB_\theta = \frac{m}{n}, \tag{2.9}$$

where m and n are the poloidal and toroidal mode numbers, and θ and ϕ are the poloidal and toroidal directions. m and n are integers so that where q is a rational number, the tearing modes are unstable. These locations are called resonant surfaces. The left-hand plot in Fig. 5.3 shows the q-profile and island widths for a typical MST equilibrium. Due to the aspect ratio and relative magnetic field component strengths, the safety factor of the MST RFP is just below 0.2 in the core, passes through zero at the reversal surface and is negative at the edge. This means that the $m = 0$ modes are resonant at the reversal surface, which is the surface where the toroidal field passes through zero before reversing direction at the edge relative to the core, and $m = 1$ modes are resonant away from that surface. The core and mid-radial resonant modes ($m = 1, n = 6 - 9$) are most unstable, with the $n = 6$ mode holding most of the energy. The $n = 5$ mode exhibits unique behavior and only appears as the core value of the safety factor surpasses 0.2, which occurs for a just small portion of the sawtooth cycle (which will be reviewed shortly). The $m = 0$ (all n but mainly $n = 1-4$) mode is linearly stable, but can be driven by nonlinearly coupling to core modes.

The width of these magnetic islands is given by,

$$\Delta_{mn} = 4\sqrt{r_{mn}|\tilde{b}_{rmn}|/(nB_\theta|q'_{mn}|)}, \tag{2.10}$$

where q'_{mn} is the gradient of the q-profile at the (m, n) rational surface [16]. As tearing modes grow in amplitude, magnetic islands begin to overlap with adjacent islands, so that deterministic field line trajectories give way to stochastic magnetic fields. Fig. 2.2 visualizes how stochasticity increases as tearing mode amplitudes increase. The "stochasticity parameter", s, which is plotted on the right-hand side of Fig. 5.3, is given by,

$$s = \frac{\Delta_{mn} + \Delta_{m'n'}}{2|r_{mn} - r_{m'n'}|}. \tag{2.11}$$

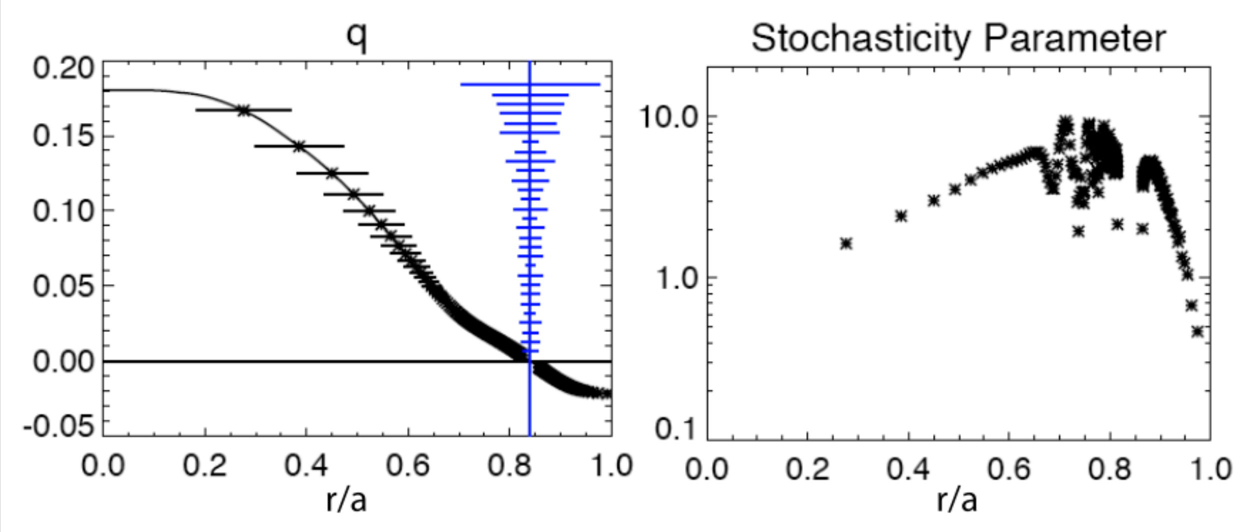

FIGURE 2.1: The left hand plot shows a typical q-profile over the minor radius for MST standard plasma with island widths depicted both in black in the plot and in blue on the right. The right hand figure plots the stochasticity parameter (Eqn. 2.11) over the minor radius of the plasma. Reproduced from [15]

and is a measure of overlap between adjacent islands. In the limit of $s \gg 1$, indicating a large amount of overlap and stochasticity, the radial thermal conductivity, χ, scales like $\chi \sim \tilde{B}_r^2$ as was put forth by Rechester and Rosenbluth[17, 16]. This is qualitatively validated by agreement between mode and temperature behavior, coupled with relatively large tearing mode amplitudes in MST, suggesting that thermal transport is dominated by stochastic transport [18, 19, 15]. When looked at through a more heuristic lens, we know that charged particles tend to follow magnetic field lines, so as the field becomes more and more stochastic with increasing magnetic field fluctuation amplitudes, confinement of these particles and, therefore, energy deteriorates. As such, reducing the magnitude of magnetic field fluctuation amplitudes, and, thereby, minimizing stochasticity, is a good mitigation strategy for this major loss mechanism in RFP plasmas. Promisingly for the RFP fusion concept, it is both theoretically predicted and observed experimentally in the

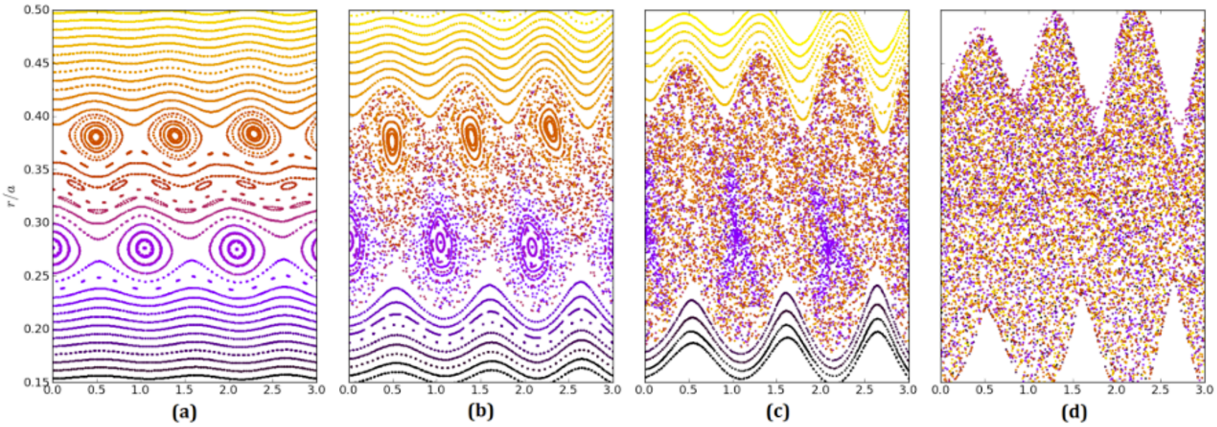

FIGURE 2.2: This figure shows poincare plots of the MST magnetic field lines. As you move from left to right the field lines go from being ordered to somewhat stochastic to completely disordered. These changes occur as tearing mode amplitudes are increased moving from left to right. Reproduced from [20]

analyses of this thesis, that magnetic field fluctuation amplitudes do in fact decrease with increasing Lundquist number (see Ch. 5).

2.1.3 Nonlinear MHD and Sawteeth in MST

Another manifestation of tearing modes in RFP plasmas are “sawteeth.” These are sharp, quasi-periodic events whose signature appears on most every MST diagnostic, an example of which is shown in Fig. 2.3. Rather than being localized to a, e.g., core or edge location, a sawtooth crash is a global event where the entire spectrum of tearing modes grow exponentially and rapidly flatten the current density profile across the entire minor radius.

RFP equilibrium is understood fairly well and can be described by Taylor’s theory

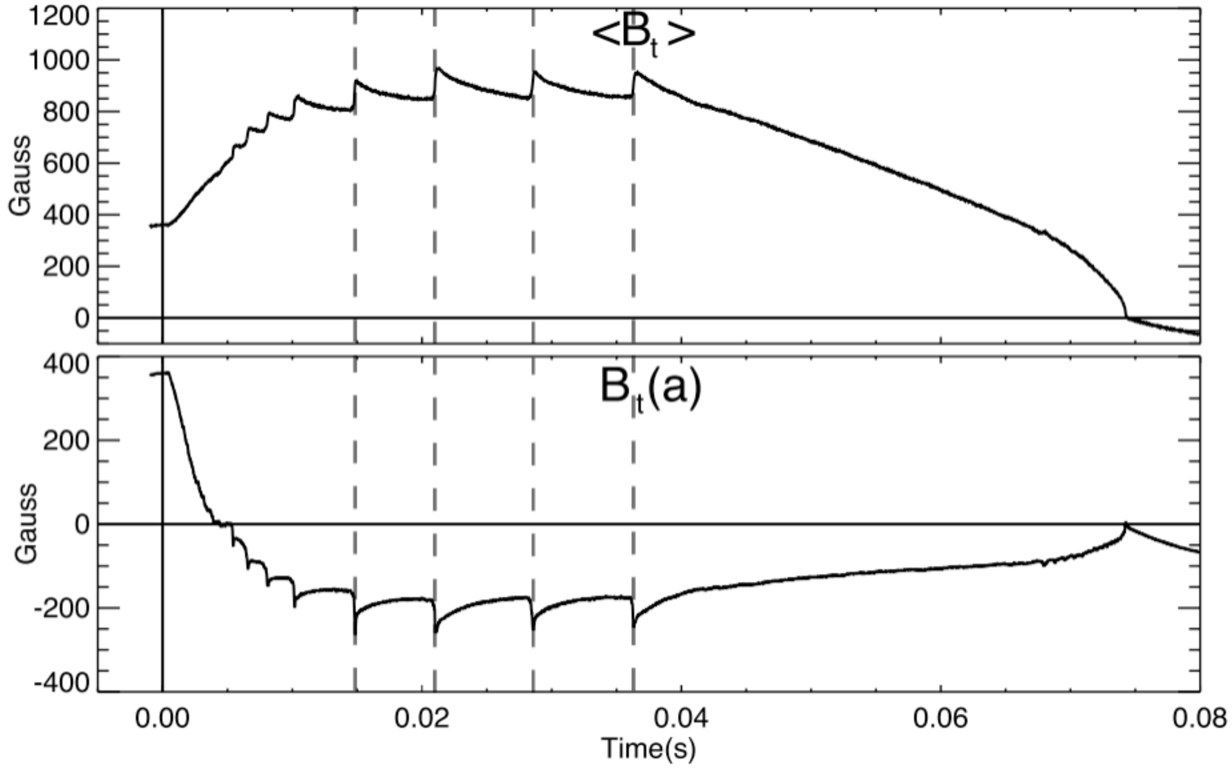

FIGURE 2.3: The top figure plots the average toroidal field and the bottom figure plot the toroidal field at the wall. The waveforms show sharp changes in magnitude at times denoted by the dashed lines. These are manifestations of sawtooth events. This figure is reproduced from [15]

of relaxation [21]. In order to maintain reversal, the plasma must create additional reversed toroidal field to compensate for the classical diffusion processes. This mechanism of anomalous electric field sustainment and generation for time scales longer than the resistive diffusion time is called the dynamo.

This dynamo mechanism is well described by the nonlinear MHD model which captures the nonlinear interactions of MHD instabilities that drive the dynamo [22]. The latter has been most relevant to the RFP dynamo and simulations incorporating this model have successfully recreated the sawtoothing behavior. In the RFP, nonlinear interaction of the m=1 mode is responsible for the RFP sawtooth. As the center of the plasma is heated, either ohmically or externally, the resistivity will decrease as a result of the inverse dependence on temperature and resistivity, and more current will diffuse radially inward so that the current profile becomes peaked in the core. This will in turn lead to a further decrease in resistivity and further peaking of the current profile, causing the on axis value of q to decrease. The $m = 1$ mode has been shown to be the fastest growing mode for the RFP [22, 23, 10], and, as we saw earlier, the RFP has many $m = 1$ modes. The coupling of two $m = 1$ modes with helicities $(m, n) = (1, n_1)$ and $(1, n_2)$ can lead to modes with helicities $(m, n) = (0, n_1 - n_2)$ and $(2, n_1 + n_2)$. The means by which these modes interact is actively being investigated.

In this thesis, as Lundquist number was decreased to values that had been inaccessible prior to the implementation of the programmable power supply system that will be discussed in Ch. 3, a transition from discrete sawtoothing activity to more quasi-continuous sawtoothing behavior was observed at a Lundquist number $S \sim 10^5$, as is depicted in Fig. 2.4. This observation aligns with results obtained in simulations. This effect is not entirely understood and its characterization has proven difficult. We will discuss it in more detail

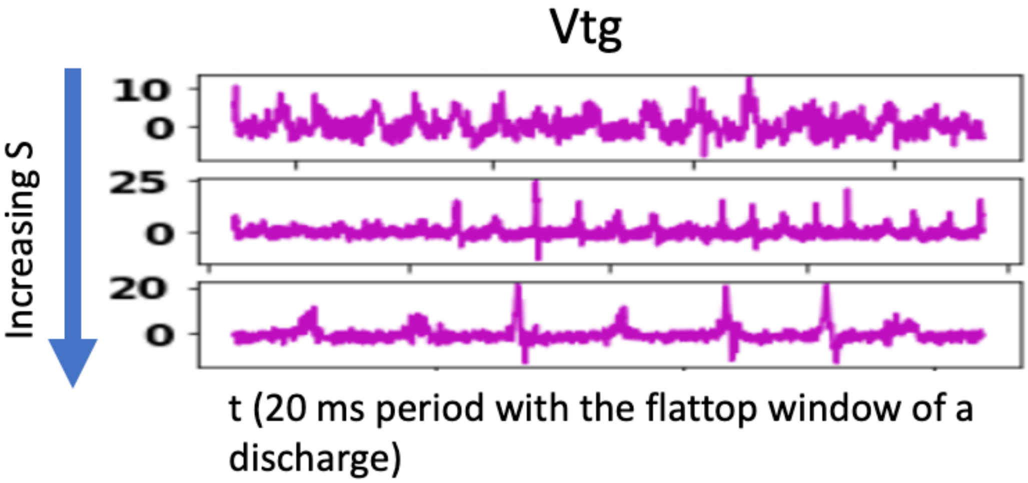

FIGURE 2.4: This figure plots the toroidal gap voltage signal of a 20 ms time window from the flattop period of three example discharges. The top row is from a discharge with $S < 10^5$, for the middle row, $S \sim 10^5$ and for the bottom row, $S > 10^5$. This visualizes the transition from quasi-continuous to the more bursty sawtoothing activity that we are familiar with in MST RFP discharges.

and its implication on analyses in Chs. 5 and 6.

2.2 Computational Codes

In this section, we will touch base on two codes used to simulate plasmas created in the MST experiment. As fusion devices scale to larger and larger sizes, the development of computational codes as a tool to predict plasma behavior is especially vital. Computational codes are limited in the range of Lundquist numbers they can simulate: as resitivity drops (Lundquist number increases) the expense of performing a simulation increases. Fig. 2.5 shows the ranges of Lundquist number accessible for the simulations and the

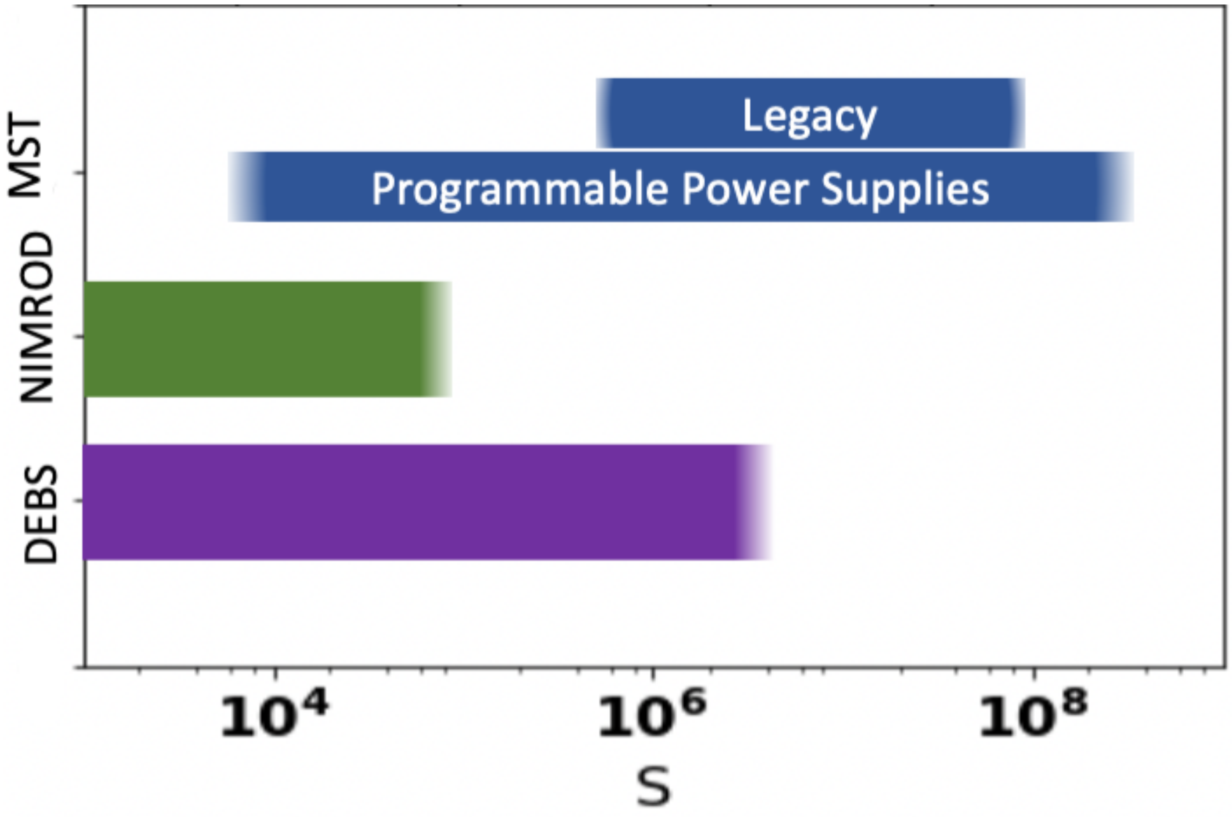

FIGURE 2.5: This diagram depicts the achievable ranges of Lundquist number with the various MST power supplies and the two simulation codes used in this thesis.

power supplies used in this thesis. As the experimentally achievable value of Lundquist number was lowered in MST, this allowed for greater overlap and more meaningful comparisons with DEBS and NIMROD simulation results. We will now briefly describe these codes. The reader may refer to the references herein for more detailed explanations of their intracacies.

2.2.1 DEBS

DEBS computes the 3-D, nonlinear, resistive, force free, single-fluid MHD equations in a periodic cylinder[24]. These single-fluid visco-resistive MHD equations are given by

$$\frac{\partial \boldsymbol{A}}{\partial t} = S\boldsymbol{V} \times \boldsymbol{B} - \eta \boldsymbol{J} \tag{2.12}$$

$$\rho \frac{\partial \boldsymbol{V}}{\partial t} = -S\rho \boldsymbol{V} \cdot \nabla \boldsymbol{V} + S\boldsymbol{J} \times B + \frac{\nu}{\eta} \nabla^2 \boldsymbol{V} \tag{2.13}$$

where $\boldsymbol{A}$, $\boldsymbol{V}$, $\boldsymbol{B}$, $\boldsymbol{J}$, ρ, ν, and η are dimensionless parameters representing the vector potential, velocity, magnetic field, current density, density, viscosity, and resistivity, and S is the Lundquist number. An advantage of using DEBS to simulate MST plasmas is that it can be run with dynamically-adjusted viscosity to dissipate energy at small scales. This allows for larger computational time steps. However, using an artificial viscosity that increases as needed to reduce grid-scale fluctuations during these relaxation events has an unclear effect on the computed evolution. Another aspect to note is that the pressure is not self-consistently evolved (i.e. $\beta = \frac{p_{thermal}}{p_{magnetic}} = 0$) so that the resistivity profile cannot be self-consistently calculated. The resistivity profile can, however, be calculated from experimental data and applied as a constraint to the simulations. DEBS has successfully reproduced the sawtooth events and q profiles observed in MST.

For the simulations used in this thesis, a neoclassical resistivity profile was used. The profile was the same as that used with the NIMROD simulations covered in the next section. The DEBS simulations were run for the $m = 1, n = 5 - 8$ modes applying a flat viscosity profile and either holding $a\lambda_0$ fixed or holding the reversal parameter fixed where a is the scale length of the system and λ_0 is a global constant for the solution of the variational problem that minimizes the magnetic energy and conserves the magnetic helicity (i.e. $\mu_0 \boldsymbol{J} = \nabla \times \boldsymbol{B} = \lambda(r)\boldsymbol{B}$, and $\lambda(r) = \lambda_0 f(r)$, where $\lambda_0 = \lambda(r = 0)$).

2.2.2 NIMROD

The NIMROD (Non-Ideal Magnetohydrodynamics, with Rotation - Open Discussion) code [25] can be used to simulate nonlinear plasma evolution in a wide variety of configurations. It is an initial value solver for the extended MHD system of equations. As was discussed earlier in this chapter, most derivations of the MHD equations ignore dissipative effects or use collisional equations as closures (e.g. Braginskii). The extended MHD equations on the other hand are developed from two-fluid equations with general closures for the conductive heat flux and the stress tensor, which provides a reasonable basis for describing macroscopic plasma effects for arbitrary collisionality regimes. As such, these equations capture effects not only from the ideal and resistive MHD models but also the reduced, neoclassical and two-fluid models. The generalized Ohm's Law and momentum equation for this set of equations are,

$$\boldsymbol{E} = -\boldsymbol{v} \times \boldsymbol{B} + \frac{\boldsymbol{J} \times \boldsymbol{B}}{en} - \frac{\nabla p_e}{en} + \eta \boldsymbol{J} + \frac{m_e}{e^2 n} \frac{\partial \boldsymbol{J}}{\partial t} \tag{2.14}$$

$$m_i n \frac{\partial \boldsymbol{v}}{\partial t} = \boldsymbol{J} \times \boldsymbol{B} - \nabla p - \nabla \cdot \boldsymbol{\Pi}_{gyro} - \nabla \cdot \nu m_i n \boldsymbol{W} \tag{2.15}$$

where m_i and m_e are electron and ion masses, n is density, $\boldsymbol{\Pi}_{gyro}$ is the gyroviscous stress tensor, and $\boldsymbol{W} = \nabla \mathbf{v} + (\nabla \mathbf{v})^{\mathbf{T}} - \frac{\mathbf{2}}{\mathbf{3}}\mathbf{I}(\nabla \cdot \mathbf{v})$.

For a more thorough discussion of the NIMROD code and how it can be used to simulate RFP plasmas, please refer to [26, 23, 25, 27].

The NIMROD simulations used as a basis of comparison for this effort were performed using a single-fluid, cylindrical geometry set-up at two electron densities in two different contexts, keeping the reversal parameter, F, fixed and keeping $a\lambda_0$ fixed. Just as with the DEBS simulations, a flat viscosity profile was applied.

Bibliography

[1] M. R. Stoneking, J. T. Chapman, D. J. Den Hartog, S. C. Prager, and J. S. Sarff, "Experimental scaling of fluctuations and confinement with lundquist number in the reversed-field pinch," *Physics of Plasmas*, vol. 5, no. 4, pp. 1004–1014, 1998. [Online]. Available: https://doi.org/10.1063/1.872670

[2] S. Cappello and D. Biskamp, "Reconnection processes and scaling laws in reversed field pinch magnetohydrodynamics," *Nuclear Fusion*, vol. 36, no. 5, pp. 571–581, may 1996. [Online]. Available: https://doi.org/10.1088/0029-5515/36/5/i05

[3] C. Sovinec, "Magnetohydrodynamic simulations of noninducitve helicity injection in the reversed-field pinch and tokamak," Ph.D. dissertation, University of Wisconsin at Madison, 1995.

[4] E. Butt, R. Carruther, J. Mitchell, R. Pease, P. Thonemann, M. Bird, J. Blears, and E. Hartill, "The design and performance of zeta," *Second United Nations International Conference on the Peaceful Uses of Atomic Energy*, 1958. [Online]. Available: (http://cds.cern.ch/record/279634/files/geneva-1958-vol-32.pdf#page=50

[5] D. Robinson and R. King, "Factor influencing the period of improved stability in zeta," *Third International conference on Plasma Physics and Controlled Nuclear Fusion Research*, pp. 263–76, 1968. [Online]. Available: https://nds.iaea.org/publications/proceedings/sti-pub-192(v1).pdf#page=279

[6] J. Freidburg, *Ideal Magnetohydrodynamics*. New York: Plenum, 1987.

[7] W. Cooper, I. Chapman, O. Schmitz, A. Turnbull, B. Tobias, E. Lazarus, F. Turco, M. Lanctot, T. Evans, J. Graves, D. Brunetti, D. Pfefferlé, H. Reimerdes, O. Sauter,

F. Halpern, T. Tran, S. Coda, B. Duval, B. Labit, A. Pochelon, M. Turnyanskiy, L. Lao, T. Luce, R. Buttery, J. Ferron, E. Hollmann, C. Petty, M. van Zeeland, M. Fenstermacher, J. Hanson, and H. Lütjens, "Bifurcated helical core equilibrium states in tokamaks," *Nuclear Fusion*, vol. 53, no. 7, p. 073021, jun 2013. [Online]. Available: https://doi.org/10.1088/0029-5515/53/7/073021

[8] I. Krebs, S. C. Jardin, S. Günter, K. Lackner, M. Hoelzl, E. Strumberger, and N. Ferraro, "Magnetic flux pumping in 3d nonlinear magnetohydrodynamic simulations," *Physics of Plasmas*, vol. 24, no. 10, p. 102511, 2017. [Online]. Available: https://doi.org/10.1063/1.4990704

[9] T. R. Jarboe, "Review of spheromak research," *Plasma Physics and Controlled Fusion*, vol. 36, no. 6, pp. 945–990, jun 1994. [Online]. Available: https://doi.org/10.1088/0741-3335/36/6/002

[10] L. Marrelli, P. Martin, M. Puiatti, J. Sarff, B. Chapman, J. Drake, D. Escande, and S. Masamune, "The reversed field pinch," *Nuclear Fusion*, vol. 61, no. 2, p. 023001, jan 2021. [Online]. Available: https://doi.org/10.1088/1741-4326/abc06c

[11] M. Yamada, R. Kulsrud, and H. Ji, "Magnetic reconnection," *Rev. Mod. Phys.*, vol. 82, pp. 603–664, Mar 2010. [Online]. Available: https://link.aps.org/doi/10.1103/RevModPhys.82.603

[12] D. Biskamp, *Nonlinear Magnetohydrodynamics*. Cambridge University Press, 1993.

[13] H. Ji, S. C. Prager, and J. S. Sarff, "Conservation of magnetic helicity during plasma relaxation," *Phys. Rev. Lett.*, vol. 74, pp. 2945–2948, Apr 1995. [Online]. Available: https://link.aps.org/doi/10.1103/PhysRevLett.74.2945

[14] R. Hazeltine and J. Meiss, *Plasma Confinement*. Mineola, NY: Dover Publications, 2003.

[15] J. Reusch, "Measured and simulated electron thermal transport in the madison symmetric torus reversed field pinch," Ph.D. dissertation, University of Wisconsin at Madison, 2011.

[16] T. Biewer, "Electron thermal transport in the madison symmetric torus," Ph.D. dissertation, University of Wisconsin at Madison, 2002.

[17] A. B. Rechester and M. N. Rosenbluth, "Electron heat transport in a tokamak with destroyed magnetic surfaces," *Phys. Rev. Lett.*, vol. 40, pp. 38–41, Jan 1978. [Online]. Available: https://link.aps.org/doi/10.1103/PhysRevLett.40.38

[18] T. M. Biewer, C. B. Forest, J. K. Anderson, G. Fiksel, B. Hudson, S. C. Prager, J. S. Sarff, J. C. Wright, D. L. Brower, W. X. Ding, and S. D. Terry, "Electron heat transport measured in a stochastic magnetic field," *Phys. Rev. Lett.*, vol. 91, p. 045004, Jul 2003. [Online]. Available: https://link.aps.org/doi/10.1103/PhysRevLett.91.045004

[19] Y. Yang, "Stochastic transport in ppcd discharges," Ph.D. dissertation, University of Wisconsin at Madison, 2010.

[20] L. Morton, "Turbulence and transport in magnetic islands in mst and diii-d," Ph.D. dissertation, University of Wisconsin at Madison, 2016.

[21] J. B. Taylor, "Relaxation and magnetic reconnection in plasmas," *Rev. Mod. Phys.*, vol. 58, pp. 741–763, Jul 1986. [Online]. Available: https://link.aps.org/doi/10.1103/RevModPhys.58.741

[22] J. Becksted, “Sawteeth in the mst reversed field pinch,” Ph.D. dissertation, University of Wisconsin at Madison, 1990.

[23] J. Sauppe, “Extended magnetohydrodynamic modeling of plasma relaxation dynamics in the reversed-field pinch,” Ph.D. dissertation, University of Wisconsin at Madison, 2015.

[24] D. Schnack, D. Barnes, Z. Mikic, D. S. Harned, and E. Caramana, “Semi-implicit magnetohydrodynamic calculations,” *Journal of Computational Physics*, vol. 70, no. 2, pp. 330–354, 1987. [Online]. Available: https://www.sciencedirect.com/science/article/pii/0021999187901860

[25] C. Sovinec, A. Glasser, T. Gianakon, D. Barnes, R. Nebel, S. Kruger, D. Schnack, S. Plimpton, A. Tarditi, and M. Chu, “Nonlinear magnetohydrodynamics simulation using high-order finite elements,” *Journal of Computational Physics*, vol. 195, no. 1, pp. 355–386, 2004. [Online]. Available: https://www.sciencedirect.com/science/article/pii/S0021999103005369

[26] C. Sovinec and J. King, “Analysis of a mixed semi-implicit/implicit algorithm for low-frequency two-fluid plasma modeling,” *Journal of Computational Physics*, vol. 229, no. 16, pp. 5803–5819, 2010. [Online]. Available: https://www.sciencedirect.com/science/article/pii/S0021999110001981

[27] U. Gupta and C. R. Sovinec, “Pressure-driven tearing and thermal transport in finite-beta reversed field pinch computations,” *Physics of Plasmas*, vol. 30, no. 1, 01 2023, 013901. [Online]. Available: https://doi.org/10.1063/5.0124281

Chapter 3

The Madison Symmetric Torus

The Madison Symmetric Torus (MST) is a toroidal device that is used to study basic plasma physics and fusion reactor concepts. It can be operated in several reversed-field pinch modes and as a low-field tokamak. In this thesis, data were collected from standard reversed-field pinch (RFP) plasmas, with no application of enhanced confinement techniques.

MST's features include an extensive diagnostic suite, enabled by minimal external field coils, and an upgraded programmable power supply (PPS) system that has expanded the range of currents and operational schemes available on the device. These features were crucial to the success of this work's endeavor to characterize Lundquist number scaling in reversed-field pinch plasmas.

In this chapter, the relevant intricacies of the MST device will be reviewed. To begin, we will discuss the device itself: its operation as a reversed-field pinch and the power supplies fueling its operation. In the subsequent sections, we will go over the systems used to diagnose the plasmas, starting with the magnetic field coil array and MSTFit, then the spectral diagnostics used to measure electron temperature and collect data for an estimate of the effective charge state of standard plasmas. A overview of the Thomson scattering diagnostic, which was particularly vital to this effort, will be reserved for the next chapter, where it can be given more attention.

3.1 Generating Standard RFP Plasmas and MST Power Supplies

Measuring RFP plasmas at a wide range of Lundquist numbers was one of the main experimental accomplishments of this thesis. In this section, MST's mechanism for generating standard RFP plasmas will be described. We will also cover the original or, as it's commonly called, ”Legacy” power supply system, then move on to describing the programmable power supplies (PPS) which have enabled access to a wider range of parameter space and were an upgrade to MST that in large part inspired this undertaking. We will conclude this section with a discussion of the fueling and conditioning done on the device during operation.

3.1.1 Standard RFP Plasma Generation and the Legacy Power Supply

Fig. 3.1 contains two depictions the MST device. Fig. 3.1a shows a rendering of the MST device, featuring the iron-core transformer, C-windings, and pumping duct. Fig. 3.1b is a top-down photo of MST before any diagnostics were added, which showcases the unusually large amount of space available to diagnostics. MST is composed of a 5-cm thick aluminum, toroidally-shaped shell with a major radius of 1.5 m and a minor radius of 0.52 m tightly wrapped around an iron core and a pumping duct designed to avoid the magnetic field errors that would arise with large pumping ports [1]. This

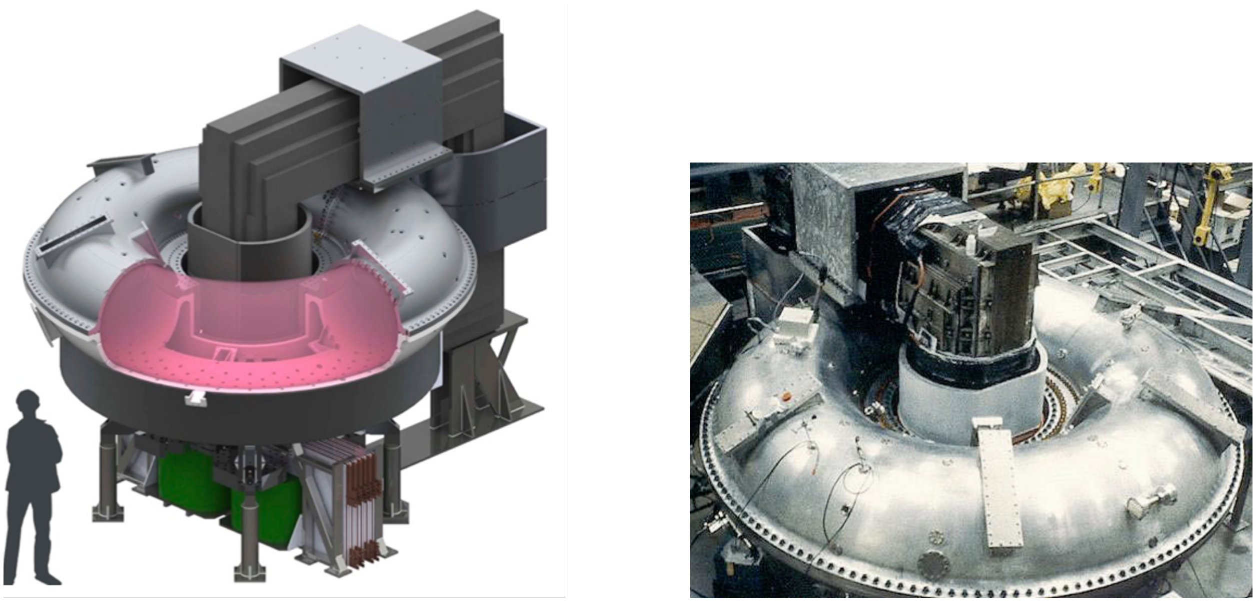

(A)

(B)

FIGURE 3.1: Fig. 3.1a shows a mock-up of the MST device. The iron core transformer that is used to drive the toroidal electric field is visible. Fig. 3.1b is a photo of the MST device from above before the installation of diagnostics.

shell acts as a vacuum vessel that maintains a pressure around 10^{-7} torr and as a single-turn toroidal field winding. It also acts to stabilize external ideal kink modes. Wrapped around this vessel is the 40-turn iron-core transformer. To generate a standard plasma discharge, deuterium gas is puffed into the vacuum vessel and an inductive electric field is applied, breaking down the gas into a plasma which then self-organizes and relaxes into the reversed-field pinch configuration that was covered in Chapter 2. In this subsection, we will go into more detail about the magnetic fields involved in this process and the ''Legacy'' power supply system.

Poloidal Field System

The poloidal field (PF) system generates the poloidal magnetic field and the toroidal plasma current. Its main components are the continuity or C-windings and the poloidal flange, the poloidal field (PF) winding, and the bias winding. A schematic is shown in Fig. 3.2 [2].

The C-winding is a conducting sheet that connects the two sides of the poloidal gap, circling around, but not connecting to, the iron transformer. It is necessary to mitigate error fields, or unwanted magnetic fields, that would otherwise arise. The C-winding in effect carries the image current on the inner surface of the vessel wall across the insulated poloidal gap. Without this, the image current would transfer to the outside surface of the vessel generating a large radial magnetic field at the gap. [2].

The PF winding magnetizes the transformer to create the inductive electric field that forms the plasma current. It consists of 40 copper bars that surround the outside of the C-winding and pierce the poloidal flange. Strong mutual coupling of the PF winding and C-winding help control the image current to minimize field errors. . The PF winding is wound in eight bundles of five turns which can be configured in series or parallel combinations to set the turn ratio between 5:1 and 40:1 [2].

The bias winding is a 40-turn winding that is situated inside the C-winding tight to the iron core. It reverses the bias flux in the iron core so that a full 2-Wb flux swing can be achieved. It is designed and wound to ensure that the flux leakage into the plasma volume is minimized. [2].

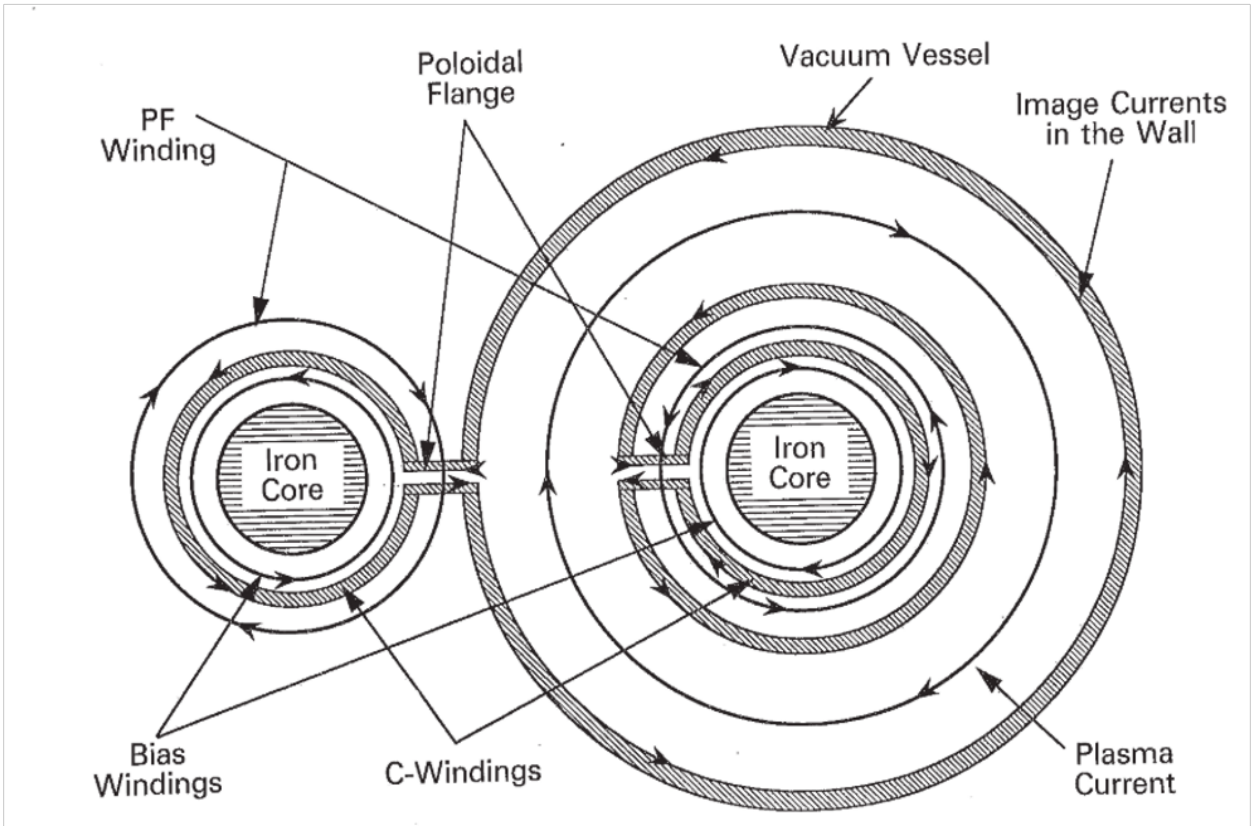

FIGURE 3.2: A schematic of the MST Poloidal Field System

Toroidal Field System

Most of MST's toroidal field is generated by poloidal current in the plasma via the pinch effect and dynamo action. The TF circuit provides a small initial toroidal field for plasma formation, then acts to sustain the reversed field at the plasma surface. The toroidal field (TF) system is shown in Fig. 3.3. Poloidal current is driven through the aluminum shell acting as a single-turn winding. Current enters the shell at the toriodal gap, located at the midplane on the inside of the torus, fed in by an axisymmetric flange system that symmetrizes the shell currents. The dominant resonant Fourier component of the ripple in the toroidal magnetic field is m= 0, n= 4 and has a normalized amplitude of ≈ 0.01 on the machine minor axis. The error is resonant at the toroidal field reversal surface, and the resultant magnetic island width is 1 cm [2, 3]. The toroidal field circuit can have an impact on the way sawteeth are formed as changes in the toroidal flux induced by the RFP's dynamo effect couple into the TF circuit.

3.1.2 Legacy Power Supply System

The Legacy power supply is a large ignitron-based pulse-forming network (PFN) that stores up to 2 MJ of energy. When using the Legacy power supply system, four large capacitor banks supply power to the PF-winding. The voltages applied and the number of banks used can be varied to control the discharge duration and plasma current (the two parameters correlated parameters). A primary B_t capacitor bank is fired 10-15 ms prior to the start of the plasma discharge to create the initial toroidal field. A low-voltage B_t crowbar capacitor bank is sometimes used to sustain field reversal late in the discharge by sending current in the reversed direction [2, 3].

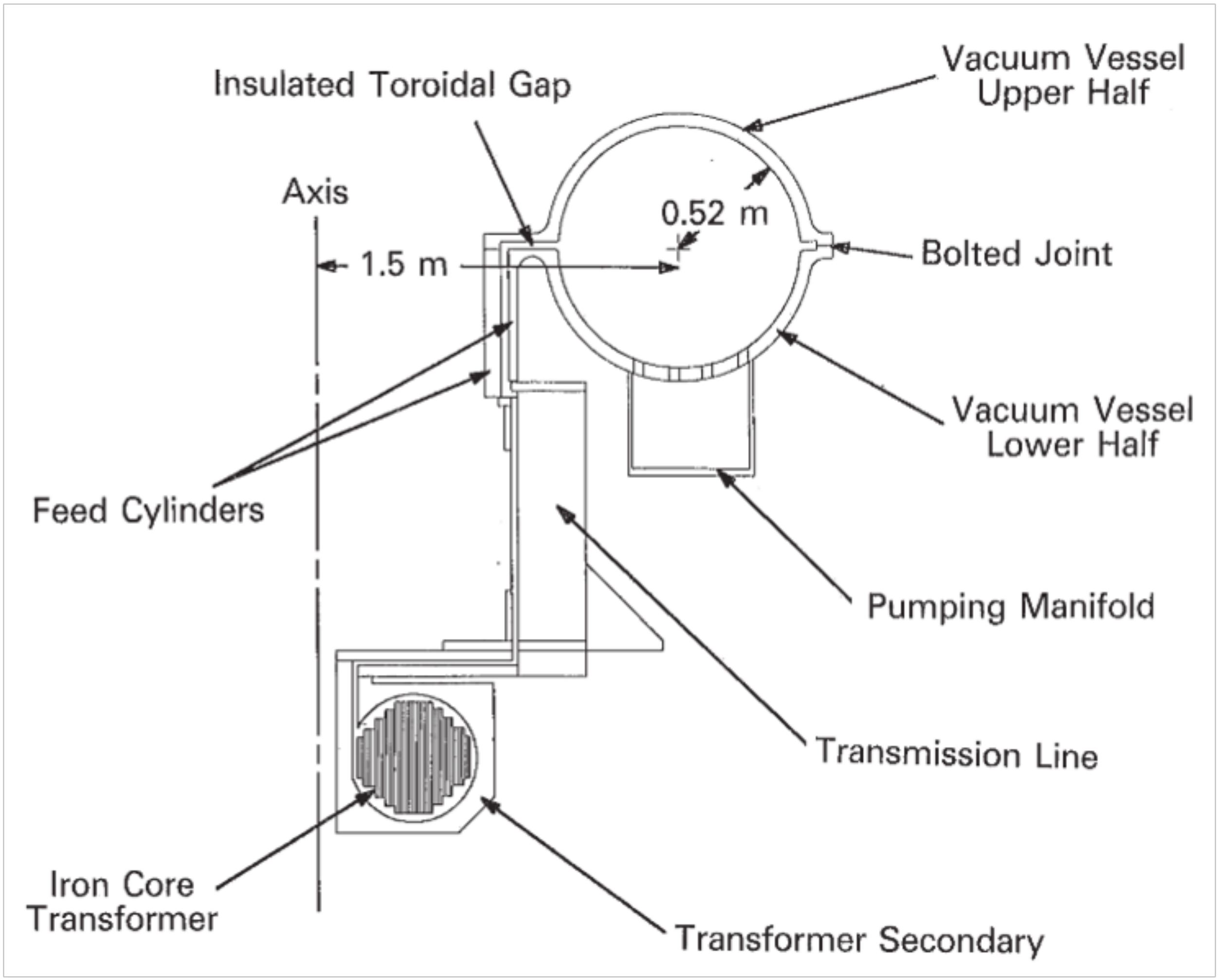

FIGURE 3.3: A schematic of the MST Toloidal Field System

The iron core transformer is capable of a flux change of 2 webers when it is initially reverse-biased to -1 weber. For reference, one weber provides one volt of inductive drive for a period of one second. With the Legacy power supply system, achievable plasma currents range from about 200 kA to 600 kA with discharges lasting less than 100 ms and inductive toroidal loop voltage peaking at approximately 20 V. The plasma current is constant during what is called the flat top phase of the discharge for about 20 ms.

3.1.3 Programmable Power Supply Systems

Inductive control is at the heart of the science and the plasma control potential of the RFP, given its nature, even more so than other fusion concepts. In this section, we will cover the programmable power supply (PPS) upgrades to both the toroidal (BT-PPS) and poloidal (BP-PPS) field generation systems. Programmable power supplies are used in several fusion experiments; the unique challenge of applying these systems to RFPs stems from the large power flow between the toroidal and poloidal magnetic field circuits via nonlinear relaxation process inherent in and regulated by RFP plasmas. At present, the programmable power supplies permit for low current operation, which has allowed experiments to achieve Lundquist numbers that overlap more with those achieved in computational results. This low current operation is also being used to test advanced control schemes before applying these to high currents [4]. The modular design of the supplies will enable scaling the power supplies to make higher plasma current discharges possible [5]. These upgrades have in large part motivated this thesis, and additionally, the profile control provided by these systems enabled the observations presented in Ch. 6. We will go over both the BT-PPS and BP-PPS systems below. Larger, more capable supplies are currently under construction.

BT-PPS

The BT-PPS grants greater control over the toroidal field. At the start of a discharge, it allows a larger toroidal field magnitude. This helps to minimize the resistance so that higher currents can be reached and the BP transformer's capacity can be more fully utilized, since less flux is consumed during the startup of the plasma discharge. Ultimately, this maximizes the I_p and the discharge duration by safely utilizing the full 2 webber swing of the iron-core transformer in the poloidal field circuit. This is in part achieved by doubling the turns ratio in the toroidal field transformer. BT transformer windings can be connected at ratios of 20:1, 40:1, and 80:1 [6, 5].

The hardware basis of the BT-PPS system is 128 fast-switching solid-state insulated gate bipolar transistors (IGBTs) H-bridges. The system controls the discharge of MST's capacitor bank. The supply's maximum voltage (± 1800 V) and current (± 25 kA) are applied with a bandwidth of several kHz. The switching cycle time for the system is 100 μs [6].

The BT-PPS for this work was operated with open-loop feedback control so that the supply's output current targeted a preprogrammed waveform. The control system was able to hold plasma currents, and therefore, other plasma parameters such as density more uniform than is achievable with Legacy system operation. This enabled the spectral analyses discussed in Ch. 6 and improved the Thomson scattering pulse summing analysis technique used to resolve low-density edge Thomson scattering measurements which will be described in Ch. 4. Three-level Pulse Width Modulation (PWM) with a carrier frequency of 5kHz generates the desired analog toroidal field waveform [5]. Open-loop feedback control is a relatively simple operational mode and more sophisticated methods are necessary to respond in real time to changes resulting from plasma relaxation.

Goumiri, et. al [4] have been developing the MST Control System (MSTCS) and basic closed-loop feedback control has been demonstrated.

BP-PPS

While the BT-PPS system increases B_t during start up, the BP-PPS system increases the range of accessible plasma currents and extends the duration of a plasma discharge. The BP-PPS system design is based on the BT-PPS design. The poloidal field is generated using MST's 40-turn iron-core BP transformer. Triplets of H-bridge modules in series generate an output voltage of ± 2500 V. Thirty-two of these triplets yield a total primary current of 75 kA. Each of the three modules of a series of triplets can be controlled independently. A seven-level PWM strategy was selected for the BP-PPS system over a three-level PWM because it demonstrated less switching noise and output ripple and can output significantly more current [5].

At present, the supplies have greatly expanded the lower bound of achievable plasma currents from 200 kA to $\lessapprox 30$ kA, or from $S \sim 10^6$ down to $S \sim 10^4$. This has enabled larger overlap with simulated results from computational codes as we will see in Ch. 5. While MST's ultimate upper bound on I_p will in part be determined by plasma behavior, a power balance calculation for relaxed-state equilibrium, which was benchmarked to actual MST plasmas, estimates that the upper bound of plasma currents could be pushed from 600 kA to as high as 800 kA [6]. In standard plasmas, $T_e \sim I_p$, and so, recalling from Ch. 2 that $S \sim T_e^{3/2} I_p$, Lundquist number scales like $S \sim I_p^{5/2}$. This expansion of the upper limit of I_p could then consequently make $S \sim 10^8$ achievable in MST plasmas.

For low current operation, plasma durations have been doubled. To generate these longer lasting plasmas, a newly added auxiliary capacitor bank (that is not suited for larger current or waveform control) is fired and the BT-PPS system is employed for higher startup B_t. Additionally and most importantly, the BP-PPS system controls currents so that output currents will be limited to safe outputs should the poloidal transformer core saturate due to, e.g., early plasma termination. Fig. 3.4 shows a block diagram summarizing the BP-PPS system.

3.1.4 Fueling and Conditioning

This subsection describes the fueling and conditioning practices followed during the data collection that generated the database for this thesis. These practices control the density and quality of plasma that are generated by the MST device. Beginning with conditioning, for typical MST operation, it is considered best practice to run the pulsed-discharge cleaning (PDC) system beginning at the end of one day of operation and concluding at the start of the next. The PDC system generates a few-ms-long 0.1 MA helium plasma [6]. Normally, discharge conditioning is not required during the run day. The PDC process is recommended for consistency but is not always necessary for quality data collection. However, its impact on the data results is not thoroughly understood.

Exceptions were made to this best practice during data collection for this study. PDC was not run during data collection with the PPS system. Running the PPS system required a change in the winding ratio of the transformers. This in turn affected the capability to operate the PDC system. Therefore these data were collected without having run PDC the night prior. Additionally, there were issues with the functionality of the PDC system during some of the data collection, so some Legacy data are also from days when the PDC system had not been run the night prior. PDC was available during 500 kA, high current, high density runs when its potential impact was most crucial as this day was challenging

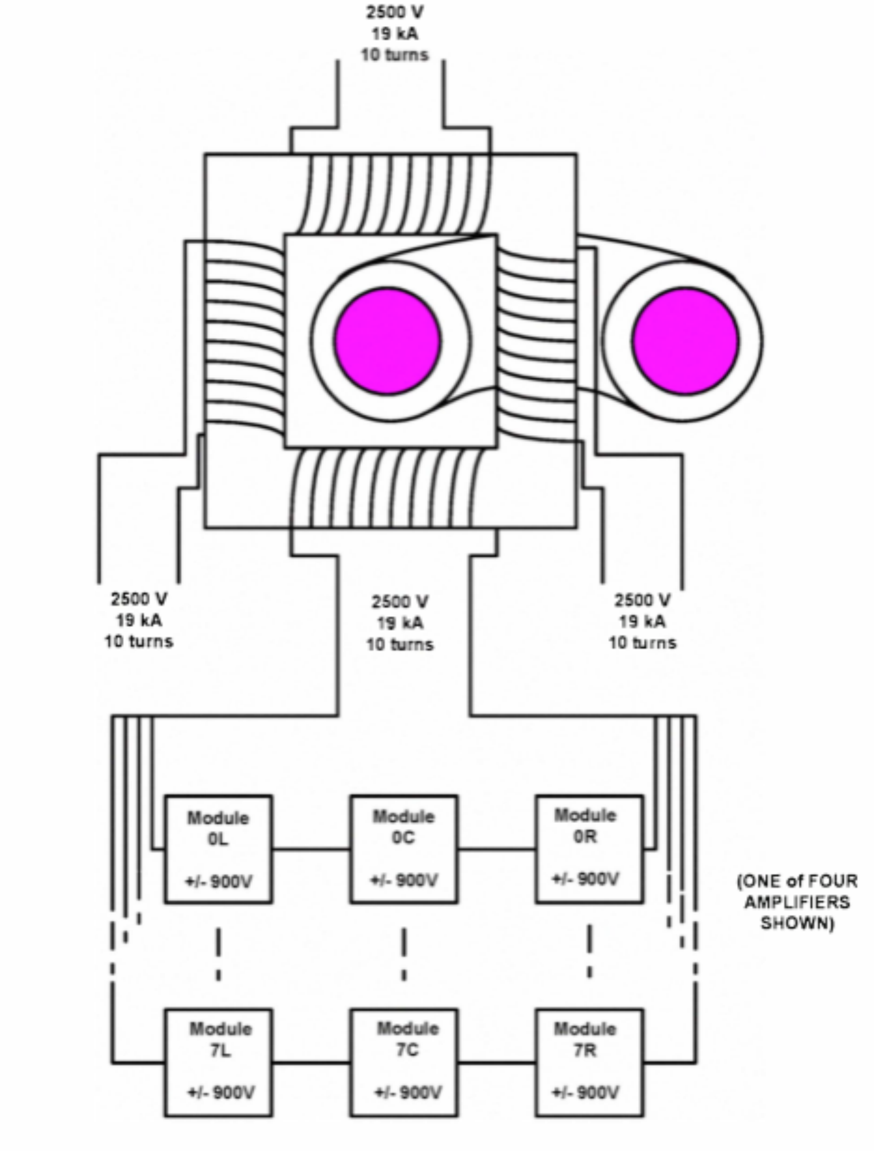

FIGURE 3.4: A block diagram of the BP-PPS system reproduced from [5]

operationally even with PDC. A spreadsheet that details the conditioning status for each run day is included with the database generated for this thesis. Instructions for accessing that can be found in Appendix A.

The plasma quality and control seemed largely unaffected by a lack of PDC conditioning on the days for the S-scaling data collection that had lacked PDC conditioning. The machine was poorly conditioned during the quasi-continuous to bursty reconnection activity data collection. However, poor conditioning can be due to a number of factors, not just a lack of PDC. Altering the operational strategy did improve data collection on these days. These data were collected using the PPS system, so conditioning was not performed using the PDC system in between run days. The density control was somewhat challenging during these days and a few strategies were adopted to improve plasma control. First, at the beginning of the run day, and following any breaks in operation, or premature plasma terminations, the plasma was conditioned with tens of shots of 250 kA plasmas. Second it was helpful to sweep the density from low to high instead of from high to low so that the wall loading of gas would gradually contribute to building up density levels. Again, the details from these run days are included in spreadsheets from the run days that are in the database.

Next, we will move onto a discussion of plasma fueling. To fuel the plasmas, deuterium gas is puffed in from the walls and is supplemented by the residual gas that is inevitably loaded onto the walls of the device [7]. For legacy operation, gas is puffed: (1) prior to the discharge, (2) at the anticipated end of the discharge, and (3) at periods during the discharge. The goals for these puffing periods are: (1) to provide enough fuel so that a plasma is generated but not so much that the gas fails to break down, (2) to maintain a load at the end of the discharge and prevent the rise of current through the transformer primary, and (3) maintain a constant electron density over the duration of the plasma flattop.

Puffing during the PPS operation using the BT-PPS system was slightly more nuanced. The firing of the PPS system is timed differently than the Legacy system. If gas is puffed too early, a pre-discharge plasma forms. This is sometimes considered to be harmful to the quality of the discharge. However, this was not strictly avoided during data collection for this project as it was sometimes useful in achieving desired density levels and did not seem to affect the quality of the discharges.

3.2 Measuring Magnetic Fields and MSTFit

The measurements of magnetic fields were crucial data for the analyses presented in this thesis. Recall from the previous chapter that the magnetic field fluctuation amplitude was a key scaling relationship studied in this work. In this section, we will cover the relevant magnetic field coil arrays that were used to measure these magnetic fields as well as the equilibrium solver, MSTFit.

3.2.1 Magnetic Field Coil Arrays

Magnetic field coils are a crucial diagnostic on MST. Tearing modes are a dominant feature of MST plasmas and the toroidal array is used to measure them. The toroidal array, shown in Fig. 3.5, consists of orthogonal triplets of magnetic pick up coils (measuring B_ϕ, B_θ, B_r) that are mounted on the inside of the vessel (i.e at $r/a = 1$) at $241°$ poloidal. The coils produce a voltage proportional to the time derivative of the local magnetic field. Integrating this signal over time gives the magnetic field amplitude. Fourier analyses, which will be covered in more detail shortly, can be and are robustly and routinely performed to determine the amplitude and phase of the tearing modes [8, 9]. The poloidal coils from these triplets were used for the scaling analysis. These coils most effectively measure the m=1 mode. The toroidal coils in the coil sets tend to collect data not only from the m=1 mode, but also from higher poloidal mode number data. However scaling from these coils is also included in the analysis presented later. The resolution and systematic errors associated with these coils is difficult to assess. Therefore systematic errors are not reported and only statistical errors are used when presenting magnetics data.

Fourier mode decomposition analysis was performed on data taken from the toroidal array. In plasma physics, it is common practice to characterize fluctuations in a framework of mode number content. As was mentioned in Ch. 2, m is the poloidal mode number, or the number of periods in one poloidal circumference, and n is the toroidal mode mode, or the number of periods in one toroidal circumference. The Fourier decompositions were performed so that,

$$B(\phi,t) = \sum_{n=0}^{N} B_n(t) cos(n\phi - \delta_n(t)) \tag{3.1}$$

where $B(\phi,t)$ is the measured magnetic field as a function of toroidal angle and time, B_n is the amplitude of the tearing mode with toroidal mode number n, δ_n is the phase of the n mode, and N is the Nyquist limit of the sampling (determined by the number of coils used). Total number of coils employed when looking at the poloidal coil was 32, and when using the toroidal coils in the toroidal array was 64 [7, 10]. Because the toroidal array is at one poloidal location, it cannot distinguish the poloidal mode number, m. The magnitudes, $B_{theta,n}$, were used to calculate the normalized magnetic field fluctuation

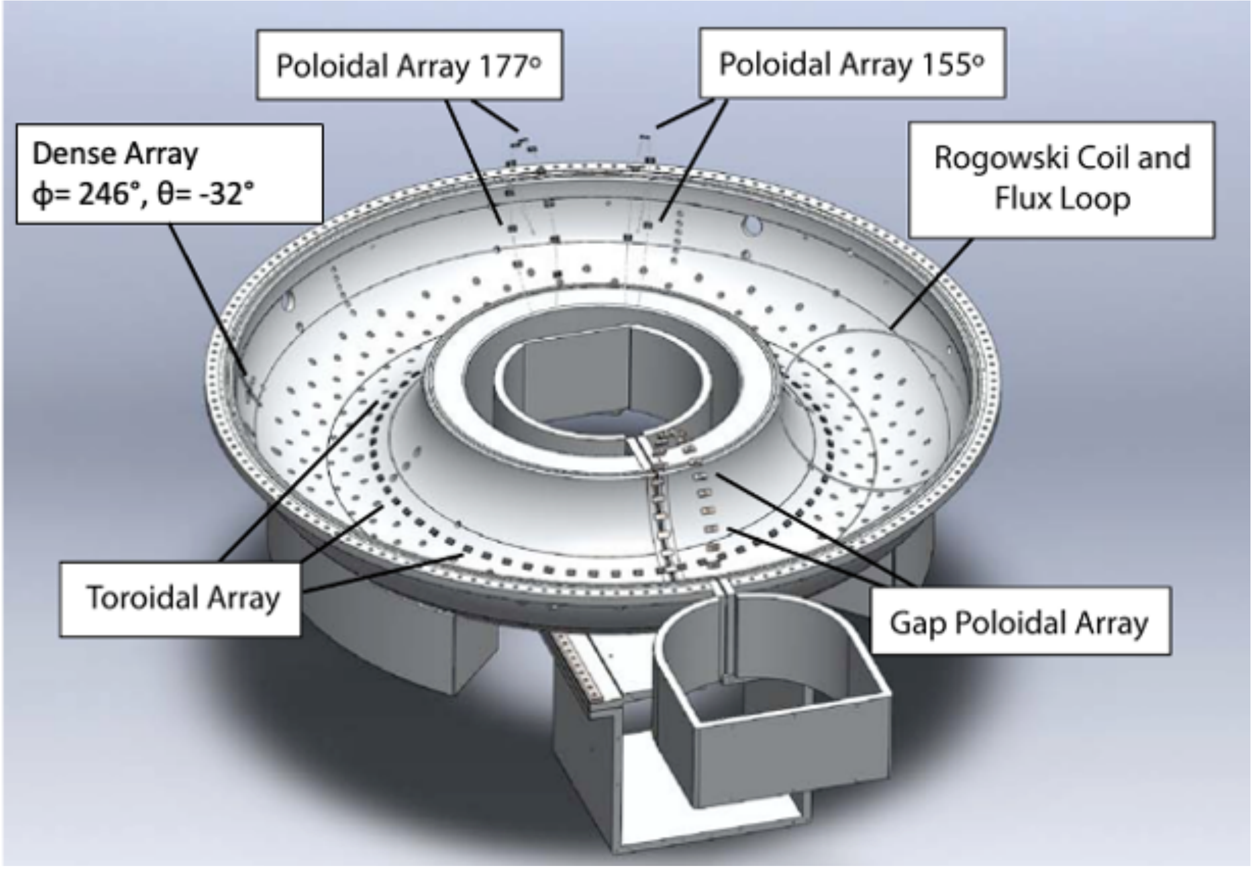

FIGURE 3.5: Diagram of MST internal magnetic field coil locations

amplitudes.

Relative calibration of the $\mathbf{B}_\phi$ coils is performed just before $t = 0$ in each shot, when a known vacuum toroidal field is present. Relative calibration of the $\mathbf{B}_\theta$ coils is performed using data from the flattop of the shot by comparing B of the average signal in each coil over a large averaging window when the plasma is rotating. Data from non-rotating plasmas are therefore disregarded.

The dense array was used for the analyses related to the transition from quasi-continuous to bursty reconnection activity in Ch. 6. Fig. 3.5 denotes its location in MST at $246°$

toroidal and $-32°$ poloidal. The dense array is a plus-sign-shaped cluster of closely-spaced, poloidal and toroidal coils. The arrays provide time derivative measurements of the magnetic field amplitudes, as the signal is amplified but not integrated.

Finally, some of the coil data are used as constraints in MSTFit equilibrium reconstructions.

3.2.2 MSTFit

MSTFit is a non-linear Grad-Shafranov toroidal equilibrium reconstruction code that was developed specifically for the MST device. The code uses Ampère's Law and the magnetic divergence constraint while assuming a cylindrically axisymmetric field, and enforcing radial force balance ($\mathbf{J} \times \mathbf{B} = \nabla \mathbf{P}$). The assumption of an axisymmetric field is generally sound during high-performance regimes of the RFP such as in between sawtooth events of standard RFP plasmas or when using enhanced confinement operation. The code uses electron profile measurements from Thomson scattering and inverted electron density profiles from the FIR diagnostic to invert the Grad-Shafranov equation [11, 12] and create flux surfaces inside MST [13]. This uses the ansatz that temperature and density are constant on flux surfaces. The results is a two dimensional geometry of the plasma flux surfaces.

The MSTFit code solves the Grad-Shafranov equation over an unstructured mesh of 746 elements. At each step in the parameter space synthetic diagnostic measurements are computed and the compared to real data gathered by diagnostics to calculate χ^2. This process is repeated a second time to minimize for χ^2 using the previous result as a starting point [13, 14].

MSTFit reconstructions can evaluate the internal stored energy in toroidal geometry so that the energy confinement time (τ_E = internal stored energy divided by ohmic input power) can be calculated. The stored internal thermal energy can be volume integrated by MSTFit and the ohmic power is simply given by $P_\Omega = I_p V_p$ during the flattop.

3.3 Spectroscopic Diagnostics

This section will briefly cover the spectral diagnostics that were used to measure the plasmas created for this dataset, leaving the Thomson scattering diagnostic for the next chapter so that it can be covered in more detail. The non-invasive, non-perturbative nature of spectroscopy is a huge advantage of these measurement techniques and a variety of spectroscopic methods exist to diagnose MST plasmas. Plasmas inherently emit radiation and this can be passively measured to infer parameters such as temperature. Alternatively, a plasma can be non-perturbatively coaxed to emit non-inherently generated radiation that can then be measured to determine temperature, density and other parameters associated with various species (i.e. ions or electrons). There is also interferometry which studies properties related to the index of refraction of the plasma which compares the phase of an electromagnetic wave sent through the plasma with a reference. Despite often measuring the same plasma parameters, these tools all make independent measurements. This means that they can be modularly combined in a Bayesian analysis framework to fully leverage the data collected by each diagnostic. This technique will be described in greater detail in Ch. 5.

One main goal of utilizing this bevy of spectral diagnostics was to infer the effective charge state, Z_eff, of standard RFP plasmas. Z_{eff} is one of the parameters needed to calculate the Lundquist number and so its updated measurement was of great interest to this project. The process for measuring this quantity has vastly improved over previous methods [15] and has determined that the effective charge state of enhanced-confinement RFP plasmas is $Z_{eff} \approx 2.3$ in the core [16]. We will leave further discussion of inferring this parameter to Ch. 5. For now, let us dive into discussing the basic overviews of the FIR, SXR and CHERS diagnostics.

3.3.1 FIR

The far-infrared (FIR) laser interferometer diagnostic is a system that is used to measure the plasma parameters that affect the index of refraction of the plasma, including the magnetic field parallel to the laser path, B_z, and the line-integrated electron density, n_e. This thesis used the FIR system to measure n_e to a high degree of accuracy with high time response. A feature of the dataset described herein is that most of its shots were diagnosed by the FIR system, which is a vast improvement over a traditional MST dataset which tended to use the less accurate and less robust CO_2 interferometry system for the majority of density measurements [17].

The idea behind interferometry is that a beam passing through the diameter of the machine is compared to a reference beam that does not pass through the plasma. From the measured phase difference between these two electromagnetic waves, the line-integrated electron density can be inferred. The relevant equation derived from the Appleton-Hartree formula for the refractive index of a cold plasma is

$$\delta\phi = \frac{e^2}{4\pi c^2 m_e \epsilon_0} \int n_e dl \tag{3.2}$$

where ϕ is the phase difference between a wave from a chord that has passed through the plasma and the reference beam, λ is the wavelength of the electromagnetic, or laser, wave, z is the distance along the length of the chord through the plasma, $\int n_e dl$ is the line-integrated electron density, and π, c, m_e, e and ϵ_0 are the numerical constants for the ratio of a circle's circumference to its diameter, the speed of light, the mass of an electron, the charge of an electron and the permittivity of free space, respectively [17].

The key components of the FIR interferometry system are two newly updated, solid state, continuous wave sources tuned to slightly different frequencies and a recently upgraded set of planar-diode mixers. When the sources are combined, a modulated signal is produced. From that, the relative phase between the lasers can be obtained. There are eleven FIR chords that pass through the machine that are separated into two sets that are toroidally displaced by five degrees. A diagram of this set up is shown in Fig. 3.6. After the lasers pass through the machine, they are combined at wave-splitters and measured with a UCLA fabricated diode/pre-amplifier assembly [17].

3.3.2 Soft X-Ray Diagnostic Systems

Plasmas passively emit x-rays that can be collected and measured at relatively much less expense than the other diagnostics that will be covered in this thesis. Soft x-rays (SXR) spectroscopy measures radiation from lower energy, or longer wavelength, section of the x-ray spectrum (100 eV $\lesssim h\nu \lesssim$ 10 keV). The SXR region is often chosen for observation because it is a much "cleaner" portion of the spectrum that is easier to interpret than vacuum ultraviolet (i.e. $h\nu \lesssim$ 100 eV) and more intense than hard x-ray ($h\nu \gtrsim$ 10 keV) emissions at thermal temperatures. We will now go over the main features and sources of this spectrum.

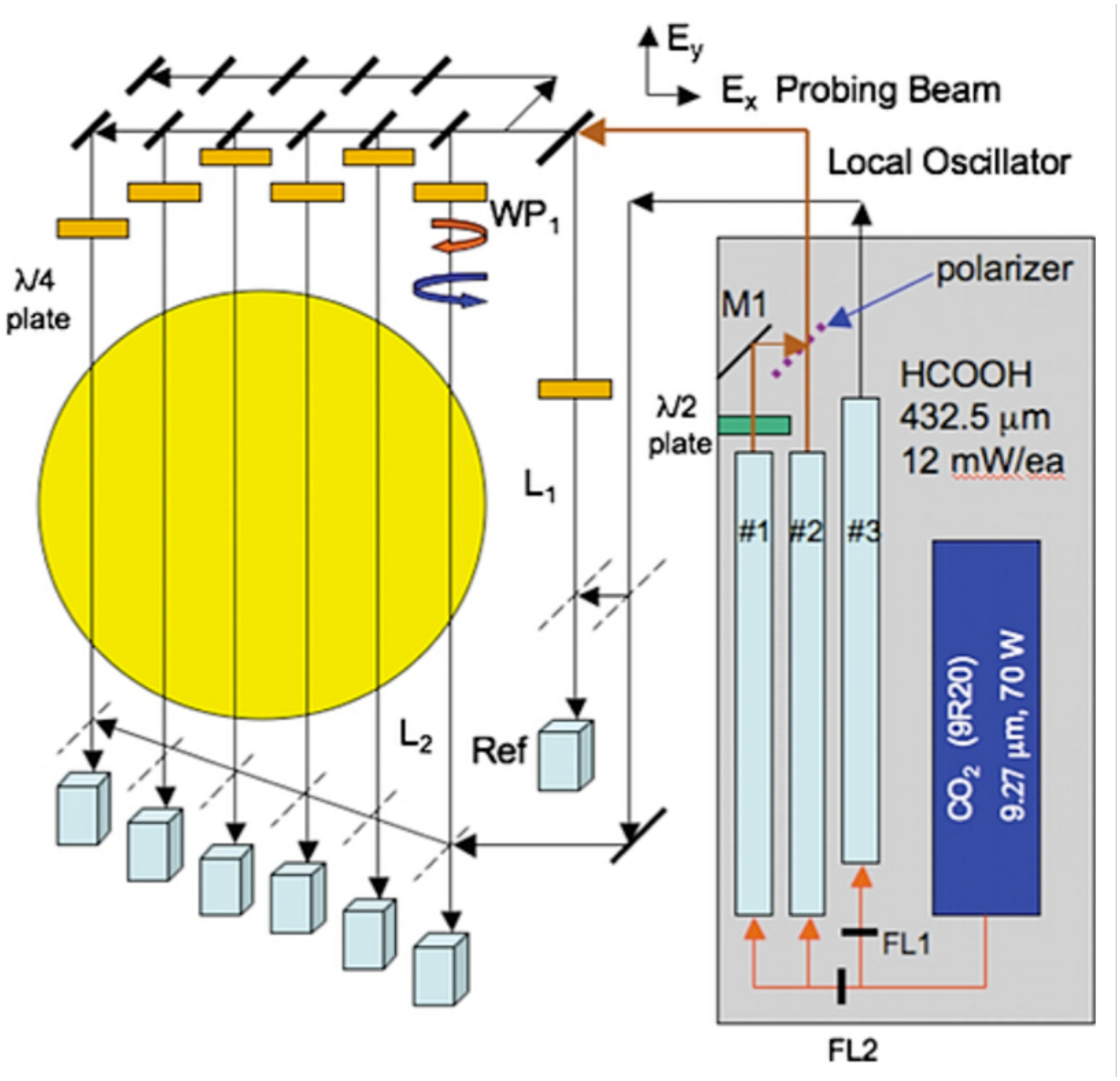

FIGURE 3.6: A schematic of the FIR system. This shows the old system that was powered by laser-pumped CO_2 sources. New solid state sources were installed by James Duff and employed for the data collection presented in this thesis [17].

Plasmas emit several varieties of electromagnetic radiation. The primary source of x-rays in MST is bremsstrahlung (braking) radiation, which is created when an electron is decelerated by passing through the field of an ion. This is the “background” radiation of the SXR spectrum. Effects from impurity ion species contribute more interesting and challenging features to the spectrum. Low-Z impurities, such as (C, N, or O), most significant contribution comes from radiative recombination, a process where an ion captures a passing electron and radiates the residual kinetic energy. This shows up in the spectrum in features that look like steps. Medium and high-Z impurities contribute additional challenging features to the spectrum. These impurity ions are not fully ionized so that when they interact with a passing electron, bound ground-state electrons of the atom are excited to higher energy levels. When this excited energy electron decays back to the ground state, photons are emitted with the residual energy. This process appears in the spectrum in the form of excitation lines. MST plasmas typically emit very bright excitation lines at $E \sim 2keV$ which significantly complicates the interpretation of the SXR measurements [14]. For a more detailed description, please refer to P.D. VanMeter’s thesis[14].

The SXR tomography diagnostic utilizes two-color measurements measure electron temperature as well as reconstruct internal features of MST plasmas [18]. A diagram depicting the lines-of-sight of the diagnostic is shown in Fig. 3.7. Four detectors at a toroidal location of $\phi = 90°$ make up this diagnostic. The detectors’ viewing geometry was selected to sample the plasma cross-section sufficiently for tomographic inversion. Each detector has 20 Si photodiodes which are approximately paired to share a line-of-sight with another photodiode so that ten chords are effectively viewed at each of the four detector locations. The diodes look through beryllium foils with either a “thick” (172

m) or "thin" (45 m) thickness. This allows the diagnostic to sample the slope of the SXR continuum so that T_e can be inferred. The signal from each photodiode is passed through a differential transimpedance amplifier and then digitized [14].

Another SXR tool used for the project was the NICKAL2 Ross filter detector. It is a single-chord spectrometer that was designed specifically to isolate the signal from Al^{+11} and Al^{+12} transition lines [19] by carefully selecting filter pairs to create pass-bands into which incoming radiation can be isolated. Fig. 3.8 shows transmission curves for the three filters installed in the NICKAL2 detector.

The detector itself is made up of three photodiodes, the same type that is used for the SXR tomography diagnostic. A more detailed description of the diagnostic can be found in N. Lauersdorf's senior thesis [20]. The filter choice was designed to, of course select for the appropriate passband, but also to provide enough structural support and ease-of-use. The three filters ultimately chosen were made up of Zr (2.0 m)+ Mylar (8.0 m), Al (6.8 m) + Be (31.2 m), and Si (10.0 m) + Be (12.7 m) [20].

The NICKAL2 Ross Filter was used to measure Al impurity densities to inform a Z_{eff} estimate for standard plasma that will be discussed in Ch. 5.

3.3.3 CHERS

To measure parameters such as density and temperature of impurity ion species, the line radiation emitted by these impurity ions is analyzed. Line radiation, which was briefly touched upon above, is the emission of light from an atom due to the transition of electrons between bound states. In a magnetically confined plasma, the dominant processes that lead to line radiation are electron impact excitation and charge exchange recombination. The charge exchange recombination spectroscopy (CHERS) diagnostic obviously

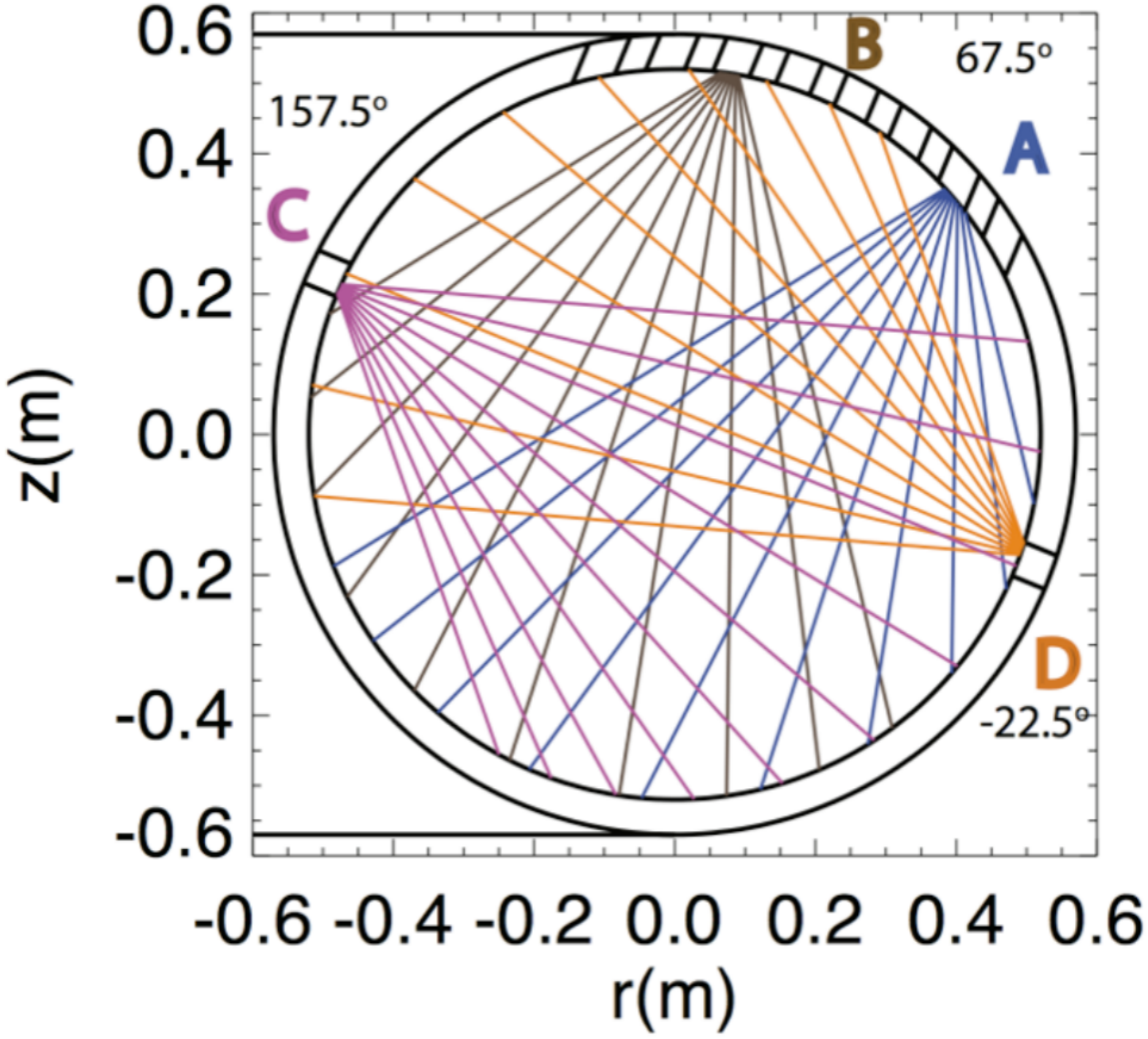

FIGURE 3.7: This figure shows the lines of sight of the SXR tomography diagnostic. It is reproduced from [14]

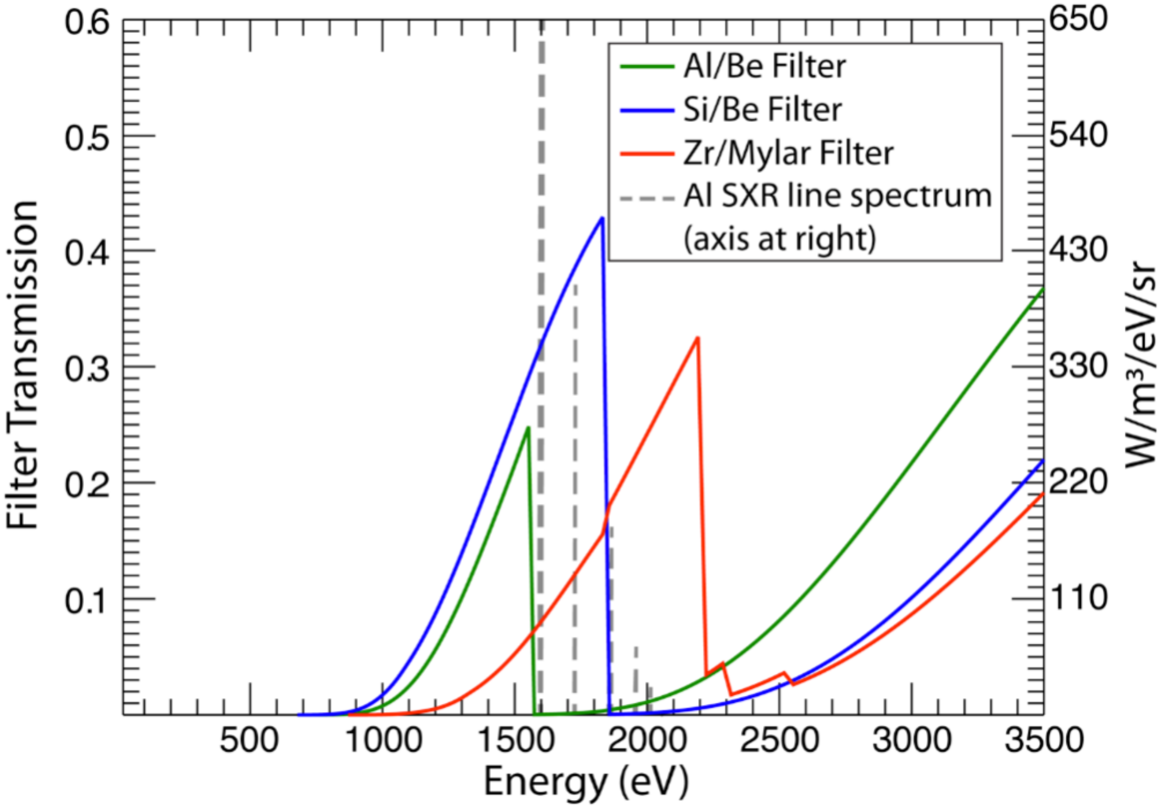

FIGURE 3.8: This figure shows the lines transmission bands for the three filters of the NICKAL2 Ross filter detector. The dashed lines represent the brightest Al emission lines in a characteristic MST plasma. The figure is reproduced from [20]

focuses on measuring the latter. Charge exchange occurs when an electron from a neutral atom is donated to an ionized atom. When the donated electron, which is initially in an excited state, quickly de-excites, it emits line radiation at a wavelength that is determined by the ionization state of the atom. This process is on the nanosecond time scale, much faster than any relevant ion dynamics of interest in the plasma [21].

One strategy to obtain local measurements of an otherwise inherently line-integrated view, is to inject a neutral beam of particles perpendicular to the optical line of sight. This actively provides a local source of charge exchange emission that can then be analyzed to infer the plasma parameters at the intersection of the neutral beam and the optical line-of-sight.

The Charge Exchange Recombination Spectroscopy (CHERS) diagnostic on MST is optimized to measure fully stripped carbon, C^{+6}, which becomes C^{+5} when an electron is donated by atoms in the neutral beam. The lines of sight and beams depictions of the beams traveling through MST are shown in Fig. 3.9. To obtain a measurement, a diagnostic neutral beam (DNB) provides the donor neutral atoms to provoke charge exchange. Eleven poloidal view ports with lines of sight perpendicular to MST retrieve the emitted light that is then fed to a high-throughput, double-grating spectrometer optimized to measure the C^{+5} line at 343.383 nm. Thirty-two photomultiplier tubes record the light from the exit slit of the spectrometers and their signal is digitized and filtered. Data from a “passive” view at a similar location through the plasma is also gathered so that the background electron impact emission can be accounted for in the total “active” signal.

CHERS data collection in this thesis was relatively limited (see Fig. 3.12) due to resource constraints. However, data was collected at key points in parameter space with an eye toward being able to extrapolate and interpolate the measurements to other locations

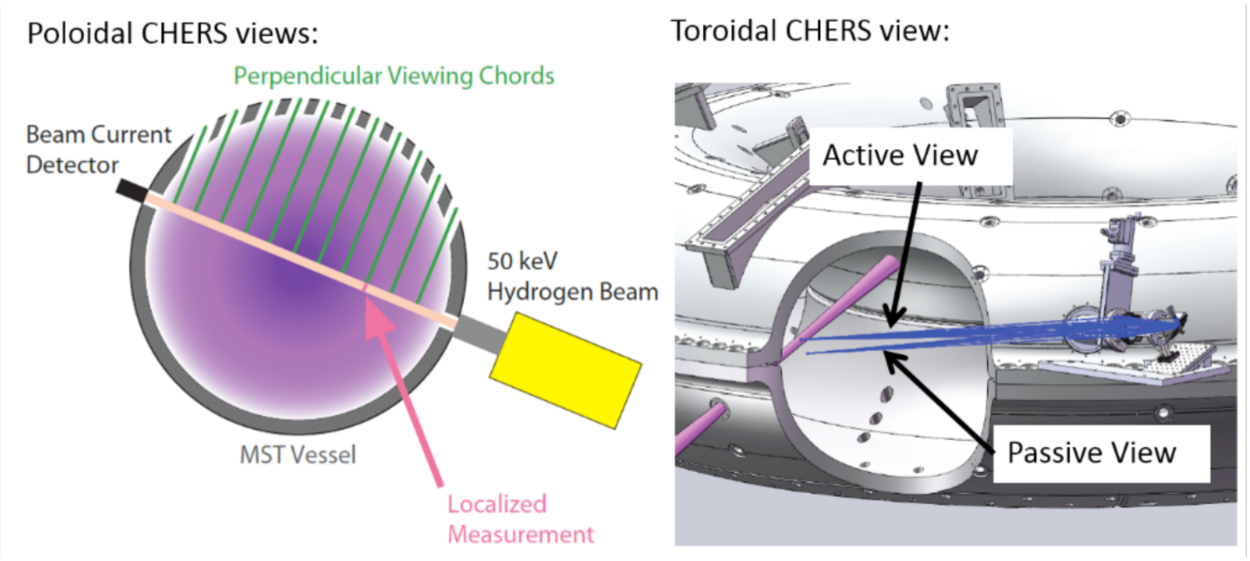

FIGURE 3.9: This figure shows a poloidal view (left) and a toroidal view (right) of the CHERS diagnostic in MST. On the left, green lines represent poloidal optical views intersecting the diagnostic neutral beam, intersecting the beam perpendicularly. On the right, we see bothe the “active” view that observes charge exchange from the neutral beam and the background impact emission as well as the “passive” view which only collects the background electron impact emission. This figure is reproduced from [21].

in parameter space.

3.4 Summary

Two aspects of the experimental set-up were discussed in this chapter: producing RFP plasmas over a wide-range of Lundquist numbers and the main tools used to diagnose those plasmas. Plasma current and electron density are the ”knobs” on MST that an operator can control to vary the Lundquist number, as is depicted in Fig. 3.10. The new PPS system enabled the plasmas created to span a wider range of Lundquist numbers than had previously been possible on MST.

To diagnose these plasmas, several diagnostics coupled with Bayesian analysis techniques and the MSTFit equilibrium solver were used to infer the plasma parameters and used in the analyses presented later in this thesis. Fig. 3.11 provides an overview of how each of the major diagnostics contributed to the inferred plasma parameters in the main scaling relationship that was studied, i.e., how magnetic field fluctuation amplitudes scaled as Lundquist number was varied.

Ultimately, the data collected create a valuable database, not only for this study, but also for future use. The utilization of the FIR diagnostic to measure density for most every shot in this data set is a vast improvement over the CO_2 interferometer density data that make up most other MST datasets. Additionally, the Thomson scattering diagnostic was able to collect data over the whole radial profile with an improved signal-to-noise ratio, which has not been possible in other Thomson scattering data collection. These data will therefore be invaluable contributions to future studies, particularly any efforts to validate computational codes and results, especially given the expensive of operating many of the spectral diagnostics employed. Information about accessing this database can be found in Appendix A.

As was mentioned earlier, the Thomson scattering diagnostic played a particularly important role in diagnosing the plasmas, and therefore, its discussion as been given its own chapter. We will be going over its nuances and contributions next.

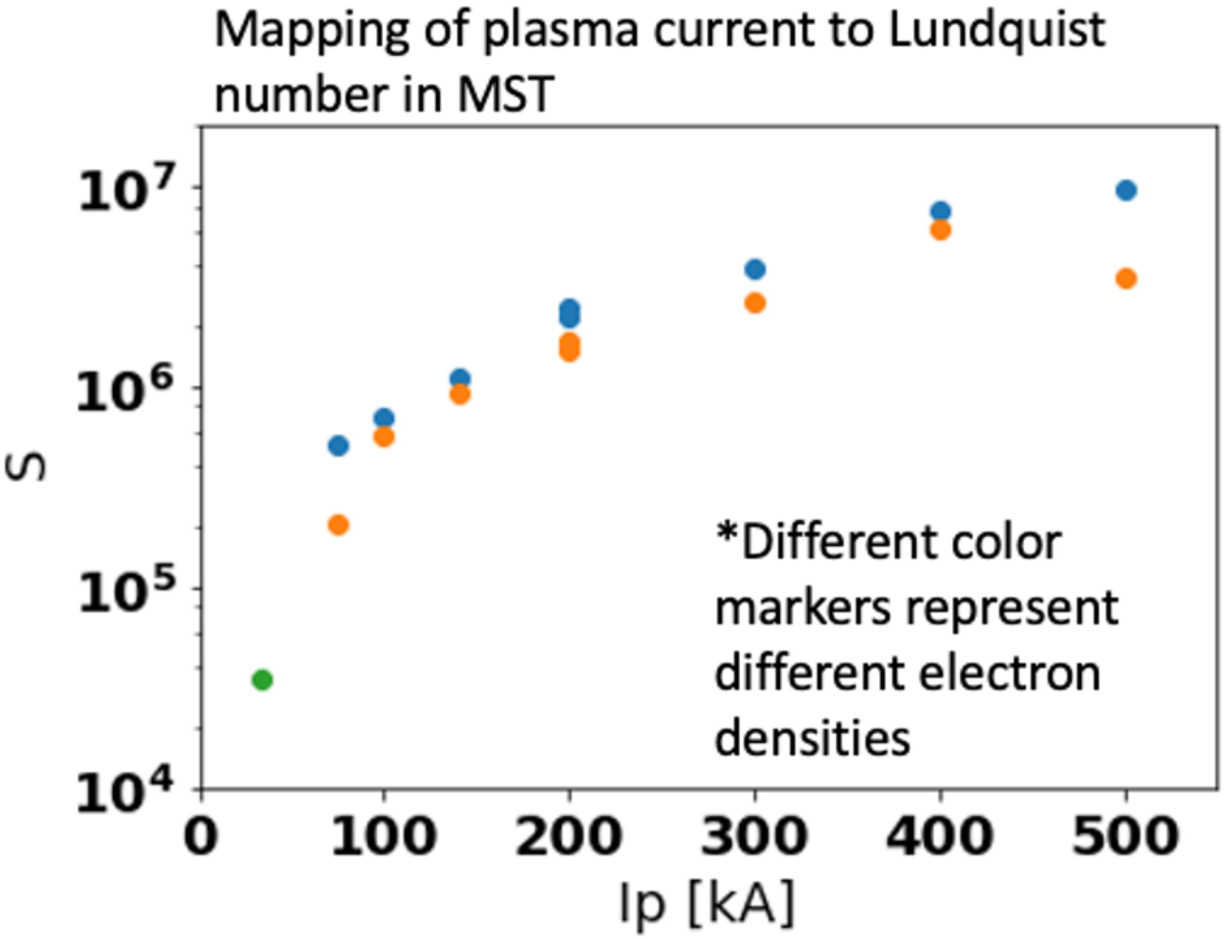

FIGURE 3.10: A figure depicting how to vary the Lundquist number on MST. The two control "knobs" are plasma current, I_p, and density, n_e. Each color represents a different density.

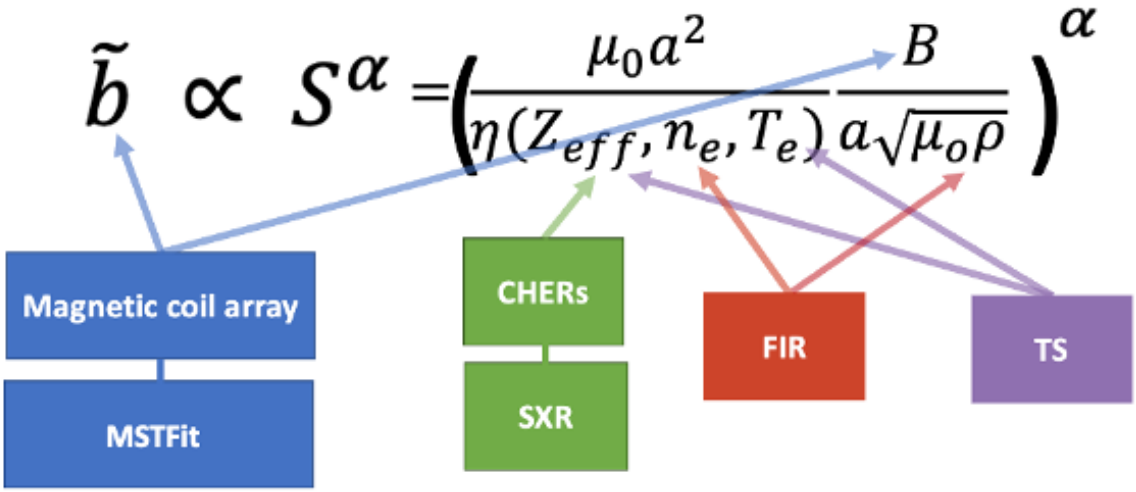

FIGURE 3.11: This is the equation covered in Ch. 2 (Eqn. 2.2). This figure depicts what tools were used to infer the quantities therein.

	35 kA	50 kA	75 kA	140 kA	200 kA	300 kA	350 kA	400 kA	500 kA
TS	X X	X X X	X X X	X X X	X X X	X X X	X X X	X X X	X X
FIR	X X	X X X	X X X	X X X	X X X	X X X	X X X	X X X	X X
SXR+							X	X X X	X X
CHERS					X X X		X	X	X X

X= low density, X= medium density, X= high density

FIGURE 3.12: This table summarizes where in parameter space the diagnostics described in this chapter and employed by this project were used.

Bibliography

[1] J. Becksted, "Sawteeth in the mst reversed field pinch," Ph.D. dissertation, University of Wisconsin at Madison, 1990.

[2] R. N. Dexter, D. W. Kerst, T. W. Lovell, S. C. Prager, and J. C. Sprott, "The madison symmetric torus," *Fusion Technology*, vol. 19, no. 1, pp. 131–139, 1991. [Online]. Available: https://doi.org/10.13182/FST91-A29322

[3] J. Sarff, "Tutorial on the magnetic design of mst," Internal Document, 2012.

[4] I. R. Goumiri, K. J. McCollam, A. A. Squitieri, D. J. Holly, J. S. Sarff, and S. P. Leblanc, "Simultaneous feedback control of toroidal magnetic field and plasma current on MST using advanced programmable power supplies," *Plasma Research Express*, vol. 2, no. 3, p. 035012, sep 2020. [Online]. Available: https://doi.org/10.1088/2516-1067/abb4c2

[5] D. J. Holly, J. R. Adney, K. J. McCollam, J. C. Morin, and M. A. Thomas, "Programmable power supply for mst's poloidal field," in *2011 IEEE/NPSS 24th Symposium on Fusion Engineering*, 2011, pp. 1–4.

[6] M. Team and Collaborators, "Magnetic mode analysis in mst," Internal Document, 2014.

[7] D. Craig, "Controlling fluctuations and transport in the reversed field pinch with edge current drive and plasma biasing," Ph.D. dissertation, University of Wisconsin at Madison, 1998.

[8] J. Koliner, “Neutral beam excitation of alfvén continua in the madison symmetric torus reversed field pinch,” Ph.D. dissertation, University of Wisconsin at Madison, 2013.

[9] *"Magnetic Mode Analysis in MST"*, "MST", May 2005.

[10] D.Craig, “Magnetic mode analysis in mst,” Internal Document, 2005.

[11] H. Grad, “Toroidal Containment of a Plasma,” *The Physics of Fluids*, vol. 10, no. 1, pp. 137–154, 01 1967. [Online]. Available: https://doi.org/10.1063/1.1761965

[12] ——, “Plasma equilibrium in a magnetic field,” *Reviews of Plasma Physics*, vol. 2, p. 103, 1966.

[13] J. Anderson, C. Forest, T.M, J. Sarff, and J. Wright, “Equilibrium reconstruction in the madison symmetric torus reversed field pinch,” *Nuclear Fusion*, vol. 44, no. 1, pp. 162–171, dec 2003. [Online]. Available: https://doi.org/10.1088/0029-5515/44/1/018

[14] P. VanMeter, “Observations of helical plasma dynamics using complementary x-ray diagnostics in the mst,” Ph.D. dissertation, University of Wisconsin at Madison, 2020.

[15] M. R. Stoneking, J. T. Chapman, D. J. Den Hartog, S. C. Prager, and J. S. Sarff, “Experimental scaling of fluctuations and confinement with lundquist number in the reversed-field pinch,” *Physics of Plasmas*, vol. 5, no. 4, pp. 1004–1014, 1998. [Online]. Available: https://doi.org/10.1063/1.872670

[16] M. Galante, L. Reusch, D. D. Hartog, P. Franz, J. Johnson, M. McGarry, M. Nornberg, and H. Stephens, “Determination ofiz/isubeff/subby integrating

measurements from x-ray tomography and charge exchange recombination spectroscopy," *Nuclear Fusion*, vol. 55, no. 12, p. 123016, nov 2015. [Online]. Available: https://doi.org/10.1088/0029-5515/55/12/123016

[17] J. Duff, "Observation of trapped-electron mode microturbulence in improved confinement reversed-field pinch plasmas," Ph.D. dissertation, University of Wisconsin at Madison, 2018.

[18] M. B. McGarry, P. Franz, D. J. Den Hartog, J. A. Goetz, M. A. Thomas, M. Reyfman, and S. T. A. Kumar, "High-performance double-filter soft x-ray diagnostic for measurement of electron temperature structure and dynamics," *Review of Scientific Instruments*, vol. 83, no. 10, p. 10E129, 2012. [Online]. Available: https://doi.org/10.1063/1.4740274

[19] D. Carvalho, D. Ferreira, P. Carvalho, M. Imrisek, J. Mlynar, H. Fernandes, and J. Contributors, "Deep neural networks for plasma tomography with applications to JET and COMPASS," *Journal of Instrumentation*, vol. 14, no. 09, pp. C09 011–C09 011, sep 2019. [Online]. Available: https://doi.org/10.1088/1748-0221/14/09/c09011

[20] N. Lauersdorf, "Development of a ross filter based aluminum line radiation (nickal2) detector in madison symmetric torus," Ph.D. dissertation, University of Wisconsin at Madison, 2018.

[21] J. Boguski, "Local ion velocity measurements in the mst saturated single helical axis state," Ph.D. dissertation, University of Wisconsin at Madison, 2019.

Chapter 4

The Thomson Scattering Diagnostic on MST

The Thomson scattering (TS) diagnostic on MST is an active spectral measurement tool that provides high spatial resolution electron temperature and relative electron density profile measurements. For this thesis, the temperature profiles from TS were utilized to infer the Lundquist number ($S \sim T_e^{3/2}$) for the Lundquist number scalings (Ch. 5), to constrain MSTFit equilibrium reconstructions, and to create a database of ensembled electron temperature profiles across a wide range of Lundquist numbers. It also has contributed to inferring an effective ion charge of MST plasmas via an integrated data analysis technique, or Bayesian approach [1]. This measurement is an important improvement to our inference of S in MST plasmas.

This chapter provides an overview of this particularly important diagnostic. To begin, we will review the salient physics and principles of the Thomson scattering diagnostic. We will then cover the components that comprise the MST TS system. Extensive calibrations and alignments of the various subsystems were performed before undertaking the experimental campaigns discussed herein. These will also be reviewed and summarized.

Following that, we will discuss the new ensembling technique developed to create $T_e(r)$ profiles at low Lundquist numbers, improving the profile quality and extending the lower bound in density at which temperature measurements can be made. We will end with a summary of the chapter.

At its peak diagnostic capacity, the TS system produces high-temporally and spatially resolved temperature measurements with the capacity to measure the absolute electron density as well. These features, however, require a great deal of resources. Even a basic Thomson system possesses a relatively high number of components, compared to say more passive spectral diagnostic such as x-ray diagnostics. All of this is to say that, given that the Thomson diagnostic during the main thrust of this thesis project was operated with a two person team and an occasional part-time engineer, rather than the previous team of seven, a challenge for this thesis was to adapt TS usage so that it could be operated with relatively limited resources. This motivated a myriad of adaptations and updates to the diagnostic's subsystems since the last graduate student to work on Thomson wrote a thesis; herein we will pay special attention to noting these changes. I hope this helps any future users who may endeavor to use of the diagnostic again. This also motivated, in part, the creation of high-quality profiles that may be employed by future MST users, should Thomson not be available during their run campaigns.

4.1 Key Physics and Principles Underlying the Thomson Scattering Diagnostic

In the classical limit ($\hbar\omega << mc^2$), when an incident electromagnetic wave impinges on a charged particle, in this context, an electron, it is accelerated by the electromagnetic wave,

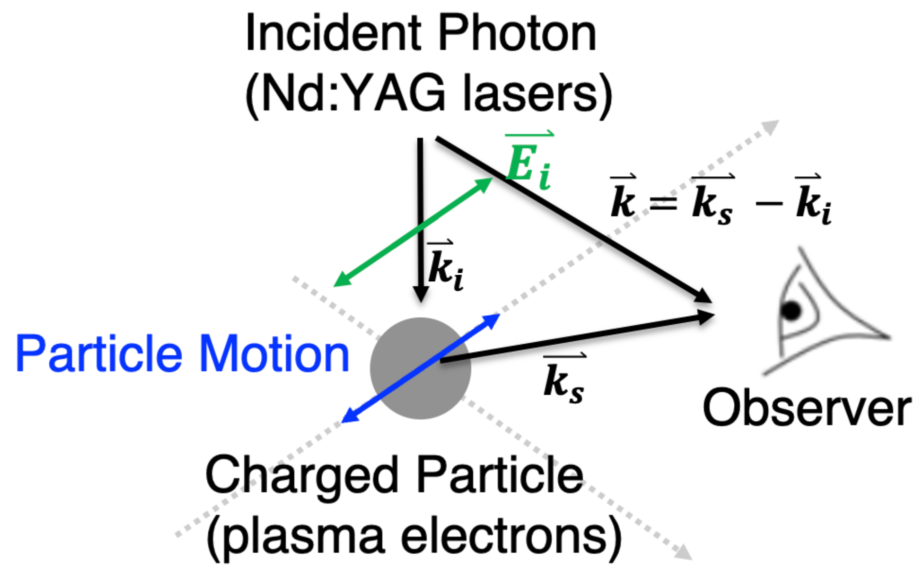

FIGURE 4.1: This figure depicts the process of Thomson scattering, including details specific to the MST diagnostic.

thereby emitting electromagnetic radiation. This re-emitted radiation is called a scattered wave, and this process is called Thomson scattering.

Fig. 4.1 depicts this sequence, including details specific to MST TS. The Thomson scattering diagnostic on MST uses a Nd:YAG (neodymium-doped yttrium aluminum garnet) laser to produce the incident radiation that accelerates the plasma electrons. The scattered light is doppler-shifted by the movement of the electron and collected by the collection optics. In the figure, $\vec{k}_s$ and $\vec{k}_i$ are the scattered and incident wave vectors respectively. The electric field of the incident laser wave, $\vec{E}_i$, is oriented in the toroidal direction. One dimension of the scattering is sampled, defined by $\vec{k} = \vec{k}_s - \vec{k}_i$, due to the nature of the experimental set-up.

The appeal of harnessing Thomson scattering to diagnose plasmas becomes clear when we look at the equation for the scattered power spectrum. To make the appeal most obvious, we will start with showing this expression in the nonrelativistic dipole approximation, where the scattered power spectrum per unit solid angle is given by,

$$\frac{d^2P}{d\Omega_s d\nu_s} = \left[2\pi r_e^2 \int_V \langle S_i \rangle d^3r |\hat{s} \times (\hat{s} \times \hat{e})|\right] f_k \left(\frac{\omega}{k}\right) \frac{1}{k} \tag{4.1}$$

where ν_s is the scattered frequency, $\langle S_i \rangle$ is the average incident Poynting vector magnitude, $\hat{s}$ and $\hat{e}$ are the unit vectors associated with the scattered wave vector and the electric field of the incident electromagnetic field respectively, and f_k is the one-dimensional velocity distribution in the k-direction. From this expression, we see that the scatter power spectrum is simply proportional to f_k. The one-dimensional velocity distribution function for a Maxwellian distribution is given by,

$$f_k = n_e \left(\frac{m_e}{2\pi T_e}\right)^{1/2} exp\left(-\frac{m_e v_k^2}{2T_e}\right), \tag{4.2}$$

where v_k is the magnitude of the electron velocity as defined by $\vec{k}$. It then follows that by measuring the power spectrum of Thomson scattering, one can infer the electron temperature and density of the plasma.

It is important to note that Eqn. 4.1 is a simplified, nonrelativistic formulation that neglects to account for headlighting effects that are significant in high temperature plasmas; neglecting to account for relativistic effects would lead to overestimating the plasma temperature. Accounting for this effect, Zhuravlev and Petrov developed a fully relativistic formulation for the power spectrum that can be solved analytically using a relativistic Maxwellian distribution [2]. TS systems in high temperature plasma applications typically employ Selden's formulation of this expression, which is computationally convenient and given by,

$$S_\omega(\lambda_s, \theta, \mu, n_e) = \frac{n_e r_e^2 x^4 \cdot q(\lambda, \mu, \theta)}{2\lambda_i K_2(\mu)\sqrt{1 + x^2 - 2xcos\theta}} exp\left(-\mu\sqrt{\frac{1 + x^2 - 2xcos\theta}{2x(1 - cos\theta)}}\right), \tag{4.3}$$

where $x = \frac{\lambda_i}{\lambda_s}$, $\mu = \frac{m_e c^2}{T_e}$ and $K_2(\mu)$ is the modified Bessel function of the second kind with order two, and the scattering angle, θ, is defined as the angle between the incident and scattered wave vectors such that $cos\theta = \vec{k}_i \cdot \vec{k}_s/|k_i||k_s|$ [3, 4].

This dependence of the scattered power spectrum on the distribution presents a significant advantage to using the Thomson scattering diagnostic, relative to say, x-ray diagnostics that passively measure the inherent electromagnetic field of the plasma to infer temperature, but whose interpretation of the data is significantly more complex. However, there are quite a few challenges associated with the TS diagnostic.

First let's consider the cross-section for Thomson scattering, given by,

$$\sigma = \frac{8\pi}{3} r_e^2 = 6.65 \times 10^{-29} m^2, \tag{4.4}$$

where r_e is the electron radius. This means that of the incident photons used to incite Thomson scattering, only a small fraction (likely around $\sim 10^{-13}$) will be collected. This necessitates the use of high-powered lasers so that the enough scattered photons can be gathered to infer the temperature.

Additionally, because Thomson scattering necessitates the use of more components than an x-ray diagnostic (laser optics in addition to collection optics), there are many added complexities for each of these subsystems. We will cover these in the next section as we go over the MST TS system's many components.

4.2 MST Thomson Scattering

In this section, we will go over the constituent components of the MST TS system. We will start by giving an overview of the system and its most relevant components. We will then touch base on the subsystems that have been adapted to increase the diagnostic's ease-of-use. Many of these improvements were spearheaded by others so they will only briefly be discussed to give a picture of the state of the system at the time of this chapter's writing.

4.2.1 System Overview

To get an idea of the components that make up the TS MST system, we will now walk-through how TS data is generated during a MST plasma discharge or "shot." The TS system also takes what are called "Thomson" or "laser shots" that are distinct from MST shots. A laser shot is the process of firing the laser and collecting data from the scattering process. Many Thomson shots are fired during a single MST shot when the diagnostic is being used. To take a Thomson shot, first the laser system- which for the data collection presented herein comprised of one of the two 2 J Nd:YAG lasers- is set to fire at set intervals for up to 15 laser shots. For the vast majority of the data collected for this effort, the laser was set to fire at 1 ms intervals for 15 laser shots during the flattop period of the plasma discharge. The laser head resides in the Thomson laser room across the hall from the MST machine area. When fired, the beam makes its way through the beamline enclosure and via a set of turning mirrors through the ceiling, across the hall to the machine area, and eventually, to a turning box directly above the MST machine at 222° toroidal.

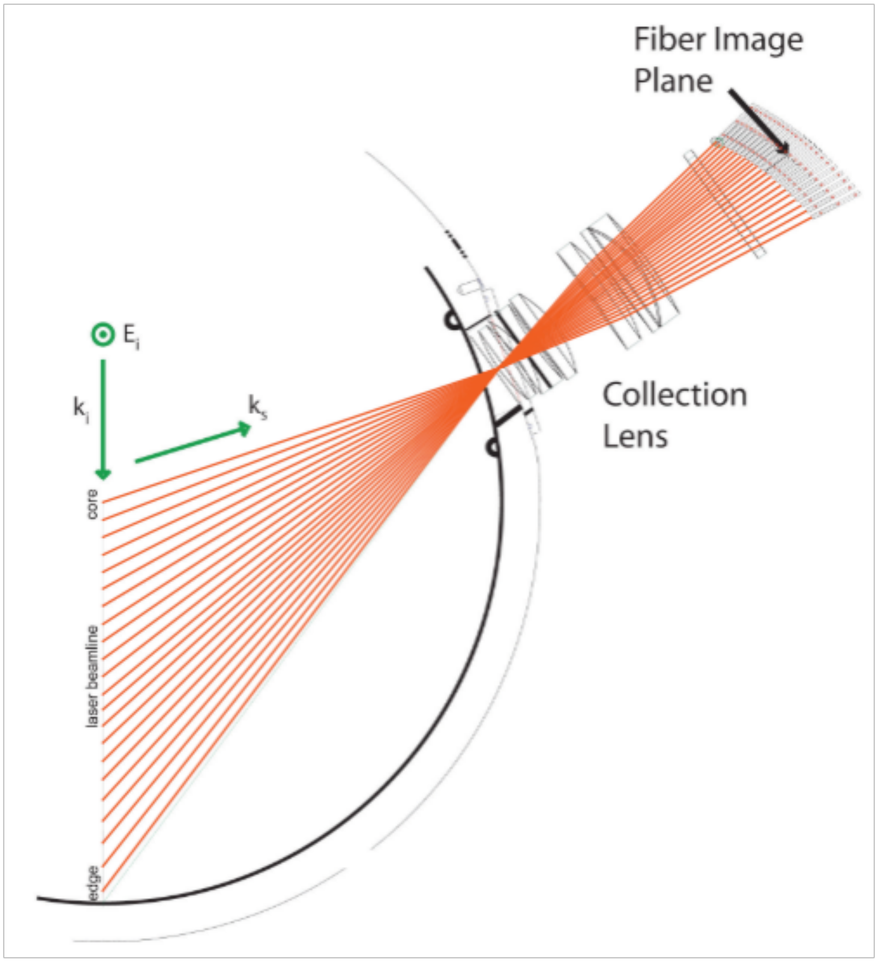

FIGURE 4.2: This figure shows the path of the laser through MST and the scattering volumes that are measured by the fiber image plane. The green vectors represent the incoming and scattered light while the red rays trace the field-of-view of the fiber optic cables in the fiber image plane that collect scattered light from 21 radial points (1-2 cm resolution).

From there, it is directed downward into MST as is shown in Fig. 4.2. The laser makes its way through the device into a beam dump at the bottom of MST.

When inside the device, the laser light is scattered by electrons and a portion of that scattered light is captured by the collection optics. The collection optics assembly, consisting of primarily a collection lens system and a bundle of fiber optic cable faces, sits at 20° poloidal. At the time of the data collection for this thesis, the lens system consisted of a seven-element lens with a replaceable plasma facing component. This plasma facing component becomes coated with repeated use, diminishing the signal strength. A new streamlined design for the collection lens system has since been implement to improve ease-of-use. This will be covered in a subsequent section. In the image plane of the collection lens, 23 fiber optic cables collect light from radial locations along the minor radius as is shown in Fig. 4.2. Each fiber samples a different direction of the distribution function: while $\vec{k}_i$ remains constant, $\vec{k}_s$ shifts slightly for each location, thereby changing the direction of $\vec{k}$. Sampling volumes at the edge are slightly larger (2 cm) while near the core the radial extent of the sampling volume is smaller (1.3 cm) [5]. The fiber optic cables transmit the scattered light to the Thomson room to a set of 6- or 8-channel General Atomics polychromators equipped with avalanche photodiode (APD) modules. Each polychromator, using light collected from a single minor radial location in MST, has a relay lens and a different bandpass filter in front of each channel so that a different passband of the scattered light spectrum is detected by that channel's APD. These APDs produce a DC signal and a delay-line subtracted 'AC' signal. The DC signals are digitized at 10 ns time resolution over a 2V full-scale range with 16 bit resolution using Struck digitizers (SIS3302), which allows for the digitization of both the signal, the background light, and any scattered laser light. The AC signals are digitized at 1 ns time resolutions with 8 bit

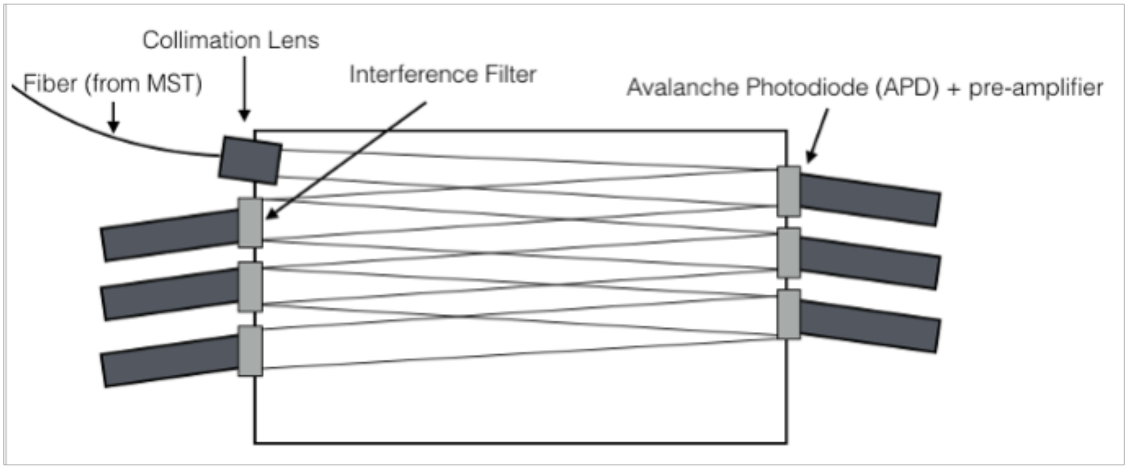

FIGURE 4.3: This diagram depicts a six-channel polychromator. Each channel of the polychromator is equipped with an APD detector and a preamplifier module.

resolution over a full scale range of ~ 200 mV. These signals are then fit and analyzed in a Bayesian framework to infer the plasma electron temperature and relative electron density.

As has been mentioned, several portions of the TS system have been modified since the last time the system as been throughly discussed in a thesis. The rest of this section covers the most significant of these updates.

4.2.2 APD Detector Power Supply and Feedthrough Panel Upgrade

In order to facilitate discussion of the upgrade of the APD power supply system, we will begin with an overview of the polychromators, APDs, and preamps that comprise the system.

Fig. 4.3 shows the layout of a six-channel polychromator. The MST system has 21 polychromators, 15 of which have six channels and six of which have eight. Each channel is equipped with and APD+preamplifier module, totaling 138 APDs. The amplifier modules and polychromators were manufactured by General Atomics. Each preamplifier module has a four step DC gain selection. The preamplifier modules are powered by ± 8 V and the APDs are biased by a steady high voltage input between 270-430 V. Each detector is set to its own specified bias voltage. The gain of the detector is dependent on the bias voltage. The output of each module includes a DC signal and an AC signal as was described above. All the detectors are housed in racks in the laser room of the TS system. Their digitizer and power supplies reside in the mezzanine above the laser room. RG 174U coax cable is used for the two gain cables (since removed), three bias cables, and two signal cables.

Before the upgrade, a single power supply powered all the detectors and distributed this power via a feedthrough panel in the roof of the laser room/floor of the mezzanine. This feedthrough panel also allowed for the gain of the preamplifier modules to be changed and also served as an interface between the digitizers on the mezzanine and the detectors in the laser room. Each of the cables interfaced with the feedthrough panel via a BNC connector.

This system left much room for improvement. First, the gains for the preamplifier modules, which were meant to be kept floating, were often shorted, leading to issues with the temperature inferences that were difficult to diagnose. Additionally, it was very possible to mix up the high voltage input with any of the others, potentially leading to damage in the preamplifier modules. Excess cable also was coiled and hung around in the room before interfacing with the feedthrough panel, introducing unnecessary signal degradation. These factors all motivated an upgrade to the feedthrough panel and power supply system for the detectors. In 2018, the upgrade was completed with the help of several student hourlies [6]. Broadly speaking, its goals were to improve the reliability, safety, and usability of the system.

Fig. 4.4 shows a diagram of the laser room and mezzanine both before and after the upgrade. The upgrade replaced the single power supply with a set of 138 modular power supplies. Each power supply is housed in a rack system and can be easily removed and replaced or repaired. Each PCB board contains two power supplies powering two detectors. Fig. 4.5 shows a simple block diagram of the power supply. A more detailed circuit diagram and PCB layout can be found in the document library. These power supplies were designed and implemented with extensive help and input from Don Holly. A major design requirement was that no new sources of noise be introduced to the system and that the output voltage be stable. ± 8 V input from the back of the rack is carried through to the front connectors. +8V is fed into a 5V regulator which is then used to power a switching regulator. This regulator utilizes a controlled transition time to retard high frequency harmonic, while efficiently "boosting" to HV. A Resonant Royer Converter (RRC) further reduces noise produced by the switching regulator by minimizing the high frequency harmonic in the power drive stage. A RRC is essentially a saturable-core transformer and saturating the transformer core leads to switching. In a RRC, transistors in a push-pull configuration conduct out-of-phase switching. The RRC outputs a square wave that is rectified to produce the HV bias. The HV bias is also provides feedback to the switch current sink to maintain a constant bias [7].

Fig. 4.7 shows the results of noise and stability testing that was performed before implementing the system. The stability testing was performed by measuring both small and long time scale voltage variations. The tolerance for a voltage change before the APD gain was impacted was calculated to be $\Delta V = \pm 0.244$ V. This was obtained by taking the temperature coefficient of the DC reverse operating voltage for constant gain, then multiplying that value by the temperature tolerance allowed during calibrations [8]. We see that the stability tests remain well below this value for both the long and short term testing.

The noise was tested by measuring the dark variance of the detectors while powered by the new and existing power supplies, as well as a linear power supply. The signal to noise ratio for the APD detectors is given by,

$$SNR = \sqrt{N * \frac{QE}{F}}, \tag{4.5}$$

where N is the number of photons, QE is the quantum efficiency of the of the detector, and F is the noise enhancement factor beyond Poisson statistics. The ratio of F/QE is given by,

$$\frac{F}{QE} = N_{APD}\frac{\sigma^2_{pulsed} - \sigma^2_{dark}}{S^2_{APD}}, \tag{4.6}$$

where σ^2_{pulsed} is the variance while the light source in pulsed, σ^2_{dark} is the variance while the light sources is off, and S_{APD} is the signal from the APD. By measuring the dark variance of the detector, we could therefore monitor the impact of the power supplies to the dectectors' signal-to-noise ratios. The results of the noise testing indicated that the performance of the new system matched the performance of the replaced system.

In addition to upgrading the power supplies, a portion of the feedthrough panel was removed so that cables could be fed directly to the mezzanine without interruption. The connector type for the HV cable was change from BNC to SMA. No other connectors used this type of connection. Cables to the power supplies and digitizer where therefore shortened significantly and the possibility of a harmful misconnection was eliminated.

In summary, the spurious issue with the preamplifier gains was the eliminated, the

FIGURE 4.4: These pictures show the ”feedthrough panel” in the Thomson detector/laser room before the upgrade. The feedthrough panel resided in the ceiling of the room/the floor of the mezzanine above the room. The photo of the left (A) is a view from the mezzanine and the photo on the right (B) is the view up from the laser room.

risk of component damage due to improper application of HV was mitigated, and the signal degradation was decreased with to the elimination of excess cables. The new power supply system supplied stable biased voltage in both short and long time scales, while introducing no new noise to the system. Additionally, its modular design added robustness to the system.

4.2.3 Beamline upgrade

Around 2018, a beamline upgrade for the Thomson scattering lasers was completed. The project was spearheaded by Craig Jacobson to enable the TS system to obtain an absolute electron density measurement and improve overall data quality. Prior to the upgrade, the abundance of straylight prohibited an absolute density calibration. The spectral channel

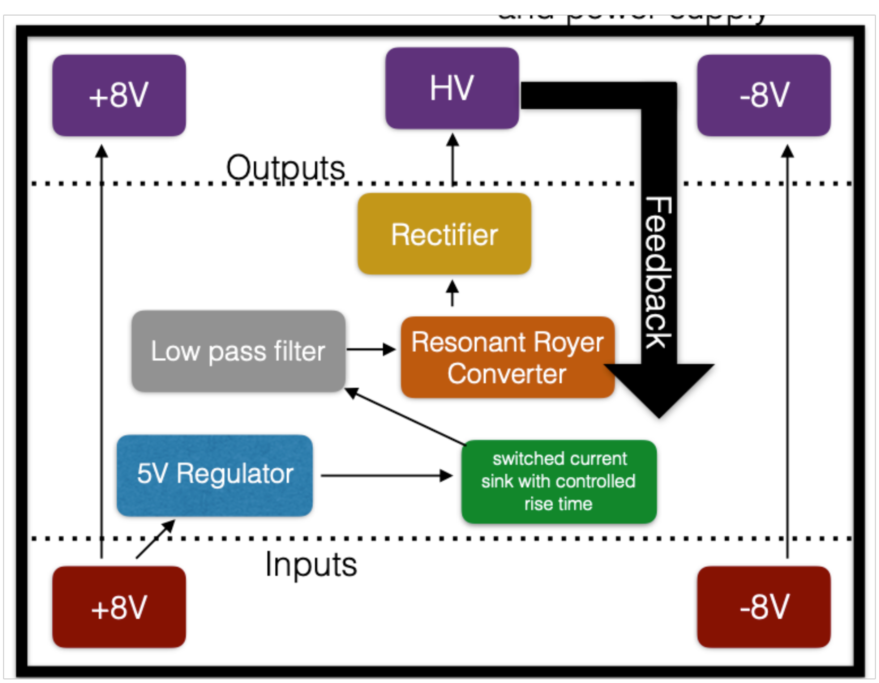

FIGURE 4.5: This is a block diagram summarizing the layout of the upgraded high voltage power supplies. A full circuit diagram and PCB layout board can be found on the MST document library.

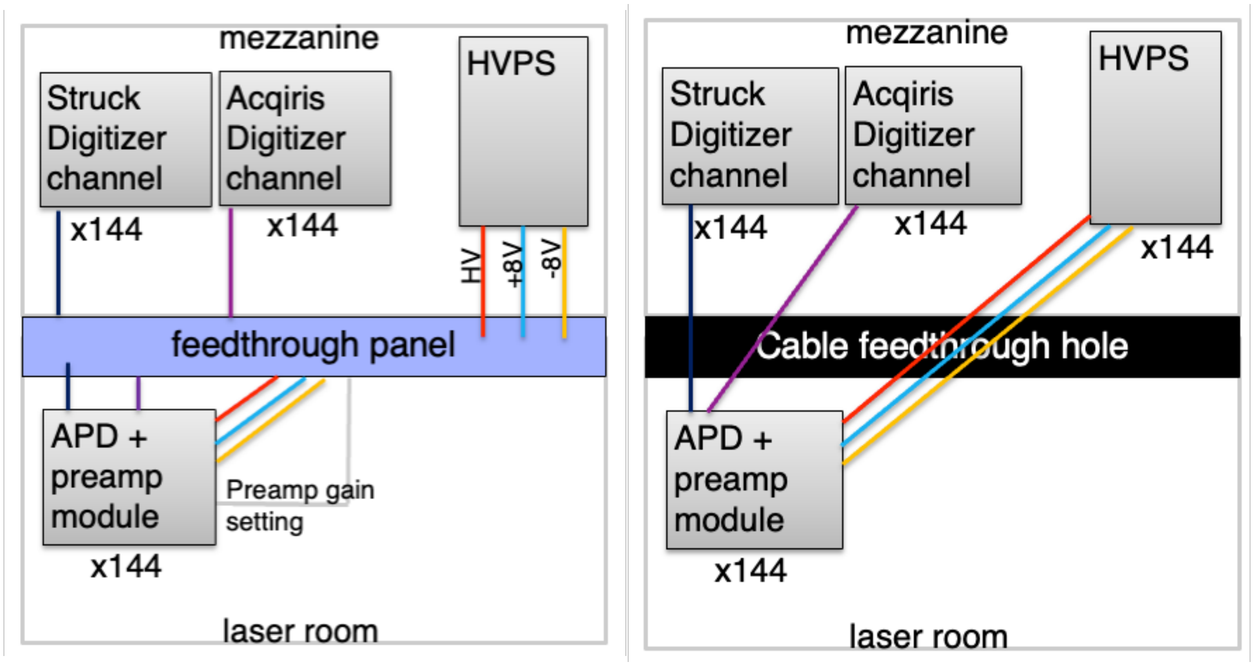

FIGURE 4.6: These diagrams show the layout of the system pre- (A) and post- (B) upgrade.

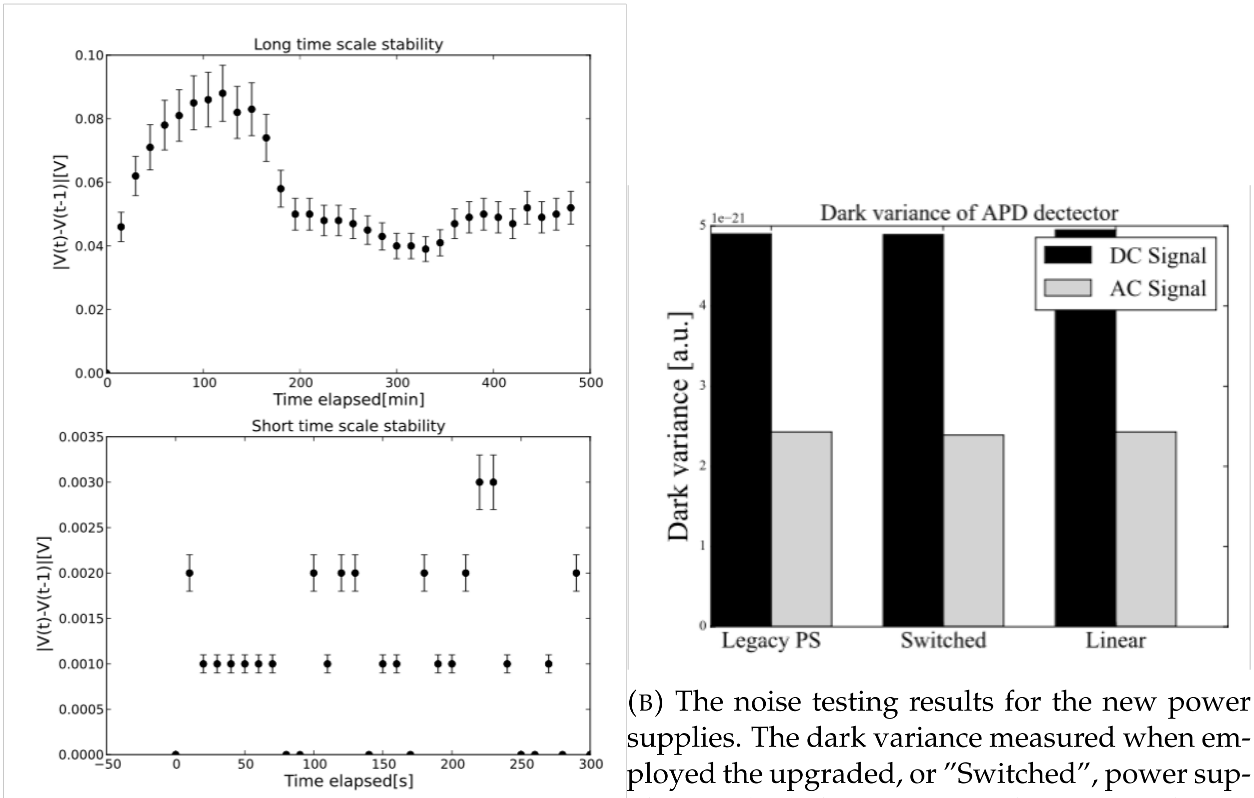

(A) Stability testing results of the new APD power supplies. The upper plot shows the long time scale results while the lower plot shows the short time scale results. The voltage change remained well below the acceptable threshold for both tests.

(B) The noise testing results for the new power supplies. The dark variance measured when employed the upgraded, or ”Switched”, power supply matched the variance when using the replaced power supply (labeled ”Legacy PS”).

FIGURE 4.7: The figures here summarize the noise and stability testing results performed on the upgraded detector power supplies.

centered around the laser line would saturate, so that the total number of scattered photons could not be measured. This in turn means that absolute electron density cannot be inferred. The beamline for the Thomson system was upgraded to include a longer beam path before entering the MST vessel so that baffles could be added to mitigate the effects of straylight. Detectors were also added to measure the laser output. Ultimately, an absolute density calibration was never performed. Fig. 4.8 shows the baffling system employed to mitigate straylight in the system [9, 10].

Although the absolute density measurement never came to fruition, the overall reduction in straylight improved data quality for standard TS temperature profile. Straylight from the laser line would often leak into adjacent spectral channels. This was particularly a problem for the edge-most points. At the edge, the plasma temperature decreases such that only a few spectral channels collect data. Temperature measurements could not be resolved with parasitic straylight leaking into neighboring channels and saturating them.

Following the beamline upgrade, the plasma temperature could be measured effectively to the edge of the device; previously the limit was around $r/a \sim 0.8$. A selection of ensembled profiles generated for this thesis will be shown in the next chapter, including temperature measurements at radial locations out to the edge of the device ($r/a \sim -0.95$).

4.3 Calibration and Alignments

Extensive TS system calibrations and alignments of subsystems were performed prior to and during any data collection presented herein. The procedures for these calibrations have been well described and documented by others [11, 4, 12]. In this section, we will summarize the procedures performed.

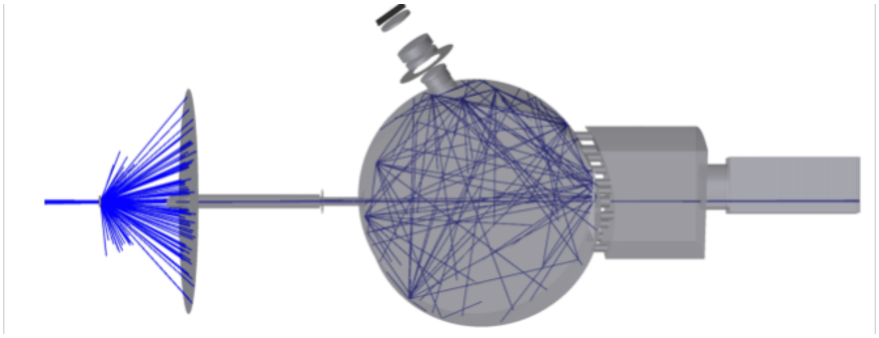

FIGURE 4.8: The figure shows the Zeemax modeling that informed the beamline upgrade. The modeled rays are shown in blue and an ideally absorbing plane plane stops the rays from scattering directly from the focal lens to the viewing optics. This figure is reproduced from Craig Jacobson's RSI paper [10].

4.3.1 Summary of Procedures Performed

A series of calibrations were performed both before and throughout the data collection process. The more time intensive procedures were performed before data collection. These included: polychromator and detector alignment, noise calibration, and a spectral calibration.

The polychromator alignment procedure involves shining a light source into the polychromator then ensuring that the relay mirrors center the light appropriately onto the next channel in the sequence. This procedure is performed on each channel, starting at the zero-channel until all the channels have been aligned. Additionally, the APD position behind the filters is adjusted to maximize the signal strength. This procedure was performed on all the polychromators.

The noise calibration procedure is adapted from what previously would have been wrapped up in the absolute gain calibration procedure. This procedure and model were developed by Lucas Morton [11, 12, 13]. The noise calibration is technically only part of the absolute gain calibration procedure. To completely replicate the result of that procedure, a gain calibration would also need to be performed, which is more time intensive than the noise calibration, though still less intensive than the absolute calibration procedure. Since the detectors themselves had not changed since a calibration was last performed, a noise calibration was deemed sufficient but necessary given the use of upgraded power supplies. The noise model written in terms of signal variance σ^2 is given by,

$$\sigma^2 = \epsilon^2 S^2 + GMFS + (GMFs_{bg} + v_e^2)\tau_{int}, \tag{4.7}$$

where ϵ is the relative uncertainty introduced by numerical integration or pulse-fitting method, S is the signal, G is the gain, M is the avalanche gain, F is noise enhancement factor, s_{bg} is the mean background signal level in volts produced by background plasma light, v_e^2 is the background electronic noise spectral density in V^2/Hz measured at the output of the detector, and τ_{int} is the integration time. The two middle terms in Eqn. 4.7 are the photonic noise contribution to the signal variance, or,

$$\sigma_{phe}^2 = GMF(S + s_{bg})\tau_{int}. \tag{4.8}$$

Luckily, it has been found that the noise model coefficients GMF are constant over the range of relevant wavelengths. These noise model coefficients can be determined simply by fitting the variance. In this updated formulation, the signal to noise ratio is given by,

$$SNR = \sqrt{\frac{S}{GMF}}. \tag{4.9}$$

The noise calibration is performed using the daily calibration system, which will be discussed again shortly. Fibers from shine 940 nm light from integrating spheres obliquely onto each APD, bypassing the interference filter. While the amplitude of the light cannot be varied, neutral density filters of varying attenuation are placed in front of the light source to vary the amplitude. The measured variances are then fit to Eqn. 4.7 to obtain the necessary noise factors to properly calibrate the system.

The last of the significant procedures was a spectral calibration. This procedure is used to create the instrument functions for each polychromator channel. The instrument function for a given polychromator, I_{poly} is given by,

$$I_{poly}(\lambda) = GM * T(\lambda) \cdot \eta_{APD}(\lambda), \tag{4.10}$$

where $T(\lambda)$ is the transmission function of the filter and $\eta_{APD}(\lambda)$ is the quantum efficiency (sometime called QE) of the detector. It is necessary to determine the instrument function so that the model signal can be determined, which we will see in the next section is necessary for fitting the data to determine temperature. The model signal is given by,

$$S_{model} = \int S_{\omega}(\lambda, T_e, n_e) GM \eta(\lambda) T() d\lambda, \tag{4.11}$$

where $S_{\omega}(\lambda, T_e, n_e)$ is the scattered spectrum in photons per nm.

The spectral calibration procedure requires a stable light source with a broad output spectrum and a calibrated reference detector. A supercontinuum (SC) light source, producing broad spectrum wavelengths covering the necessary range from 700-1200 nm, is passed through a SpectraPro 500i scanning monochromator. The monochromator transmits a narrow spectrum with a selectable central wavelength and selectable width. This

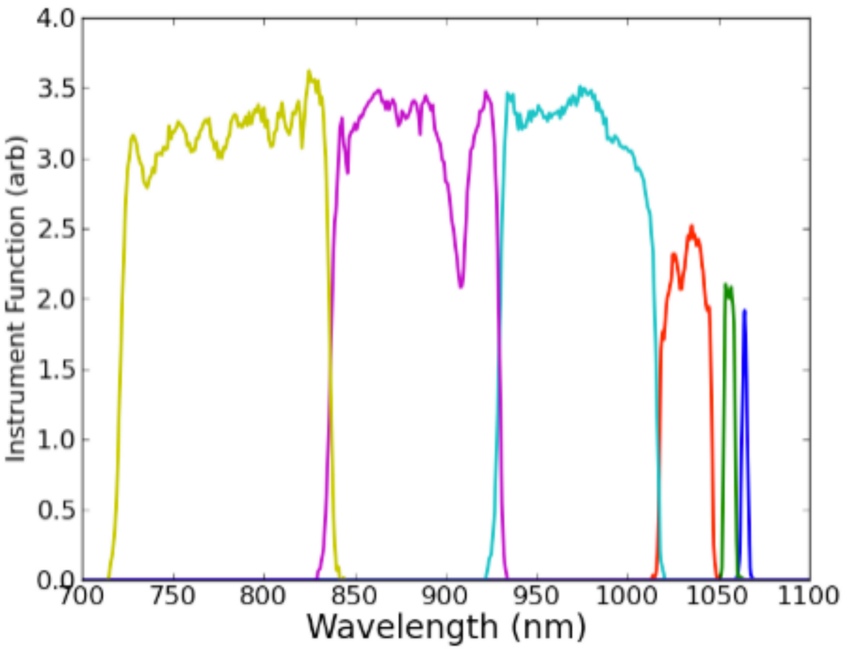

FIGURE 4.9: This figure shows an example instrument function. The dip at 910 nm is a result of a dip in the fiber transmission at that wavelength.

light is sent via fiber optic cable to a reference detector and the polychromator being calibrated. The monochromator central wavelength is scanned over the range of relevant wavelengths in 1 nm intervals with 100 repeated trials at each step. For the calibration performed for this thesis, this wavelength range included the zero-channel which includes the laser line. However, the zero-channel was not included in the fit procedure because a method had not been developed to subtract the laser light from the total signal, even though the straylight mitigation effort made it so that these channels were no longer always saturated. Following the sweep, the dark voltages are recorded. The measured signals from the polychromator APDs are divided by the reference APD signal to eliminate variations caused by the lamp spectrum and monochromator transmission. Fig. 4.9 shows an example of a resulting transmission function for a polychromator.

During the data collection, radial calibrations of the system were performed fairly regularly. The radial calibration procedure determines from where in the minor radius a polychromator is collecting data. This procedure had to be performed every time the plasma-facing component of the collection lens was replaced. Additionally, the fiber mount holding the fiber optic cables in place had to be realigned at this time. Nominally to perform this procedure, a radial calibration probe with a 1064 nm HeNe laser is sent up through the machine from the beam dump, driven upward by a stepper motor. This probe design was flawed such that the pinhole was not wide enough to emit light and all emitted light came from an aperature in the side of the probe that was too wide to localize the probe's location. While the probe is inserted into the device, the Struck digitizers simulataneously collect data from the zero-channel APDs. The stepper motor was roughly calibrated to a specific radial locations, however, it is possible for these values to drift and it is not a reliable way to set locations. Some fibers were also used as reference values, although, this too was less than ideal, as the fiber mount and focusing can shift when replacing the lens and aligning the fiber mount. Essentially, a reliable radial calibration could not be performed and the values are rough estimates. This system has since been updated by Daniel Den Hartog and Mark Thomas. The radial calibration probe is now designed to emit only light out of a pinhole aperature so that the radial location can be precisely determined. Additionally, the stepper motor driver has been updated and has been calibrated so that exact position can be determined. The software to operate this procedure has also been upgraded so that it can now be more easily performed by one person. Finally, a new collection lens assembly has been designed and installed so that the collection lens can be easily replaced without the use of the crane and needing to realign the fiber mount.

The radial calibration procedure was also used to monitor the degree to which the collection lens had become coated. It has been observed that relatively high temperature discharges, and particularly disruptions, lead to the collection lens becoming coated faster. Therefore data collection was performed starting at lower current and working upward.

Finally, each day before data collection, a daily calibration procedure was performed. This procedure is used to monitor the signals from the detectors before any data collection begins so that any issues may be addressed from the outset. It is meant to provide a quick check of the detector system and provide a record should any questions arise during analysis. To perform this procedure, a pulsed, near-infrared LED emits 940 nm light that is sent to three integrating spheres. This light is near the peak sensitivity for the APD detectors. These then distribute light to each of the 138 APD channels via a port at the top of the channel that bypasses the bandpass filters. The digitized signals are collected by the Struck digitizers and then plotted to be quickly checked by the Thomson operator as part of the Thomson set-up checklist to ensure that there are no obvious issues.

4.4 Low Density Analysis Technique

During data collection, many low density and temperature shots were taken. This pushed the limits of what the Thomson system could diagnose. To improve the quality of these low temperature fits, a new ensembling technique was developed.

The typical APD response to a signal is a negative-going pulse in the DC signal at around ~ 1300 ns, and after the short duration of the laser pusle the APD current signal quickly returns to the background level with a time constant ~ 40 ns. These pulses are then fit with a pulse fitting routine [5, 4, 14], and then the signal is integrated to obtain the number of photons measured by the detector. Using this data the temperature is then determined in a Bayesian framework [5]. Bayes Theorem says:

$$P(X|D,I) = \frac{P(D|X,I)P(X|I)}{P(D|I)} \tag{4.12}$$

where X is the model or inference, D is the data and I is additional background information. $P(D|X,I)$ is the likelihood and represents the probability of recording the data given the model and background information. $P(X|I)$ is the prior probability and represents information already known, such as constraints on the measured parameters (i.e. temperature and density must be positive). $P(D|I)$ is referred to as the evidence and is significant when comparing different models but otherwise simply serves as a normalization factor.

When we apply Eqn. 4.12 to the Thomson diagnostic we obtain the following formula:

$$P(T_e, n_e|D, \sigma, I) = \frac{P(D|T_e, n_e, \sigma, I)P(T_e, n_e|I)}{P(D|I)}, \tag{4.13}$$

where σ represents the error. We neglect the evidence, and set the prior such that it is uniform over the measurement range. Then, assuming that the signals from each polychromator channel are independent and Gaussian distributed, we can obtain the following expression for the posterior:

$$P(T_e, n_e|D, \sigma, I) = \frac{1}{\prod_{j=1}^{N_D} \sqrt{2\pi}\sigma_j} exp\left(-\frac{1}{2}\chi^2\right) \tag{4.14}$$

$$\chi^2 = \sum_{j=1}^{N_D} \frac{\left[S_{APD,j} - S_{model_j}\right]^2}{\sigma_j^2} \tag{4.15}$$

where S_{APD} represents the number of photons determined analyzing the APD signal, S_{model} represents the number of photons expected by the model, and N_D represents the total number of polychromator channels. Because the absolute density measurement is not incorporated, that parameter is marginalized out:

$$P(D|T_e) = \int P(D|T_e, n_e) dn_e \tag{4.16}$$

The error is estimated from the 1/e width of the one-dimensional probability distribution.

For low temperature data, a relatively small number of channels pick up a signal so it is important to maximize the quality of fit in these channels. Additionally, since the density will also be smaller at lower temperatures, the signal strength is diminished. To compensate for this, a technique was developed to ensemble data. The pulses from each laser shot within a single MST discharge were summed and then fit. This improved the signal-to-noise ratio for the temperature determination. A prerequisite to performing this procedure is to ensure that the data that are being ensembled are taken during period when the plasma conditions are held constant, particularly the electron density. Most of the low temperature and density data were collected using the PPS system on MST, which is remarkably good at maintaining constant conditions. The results of the fit are reviewed by eye to eliminate any overfitting or to exclude any channels whose data looks suspect. This further improves the result, but is much more time intensive than the standard fitting procedure. Fig. 4.10 shows an example of a plot generated for review when performing this procedure. It shows data from “Polychromator 4” which has six channels. The zero-channel, which surrounds the laser line, is excluded from the fit. The blue traces represent four laser shots during a single MST discharge. Here we only show four traces for clarity. The red trace represents the summed result. These traces are processed to be in volts but the summation is performed on the raw data and then processed the same as the other traces. The black dashed lines shows the fitted pulse. Channels one and two look reasonable. Channel three appears to be overfit and was manually set to be zeroed. Channels four and five are also set to zero and also show signs of overfitting resulting in a photon count that would be negative. Typically these channels are disregarded in the fit but here the results are set to zero, which a is reasonable result when looking at the signals. It is also possible to exclude a channel from the fit, rather than setting the result to zero if it displays any signs of not functioning. This is done, for example, with channels one and five for Polychromator 5 shown in Fig. 4.11.

A template Jupyter notebook has been created so that others may utilize this procedure and instructions on how to do so have been documented on the Thomson scattering plasma wiki under the MST wiki. The results of these improved fits are shown in both the Appendix and in Ch. 5.

4.5 Summary

The Thomson scattering diagnostic was a vital component to the S-scaling effort. It provided electron temperature measurements, contributed to an IDA determination of Z_{eff}, and a set of electron temperature profiles with r/a values > 0.8 thanks to the beam line upgrade spearheaded by Craig Jacobson. It was adapted to be run with a team of two to three people down from seven at its peak. These efforts increased the ease which which the diagnostic can be used. A new ensembling technique was developed to improve the

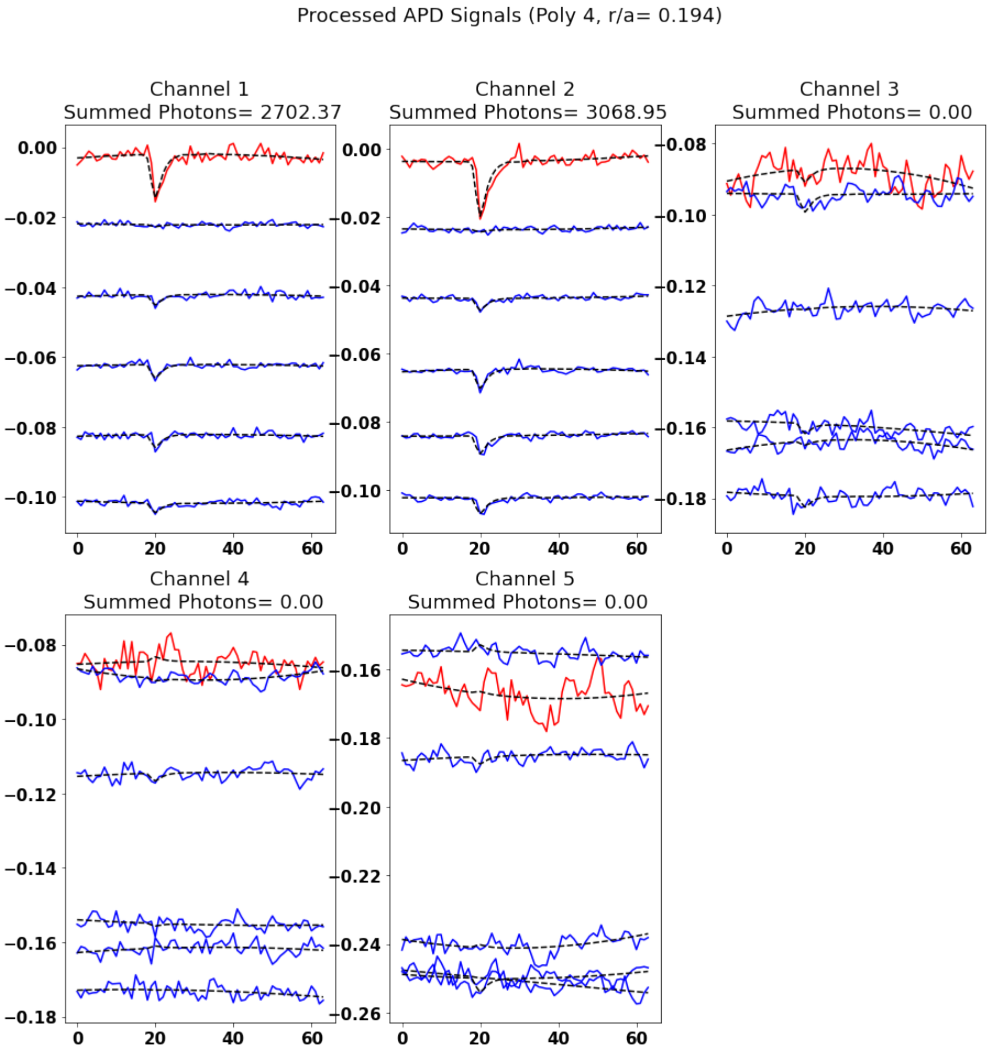

FIGURE 4.10: This figure demonstrates how the summing procedure may be used to improve the temperature measurement. The traces are plotted in volts versus time. Each blue trace represents data generated during a single laser shot. The red trace represents the sum of the blue traces. The black dashed lines overlaying the data represent the result of the pulse fitting routine. The traces are offset to provide an unimpaired view of the signal. Typically, this is done for all 10-15 laser shots taken during the MST discharge, or for as many TS laser shots that are valid to include in the ensemble. The data shown here are from a low temperature discharge (~ 50 eV). There is an overfit of the data in channel 3 that can be zeroed by the person ensembling the data, preventing an overestimation of the temperature.

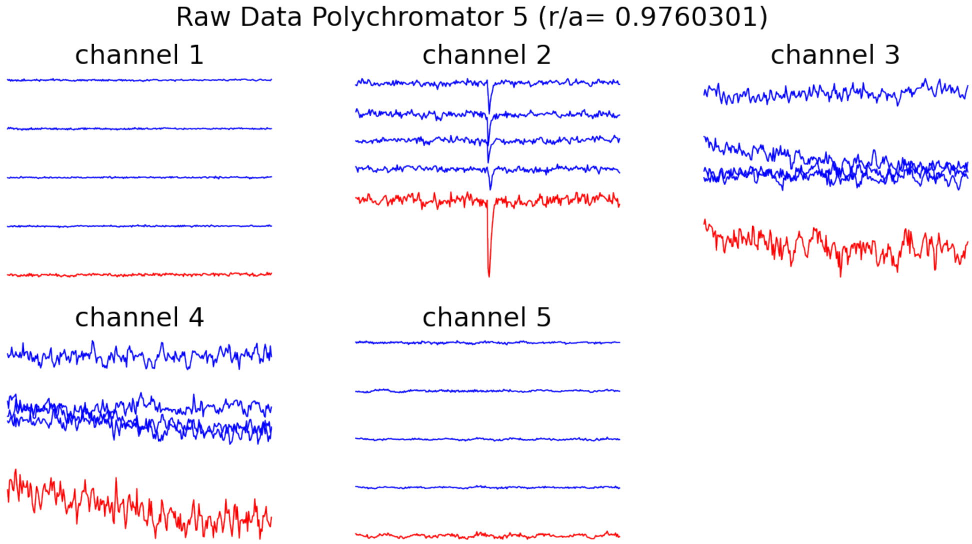

FIGURE 4.11: This figure shows a polychromator with two faulty channels as an example for the type of channel that is excluded from the fit with the new ensembling technique. Channels one and five show evidence of not collecting data and should therefore be excluded from the fit.

quality of low density and low temperature data so that the database of T_e profiles created could span a large range of Lundquist numbers.

Bibliography

[1] M. Galante, L. Reusch, D. D. Hartog, P. Franz, J. Johnson, M. McGarry, M. Nornberg, and H. Stephens, "Determination ofiz/isubeff/subby integrating measurements from x-ray tomography and charge exchange recombination spectroscopy," *Nuclear Fusion*, vol. 55, no. 12, p. 123016, nov 2015. [Online]. Available: https://doi.org/10.1088/0029-5515/55/12/123016

[2] V. Zhuravlev and G. Petrov, "Scattering of radiation by finite volumes of relativistic plasma streams," *Soviet Journal of Plasma Physics*, vol. 5, no. 5, p. 3, 1979.

[3] A. Selden, "Simple analytic form of the relativistic Thomson scattering spectrum," *Review of Scientific Instruments*, vol. 79, no. 5-6, p. 405, 1980.

[4] E. Parke, "Diagnosis of equilibrium magnetic profiles, current transport, and internal structures in a reversed-field pinch using electron temperature fluctuations," Ph.D. dissertation, University of Wisconsin at Madison, 2014.

[5] H. Stephens, "Electron temperature structures associated with magnetic tearing modes in the madison symmetric torus," Ph.D. dissertation, University of Wisconsin at Madison, 2010.

[6] S. Z. Kubala, M. T. Borchardt, D. J. Den Hartog, D. J. Holly, C. M. Jacobson, L. A. Morton, and W. C. Young, "Upgrades to improve the usability, reliability, and spectral range of the MST Thomson scattering diagnostic," *Review of Scientific Instruments*, vol. 87, no. 11, 09 2016, 11E547. [Online]. Available: https://doi.org/10.1063/1.4962251

[7] J. Williams", *"Application Note 118: High Voltage, Low Noise, DC/DC converters"*, "Linear Technology", 2008.

[8] *"Photodiode C30954E, C30955E, C30956E Datasheet"*, "EGG Canada (formerly RCA)", January 1991.

[9] C. Jacobson, "'lundquist number scaling in reversed field pinch'," 'APS DPP Conference 2017 Milwaukee, WI' Poster Presentation, 2017.

[10] C. M. Jacobson, M. T. Borchardt, D. J. Den Hartog, A. F. Falkowski, L. A. Morton, and M. A. Thomas, "Identification and mitigation of stray laser light in the Thomson scattering system on the Madison Symmetric Torus (MST)," *Review of Scientific Instruments*, vol. 87, no. 11, 08 2016, 11E511. [Online]. Available: https://doi.org/10.1063/1.4960063

[11] L. Morton, "Turbulence and transport in magnetic islands in mst and diii-d," Ph.D. dissertation, University of Wisconsin at Madison, 2016.

[12] L. A. Morton, E. Parke, and D. J. D. Hartog, "Detailed modeling of the statistical uncertainty of thomson scattering measurements," *Journal of Instrumentation*, vol. 8, no. 11, p. C11003, nov 2013. [Online]. Available: https://dx.doi.org/10.1088/1748-0221/8/11/C11003

[13] L. Morton, *Avalanche Photodiode Detector Noise and Resulting Error in Thomson Scattering Temperature Estimation*, University of Wisconsin at Madison, 2013.

[14] J. Reusch, "Measured and simulated electron thermal transport in the madison symmetric torus reversed field pinch," Ph.D. dissertation, University of Wisconsin at Madison, 2011.

Chapter 5

Lundquist Number Scaling Results

What follows is a presentation of the results from the main question posited by this study:

How do RFP dynamics scale with Lundquist number?

This question is explored to provide insights into how the RFP configuration might scale to reactor-relevant sizes as well as how to better capture and investigate its physics with simulations. Important performance metrics scale with Lundquist number, namely, the magnetic field fluctuation amplitudes for various mode numbers, energy confinement time, poloidal beta and the stochastic thermal diffusion. First, we will cover the framework used to conduct the investigation and define relevant parameters and jargon for this study. We will then go over the scaling results obtained from experimental data. Then these results will be compared to those obtained from the modeling codes briefly described in Ch. 2. We will also use the results to extrapolate to fusion-relevant scales. The chapter will conclude with a summary of key take-aways and a discussion of how the results align with stochastic theory.

5.1 Framework

In this section, we will discuss the framework for the experimental data collection, establish the vocabulary used to describe these data, and go over the experimental definition and significance of the various parameters of relevance. The "scaled parameters", or parameters that were analyzed as Lundquist number was scaled, were the magnetic field fluctuation amplitudes for many of MST's magnetic modes, or b_n, and several transport-related quantities including the energy confinement time, τ_E, toroidal β_θ, and the thermal electron diffusivity, χ_e. The word "parameter" is used broadly herein to refer to a values that can be easily controlled by an operator of MST, such as plasma current and plasma density, as well as values that are more indirectly controlled, such as the Lundquist number. To start, we will begin with a discussion of Lundquist number and then we will briefly review each of the parameters whose scaling was studied as Lundquist number was varied.

5.1.1 Data Collection: Scaling Lundquist Number on MST and the Greenwald Fraction

The Lundquist number, S, served as the independent variable against which the scaling study was performed (see Ch. 2 for a discussion on the theoretical and practical basis for this choice of independent parameter). Recall that the Lundquist number is the resistive diffusion time over the Alfven time, or,

$$S = \frac{\tau_R}{\tau_A} \sim T_e^{3/2} I_p n_e^{-1/2}. \tag{5.1}$$

This parameter was varied on the MST device through a choice of plasma current, I_p, and the line-integrated electron density, n_e, where I_p served as a coarse adjustment "knob" and varying density then more precisely adjusts the S value. Electron density and temperature are correlated so that varying density affects the electron temperature. For these scaling studies, data collection focused several plasma currents spaced across the range of currents which MST is capable of generating, ranging from $35kA \lesssim I_p \lesssim 500kA$. The spacing between selected currents is not even and was chosen based on practical considerations when employing the PPS system. At each of these currents, data collection was focused at primarily on two density fractions of the Greenwald limit, or what will be referred to as the Greenwald fraction, or n_e/n_G, herein. These values were $n_e/n_G = 0.23$ and $n_e/n_G = 0.34$ and were selected somewhat early on in the data collection. Due to time constraints, data collection was concentrated over a relatively short period of time. These values worked well for low current plasmas, while still being feasibly achievable at high currents. Sometimes, these Greenwald fractions will be referred to as the low density data and the latter will be referred to as the high density data respectively.

The Greenwald limit is an empirical upper bound on the achievable density at a given plasma current in tokamak plasmas. It is given by $n_G = \frac{I_p}{\pi a^2}$, where I_p is the current in MA, n_e is the line-averaged density in $1^2 0$ m^{-3}, and a is the relevant scale length in m, the minor radius of MST in this case [1, 2]. In practice, the RFP density limit is a soft limit above which impurity and radiation losses are so significant that confinement degrades and the plasma discharge prematurely terminates [3]. MST has achieved densities above the Greenwald limit, however, for normal operation, MST plasmas obey the $n_{eG} < 1$ criterion, as do tokamaks. The use of this parameter has become somewhat standard in RFP scaling studies.

Fig. 5.1 shows a mapping of Greenwald fraction and current to Lundquist number values to illustrate how Lundquist number was varied on the MST device. The Lundquist number itself is not directly measured and the process employed to infer the Lundquist number will be covered shortly. For the high density case, the high value does not follow the expected pattern. Briefly, the data that make up the ensemble at that point are less robust and fewer shots were included in that ensemble. This will be discussed in more detail later on in the chapter.

The Greenwald fraction, or n_e/n_G, is equivalent to the inverse of the I_p/N parameter that was used by Stoneking [4] and others in past RFP studies, where $N = n_e * \pi a^2$. In that study, data collection was also focused around two values of $I_p/N = 2, 6$ which are equivalent to $n_e/n_G = 0.5, 0.17$ respectively. The full range of I_p/N, and thus the full range of n_e/n_G, is accessible for any I_p such that the parameter space of I_p versus Greenwald density fraction is rectangular. Stoneking's study used a smaller range of Lundquist numbers, but a wider range in Greenwald fraction. For this S-scaling study, some data were collected for a Greenwald fraction $n_e/n_G = 0.45$. A fewer number of shots were obtained for this high Greenwald fraction value, so those data were not analyzed or included herein, though it would be possible to analyze these data for a smaller range of Lundquist numbers than was done for $n_e/n_G = 0.23, 0.34$ cases.

Fig. 5.2 shows the data collected for this study. In the figure, n_e/n_G versus I_p space is depicted and each dot represents an MST shot taken at that point in parameter space. The magenta points represent data collected using the PPS system and the blue points represent data collected using the Legacy power supply system. Lines of constant n_e, a more intuitive variable for most MST operators and users, are included for reference. The yellow tinted area represents the band of parameter space that was used to create the low density, or $n_e/n_G = 0.23$, ensemble and the orange tinted band represents the high density ensemble, or $n_e/n_G = 0.34$. Both these bands are centered at the precise value and bounded by a 10% variation in this central value. A third band representing $n_e/n_G = 0.45$, shaded in gray, is also depicted. Data collection was also done at this band where possible, however, because it is at a high density, ensembling these data over the entire range of accessible Lundquist values was experimentally challenging, namely at high current data collection. Using high densities was particularly challenging when using the Thomson scattering system. High density operation typically leads to more disruptions that coat the Thomson collection lens. Thomson personnel resources were limited, so a balance was struck between pushing to high density operation and limiting resource-intensive maintenance to the Thomson scattering system. Like was mentioned earlier, these $n_e/n_G = 0.45$ data are included in the database created by this experimental effort, but analyses of them are not presented here. In total, the dataset consists of over three thousand MST shots and are accessible for any other analyses that subsequent WiPPL users may utilize. Appendix A provides details on how to access and utilize this database.

5.1.2 Inferring Lundquist Number from Experimental Data

For the results presented herein, the Lundquist number was inferred from its constituent experimentally-diagnosible plasma parameters. Looking at the expression for Lundquist number again, this time expanding the expression, we have,

$$S = \frac{\tau_R}{\tau_A} = \frac{\mu_0 a^2}{\eta(Z_{eff}, n_e, T_e)} \frac{B}{a\sqrt{\mu_0 \rho}}, \tag{5.2}$$

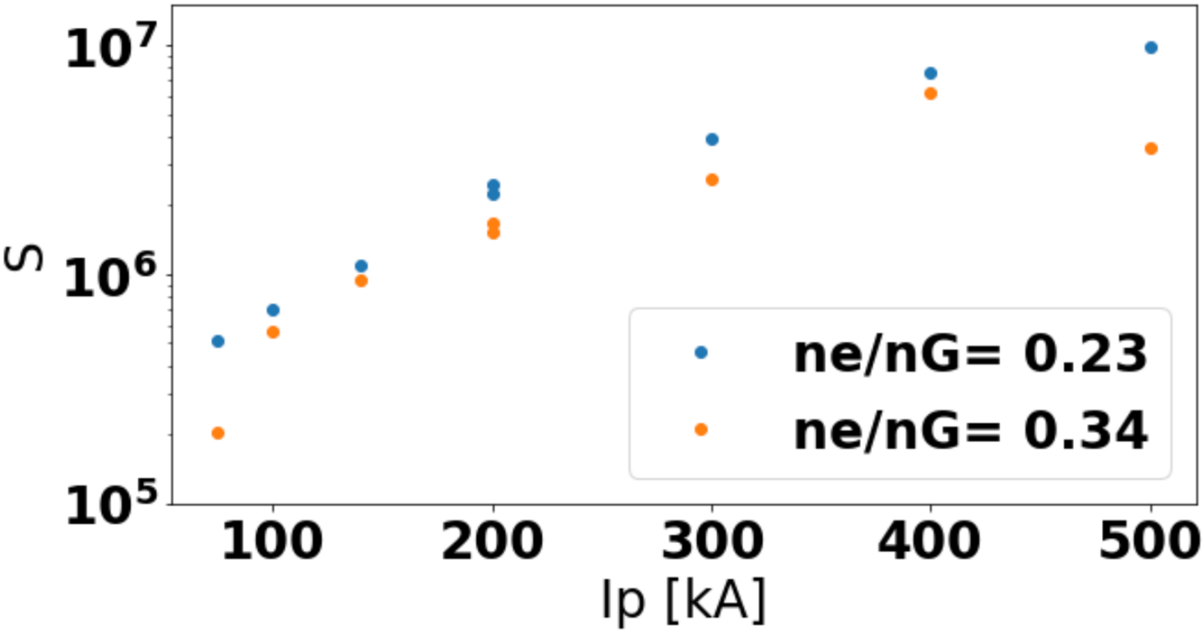

FIGURE 5.1: Mapping of density and plasma current to Lundquist number. This mapping was done ensembling data of the measured quantities used to determine Lundquist number to then make the Lundquist number determination. Two points exist at currents where both Legacy and PPS data were collected.

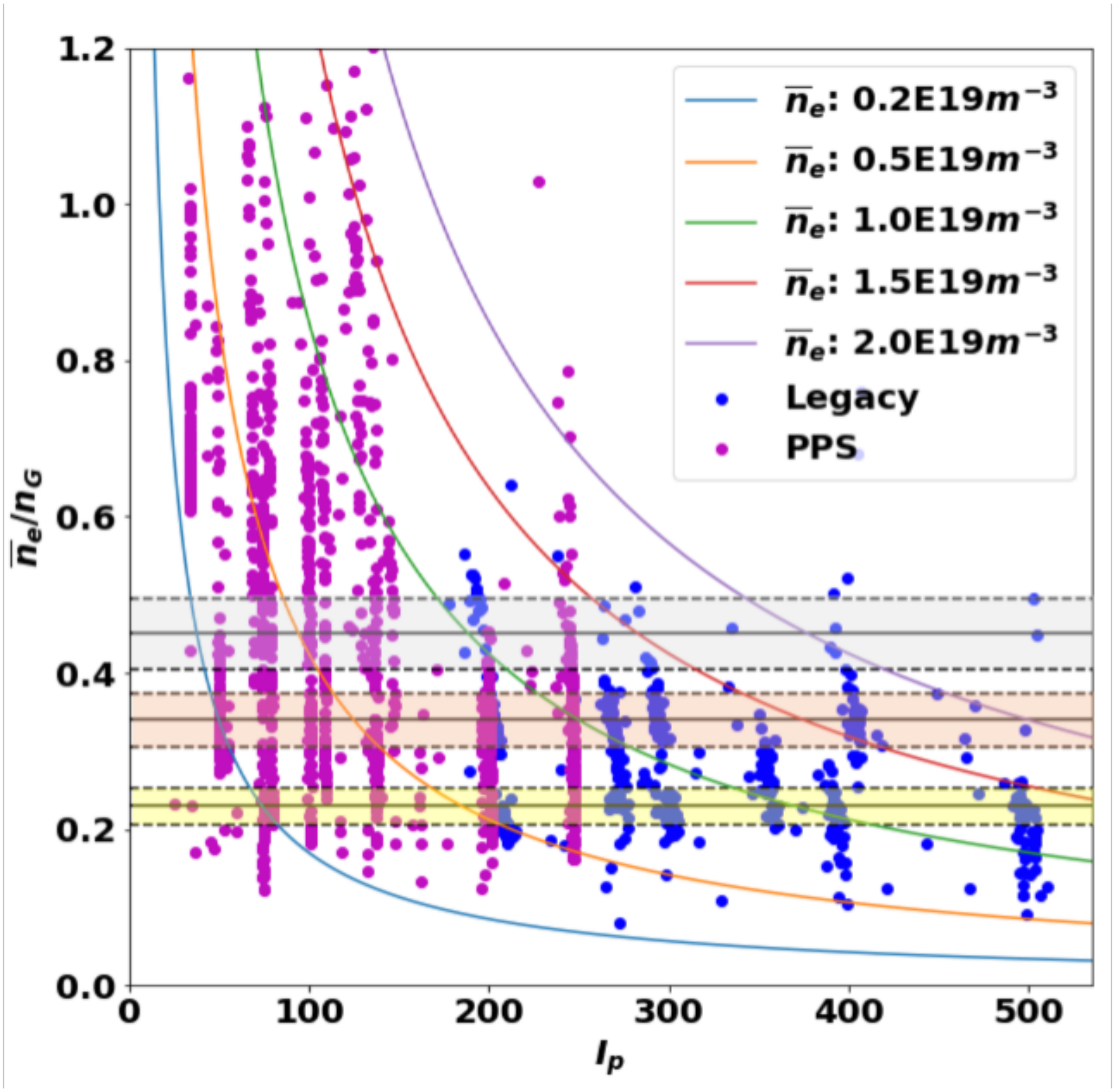

FIGURE 5.2: Plot depicting the data collected for this experimental effort in Greenwald fraction over plasma current space. Over three thousand MST shots are included. Not all shots shown here were used in the ensembles used to create the S-scaling results presented in this chapter. The yellow and orange shaded bands represent the low and high density ranges used for those S-scaling ensembles. The magenta points were created using the PPS system and the blue points were created using the Legacy system. The solid colored lines represent constant electron density.

where η is the resistivity, Z_{eff} is the effective ion charge, T_e is the electron temperature, B is the magnetic field, and a is the minor radius of MST. B, n_e and T_e are relatively straightforward to infer via measurement. However, the determination of resistivity, η, in part due to its constituent parameter Z_{eff}, is a more complex and much less standardized inference on MST. Its value will be discussed in more detail later, but to start, we will first formulate a more practicable expression for the Lundquist number.

First, let's take a look at our expression for the resistive diffusion time, which is given by,

$$\tau_R = \frac{\mu_0 a^2}{\eta} \tag{5.3}$$

where a is the minor radius of MST, μ_0 is the magnetic permeability of free space, and η is chosen to be defined as a Spitzer resistivity, η_{Spitz}, following the formulation laid out by Stoneking [5, 6, 4, 7], which is given by,

$$\eta_{\parallel} = \frac{5.22 \times 10^{-5} Z_\sigma \ln\Lambda (T_e[\text{eV}])^{-3/2}}{1 - f_t} \Omega\text{m}, \tag{5.4}$$

where $\ln\Lambda$ is the Coulomb logarithm, f_t is the trapped particle fraction, and Z_σ is given by,

$$Z_\sigma \approx 0.4 + 0.6 Z_{eff}. \tag{5.5}$$

This functional relationship between Z_σ and Z_{eff} is taken from Hirshman and Sigmar following Hutchinson's notation and is an approximation via linearization [7, 6, 4, 8, 9]. Z_{eff} is taken to be constant from a core value of the profile as Lundquist number is varied ($Z_{eff} = 2.0$). It is an estimation that was not directly measured from the plasmas generated for this study. This will be discussed in more detail later. The neoclassical correction is $1/(1 - f_t)$ and is a volume averaged value that assumes that the plasma is collisionless.

Its value was set to f_t =0.38 which was obtained via equilibrium modeling [4, 10]. The implications of these choices will be discussed in a subsequent subsection.

Next we look at the normalization factor, τ_A. This is given by,

$$\tau_A = a/v_A = \frac{a(\mu_0\rho)^{1/2}}{B}, \tag{5.6}$$

where $\rho = A_i m_p n_i$ is the ion mass density for deuterium (i.e. $A_i = 2$) and $B = \mu_0 I_p/(2\pi a)$ is used as the characteristic magnetic field.

Ultimately, we get the following expression for the Lundquist number in terms of experimentally measurable and convenient values:

$$S = \frac{30 \cdot I_p T_{e,0}^{3/2}(1 - f_t)}{(0.4 + 0.6Z_{eff})\mathrm{ln}\lambda\sqrt{A_i\bar{n}_{e,0}}}, \tag{5.7}$$

where $\bar{n}_{e,0}$ is the line-integrated electron density for the central cord in units of 10^{19} m^{-3} measured by the FIR diagnostic, I_p is the plasma current in kA obtained by integrating the signal from the Rogowski coil that encircles the plasma, and $T_{e,0} = T_e(r \sim 0)$ is the core electron temperature in eV from averaging the three core-most points measured by the 21-point Thomson scattering system and is used as the characteristic temperature for this study. Ultimately, the Lundquist number is a global quantity and this definition is a combination of core and line-averaged parameters. In order to scale with Lundquist number, however, S needed to be distilled to a single value. Profile considerations will be discussed in a subsequent subsection.

5.1.3 Parameters Scaled

Magnetic field fluctuation amplitudes

The main parameter around which the scaling study was focused was the magnetic field fluctuation amplitude. As was discussed in greater detail in Ch. 2, magnetic field stochasticity leads to a rapid loss in particle confinement radially (i.e. out of the device). Large magnetic field fluctuations lead to overlap in magnetic islands so that the magnetic topology is stochastic rather than deterministic. The goal was to see how magnetic field fluctuation mode magnitudes varied with Lundquist number. Should field fluctuation amplitudes diminish significantly as Lundquist number is increased, field lines in the RFP will be deterministic enough that stochasticity would no longer be the major contributor to radial particle transport.

For this study, normalized magnetic field mode amplitudes were investigated by mode number. The expression for the normalized magnetic field fluctuation amplitude is,

$$\tilde{b}_{m,n} = \tilde{B}_{m,n}/B_{0,\alpha}, \tag{5.8}$$

where m and n are the poloidal and toroidal mode numbers respectively, $\tilde{B}_{m,n}$ is the mode fluctuation amplitude, and $B_{0,\alpha}$ is magnetic field on axis as determined by the alpha model [11, 12]. The fluctuations, $\tilde{B}$, are measured with sets of magnetic field coils situated in the toroidal shell of the device (i.e. $r/a = 1$). As was described in Ch. 3, these measurements are then Fourier decomposed into mode numbers that are resonant within the plasma at locations shown in Fig. 5.3. The poloidal mode number for most of the modes is $m = 1$ except at the reversal surface where all the $m = 0$ modes are present. The toroidal field array cannot resolve the poloidal mode number, therefore, $\tilde{b}_{m,n}$ is in reality

$\tilde{b}_n$. For the majority of the data presented herein, $\tilde{B}_n = \tilde{B}_{n,\theta}(r = a)$ is the the poloidal component of the magnetic field measured by the toroidal array of the magnetic field coils in MST's shell. $\tilde{B}_{\theta,n}(r = a)$ primarily contains the $m = 1$ mode.

In this chapter, we look at the $m = 1, n = 5 - 15$ and the $m = 0$ modes. The $m = 0$ is denoted as the $n = 1$ mode (see q-profile in Fig. 5.3). Though we are discussing plasmas in the multi-helicity regime herein, and so there are no "dominant" modes as such, the $n = 6$ mode exhibits distinct behavior and contains the most magnetic energy as is shown in Fig. 5.4, particularly during a sawtooth crash. The $n = 5$ mode intermittently appears in standard plasmas: it only exists for portions of the sawtooth cycle when q is larger than 0.2. Its signal shows an inverse sawtooth behavior, increasing at the crash when $q(r = 0)$ suddenly increases, then decreases until the next sawtooth crash. The $m = 0$ modes at the reversal surface and $m = 1$ modes resonant in the core interact nonlinearly to produce sawtooth events. The $m = 0$ of when the reversal parameter $F = 0$, thereby eliminating the reversal surface [13, 14]. We will not focus on the regime where this occurs but will look at the $m = 0$ mode keeping in mind its role in fueling these large dynamo events.

Sets of $\{S, \tilde{b}_n\}$ data were fit to the following equation:

$$\tilde{b}_n = c_n S^{-\alpha_n}, \tag{5.9}$$

where c_n is the coefficient of the fit and α_n is the scaling parameter of the fit.

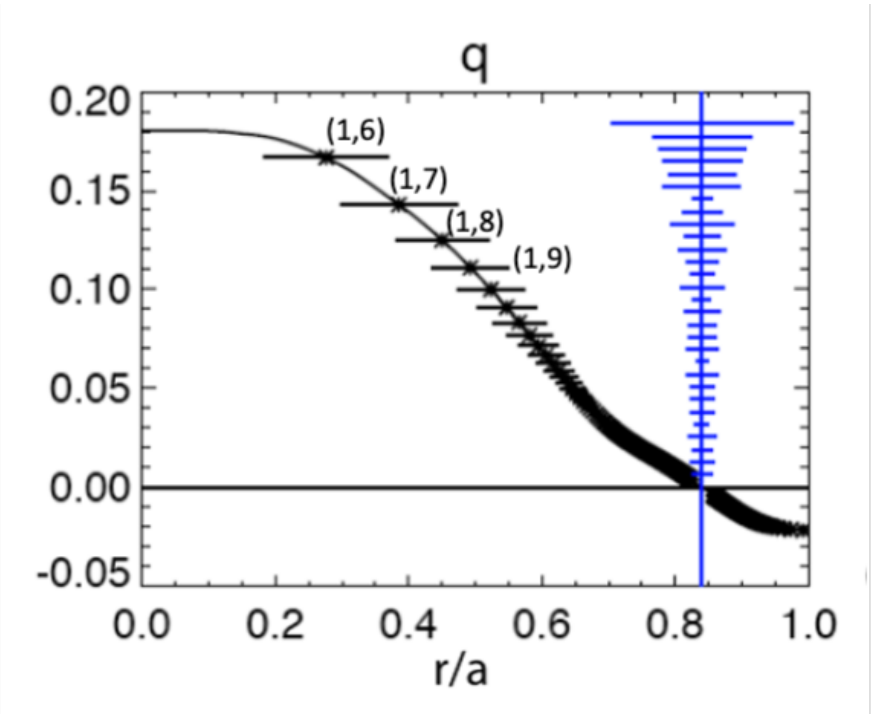

FIGURE 5.3: Example of an MST q-profile for a standard plasma. The island widths are depicted by the horizontal bars. We see that the $m = 0$ low n modes are all located at the reversal surface. The innermost mode is the $n = 6$ mode though the $n = 5$ can sporadically appear during sawtooth events.

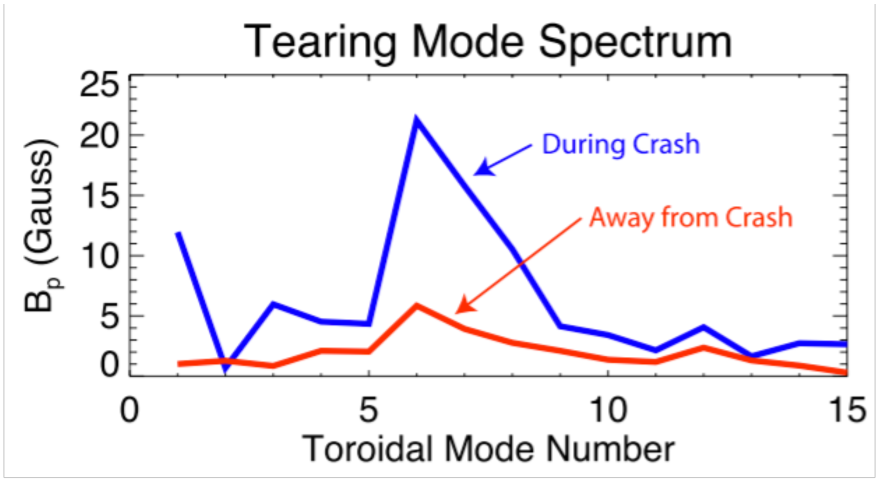

FIGURE 5.4: Distribution of magnetic mode energy away from and during a sawtooth crashed. Reproduced from [15].

Energy Confinement Time

The global energy time, τ_E, was also investigated in this study. This quantity represents the e-folding relaxation time of the plasma energy due to heat conduction. It is given by,

$$\tau_E \equiv \frac{U}{W_{in}} \tag{5.10}$$

where U is the global energy content in the plasma and W_in is the net rate of energy input [16].

The energy confinement time is of particular interest in the context of fusion. It is one of the terms in the fusion triple product, a quantity that encapsulates the parameters that need be maximized in order to increase the efficacy of a fusion reactor. For the RFP concept, the energy confinement times are relatively low and this low magnitude is cited as a weakness of the concept [17, 18].

Typical energy confinement times for standard discharges in MST are $\sim$ 0.5 - 1.0 ms [19, 20]. The confinement times shown in the following section were estimated in one of two ways: (1) using MSTFIT code, which was briefly described in Ch. 3, to create profiles on ensembles constrained by the ensembled electron temperature profiles, and (2) by plugging diagnosed values into a simplified formula on a shot-by-shot basis. There is no firmly established, universal scaling relationship for this parameter.

Electron Thermal Conductivity

Rechester-Rosenbluth type diffusion of thermal electrons is expected to behave as $\chi_{R-R} \approx D_{st} v_{th,e}$ where D_{st} is the stochastic diffusion coefficient and $v_{th,e}$ is the thermal electron velocity. The diffusion coefficient is given by

$$D_{st}(r) \approx \pi L_{AC} \frac{|\tilde{B}_r(r)|^2}{B^2(r)} \tag{5.11}$$

where L_{AC} is the autocorrelation length for magnetic fluctuations and is $L_{AC} \sim 0.7 - 1.0$ m and λ_{mfp} is the collisional mean free path and is on the order of 10s of meters [10].

The electron heat flux, Q_e, is given by,

$$Q_e = -\chi_e n_e \nabla_r T_e, \tag{5.12}$$

where χ_e is the electron thermal conductivity. In areas where the magnetic field is stochastic, it has been established that the collisionless stochastic transport model adequately describes the measured heat diffusivity, i.e. $\chi_e \approx \chi_{R-R}$ [21, 22]. For reference, Fig. 5.5 shows how the measured χ_e aligns well with the stochastic model result, χ_{R-R} for standard plasmas. It also shows that in enhanced confinement plasmas in MST (i.e. PPCD plasmas), the magnetic field is much less stochastic so that non-stochastic transport is dominant and the magnitude of χ_e is an order of magnitude lower.

The χ_{R-R} values presented in the next section are estimated using the measured magnetic field fluctuations, the measured T_e, L_{ac} from a field line tracing program, and RESTER profiles to translate edge measurements to the radial component magnetic field fluctuations. More detail will be given about the RESTER calculations in the subsequent sections.

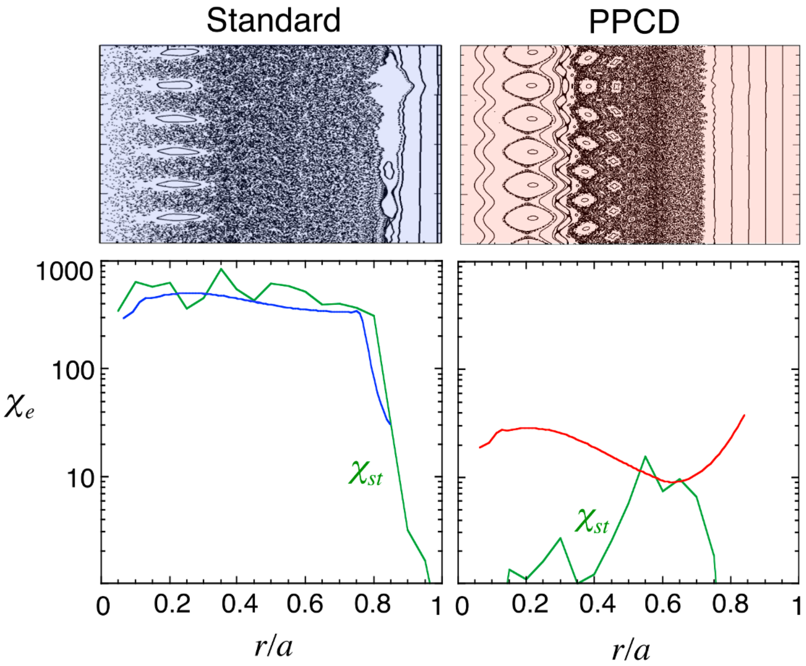

FIGURE 5.5: The top row of plots show Poincarè plots of MST standard (left) and enhanced confinement (PPCD) plasmas. The bottom row plots the respective χ_e values for these types of MST plasmas compared to the model χ_{st}. It is reproduced from [22, 23]

Poloidal Beta

The β parameter is the ratio of the plasma pressure to the magnetic pressure in the plasma. Therefore, the poloidal beta is given by,

$$\beta_\theta = \frac{<p>}{(B_\theta^2/2\mu_0)} \tag{5.13}$$

taking only the poloidal component of the magnetic field at $r = a$. It is advantageous for a reactor to have a high β value as this corresponds to having high density and temperatures with relatively little applied magnetic field. Producing high magnitude magnetic fields is expensive and reduces the efficiency of a reactor. The RFP concept possesses a relatively high β, with experimental values in MST measured as high as 26% and an ideal β limit on the order of 40% [18]. In RFPs, high β regimes are associated with a reduction in dynamo activity and large reduction in magnetic field fluctuation power [24]. These high β values are cited as an advantage of the RFP concept.

The β_θ values reported in the next section were calculated using the MSTFIT equilibrium reconstruction code.

5.1.4 Ensembling Methodology

"Ensembling", a common practice in laboratory plasma physics, is an averaging technique that averages data from similar plasma discharges to improve the statistics of a result. The typical methodology for creating ensembles in MST is to use a sawtooth event as an anchoring for the time axis. One can then either average over the sawtooth event, avoid it altogether by looking at times far away from an event, or look at specific periods during the sawtooth cycle. See Fig. 5.6, reproduced from J. Reusch's thesis [15], as an example for such a technique. This methodology was feasible in this context, because, for plasmas generated via the Legacy power supply system, the range of available plasma current (i.e. Lundquist numbers) was limited to relatively high values where sawtoothing in MST was limited to large discrete events.

However, this traditional approach was untenable for the work presented here. Fig. 5.7 shows the range of Lundquist number values accessible to each of the simulations and experimental power supplies applicable to MST. As we'll see in more detail in Ch. 6, as the Lundquist number is lowered, sawtoothing becomes more complex, making it no longer feasible to use a sawtooth event as an anchoring for time-based averaging and ensembling, as the reconnection activity moves from being discrete to more quasi-continuous. Additionally, given the nature of the study, it makes sense in the context of this investigation to average data over the entire flattop. We are not interested in the dynamics of the reconnection events but instead in the general behavior of the plasmas. It also happens to allow values measured at lower Lundquist numbers to be compared to those measured at higher Lundquist numbers, despite not having easily distinguishable sawtooth events.

We will now walk through in more detail the ensembling methodology employed, using the magnetic field fluctuation amplitude scaling as the relevant example. Each point in the plots containing the results of this study, more specifically, each point in one of the subfigures in Figs. 5.19 and 5.20, represents an ensemble. Plasma discharges are very reproducible and it is reasonable to treat each shot at similar plasma parameters as a"trial" in a set of repeated experiments.

To create an ensemble, first, a set of parameters is selected to be desired operating point at which data will be gathered. In this case, a specific plasma current and electron

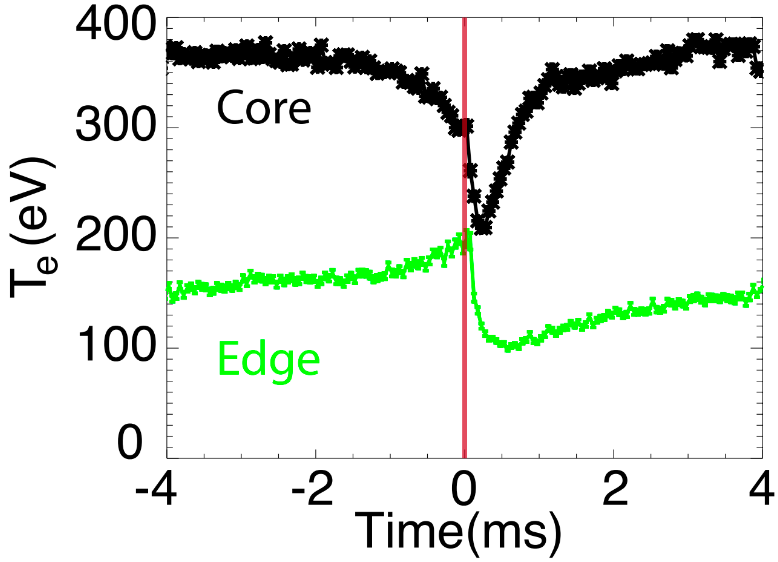

FIGURE 5.6: An example where ensembling was performed using the sawtooth as an anchoring for the time basis. Here the electron temperature was ensembled over the sawtooth event where $t = 0$ is the peak of the sawtooth event. [15]

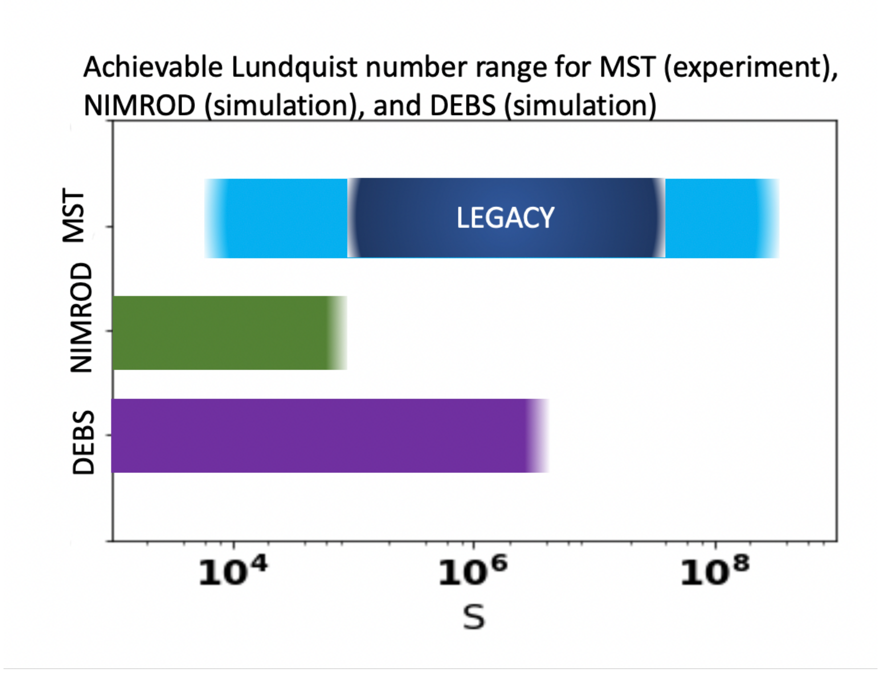

FIGURE 5.7: This chart shows the ranges of Lundquist number accessible to MST, NIMROD (as applied to RFP computations), and DEBS. The latter two are simulation codes that will be discussed later in the chapter. For the MST bar, the darker blue region represents the Lundquist number range accessible with the Legacy power supply system. The lighter blue bumpers of this bar represent the Lundquist number space that has been (the lower S values) or will be (the higher S values) made accessible by the upgraded Programmable Power Supply (PPS) system.

density with the reversal parameter, $F = B_t(a)/ < B_t >$, held relatively constant at $F = -0.2$ across all ensembles. Then plasma operation and data collection is targeted at these parameters.

To begin processing these gathered data, a time window is selected across which the data will be averaged. This window was selected to be during the majority of the flat-top duration. When ensembling, the practical yet effective approach used here was to briefly scan over all the relevant shots from a given day to select a uniform time window that would apply to all shots within the shot list from that sequence of repeated shots. This window lasted at least 10 ms and typically encompassed the times during which the Thomson laser was firing. This time window was then used when assessing which shots to include in an ensemble. More details about the specific time windows used for each ensemble can be found in the Jupyter Notebooks in the database information (see Appendix A).

A list of MST shots whose data would be averaged for each ensemble data point was then created. The shots included in this list have plasma parameters that match the desired parameters within a certain tolerance. For the ensembling here, the tolerance was set to 10-15% of the target value. The shots were scanned by eye to determine which would be included based on meeting the plasma parameter targets. Again, a Jupyter notebook containing the results of this ensembling, as well as routines for repeating the procedure, is included in the database.

Fig. 5.8 below summarizes the target parameters that were used for each ensemble. The values in the figures represent the average over the time window. The pinch parameter, or $\Theta = B_p(a)/ < B_t >$, while not controlled for, is included for reference as well. Generally speaking, Θ was fairly constant across all ensembles. The reversal parameter

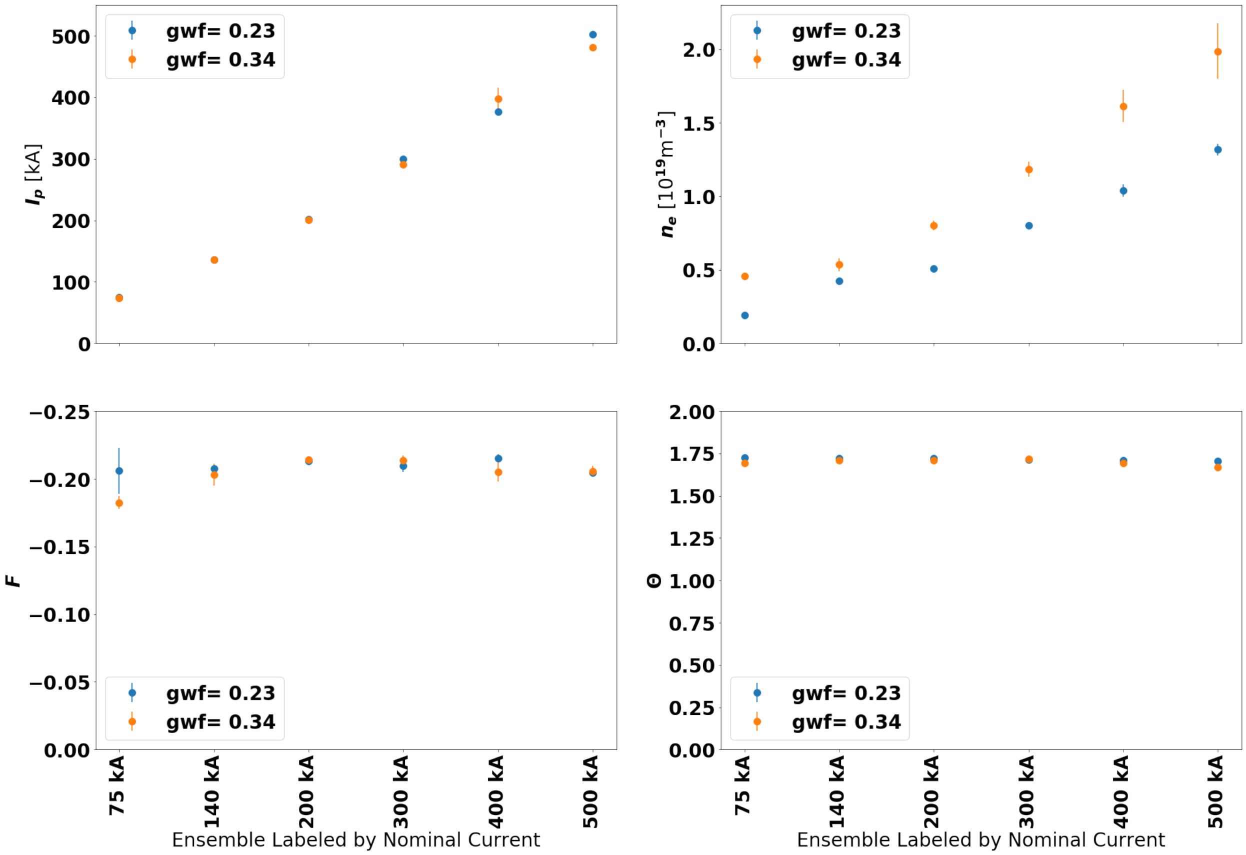

FIGURE 5.8: This plot summarizes the operating parameters used for each ensemble in the magnetic field fluctuation amplitude scaling results. For the shots included in an ensemble shot list, these parameters were held fairly constant over the time window during which averaging was performed for the shot.

for the lowest current, high density ensemble is slightly less reversed. This was simply due to an operational oversight. The difference is still within 15% of the other values. The error bars represent the standard deviation of the average values for each shot.

Fig. 5.9 shows an example of plot used to filter a 500 kA, low n_e/n_G shot. The red dashed lines represent the time window of the averaging. The green dashed line represent the target value for the scope. We see that these values differ from the target values. The shot shown was included in the ensemble based on the top three plot and that the plasma was rotating.

The shots were also checked to see if mode locking had occurred. This was done by looking at the velocity of the magnetic modes given by the poloidal coil of the toroidal array (velocity of $B_{p,n}$). If the plasma is not rotating, the recalibration procedure performed for the magnetic coil array will not have been effective so that shot and its data must be excluded.

To create the ensemble points in the plots in Figs. 5.19 and 5.20, the Lundquist number and magnetic field fluctuation amplitudes had to be determined for each ensemble. The Lundquist number will be covered in more detail in the next subsection, but broadly speaking, it depends on the plasma current, electron density and electron temperature. The plasma current and electron density values used to determine S were averaged over the flattop time window. The electron temperature data was taken from the central cord of the FIR diagnostic. Obtaining the temperature value for a shot was a distinct process due to the nature of the Thomson scattering which does not provide as many time points for the temperature data as can be obtained for these other parameters. For high and mid-range temperature data (i.e. data from $I_p \geq 200$ kA plasmas), which were not summed raw signals as described in Ch. 4, the electron temperature was taken for a shot by using the average core temperature from the three most radial points and averaging those values for all laser pulses that were fired within in the time window selected for the shot. For temperature data from shots with $I_p < 200$ kA, the average core temperature from the three core-most points was taken from the ensembled temperature profile generated by summing the raw signals. In the vast majority of cases, all the Thomson time points were used. Occasionally, particularly at lower plasma current data collection where maintaining a constant density was deemed especially important for the ensembling process, a

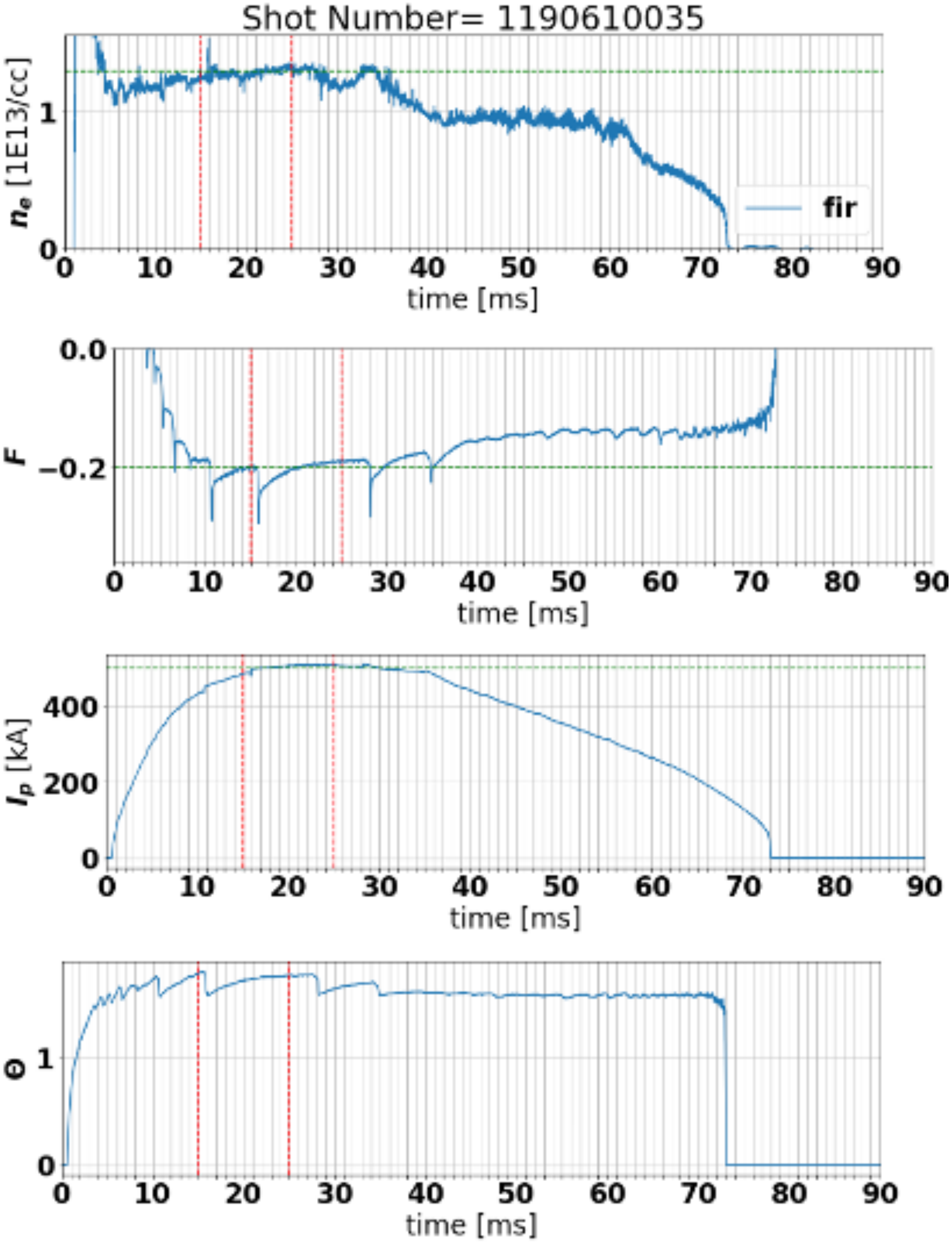

FIGURE 5.9: This figure shows example traces used for filtering 500 kA, low Greenwald fraction data. The signals are from a single shot that was ultimately included in the shot list. The pinch parameter was not used for filtering data but is included for reference. The target values for the ensemble are represented by the dashed green line and the window over which the shot was averaged is bracketed by the dashed red lines.

few Thomson time points were excluded from the window. Ultimately, the core temperature, core from a single shot were used to determine the Lundquist number for that shot. All the Lundquist numbers for the shot list were then averaged to obtain the Lundquist number for the ensemble.

The magnetic field fluctuation magnitudes were ensembled in a similar method. The magnetic field fluctuation value for a given shot was taken to be the average fluctuation over the time window of the shot normalized by the average on-axis magnetic field as given by the alpha model. The error was taken to be statistical, using the standard deviation of each of the values as their respective error and then taking the error for the normalized magnetic field fluctuation amplitude to be the propagation of these statistical errors. As will be discussed later, the systematic errors for the magnetic field coils are difficult to determine. The data were then averaged for all the shots in the shot list. The error for the ensemble was propagated through this averaging. Ultimately, these statistical errors are too small to appear on the plots.

5.1.5 Implications of Experimental Limitations and Definitions

This subsection will address the impact of the choices described in the previous subsection and other experimental limitations to that will be presented shortly. The Lundquist number is a global quantity and not a single localized value. The Lundquist number for this study was defined as a combination of central point and line-integrated values. We will discuss the profiles of the parameters that were distilled into a single point, including Z_{eff}, T_e, and f_t. But first, we will discuss experimental limitations and considerations, namely the resolution limit of the magnetic field coil array and the use of different power supply systems.

Magnetic Field Coil Array Resolution

Assessing the resolution of the magnetic field coil array is not straightforward, but it is important to consider when looking at results from higher mode numbers. Since the integrator circuit gain, coil areas, and other parameters related to the coils are fixed, we assume that it is some fixed value, based on the relative calibration values, likely around 0.2 G. When looking at the scaling data, if the resolution limit is hit, the scaling will not lose its dependence on Lundquist number as one might initially expect because the values are normalized. It may therefore not be obvious that the resolution limit has been reached by looking at the scaling results alone. At low Lundquist numbers, where the resolution limit is most likely to be reached, the value for $\tilde{b_n}$ would increase as S decreased: this is due to the normalizing magnetic field decreasing. Ultimately this would show up in the data as a having two different scaling parameter values for different segments of the fit and would ultimately raise the value of scaling parameter α. This does not appear to be the case in the n=5-15 modes that were investigated.

To get a sense if this was accurate, the scalings of the toroidal component of the magnetic field coil array were examined. The results of scaling these values are summarized in Fig. 5.10. The mode numbers for the toroidal components go to higher n because more coils are in the array that measure this component of the field. However, the measurements are more likley to include contributions from higher order poloidal modes (i.e. m=2). Additionally, several of the coils in the array are not working. Their reported measurement values are given by an average of the two neighboring coils. This could lead to a resonance effect in the data with certain mode numbers. Therefore these data are harder to interpret. The scaling for $\tilde{b}_T$ and $\tilde{b}_P$ appear to be consistent for n=7-15 modes. The range n=5-15 is likely most clearly m=1 dominant. In the figure, we also observe an effect in the n=22 mode that might be due to field errors in the device.

To summarize, the mode numbers presented later in this thesis were deemed to most likely not be suspect.

Comparing Legacy and Programmable Power Supply Results

Another experimental constraint of this study was the use of multiple power supply systems. This could introduce errors in the data due to, for example, noise in one system that the other system would not contribute. Switching noise was of particular concern due to the nature of the upgraded power supply system that provided access to the lower Lundquist numbers of the parameter space investigated (see Ch. 3). In order to assess whether this noise had a significant impact, data was collected at $I_p = 200$ kA using both the Legacy and the PPS power supply. Measured data were then compared to look for any significant variations between the data from the two different power supply systems. Fig. 5.11 shows the magnetic field fluctuation data from both systems for both the high and low density scenarios. In each case we see no concerning difference between the two data sets. This sort of comparison was also performed for the T_e and n_e measurements with no concerning discrepancies observed.

Impact of Z_{eff}

The effective ion charge state of a plasma, Z_{eff}, is a challenging quantity to measure. It is given by the following equation,

$$Z_{eff} = \sum_j \frac{Z_j^2 n_j}{n_e} \tag{5.14}$$

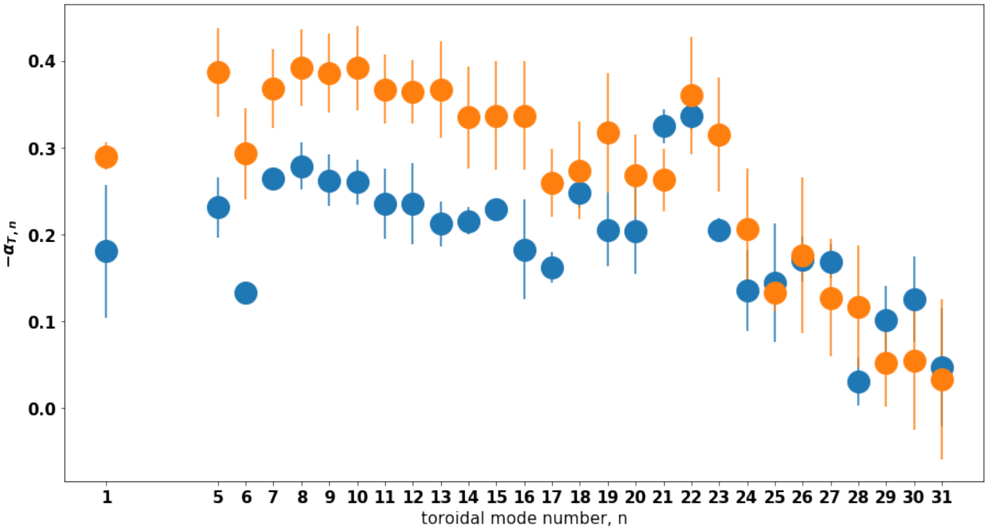

(A)

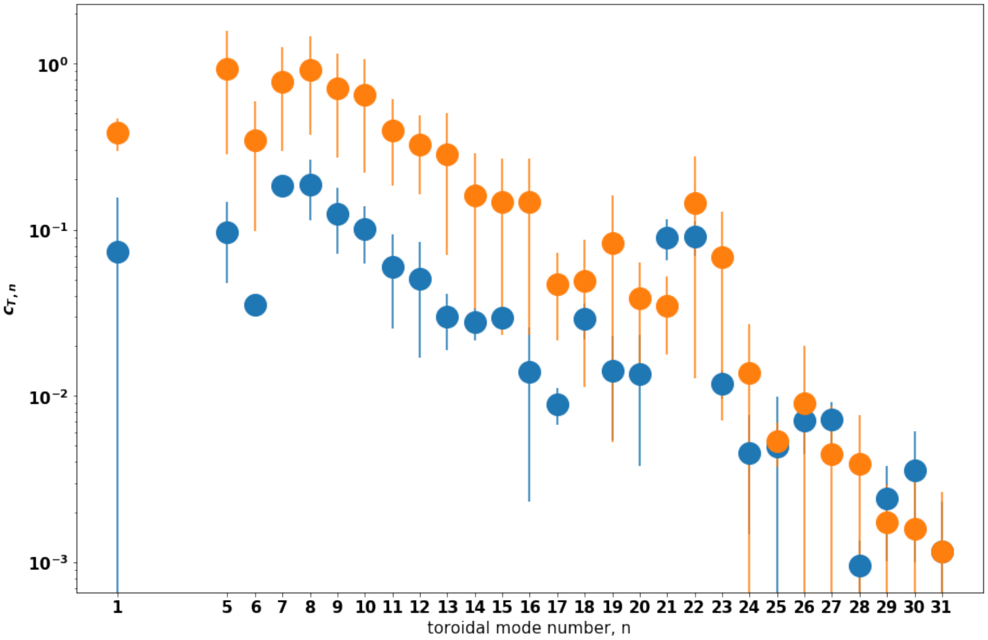

(B)

FIGURE 5.10: These plots summarize the $\tilde{b}_T$ scalings. These were looked at to assess if the resolution limit of the magnetic field coil array has been reached.

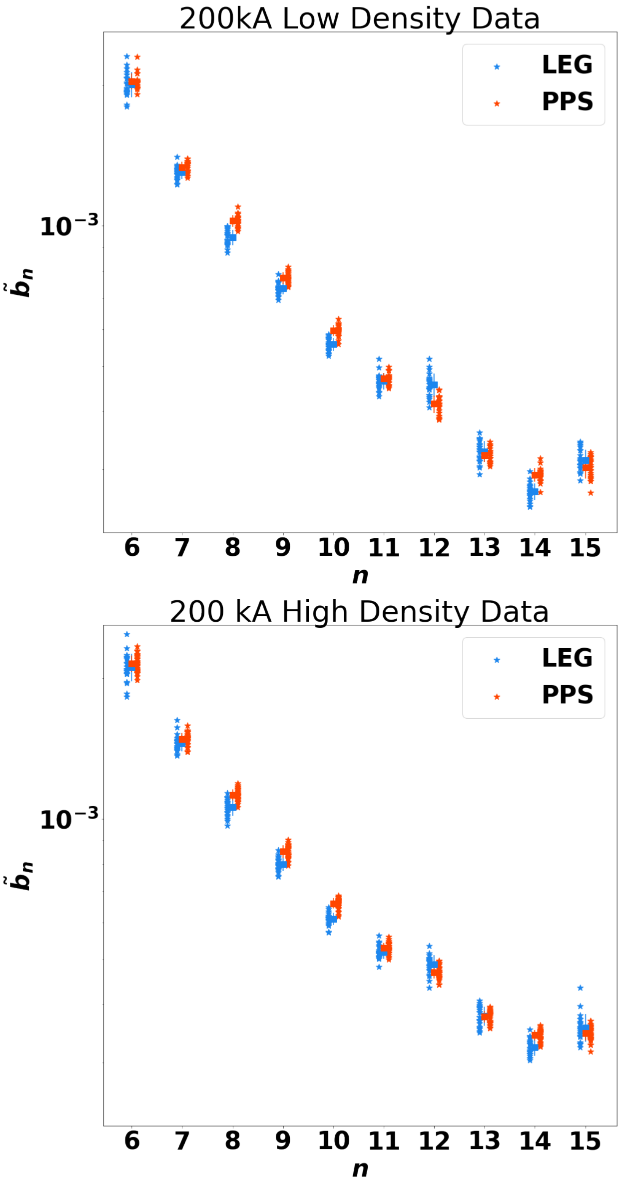

FIGURE 5.11: This figure compares the data generated by plasmas powered by the PPS system with those generated by the Legacy power supply system. This is done at $I_p = 200$ kA where the two systems overlap. The example shown here shows that there is not significant difference between the two systems when looking at that magnetics data.

where j is each of the constituent ion species in the plasma, Z_j is the charge of the species, and n_j is the density of the species. As we see in Eqn. 5.2, the effective ion charge state is a significant component used in the determination of the resistivity of a plasma, and, therefore, also the Lundquist number. It can be inferred by measuring the bremsstrahlung radiation. On MST, the soft X-ray diagnostic is used to measure the continuum spectrum, including bremsstrahlung, line, and recombination radiation. From these data, a Z_{eff} determination can be made. The measured emissivity follows the form,

$$\epsilon \propto \sum_j \frac{n_e n_j Z_j^2}{\sqrt{T_e}} e^{-E/T_e} \times [g_{ff} + recomb.] \tag{5.15}$$

where ϵ is the emissivity, E is the energy of the emitted X-ray photon, g_{ff} is the gaunt factor, and $recomb.$ is a recombination radiation factor [25, 7]. Limitations in the model used to interpret the X-ray radiation data used to infer Z_{eff} led to errors in inferring the value of Z_{eff} when Stoneking attempted to measure the Lundquist number in his S-scaling study [4]. Namely, contributions to the spectrum made by line radiation led to a significant overestimation in low-density values of Z_{eff} ($Z_{eff} \sim 10$) [4]. Thus, when Galante, et al. made significant improvements in inferring Z_{eff}, it in part motivated a new study investigating Lundquist number scaling [26]. As of this writing, the most up-to-date inference of Z_{eff} was performed by L.M. Reusch et. al. It utilized Bayesian analysis to combine information from independent diagnostics so as to not unnecessarily discard information these tools gather, thus arriving at a more informed estimate for Z_{eff}[26, 25]. Fig. 5.12a shows the results from applying this process to enhanced confinement plasmas.

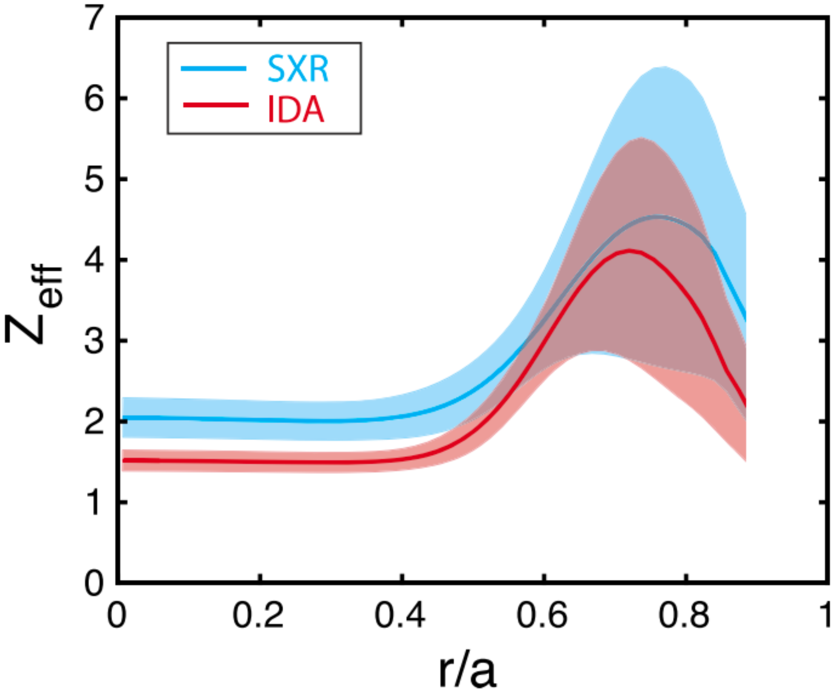

(A) Z_{eff} inference from Reusch et. al 2018 [25]. This inference was obtained utilizing integrated data analysis (IDA) techniques, a subset of Bayesian analysis, to combine information from the soft x-ray two-color diagnostic and Thomson scattering diagnostic. The blue curve and shading show the soft X-ray determination of Z_{eff}. The red curve shows the IDA result. The shading represents the 1σ uncertainty.

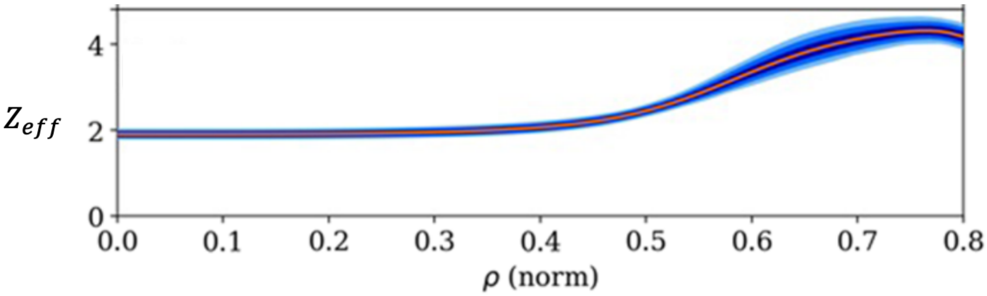

(B) A determination of Z_{eff} from enhanced confinement plasmas. This inference was arrived at by employing a multi-energy X-ray camera, soft x-ray tomography and Thomson scattering data. It is adapted from a figure in [27]

Due to resource limitations, a Z_{eff} determination for standard plasmas was not performed. In addition to the thorough parameter space coverage with the Thomson scattering diagnostic, CHERS, multi-energy and soft X-ray data were gathered for higher range plasma temperature (i.e. where the emissivity was sufficient to be measured). These data may be employed by future users to infer a Z_{eff} value for high current standard plasmas. For the results presented herein, the Z_{eff} value was taken to be approximately the core result from the red IDA curve in Fig. 5.12a. Z_{eff} is a constant in the formulation for S given by Eqn. 5.7 so this choice has a negligible impact on the scaling results.

Trapped Electron Fraction Impact

Here we will consider impacts of the resistivity profile on the Lundquist number determination and scaling, more specifically, the impact of trapped electrons. The resistivity profile as a whole does have an effect on MHD dynamics, however this impact is not well understood. The resistivity was taken to be a Spitzer resistivity with a small correction for the trapped electron particle fraction ($\frac{1}{1-f_t}$) that was held constant across all Lundquist numbers. Here, we will describe the shortcomings and significance of this choice. To begin, we will look at the neoclassical expression for the resistivity. Following Hirshman's approach [28, 29], this resistivity is effectively given by,

$$\eta_{neo} = \eta_{\perp}\Lambda_E^{-1}(Z_{eff})(1 - \frac{f_t}{1 + \xi\nu_e^*}), \tag{5.16}$$

where Λ_E is the Coulomb parameter, ξ is a factor that approximately equals one for $Z_{eff} = 2.0$, and ν_e^* is the effective electron collision frequency given by,

$$\nu_e^* = \epsilon^{-3/2}\nu_e\tau_b = \nu_e\frac{\pi a}{v_{th,e}}f_t^{-3}, \tag{5.17}$$

where τ_b is the bounce time, ϵ is the inverse aspect ratio, a is the minor radius, $v_{th,e}$ is the electron thermal speed, and ν_e is the electron collision frequency. When $\nu_e^* < 1$, the plasma is said to be in a collisionless regime.

Again, this study chose to define the resistivity with a constant trapped particle correction. This followed the convention chosen by Stoneking [4]. The choice of Lundquist number used herein is a hybrid of core and line-averaged values. Fig. 5.14 shows the trapped particle fraction profile. The trapped particle fraction goes to zero at the core, but the profile shape varies with Lundquist number. Stoneking concluded that MST plasmas were purely in the collisionless regime, however, it is likely that at low Lundquist numbers, this is no longer the case and neoclassical enhancements would start to become significant as shown in Fig. 5.13 which plots the neoclassical correction factor, R_{ν^*}, which is given by

$$R_{\nu^*} = \frac{1 - \frac{f_t}{1+\nu_e^*}}{1 - f_t}. \tag{5.18}$$

If the neoclassical correction were to be omitted at lower Lundquist numbers, it would lead to relatively larger S inferences at the lower range of Lundquist numbers, therefore increasing the value of the scaling parameter α_n [28]. Ultimately the largest this factor's impact would be is $\frac{1}{1-f_t} = \frac{1}{1-0.38} =\approx 1.6$. This factor is relatively small especially relative to other profile effects that might be considered such as electron temperature which as a stronger impact on S.

Electron Temperature and Density Profile Considerations

The electron temperature has the most significant impact on the Lundquist number determination ($S \sim T_e^{3/2}$) of any of the other parameters. The electron temperature was

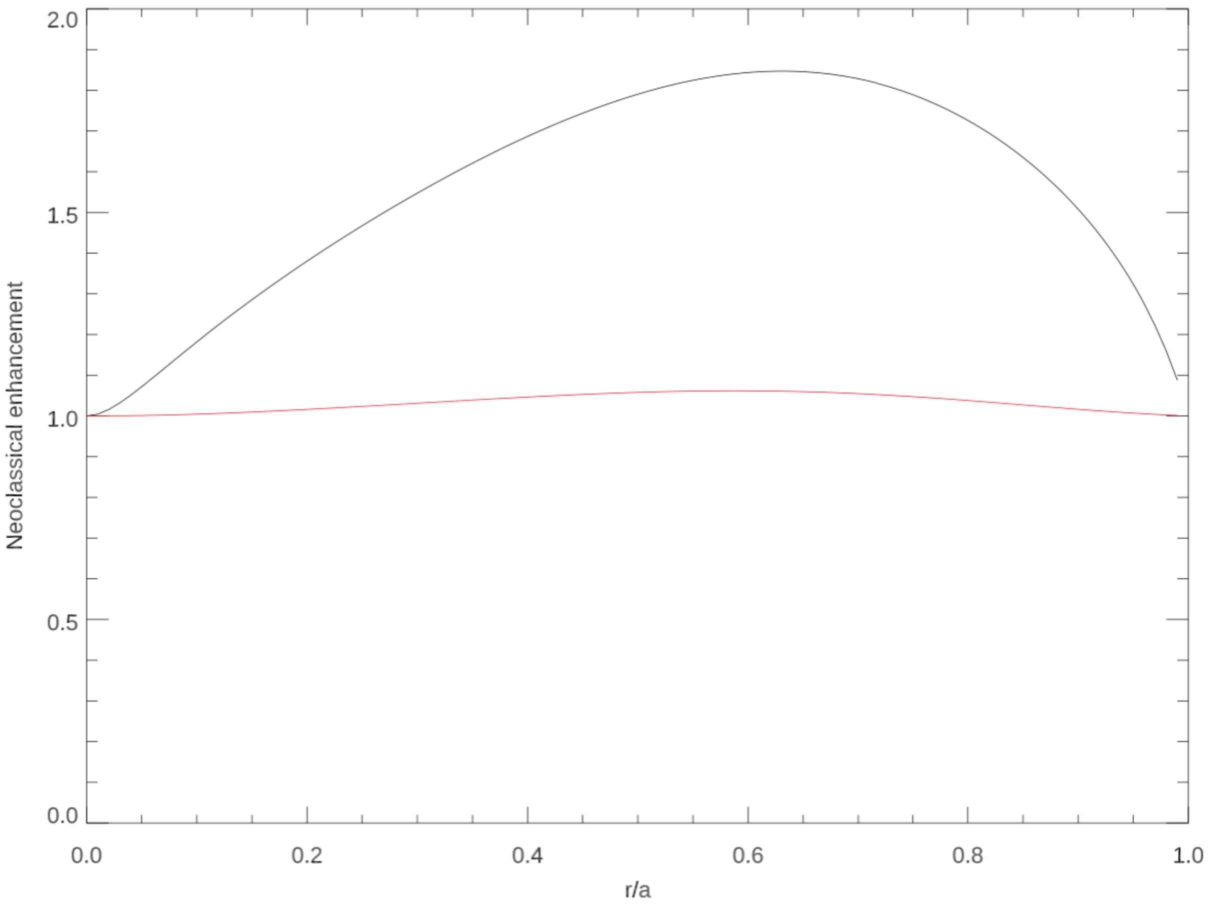

FIGURE 5.13: This plots the neoclassical correction factors to illustrate the impact of the trapped particle fraction on the Lundquist number value. The black curve represents $T_{e,0} = 300eV$ and the red curve represents $T_{e,0} = 30eV$ with constant density $n_e = 1E19\ \mathrm{m}^{-3}$. This plot was provided courtesy of John Sarff [29].

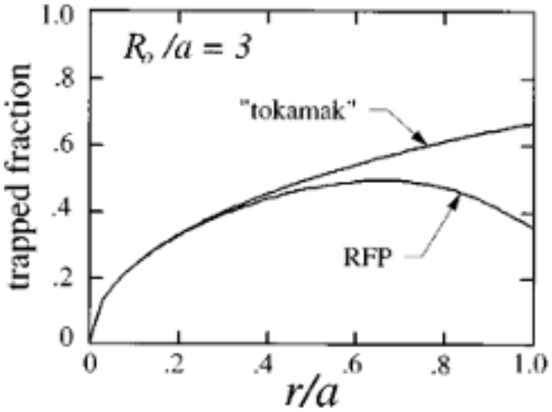

FIGURE 5.14: The trapped particle fraction profile. This is reproduced from Stoneking's paper [4]

taken to be the average of the three core most points. Here, we consider the impact of the electron temperature profile as a whole.

Figs. 5.15 and 5.16 show ensembled Thomson electron temperature profiles for the low and high Greenwald fraction cases respectively. We see that at low current, the profile is flatter and progressively becomes more peaked in the core as the current is increased. Therefore, if the characteristic temperature were taken to be at the mid-radius, the Lundquist number would increase more slowly, while the magnetic field fluctuations remain the same. This would lead to an increase in the value of scaling coefficient α.

Fig. 5.17 shows how the core electron temperature scales with plasma current grouped by Greenwald fraction. Craig Jacobson performed a similar scaling grouped by constant electron density [30]. The results of the scaling by Greenwald fraction are, for the $n_e/n_G = 0.23$ case:

$$\frac{T_{e,0}}{\text{eV}} = (0.87 \pm 0.04)\frac{I_p}{\text{kA}} + (59.72 \pm 13.25), \tag{5.19}$$

and the results of the scaling for the $n_e/n_G = 0.34$ case:

$$\frac{T_{e,0}}{\text{eV}} = (0.84 \pm 0.09)\frac{I_p}{\text{kA}} + (19.51 \pm 19.61). \tag{5.20}$$

For the latter, the 500 kA data point was excluded from the fit. The 200 kA data are broken into two points: one for PPS data and one for Legacy which can be distinguished by referring to Figs. 5.15 and 5.16. The slopes for each Greenwald fraction case are very similar, which is not the case when density is held constant when doing an analogous temperature scaling [30].

The electron density profiles do no exhibit the same peaking that the temperature profiles do. Additionally the Lundquist number is not as obviously dependent on the electron density (recall $S \sim n_e^{-1/2}$). MSTFIT provides electron density profile inversions of the FIR data, however, the Lundquist number definition used here takes the line-integrated density value from the core most point. The general shape of the electron density profile, aside from the peaking in the core, is similar to the shape of the electron temperature measurement. Example profiles are given in Fig. 5.18. The density is relatively flat through the core and mid-radius before dropping off.

5.2 Scaling Results

In this section we will present and discuss the results of the scaling study performed over the range of MST-achievable Lundquist numbers. We will start by going over the most direct measurement, the magnetic field fluctuation amplitudes scalings. We will then review quantities that are related to transport and are calculated either via estimates based on the measured data or the use of the MSTFIT equilibrium code.

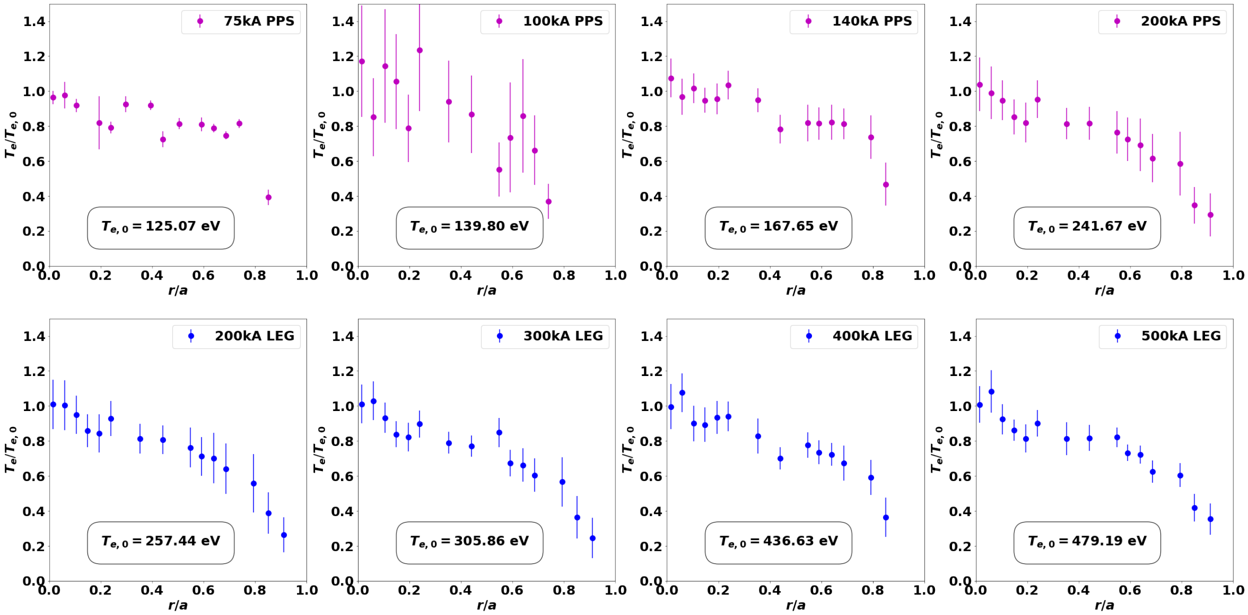

FIGURE 5.15: The set of ensembled temperature profiles are shown as the plasma current is varied. These profiles are for the low Greenwald fraction case. The 100 kA case includes fewer shots in the ensemble because it is data taken from a run day that was not employing the Greenwald fraction framework.

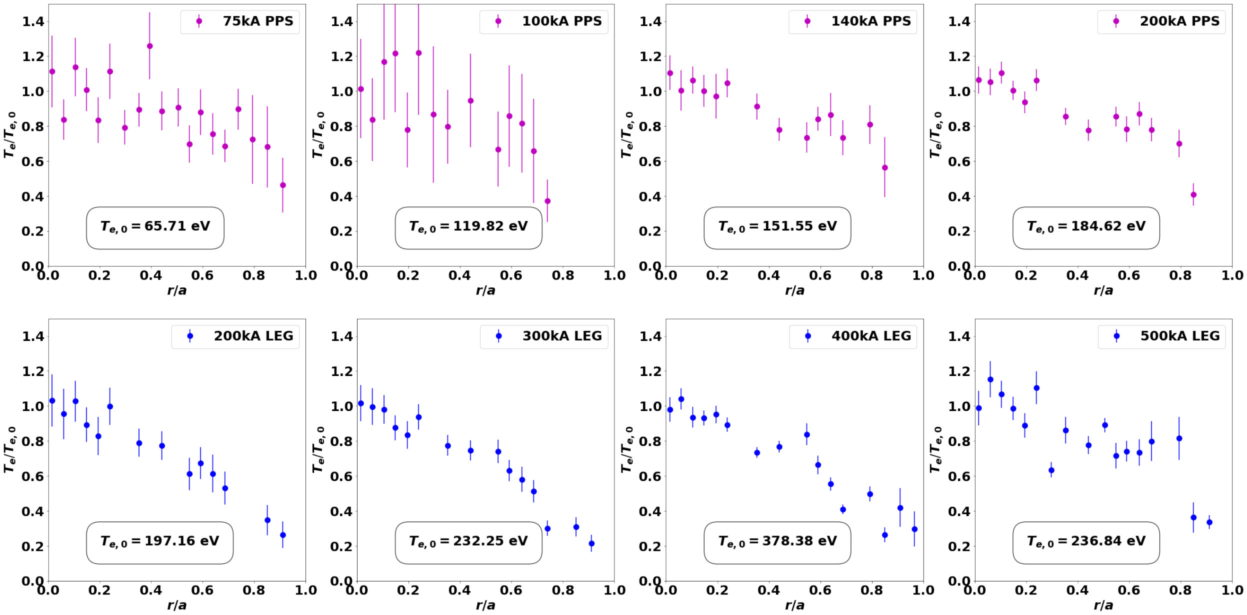

FIGURE 5.16: The set of ensembled temperature profiles are shown as the plasma current is varied. These profiles are for the high Greenwald fraction case. The 100 kA case includes fewer shots in the ensemble because it is data taken from a run day that was not employing the Greenwald fraction framework.

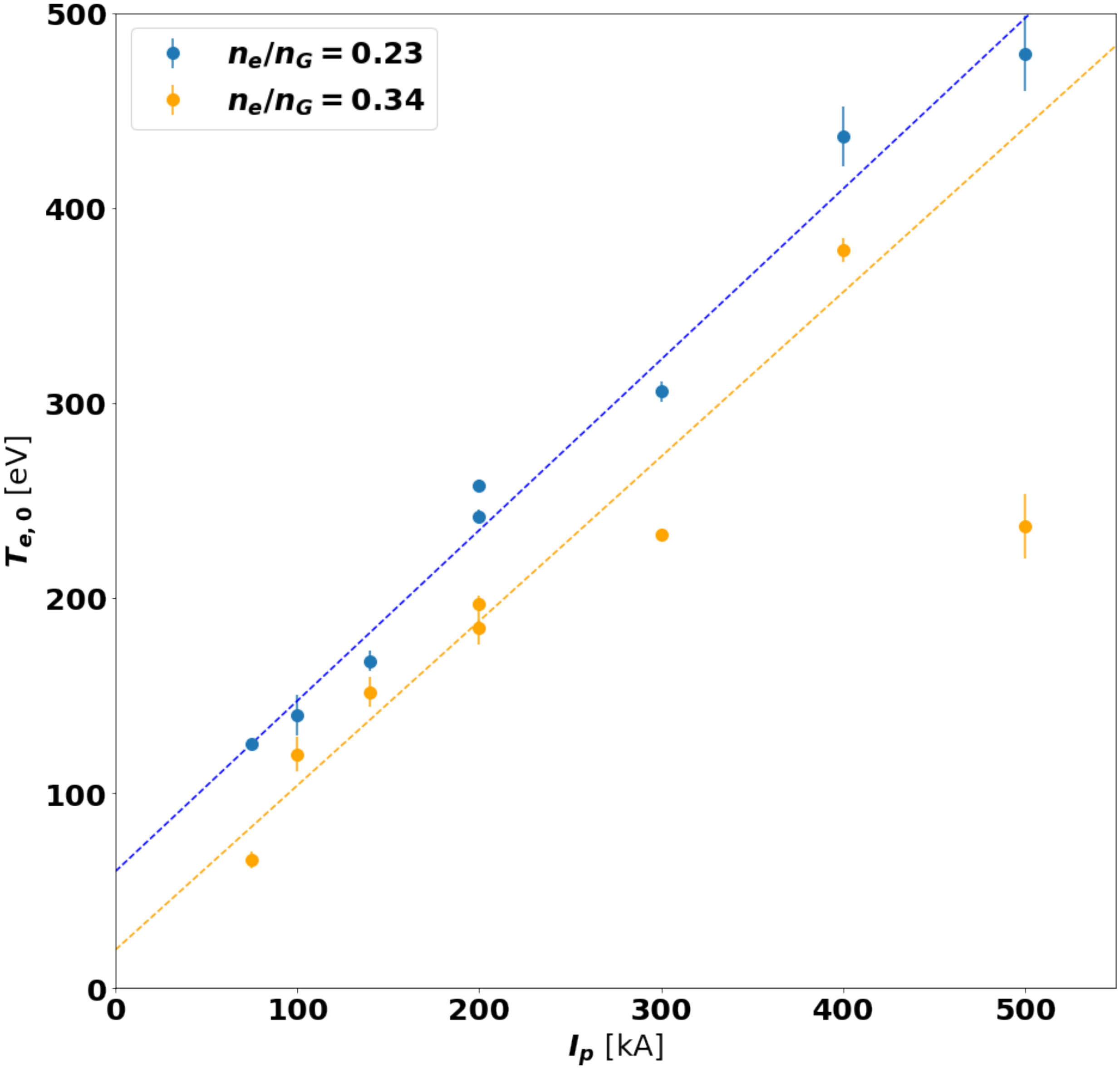

FIGURE 5.17: The core temperature values are scaled with plasma current here. The dashed lines represent the best fit of the data grouped by Greenwald fraction. For the high Greenwald fraction case, the 500 kA data point was excluded from the fit. The 200 kA data in each case include two points. These are separated by the power source used.

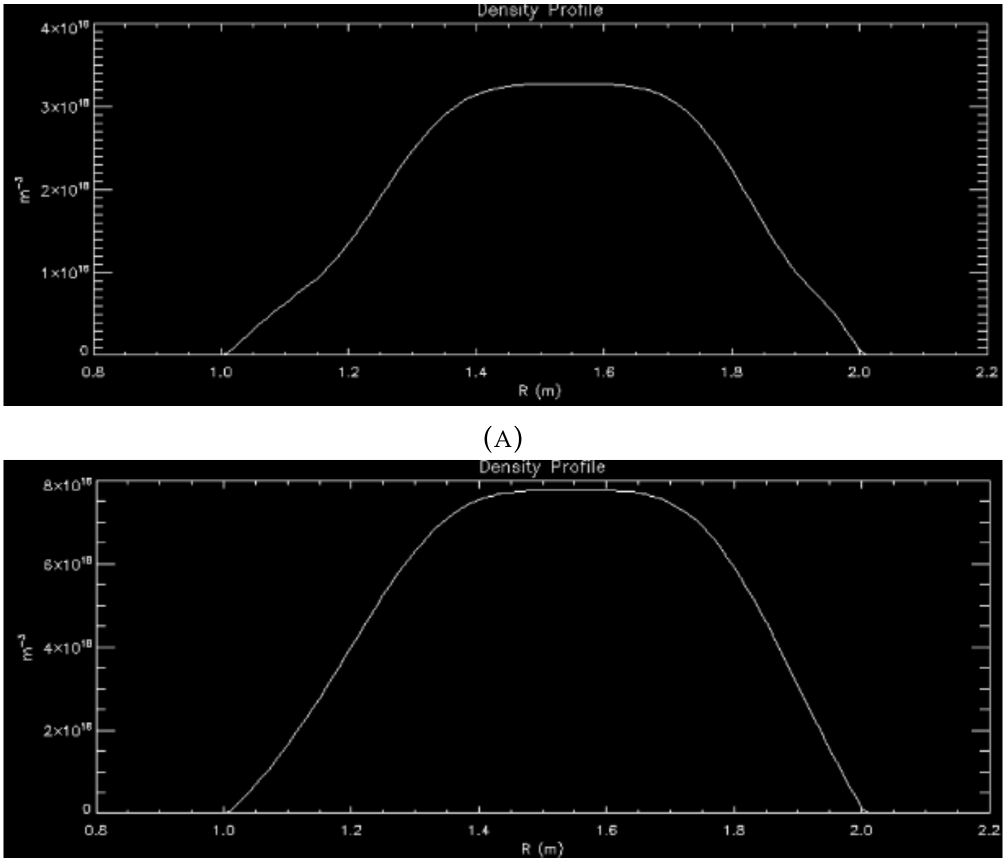

(A)

(B)

FIGURE 5.18: This figure shows and example electron density profile inversions performed by MSTFIT using the FIR data. This data is for the low Greenwald fraction 75 kA case (A) and the low Greenwald fraction 200 kA case (B).

5.2.1 Magnetic Field Fluctuation Scalings

Before diving into a presentation of the magnetic field fluctuation amplitude scaling results, we will briefly recap a few relevant details regarding the measurement and the notations used. For even more detail, please refer to the first section of this chapter. The magnetic field fluctuations were measured using the toroidal array in the shell of MST. These fluctuations are then normalized by the magnetic field amplitude on the magnetic axis as calculated by the alpha model. We define this scaled quantity as $\tilde{b}_n = |\tilde{B}_{\theta,n}/B_{0,\alpha}|$.

These measurements were taken for two Greenwald fractions across a range of Lundquist numbers. Multiple shots were ensembled to create an average value for each data point for a given S. Once an ensembled data point is obtained for Lundquist numbers spanning the range accessible to the MST, the data were then fit to the following equation:

$$\tilde{b}_n = c_n S^{-\alpha_n} \tag{5.21}$$

where c_n and α_n are the fit parameters.

The results for these scalings are shown in Figs. 5.19 and 5.20. The figures plot the same data for different mode numbers and have been divided between two figures to improve the visibility of the plots. In these figures, the left column shows the low density Greenwald fraction data while the right column shows the high density Greenwald fraction data. Each point represents an ensemble of data. The errors for each ensembled data “point” were taken to be average error of each MST shot measurement. The error of each measurement is the standard deviation in the magnetics signal over time window for the measurement. Because ensemble sizes are large and the plots are log-log, the error bars are too small to appear on the plots but can be found in the database (Appendix A).

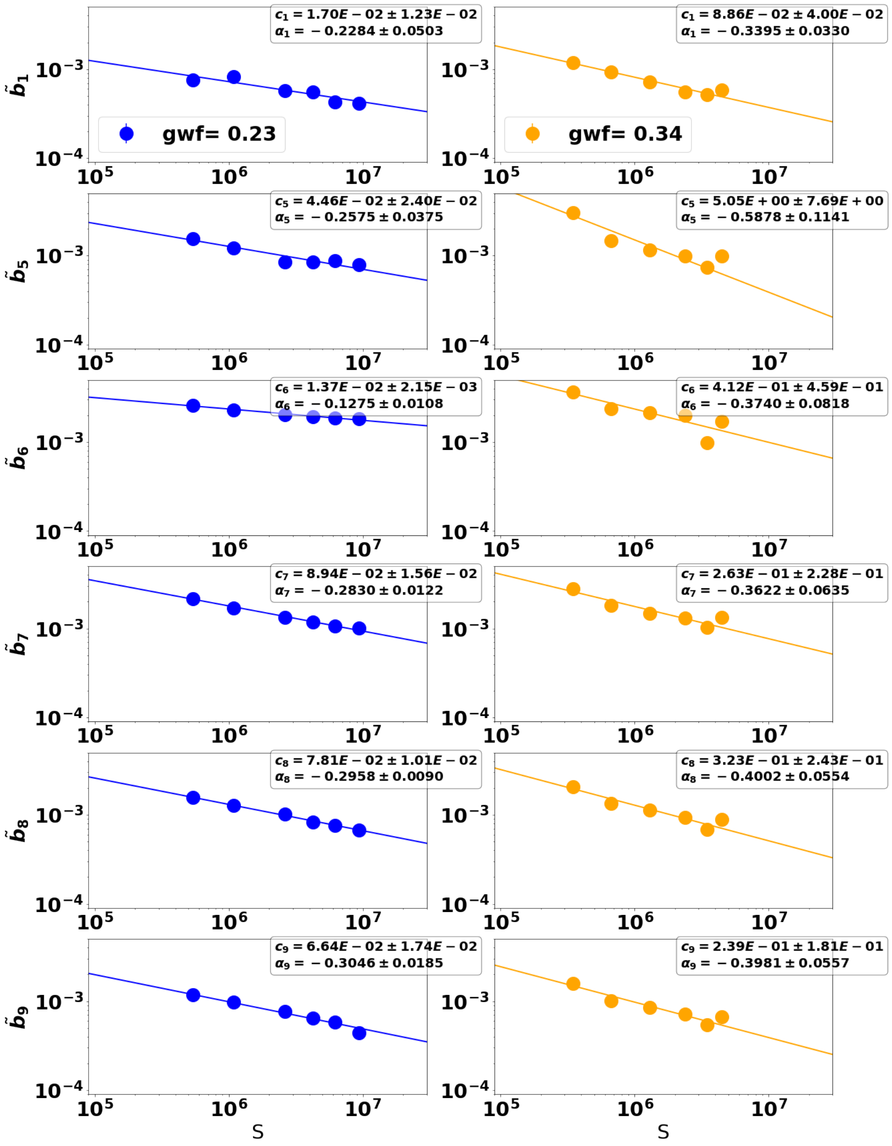

FIGURE 5.19: These plots show the data for the magnetic field fluctuation amplitudes and their respective inferred Lundquist numbers. This is meant to be viewed in conjunction with Fig. 5.20 but has been split up to improve the visibility of the plots. Each point represents the results from an ensembled data at that point in parameter space. The lines are the best fit of the data to Eqn. 5.21. The left column contains the low density Greenwald fraction, gwf= 0.23, and the right column contains the high density Greenwald fraction, gwf= 0.34.

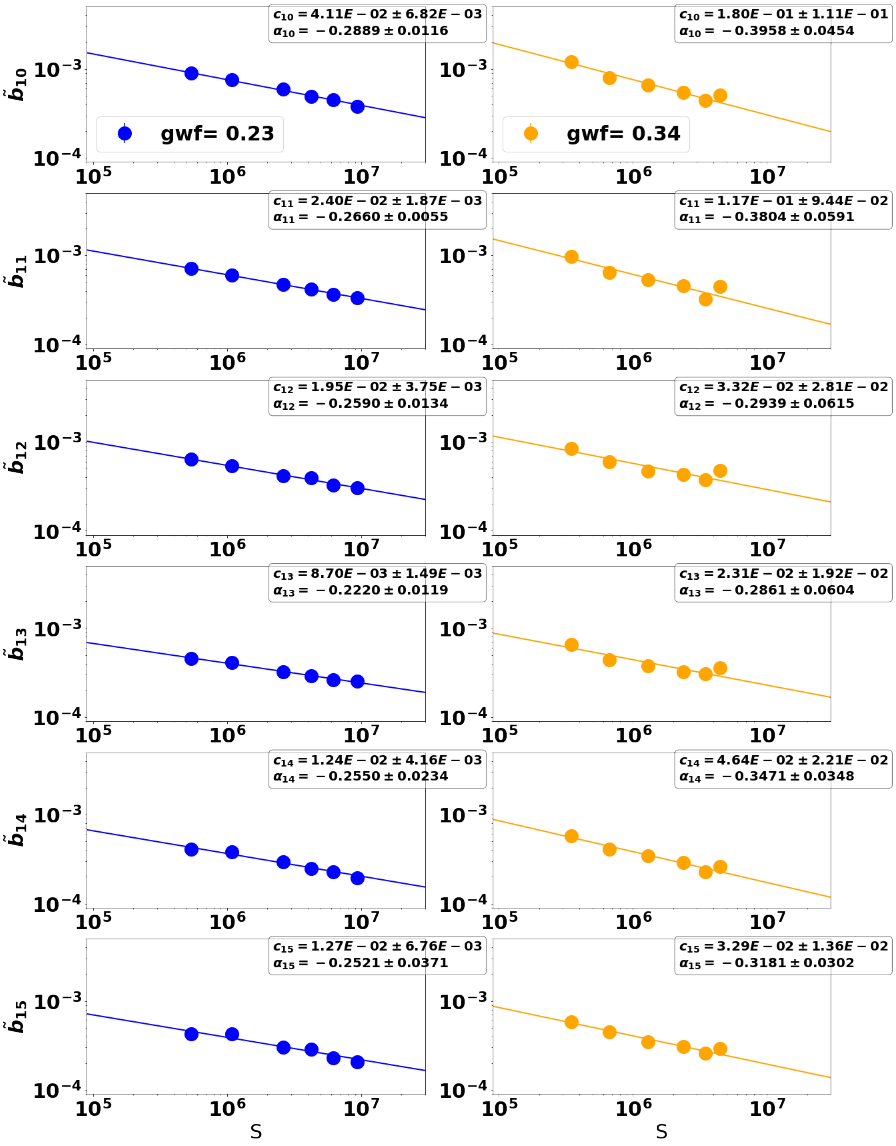

FIGURE 5.20: These plots show the data for the magnetic field fluctuation amplitudes and their respective inferred Lundquist numbers. This is meant to be viewed in conjunction with Fig. 5.19 but has been split up to improve the visibility of the plots. Each point represents the results from an ensembled data at that point in parameter space. The lines are the best fit of the data to Eqn. 5.21. The left column contains the low density Greenwald fraction, gwf= 0.23, and the right column contains the high density Greenwald fraction, gwf= 0.34.

The high density data set was challenging to collect at the high end of plasma currents that MST generates. The highest Lundquist number was collected at $I_p = 500$ kA. For a Greenwald fraction $gwf = 0.34$ (the high density case), this requires a line-averaged electron density $n_e = 2.0 \times 10^{19}$ m^{-3}. With densities this high, MST struggles to breakdown the gas to form a plasma and discharges usually terminate early if they manage to generate a plasma at all. And so, at this highest current at which data were gathered, only a few usable shots were generated. These points are still shown because high density corresponds to a relatively high Thomson scattering signal. However, these data may not be as robust as other ensembles, as the ensemble consists of only a couple of MST shots. Additionally, the data at this point actually produced a Lundquist number lower than that of the next highest current data point at $I_p = 400$ kA. Even at $I_p = 400$ kA, for $gwf = 0.34$, a line-averaged electron density $n_e = 1.6 \times 10^{19}$ m^{-3} is required. This was more practicable than the 500 kA case but is still challenging operationally.

A summary of the fit parameter values obtained from these data can be found in Fig. 5.21 where the exponential parameter of the fit, α_n, and the coefficient parameter of the fit, c_n, are plotted against the toroidal mode number. The coefficient data is displayed on a semi-log plot as most of the values were similar except for the high density n=5 mode. The behavior of n=5 mode data is notably different. The safety factor profile is such that the n=5 mode is sometimes not resonant. We ensemble over the entirety of the flattop duration in these data, without consideration for the evolution the safety factor at $r = 0$.

The parameter of great interest in a scaling study is the exponential scaling parameter, α_n. Apart from the n=5 mode, we see that the high Greenwald fraction data generate higher α_n. This would correspond to a stronger mitigation of the magnetic field fluctuation amplitudes with increasing Lundquist number for the high density case. This is

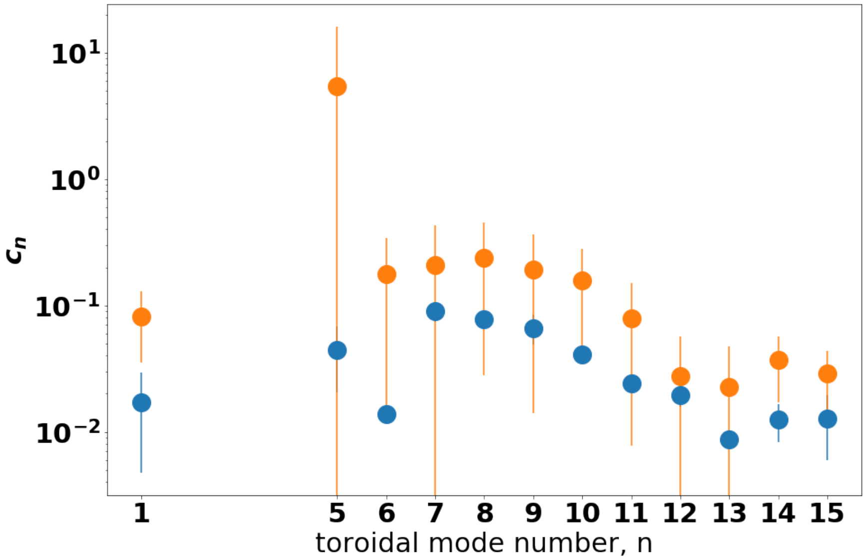

(A)

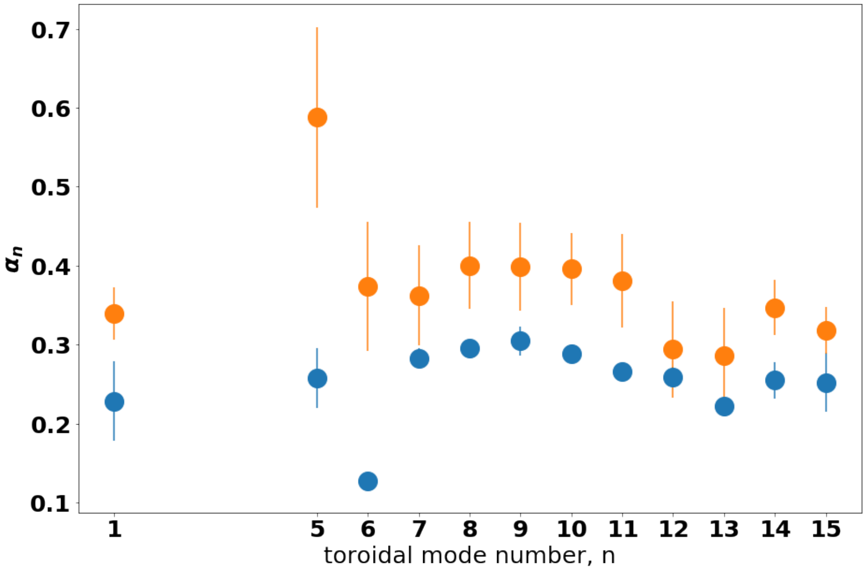

(B)

FIGURE 5.21: This set of figures summarizes the results of fitting the magnetic field fluctuation amplitude scaling data to Eqn. 5.21. The top figure shows the results of the coefficient of the scaling fit on a semilog plot against the toroidal number. The bottom figure shows the scaling parameter, α, on a linear plot against the toroidal mode number. In keeping with the convention of all data presented herein, the low density Greenwald fraction data is shown in blue while the high density Greenwald fraction data is shown in orange.

encouraging for the potential of the RFP as a reactor concept given that a reactor will most likely need to operate with relatively high electron densities.

Another interesting data point to note is the low Greenwald fraction ($gwf = 0.23$) n=6 mode scaling parameter, or $\alpha_{n=6}$, value. It is very low indicating that the magnitude of the fluctuations for this mode will not change much as Lundquist number is varied. Additionally, referring back to Fig. 5.19, looking at the $gwf = 0.34$ and the n=6 data in the third row of the righthand column, and recalling that the second highest Lundquist number data point is less robust that other data points, an argument could be made that even for this high-density case, the n=6 mode number does not vary much with the Lundquist number, especially relative to other modes. This n=6 mode carries the most magnetic energy in MST and distinguishable island structures associate with the mode have been observed in MST [31, 32, 10]. This seems to be further evidence that the mode is acting differently from the other $m = 1$ modes.

We can also see that the $m = 0$ $\alpha_{n=1}$ value is relatively high for the high density case. This could bode well for confinement scaling to higher Lundquist number given that the nonlinear interaction of this mode with the $m = 1$ modes inside of the reversal surface has been attributed to fueling large sawtoothing events that lead to transport.

Finally, we see in Fig. 5.21 a drop in both c_n and α_n for modes $n = 12 - 15$ is observed. This indicates that these modes will be relatively small in the range of Lundquist numbers accessible to MST and may not decrease in amplitude as rapidly and the more inward modes as the Lundquist number is increased beyond the values accessible to MST. We will discuss the degree to which we can expect this to be a concern in a subsequent section.

5.2.2 Transport and Confinement Scaling

Our interest in measuring the magnetic field fluctuation amplitudes is anchored in their relationship to transport in the RFP. So, let's now consider the scaling of some of the transport-related quantities. To begin with, we look at the energy confinement time, τ_E. This was calculated for ensembles of data (few data points). τ_E was also calculated using the equation below on a shot-by-shot basis: each shot in the ensemble and many of that were excluded from the above calculation because they did not fit into the Greenwald fraction were included in this τ_E scaling. The relatively low values of RFP τ_E is often cited as a relative disadvantage of the RFP concept to the tokamak. The formula used to determine the τ_E on a shot-by-shot basis is given by,

$$\tau_E = \frac{9\overline{n}(T_{e,0} + T_i)V}{8P_\Omega}, \tag{5.22}$$

where V is the plasma volume,T_i is the ion temperature, and $P_\Omega \approx I_\phi V_\phi$ is the Ohmic input power. The ion temperature was taken to be equal to to two thirds the electron temperature based a calculation done with data collected from the CHERS diagnostic at high Lundquist numbers and a number quoted by J. Boguski in his thesis [33]. This formulation is arrived at by assuming a parabolic density profile and a flat temperature profile.

The τ_E data gathered from MSTFIT equilibrium reconstruction calculations of the ensembles were used to generate Figs. 5.19 and 5.20. These reconstructions were constrained by ensembled electron temperature profiles and assuming the ion temperature relationship used in Eqn. 5.22. The energy confinement time results are plotted against Lundquist number in Fig. 5.22. However, the quality of this fit is somewhat poor and it does not necessarily follow that the energy confinement has a scaling relationship to Lundquist number in the same way that the magnetic field fluctuation amplitudes are expected to.

Scaling the energy confinement time based on current and density makes more sense. The plasma thermal energy scales like $W \propto a^3 nT$ and the input powers scales like $P \propto a^{-1} I^2 T^{-3/2}$. It follows that the energy confinement time scales as $\tau_E \propto a^4 I^{-2} n T^{5/2}$. Then, applying similar scaling relationships from stochastic transport where $\chi \propto a I^{-2\alpha} n^{\alpha} T^{1/2-3\alpha}$, where α is the exponential scaling parameter determined in the previous section. Putting this together, using a value of $\alpha = 1/3$, we expect $\tau \propto I^{4/3}(n)^{-2/3}$, or equivalently, $\tau \propto I^{2/3}(n_e/n_G)^{-2/3}$. A calculation of τ_E was also done on a shot-by-shot basis as described by Eqn. 5.22 and the results are displayed in Fig. 5.23. The results of the fit do not match with this stochastic scaling for the density dependence, only weakly displaying any dependence on the density, implying that there is physics that the stochastic model may not be capturing all the dynamics at play related to this parameter. However, the current scaling very closely follows the scaling relationship predicted by the stochastic transport model, particularly when the Greenwald fraction is held constant.

The next confinement related parameter that was scaled was the poloidal beta of the plasma, β_θ, which is given by

$$\beta_\theta = \frac{< p >}{B_\theta^2/(2\mu_0)}. \tag{5.23}$$

Fig. 5.24 shows the results of scaling β_θ against the Lundquist number. These values were also fit to I_p and the gwf following the form of Eqn. 5.23. This fitting is shown in Fig. 5.24. The β_θ values were generated by MSTFIT and therefore do not have associated uncertainties. In both these cases, we see β_θ decreases as Lundquist number or other operational parameters are increased.

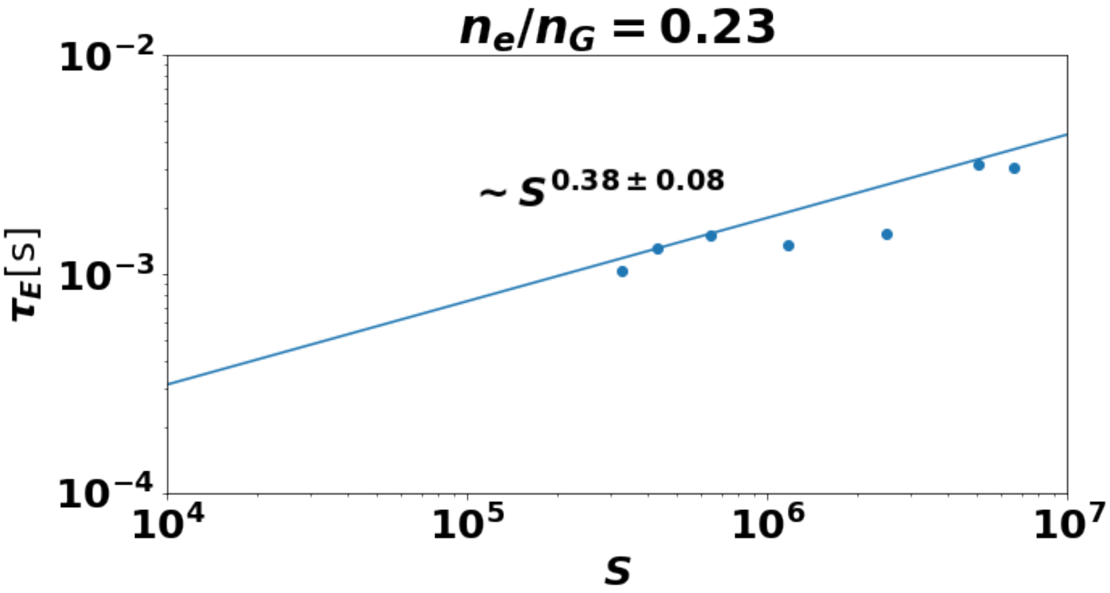

(A) Low density ensemble

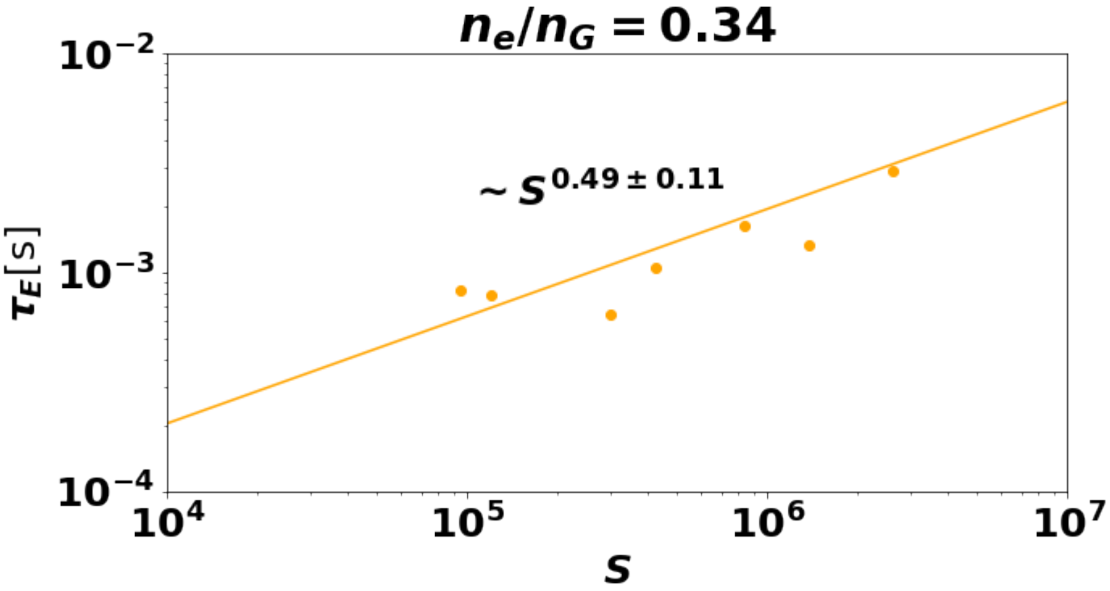

(B) High density ensemble

FIGURE 5.22: Scalings of the energy confinement time for the low density case (a) and the high density case (b) against Lundquist number. A note on the τ_E values plotted here: a set back of using the MSTFIT results for τ_E is that uncertainty estimates cannot be practicably made for the results of the code. For this reason, energy confinement times displayed here lack error bars.

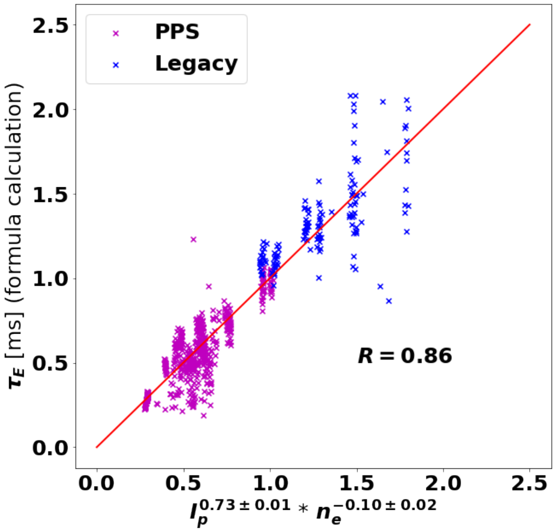

(A) Energy confinement time scaled by Lundquist number. These energy confinement data were calculated with MSTFIT.

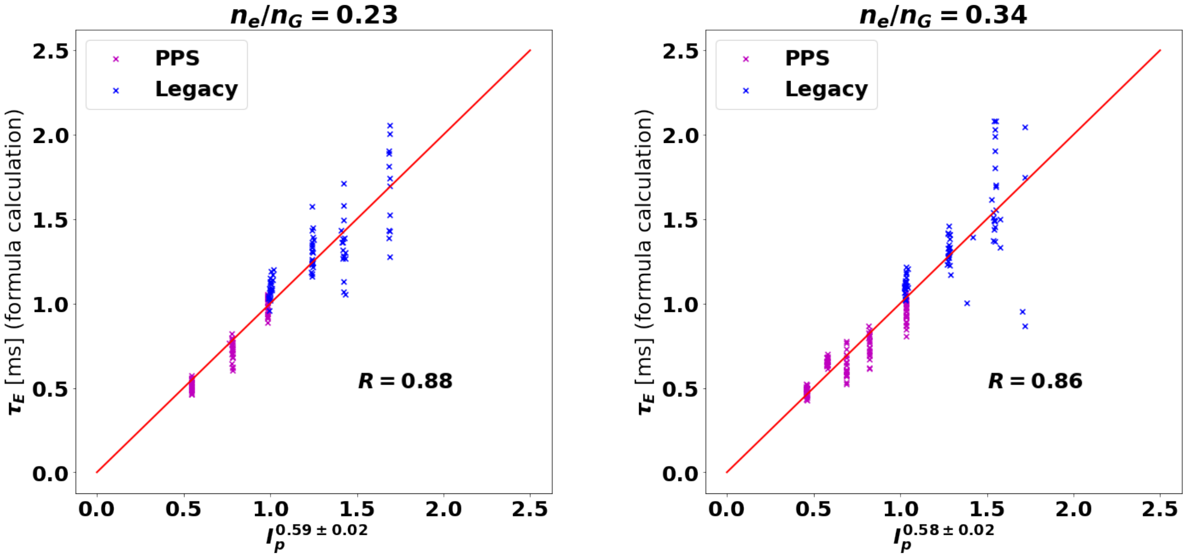

(B)

(C)

FIGURE 5.23: The scaling of energy confinement times on a shot by shot basis using Eqn. 5.22. Figure (A) includes all data, while Figures (B) and (C) include only specific Greenwald fractions (and therefore only scale with plasma current).

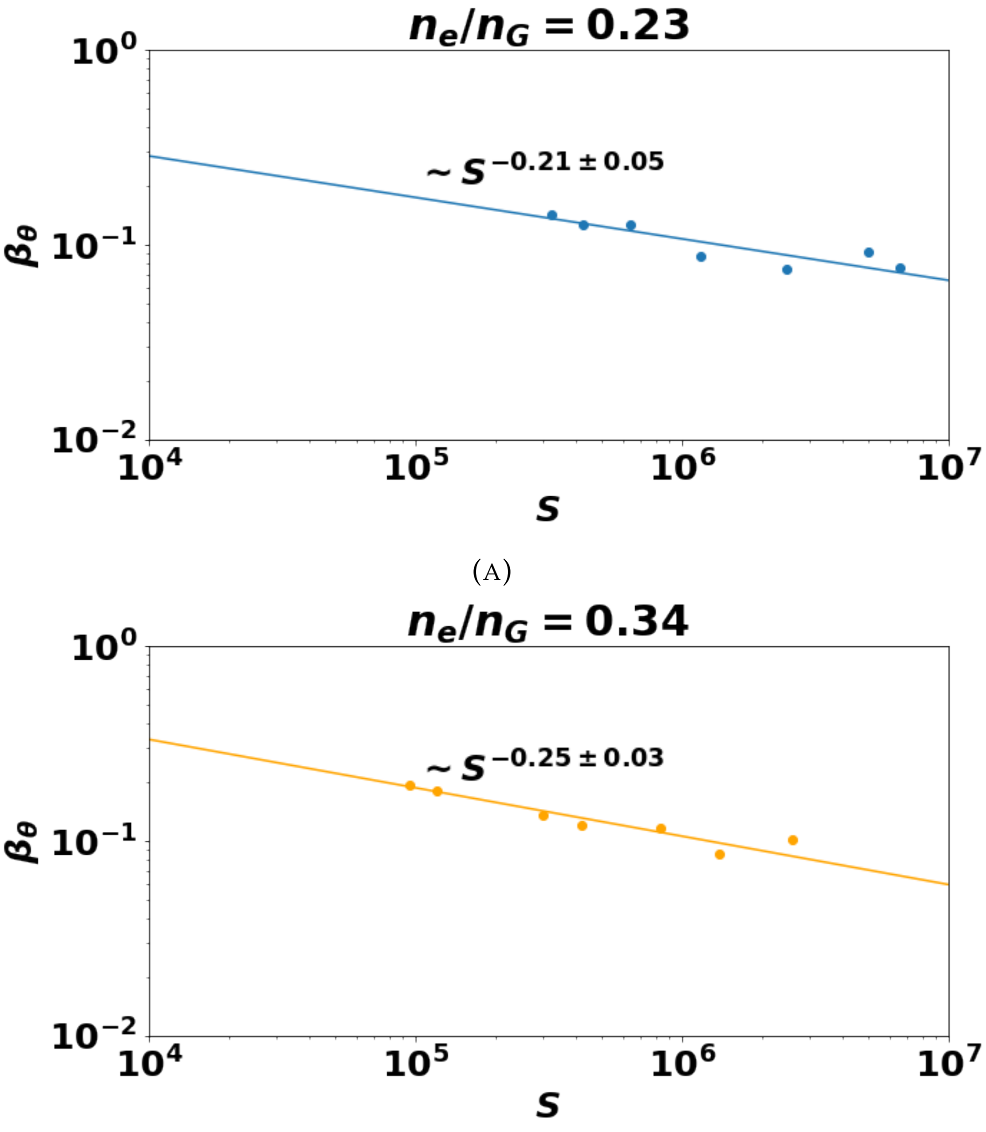

FIGURE 5.24: Poloidal β for the low density case (a) and the high density case(b) against Lundquist number. β_θ values were generated using MSTFIT on the same ensembles used to create the $\tilde{b}_n$ vs. S scalings.

The results are consistent with what has been observed in the past [4].

The final parameter in this category that we will look at is the electron thermal diffusion, $\chi_{e,st}$, which is approximately given by

$$\chi_{R-R} \sim v_{th} L_{ac} (\tilde{B}_r / B)^2, \tag{5.24}$$

where L_{ac} is the autocorrelation length, v_{th} is the thermal velocity, and B_r is the radial component of the magnetic field fluctuation. In MST, a field line tracing routine has estimated that $L_{ac} \approx 0.75$ m [10]. Scalings for this parameter are not shown here but it will come into play in a subsequent section when discussing magnetic field fluctuation amplitude results.

5.3 Comparing Experimental Results to Preliminary Computational Data

5.3.1 Computational Results

Although there are plans to extend the upper bound of MST-accessible S values via the programmable power supply system, at the time of this study's data collection, the upgrade had started by expanding the lower range of Lundquist numbers accessible on the device. The main virtue of creating access to this portion of parameter space is that experimental results can have more overlap with simulated results, which are bounded by computational capacity in producing data at Lundquist numbers high enough to have substantial overlap with MST plasmas produced by the traditional power supply system.

Fig. 5.7 shows the span of Lundquist numbers accessible to all the tools discussed in this section.

In this section, we will present the results of some preliminary simulated data and how they compare to the data presented in this study. Comparison of these data have some shortcomings. The choice of definition for experimental parameters such as Lundquist number were selected for experimental convenience rather than alignment with computational results. Additionally, results for only four toroidal mode numbers were reported [30]. The simulated were also run with a different data collection framework in mind and were only performed for essentially three toroidal mode numbers. Ultimately, resource limitations precluded an extensive validation effort. However, the database of experimental results produced here can be used in more thorough future validation efforts. Information on accessing this database can be found in Appendix A.

Two computational codes frequently used to simulate MST plasmas are DEBS and NIMROD [34, 35]. Brief descriptions of these codes can be found in Ch. 3. Several simulated runs (performed by C. Jacobson) were performed using each code in order to gather $\tilde{b}$ simulated scaling data [30]. These simulations were originally performed with a different framework in mind, where n_e was kept constant instead of the n_e/n_G as current was varied. For each of these codes, two sets of simulations were run. Here we focus on one set of simulations where the reversal parameter, F, was held constant which aligns with how the experimental data were gathered.

Fig. 5.25 shows the results from these NIMROD runs. These were performed using a single-fluid, cylindrical geometry with an aspect ratio $R/a = 3$, Prandtl number $Pm = 1$,

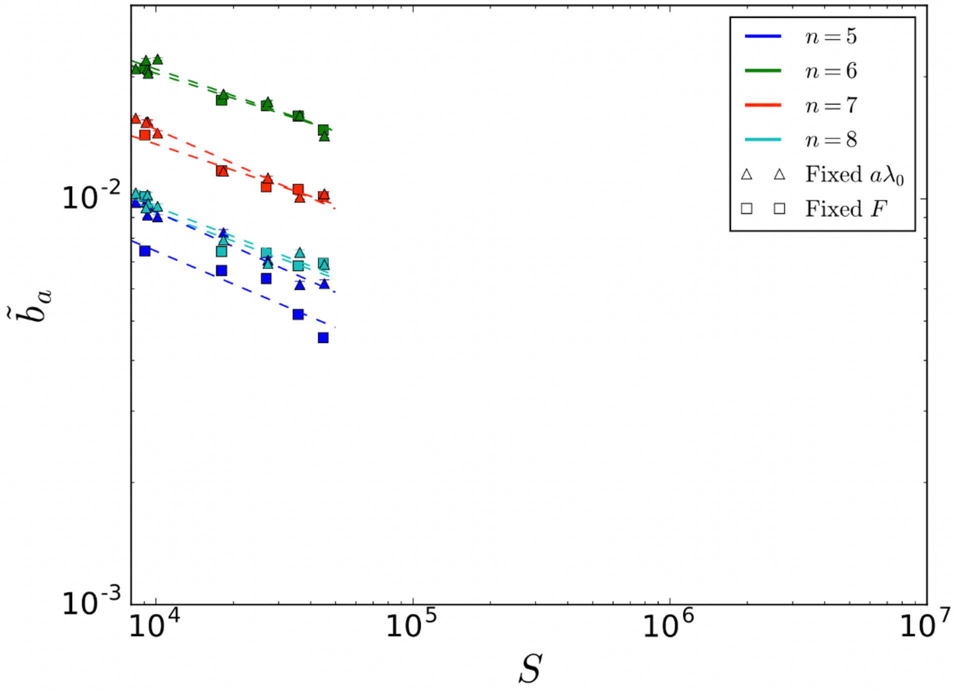

FIGURE 5.25: NIMROD simulations run by C. Jacobson to study magnetic field fluctuation scaling against Lundquist number in the computational code.

NIMROD scaling results summary for fixed $F = -0.2$		
Mode number	c_n	α_n
m=1,n=5	0.09 ± 0.047	0.27 ± 0.053
m=1,n=6	0.13 ± 0.026	0.20 ± 0.020
m=1,n=7	0.10 ± 0.028	0.21 ± 0.028
m=1,n=8	0.08 ± 0.049	0.23 ± 0.062

TABLE 5.1: This table summarizes the results to fitting the fixed $F = -0.2$ NIMROD runs to the equation $\tilde{b}_n(a) = c_n S^{-\alpha_n}$.

a flat viscosity ν profile, and the following resistivity profile:

$$\eta(r) = \eta_0(1 + (\sqrt{20} - 1))(\frac{r}{a})^{20})^2. \tag{5.25}$$

In order to keep $F = -0.2$ constant, the initial dimensionless parameter for the parallel current, $a\lambda_0$, was set to 4.13, 4.08, 4.05, 4.02, and 4.01 respectively for each step increasing in Lundquist number. These simulations were run for $\tau_R \sim 10^4 \tau_A$. The average fluctuation at $r = a$ was taken over the nonlinear saturated state. Table 5.1 summarizes the results of fitting these results to the equation $\tilde{b}_n(a) = c_n S^{-\alpha_n}$.

Fig. 5.26 shows the results from DEBS runs created with a similar aim. As with the NIMROD simulations, a single-fluid, cylindrical geometry with aspect ratio $R/a = 3$, Prandtl number $Pm = 1$, a flat viscosity ν profile, and the same resistivity profile above in Eqn. 5.25 were used to generate the data. The nonlinear numerical viscosity was turned off. Table 5.2 summarizes the results of fitting these data to the scaling equation.

With an experimental database that is freshly capable of directly overlapping in Lundquist number with the simulated runs, it is possible to compare experimental data generated in the upper range of Lundquist numbers accessible to the NIMROD and DEBS codes. However, for the comparisons that follow, we simply employed the scaling results that

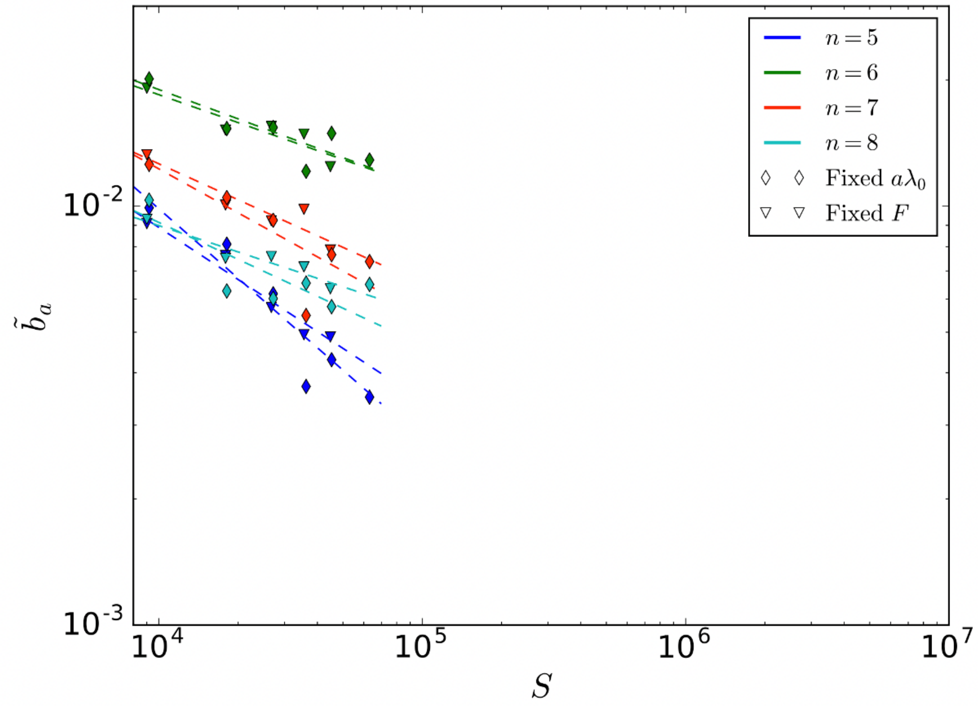

FIGURE 5.26: DEBS simulations run by C. Jacobson to study magnetic field fluctuation scaling at the edge of the plasma against the Lundquist number.

DEBS scaling results summary for fixed $F = -0.2$		
Mode number	c_n	α_n
m=1,n=5	0.40 ± 0.197	0.41 ± 0.050
m=1,n=6	0.14 ± 0.069	0.22 ± 0.049
m=1,n=7	0.17 ± 0.097	0.29 ± 0.056
m=1,n=8	0.06 ± 0.022	0.21 ± 0.036

TABLE 5.2: This table summarizes the results to fitting the fixed $F = -0.2$ DEBS runs to the equation $\tilde{b}_n(a) = c_n S^{-\alpha_n}$.

were gathered over the range of Lundquist number values accessible to the MST. We will now go over comparison between these experimental data and the preliminary simulated data.

Fig. 5.27 compiles the magnetic field fluctuation scaling results from both computational and experimental data. A common technique for assessing the degree of agreement between computational and experimental data is to employ validation metrics. The selection of which metric or metrics to use is more of an art than a science. Three metrics that we will look at are the relative error metric, the χ^2 metric, and the Hyperbolic Tangent Metric. Below are expressions for each where y_i is the set of simulated values with standard error σ_{y_i} while Y_i and σ_{Y_i} are the experimental data and errors. The Relative Error Metric is given by,

$$M = \frac{1}{n}\sum_{i=1}^{n}|\frac{y_i - Y_i}{Y_i}|, \tag{5.26}$$

where $M = 0$ represents perfect agreement and $M = \infty$ represents perfect disagreement. The χ^2 Metric is given by,

$$M = \chi_y^2 = \frac{1}{N_{degrees}}\sum_{i=1}^{n}(\frac{y_i - Y_i}{\sigma_{y_i} - \sigma_{Y_i}})^2, \tag{5.27}$$

where, once again $M = 0$ represents perfect agreement and $M = \infty$. Finally, the Hyperbolic Tangent Metric is given by,

$$M = 1 - \frac{1}{n}\sum_{i=1}^{n} tanh(|\frac{y_i - Y_i}{Y_i}| + |\frac{\sigma_{Y_i}}{Y_i}| + |\frac{\sigma_{y_i}}{y_i}|), \tag{5.28}$$

where $M = 1$ indicates perfect agreement and $M = 0$ indicates perfect disagreement [36].

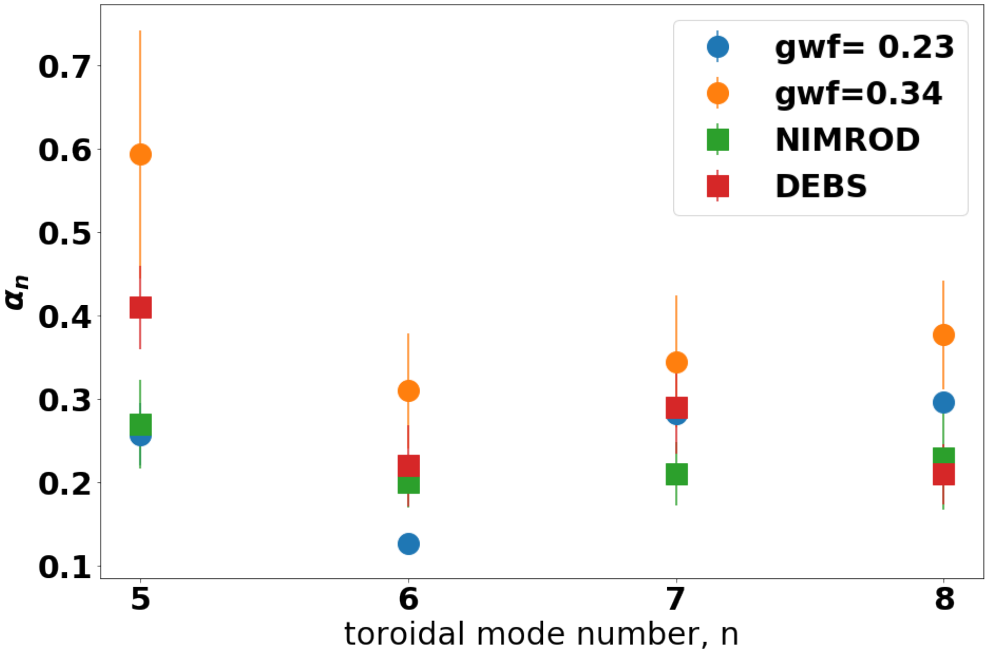

(A)

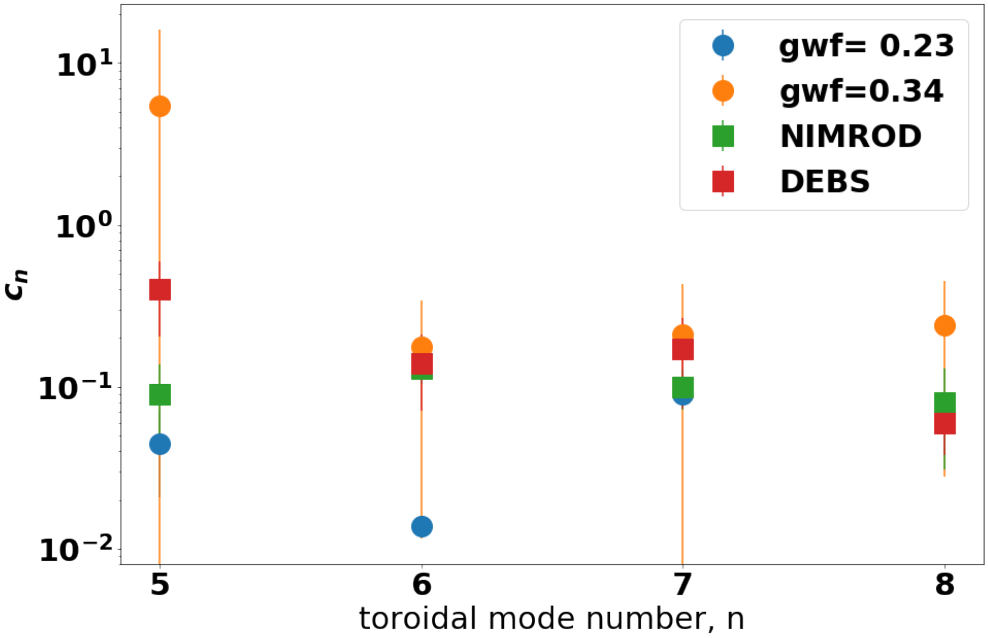

(B)

FIGURE 5.27: This figure summarizes the results of fitting experimental and computational data for magnetic field fluctuation magnitudes at the edge scaling with Lundquist number to the equation $\tilde{b}_n(a) = c_n S^{-\alpha_n}$.

Tables 5.3-5.5 summarizes the results of employing these metrics to quantify the degree of agreement between experimental and simulated data where the data for each mode number n=6-8 were summed to calculate a given metric. The n=5 mode data is excluded given that this mode is only sporadically present in the experimental plasmas. Generally speaking, we see good agreement between simulation and experimental data for both the scaling parameters, α_n and the coefficient for the fits, c_n. Experimental parameter definitions were selected to be intuitive to an experimentalist rather than to align well with simulated results. Focusing on the metrics that incorporate uncertainties into their calculations, there is some disagreement as to whether the higher Greenwald fraction data agree better with the simulated data or if the lower Greenwald fraction data do. Finally, the degree of agreement for the scaling parameter comparisons is similar between the NIMROD and DEBS for all three of the metrics employed here.

Many improvements can be made to these comparisons. It would be prudent to expand the simulated data set to account for two-fluid effects which were neglected for the results presented here. Additionally, the validity of these comparisons could be further improved using all the experimental data have been gathered since the simulated results were generated.

5.4 Comparing and Extrapolating Results

In this section, we will apply the scaling results obtained within the range of MST-achievable Lundquist numbers to estimate the performance of the RFP at larger Lundquist numbers. As has been previously discussed, the RFP is an underexplored avenue of investigation en

Relative Error Metric Values (0= perfect agreement, ∞= perfect disagreement)		
c_n	NIMROD	DEBS
$gwf = 0.23$	2.88	3.46
$gwf = 0.34$	0.48	0.38
α_n	NIMROD	DEBS
$gwf = 0.23$	0.35	0.35
$gwf = 0.34$	0.38	0.30

TABLE 5.3: This table shows the results of applying the Relative Error Metric (Eqn. 5.26) to the n=6-8 modes for the experimental and both NIMROD and DEBS simulated data for the coefficient of the fits, c_n as well as the scaling parameters, α_n.

χ^2 Metric Values (0= perfect agreement, ∞= perfect disagreement)		
c_n	NIMROD	DEBS
$gwf = 0.23$	5.71	1.32
$gwf = 0.34$	0.21	0.21
α_n	NIMROD	DEBS
$gwf = 0.23$	2.05	2.01
$gwf = 0.34$	1.30	1.15

TABLE 5.4: This table shows the results of applying the χ^2 Metric (Eqn. 5.27) to the n=6-8 modes for the experimental and both NIMROD and DEBS simulated data for the coefficient of the fits, c_n as well as the scaling parameters, α_n.

Hyperbolic Tangent Metric Values (1= perfect agreement, 0= perfect disagreement)		
c_n	NIMROD	DEBS
$gwf = 0.23$	0.28	0.15
$gwf = 0.34$	0.06	0.05
α_n	NIMROD	DEBS
$gwf = 0.23$	0.47	0.50
$gwf = 0.34$	0.34	0.40

TABLE 5.5: This table shows the results of applying the Hyperbolic Tangent Metric (Eqn. 5.28) to the n=6-8 modes for the experimental and both NIMROD and DEBS simulated data for the coefficient of the fits, c_n as well as the scaling parameters, α_n.

route to a viable fusion reactor. The vast majority of resources in magnetic confinement fusion research are devoted to the tokamak concept and so it is often an intuitive reference. Fig. 5.28 depicts the performance of past, current, and planned tokamak experiments and reactors [37]. The MST RFP is added to the figure at two points. The MST point with the shorter energy confinement time represents standard RFP operation and the MST point with the longer energy confinement time represents MST operating in an improved confinement mode, where magnetic field fluctuations are reduced. When implementing this performance improvement, the RFP's becomes competitive - out-competes even- with similarly-sized tokamak devices. This makes a compelling case for creating more RFPs to fill out a similar expanse of parameter space. However, should we want to employ the RFP as a reactor, steady-state operation will be advantageous. This is not possible with the current mechanism for minimizing magnetic field fluctuations that is depicted on the graphic in Fig. 5.28. So here, we delve into what stochasticity decreases one might expect to see simply by increasing the Lundquist number.

In this section, extrapolations of the scaling results to reactor-relevant scales ($S \sim 10^9 - 10^{10}$) will first be presented. We will also discuss the implications for how some tranpsort-related quantities might scale to larger Lundquist numbers and the implications of those results for the performance of a RFP device.

5.4.1 Magnetic field fluctuation amplitude scaling extrapolation

Fig. 5.29 shows results of the magnetic field fluctuation amplitude scalings extrapolated to estimated reactor-relevant Lundquist numbers. The blue data represent low Greenwald fraction results and the orange data represent high Greenwald fraction results. The

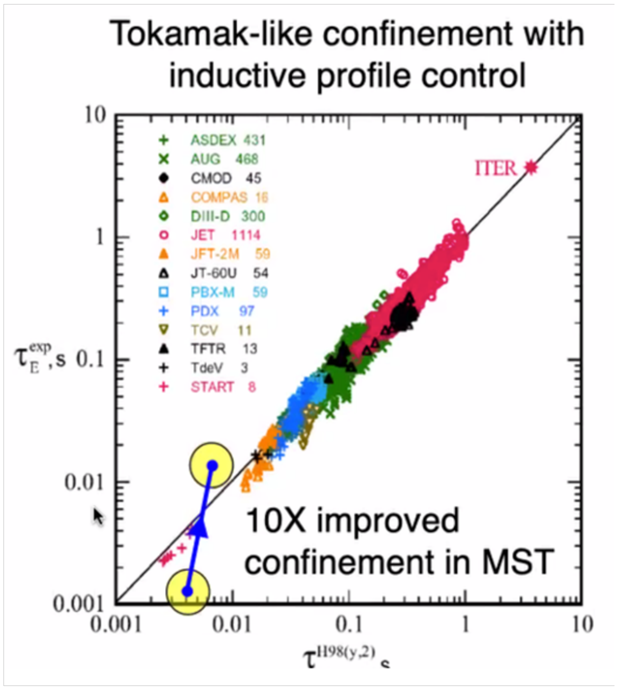

FIGURE 5.28: This figure, adapted from [37] with updates to include improved enhanced confinement performance, shows the MST RFP in context with past, current and projected tokamak experiments.

lines come from the best fits of the data to the equation: $\tilde{b}_n = c_n S^{-\alpha_n}$. Within this subsection, data shown is for the $m = 1, n = 6 - 15$ modes and since any RFP reactor will most likely run with relatively high density plasmas, discussion will focus on the high Greenwald fraction results.

Also shown on Fig. 5.29 is a dashed line which represents an estimate for the magnetic field fluctuation amplitude at which the island corresponding to that mode number will no longer overlap with its neighboring island. To obtain an estimate for this point, first the island widths for each mode number were determined working from the edge inward such that each island would just touches its nearest neighbors [38]. To obtain an expression for these widths, we start with the stochasticity parameter, s, which quantifies the degree of stochasticity in a plasma where the larger the s, the more stochastic the plasma and $s = 1$ represents the threshold at which the field lines no longer overlap. At this point $s = 1$, the plasma at that resonant location transitions from stochastic to deterministic field lines. The expression for s for the $m = 1, n = n$ island and its neighboring $m = 1, n = n'$ is given by,

$$s = \frac{1}{2}\frac{(w_n - w_{n'})}{|r_n - r_{n'}|}, \tag{5.29}$$

where w_n represents the width of the island for the n mode and r_n is its resonant location. Taking $s = 1$, assuming that, for large n, $w_n \approx w_{n+1}$, and Taylor expanding the safety factor near $r = r_n$, yields the following expression for the island width at the threshold between stochastic and deterministic field lines:

$$w_n = \frac{1}{n(n+1)|q_n'|}, \tag{5.30}$$

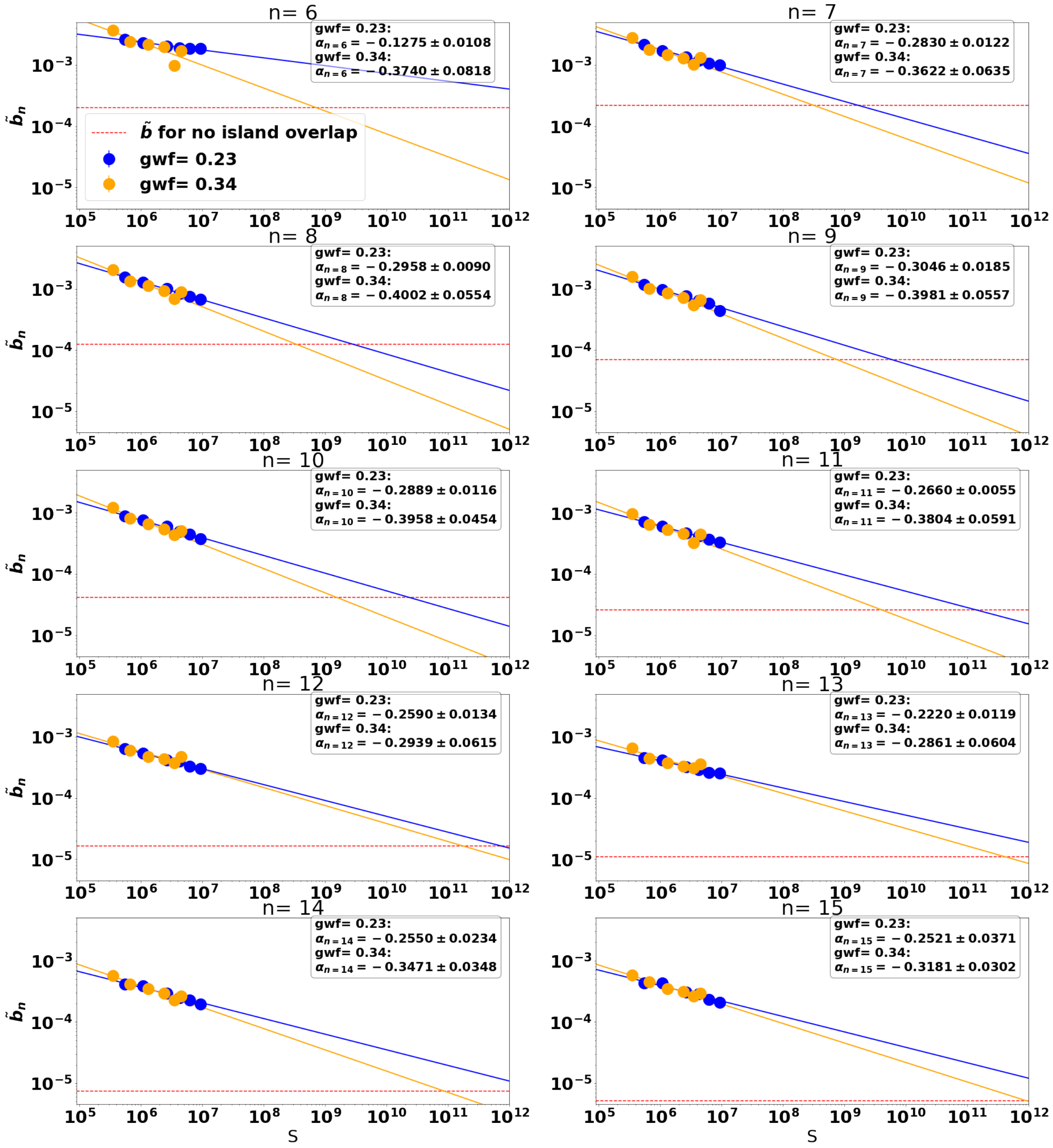

FIGURE 5.29: This figure plots the results from S-scaling the magnetic field fluctuation amplitudes out reactor-relevant Lundquist numbers. The red dashed lines indicate the point at which island overlap with the neighboring mode is projected to be eliminated via a decrease in the field fluctuation amplitude. The orange data represent the high Greenwald fraction case which is more relevant in the context of considering what RFP reactor dynamics may be.

where $|q_n'|$ is the radial derivative of the safety factor at the resonant location of the mode, $\frac{\partial q}{\partial r}(r_n)$.

We can relate this result to the measured magnetic field mode amplitudes by looking at the more general expression for the island width. The width of the magnetic island for the m=1,n mode is given by,

$$w_n = 4\sqrt{\frac{\tilde{B}_{r,n}(r_n)}{B_{\theta,n}(r_n)}\frac{r_n}{n}\frac{1}{|q_n'|}}, \tag{5.31}$$

where $\tilde{B}_{r,n}$ is the (unnormalized) radial component of the magnetic field fluctuation, B_θ is the (unnormalized) poloidal component of the magnetic field, and r_n is the resonant location of the mode, n is the relevant toroidal mode number. So, by equating Eqn. 5.30 and Eqn. 5.31, we obtain an expression for the magnetic field fluctuation at the $s = 1$ threshold.

However, the values measured when presenting the scaling results are $\tilde{b}_n(r = a) = \frac{\tilde{B}_\theta(r=a)}{B_{0,\alpha}}$ where $B_{0,\alpha}$ is the magnetic field amplitude on the magnetic axis according to the alpha model, and a is the minor radius. So, we need a way to relate this measurement at the edge to $\frac{\tilde{B}_r(r_n)}{B_\theta(r_n)}$ at the resonant surface. To get an approximation for this value, the RESTER code was utilized. RESTER is a numerical tool that calculates the stability of cylindrical, force-free profiles [39, 40]. This code does not include non-linear effects and utilizes a cylindrical plasma approximation, however, is sufficiently detailed for the purposes of this estimation. These RESTER plots, made for standard plasmas of $\beta = 0$ and are included in Appendix B for future reference [38].

Fig. 5.30 summarizes the results from Fig. 5.29, plotting the Lundquist number for each mode at which the stochasticity parameter is projected to equal one. Fig. 5.30a plots this value against the mode number and Fig. 5.30b plots this quantity against r/a by placing the results at the resonant location for the mode. If we assume that a RFP reactor will have a Lundquist number around $S \sim 10^9 - 10^{10}$, the islands corresponding to $n < 12$ would have fluctuations small enough such that the islands would not overlap, corresponding to the plasma volume $r/a \lesssim 0.662$ having deterministic magnetic field structure. This implies that stochasticity would cease to be the dominate loss mechanism within this significant core portion of the plasma volume (43% of the core-most volume).

5.4.2 Extrapolating Confinement to Reactor Conditions

Using the results presented herein, one can extrapolate energy confinement time to assess the feasibility of an ohmically ignited RFP reactor plasma. In order to make such an estimate, an operating point needs to be chosen. Here we use TITAN and an ARIES-like scenario as examples [41, 18, 42, 43, 44, 45]. Each has a fusion power $P_f = 2.3$ GW and a net electric power $P_e = 1.0$ GW. A major caveat when considering these targets, particularly TITAN, is the neutron wall loading. TITAN's ultra compact design comes with a neutron wall loading of $P_n = 18$ MW/m^2 and the ARIES-like scenario's neutron wall loading is $P_n = 5$ MW/m^2. Materials able to handle even $P_n = 5$ MW/m^2 are not yet developed. The ARIES scenario is therefore most realistic. In any case, we are extrapolating over many orders of magnitudes and do not have information as to how Lundquist number scalings change over that range of Lundquist number. That being said, these extrapolations are still of interest, and make use of the data currently available.

Assuming an ohmically heated plasma with stochastic transport, it can be shown that

$$\tau \propto [a^{(7-2\alpha)} I_p^{(-1+11\alpha)} (n_e/n_G)^{(1-11\alpha)}]^{\frac{1}{6-6\alpha}}, \tag{5.32}$$

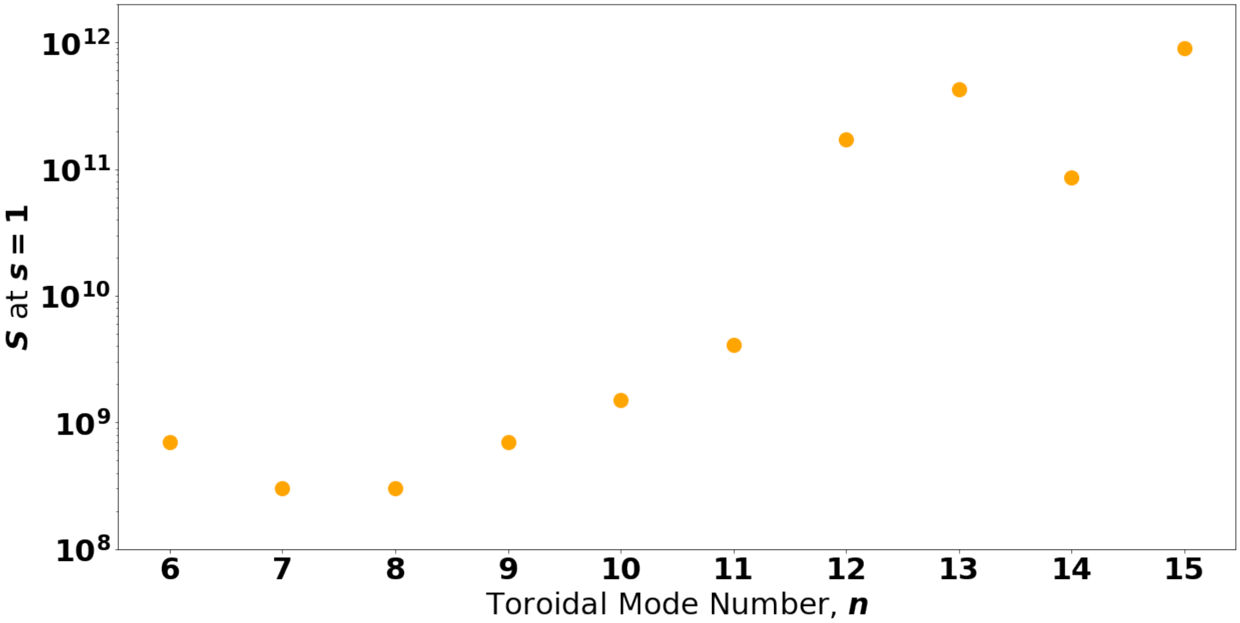

(A)

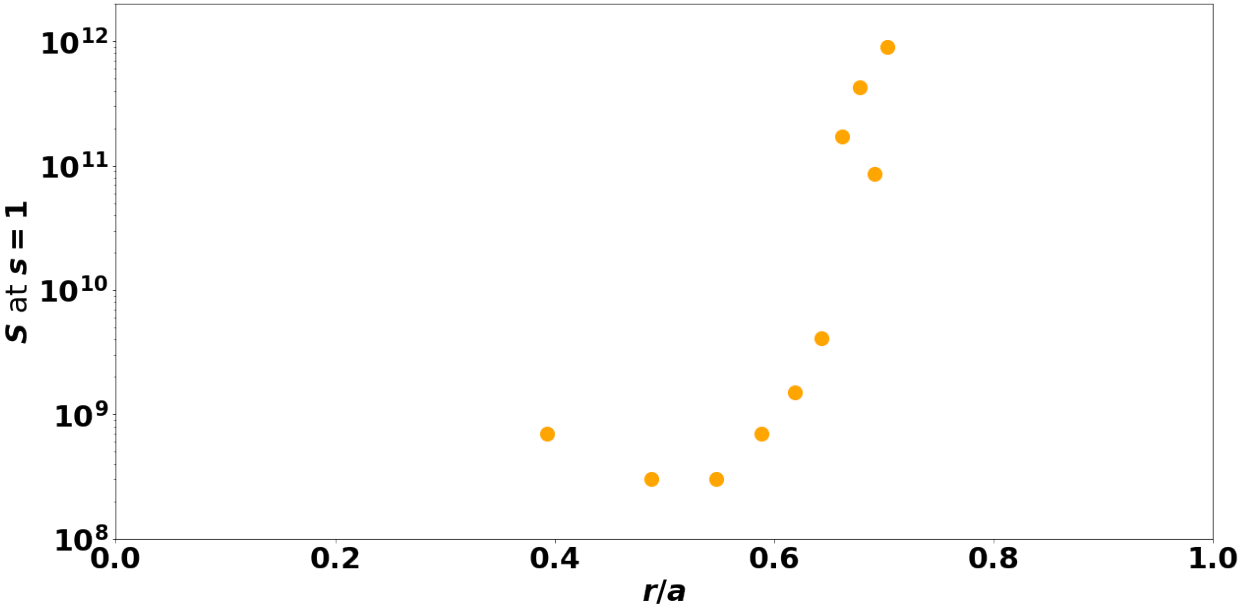

(B)

FIGURE 5.30: This set of figures summarizes the results from extrapolating the magnetic field fluctuation amplitude S-scaling results to a point where magnetic island overlap is just eliminated. The upper plot plots the Lundquist number value at which the magnetic field fluctuation amplitudes are projected to diminish to this point by toroidal mode number. The lower figure plots the same information by the resonant location for each mode.

TITAN (τ= 0.2s)			
α	0.3	1/3	0.4
scaled τ [s]	0.023	0.036	0.10
$n\tau$ [1E20 s/m^3]	0.127	0.196	0.55

TABLE 5.6: This table summarizes scaling to TITAN operational parameters using MST results as a benchmark. The columns show results for different scaling parameter, or α, values. The high Greenwald fraction is used to obtain density and the Lawson criterion ($n\tau$).

where a is the minor plasma radius [46]. For the results here, we find that the electron confinement time scales close to $\tau_E \propto I_p^{2/3}$, while holding Greenwald fraction constant. This matches the stochastic transport scaling for $\alpha = 1/3$. Table 5.6 summarizes results from extrapolating MST confinement to the TITAN case where $a = 0.6$ m and $I_p = 18$ MA. The Greenwald fraction is taken to be $n_e/n_G = 0.34$. TITAN's operating point requires $\tau_E = 0.2$ s. The projected confinement falls short by an order of magnitude for $\alpha = 0.3$ but only a factor of two short for $\alpha = 0.4$ [47]. The projected confinement for the ARIES-like scenario with a =1.5 m, I_p = 30 MA, and a consequent $\tau_E = 0.8$ s is summarized in Table 5.7. In this case, the confinement is sufficient for ohmic ignition for $\alpha = 0.4$, which is the value measured for $n_e/n_G = 0.34$ case.

Stoneking did a similar estimate using TITAN as a target and MST as a benchmark. Fig. 5.31 reproduces his results [4] where he plots the scaling parameter, α, against the operating current of the machine. The blue and orange lines mark the average α values obtained for the mid-radial modes for the low and high Greenwald fraction cases respectively. Tracing where these values overlap with the current provides a estimate for the operating current for TITAN for these two Greenwald fraction cases. This plot, combined with the scaling estimates for TITAN and ARIES-like reactors, show how strongly these scalings depend on α when extrapolating the results.

ARIES-Like (τ = 0.8 s)			
α	0.3	1/3	0.4
scaled τ [s]	0.13	0.22	0.79
$n\tau$ [1E20 s/m^3]	. 0.18	0.31	1.14

TABLE 5.7: This table summarizes scaling to ARIES-like operational parameters using MST results as a benchmark. The columns show results for different scaling parameter, or α, values. The high Greenwald fraction is used to obtain density and the Lawson criterion ($n\tau$).

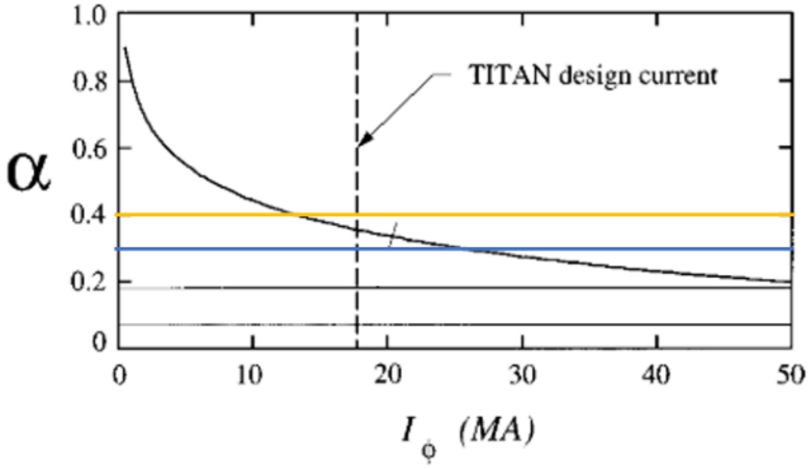

FIGURE 5.31: This figure plots the results from S-scaling the magnetic field fluctuation amplitudes out reactor-relevant Lundquist numbers. The red dashed lines indicate the point at which island overlap with the neighboring mode is projected to be eliminated via a decrease in the field fluctuation amplitude. The orange data represent the high Greenwald fraction case which is more relevant in the context of considering what RFP reactor dynamics may be.

5.4.3 Stochastic Diffusion at Fusion Relevant Scales

Now let's consider the electron thermal stochastic diffusion, χ_{R-R}. Recall, that $\chi_{R-R} \sim v_{th,e} L_{AC} (\tilde{B}_r)^2$. Given this, the extrapolated results of the the magnetic field fluctuation amplitudes can be used to estimate the stochastic transport at reactor relevant scales. To do so, we again use the results from RESTER to translate the edge measured quantities, $b_n = \tilde{B}_{\theta,n}/B_0$ to $\tilde{B}_r$. The autocorrelation length is assumed to be $L_{ac} = 3.14$ m (i.e. a minor radius equal to one meter for the reactor). Additionally, an estimated core electron temperature $T_{e,0} = 10$ keV is used to create a temperature profile along the minor radius using the alpha model ($T_e(r/a) = T_{e,0}(1 - (r/a)^{\alpha})^{\beta}$) to obtain the approximate electron thermal velocity at the resonant location of each mode.

Fig. 5.32 shows the results of these estimated reactor (i.e. $S \sim 10^9 - 10^{10}$) diffusion coefficients for the n= 6-15 modes for the high Greenwald fraction scenario. $\chi_{e,st}$ is plotted at the resonant location and the blue dashed lines mark these locations. The green solid line marks where $\chi_{R-R} = 1$ m^2/s. $\chi_{e,st}$ will likely need to be less than this value for stochastic diffusion to be minimized to a point that is sufficient for competitive fusion reactor design.

When we think about minimizing the magnetic field fluctuations for higher mode numbers and refer to the safety factor profile, we see that the spacing between adjacent modes becomes smaller as we move out along the minor radius. It would then intuitively follow that it should be more difficult to eliminate stochastic diffusion via a reduction in magnetic field fluctuation at larger toroidal mode numbers. However, we see that this intuition is misleading given that $\chi_{e,st} \propto \tilde{B}_r^{\,2}$. So, even though the resonant locations grow closer together, they do so while the magnetic field fluctuation strengths grow weaker. Since stochastic transport goes like this quantity squared, stochastic transport is not as significant at higher mode numbers as one might initially expect.

We see this dynamic evidenced in Fig. 5.32. For many mid-radial mode numbers, $\chi_{e,st}$ dips below 1 m^2/s. A cluster of modes that does so exists for n= 9-11. So in this region, while there still maybe some slight stochasticity, stochastic transport is not significant. If this cluster of modes acts as a buffer to stochastic transport, it would confines the plasma at $\mathrm{r/a} < \mathrm{r}_{s,n=9}$, which amounts to a significant 35% of the plasma volume being well-confined in the core.

A few modes raise back above $\chi_{e,st}$ = 1 m^2/s in large part due to the magnitude of the alpha exponential value for the scaling decreasing for modes n= 12-13 leading to relatively high fluctuations for these modes at higher Lundquist numbers and in smaller part due to an increase in the ratio of the radial magnetic field at the resonant location to the poloidal magnetic field at the edge obtained from RESTER. However, these values are still close to the desired $\chi_{e,st}$, and, given that these are rough estimates, these results indicate that there is good reason to expect stochastic transport to be within in the ballpark of being sufficiently ameliorated through a natural tendency for the magnetic field mode amplitudes to decrease as Lundquist number is ramped up.

5.5 Summary

For this study, we produced a large cache of data across the range of Lundquist numbers accessible to MST. These data were ensembled at points across this expanse to obtain a relationship for how the magnetic field fluctuation amplitudes measured at the edge of MST scaled with Lundquist number. A summary of these results is given in Fig. 5.21.

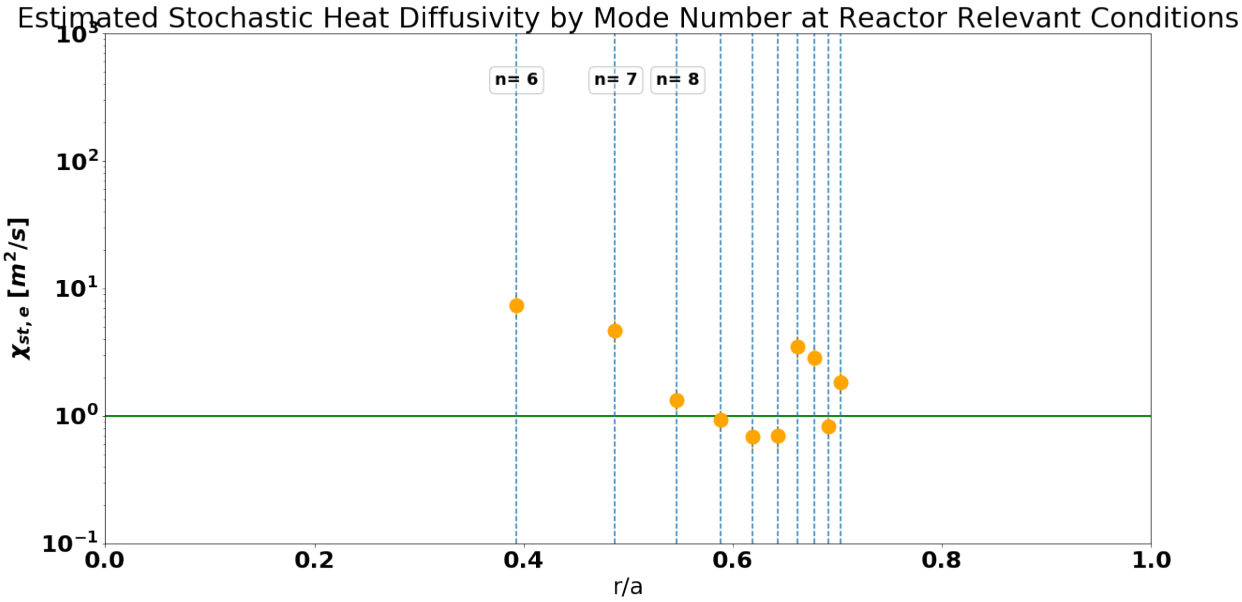

FIGURE 5.32: This plot uses the extrapolated values for magnetic field fluctuation amplitudes to estimate the stochastic transport for reactor relevant parameters and scales ($S \sim 10^9$) for magnetic modes n=6-15. Each result is plotted at its resonant location. The green line marks the $\chi_{st} = 1$ threshold below which stochastic transport would be minimized enough so that a reactor could obtain sufficient confinement.

In the scaling fit results, we observe stronger scaling for the higher density scenario. The $n = 6$ modes exhibits unique behavior where its magnetic field fluctuation amplitudes seem to level off and not vary strongly with Lundquist number. This effect is less obvious in the high density case but may still be present when considering extenuating factors of the data collection constraints. For a chunk of modes $n = 7, 8, 9, 10$ we see highly favorable scaling terms, implying that should we extrapolate conditions to reactor-relevant scales, we have reason to suspect that stochastic transport would cease to be a dominant transport mechanism for the RFP. This suspicion is further supported by the estimation for $\chi_{e,st}(r)$ performed in the chapter. In all, having an average $\alpha_{n,gwf=0.34} \sim 0.38$ for the core most modes is a very encouraging result for the RFP magnetic confinement fusion concept.

Some preliminary analyses were also done to compare these data to simulations performed in DEBS and NIMROD. These data have a large range of Lundquist number value overlap with simulated data. Metrics indicate that α_n values are better aligned between experiment and simulation than c_n values. This is somewhat expected given that the choice of parameters used to determine Lundquist number was chosen for experimental convenience and as opposed to being selected for easy comparisons with simulation results. In general, simulations and choice of experimental parameter definitions could be iterated upon to better match each other. Additionally, a more thorough and extensive validation effort using these experimental data would be a future project of great interest.

Extrapolating results to high Lundquist number values argues for the promise of expanding the RFP fusion research program to larger scales. When looking at the magnetic field fluctuation amplitude and electron thermal diffusion extrapolations, we see these quantities that are most closely tied to direct measurements are expected to scale very favorably at $S_{reactor} \sim 10^9 - 10^{10}$.

Finally, considering τ_E, these scalings did not produce results consistent with values that we would expect from a stochastic model and $\alpha \sim 0.333$. This indicates that there may be physics at play that is not captured by the stochastic model. This somewhat tempers the promising scaling parameter results.

Bibliography

[1] M. Greenwald, J. Terry, S. Wolfe, S. Ejima, M. Bell, S. Kaye, and G. Neilson, "A new look at density limits in tokamaks," *Nuclear Fusion*, vol. 28, no. 12, pp. 2199–2207, dec 1988. [Online]. Available: https://doi.org/10.1088/0029-5515/28/12/009

[2] M. Greenwald, "Density limits in toroidal plasmas," *Plasma Physics and Controlled Fusion*, vol. 44, no. 8, pp. R27–R53, jul 2002. [Online]. Available: https://doi.org/10.1088/0741-3335/44/8/201

[3] S. Ortolani and G. Rostagni, "Density limits and scaling laws in reversed field pinches," *Nuclear Instruments and Methods in Physics Research*, vol. 207, no. 1, pp. 35–48, 1983. [Online]. Available: https://www.sciencedirect.com/science/article/pii/0167508783902211

[4] M. R. Stoneking, J. T. Chapman, D. J. Den Hartog, S. C. Prager, and J. S. Sarff, "Experimental scaling of fluctuations and confinement with lundquist number in the reversed-field pinch," *Physics of Plasmas*, vol. 5, no. 4, pp. 1004–1014, 1998. [Online]. Available: https://doi.org/10.1063/1.872670

[5] L. Spitzer and R. Härm, "Transport phenomena in a completely ionized gas," *Phys. Rev.*, vol. 89, pp. 977–981, Mar 1953. [Online]. Available: https://link.aps.org/doi/10.1103/PhysRev.89.977

[6] S. Hirshman and D. Sigmar, "Neoclassical transport of impurities in tokamak plasmas," *Nuclear Fusion*, vol. 21, no. 9, p. 1079, sep 1981. [Online]. Available: https://dx.doi.org/10.1088/0029-5515/21/9/003

[7] I. H. Hutchinson, *Principles of Plasma Diagnostics*. Cambridge University Press, 2002.

[8] A. Richardson, *NRL Plasma Formulary*. Washington, DC: Naval Research Lab., 2019. [Online]. Available: https://www.nrl.navy.mil/News-Media/Publications/nrl-plasma-formulary/

[9] J. Callen, *Plasma Kinetic Theory and Radiation Processes*. Madison,WI: self-published, 2014.

[10] T. M. Biewer, C. B. Forest, J. K. Anderson, G. Fiksel, B. Hudson, S. C. Prager, J. S. Sarff, J. C. Wright, D. L. Brower, W. X. Ding, and S. D. Terry, "Electron heat transport measured in a stochastic magnetic field," *Phys. Rev. Lett.*, vol. 91, p. 045004, Jul 2003. [Online]. Available: https://link.aps.org/doi/10.1103/PhysRevLett.91.045004

[11] V. Antoni, D. Merlin, S. Ortolani, and R. Paccagnella, "Mhd stability analysis of force-free reversed field pinch configurations," *Nuclear Fusion*, vol. 26, no. 12, p. 1711, dec 1986. [Online]. Available: https://dx.doi.org/10.1088/0029-5515/26/12/012

[12] H. Ji, S. C. Prager, and J. S. Sarff, "Conservation of magnetic helicity during plasma relaxation," *Phys. Rev. Lett.*, vol. 74, pp. 2945–2948, Apr 1995. [Online]. Available: https://link.aps.org/doi/10.1103/PhysRevLett.74.2945

[13] L. Marrelli, P. Martin, G. Spizzo, P. Franz, B. E. Chapman, D. Craig, J. S. Sarff, T. M. Biewer, S. C. Prager, and J. C. Reardon, "Quasi-single helicity spectra in the Madison Symmetric Torus," *Physics of Plasmas*, vol. 9, no. 7, pp. 2868–2871, 06 2002. [Online]. Available: https://doi.org/10.1063/1.1482766

[14] P. Martin, L. Marrelli, G. Spizzo, P. Franz, P. Piovesan, I. Predebon, T. Bolzonella, S. Cappello, A. Cravotta, D. Escande, L. Frassinetti, S. Ortolani, R. Paccagnella, D. Terranova, the RFX team, B. Chapman, D. Craig, S. Prager, J. Sarff, the

MST team, P. Brunsell, J.-A. Malmberg, J. Drake, the EXTRAP T2R team, Y. Yagi, H. Koguchi, Y. Hirano, the TPE-RX team, R. White, C. Sovinec, C. Xiao, R. Nebel, and D. Schnack, "Overview of quasi-single helicity experiments in reversed field pinches," *Nuclear Fusion*, vol. 43, no. 12, p. 1855, dec 2003. [Online]. Available: https://dx.doi.org/10.1088/0029-5515/43/12/028

[15] J. Reusch, "Measured and simulated electron thermal transport in the madison symmetric torus reversed field pinch," Ph.D. dissertation, University of Wisconsin at Madison, 2011.

[16] R. Hazeltine and J. Meiss, *Plasma Confinement*. Mineola, NY: Dover Publications, 2003.

[17] J. Freidburg, *Plasma Physics and Fusion Energy*. New York: Cambridge University Press, 2007.

[18] L. Marrelli, P. Martin, M. Puiatti, J. Sarff, B. Chapman, J. Drake, D. Escande, and S. Masamune, "The reversed field pinch," *Nuclear Fusion*, vol. 61, no. 2, p. 023001, jan 2021. [Online]. Available: https://doi.org/10.1088/1741-4326/abc06c

[19] S. Hokin, A. Almagri, S. Assadi, J. Beckstead, G. Chartas, N. Crocker, M. Cudzinovic, D. Den Hartog, R. Dexter, D. Holly, S. Prager, T. Rempel, J. Sarff, E. Scime, W. Shen, C. Spragins, C. Sprott, G. Starr, M. Stoneking, C. Watts, and R. Nebel, "Global confinement and discrete dynamo activity in the mst reversed-field pinch," *Physics of Fluids B: Plasma Physics*, vol. 3, no. 8, pp. 2241–2246, 1991. [Online]. Available: https://doi.org/10.1063/1.859642

[20] N. E. Lanier, D. Craig, J. K. Anderson, T. M. Biewer, B. E. Chapman, D. J. Den Hartog, C. B. Forest, S. C. Prager, D. L. Brower, and Y. Jiang, "Control of density fluctuations and electron transport in the reversed-field pinch," *Phys. Rev. Lett.*, vol. 85, pp. 2120–2123, Sep 2000. [Online]. Available: https://link.aps.org/doi/10.1103/PhysRevLett.85.2120

[21] A. B. Rechester and M. N. Rosenbluth, "Electron heat transport in a tokamak with destroyed magnetic surfaces," *Phys. Rev. Lett.*, vol. 40, pp. 38–41, Jan 1978. [Online]. Available: https://link.aps.org/doi/10.1103/PhysRevLett.40.38

[22] J. Sarff, "Heat transport in stochastic magnetic field," CMPD and CMSO Winter School 2009.

[23] J. Duff, "Observation of trapped-electron mode microturbulence in improved confinement reversed-field pinch plasmas," Ph.D. dissertation, University of Wisconsin at Madison, 2018.

[24] Y. Hirano, Y. Maejima, T. Shimada, I. Hirota, and Y. Yagi, "Improved confinement in a high pinch parameter region of the reversed field pinch plasma," *Nuclear Fusion*, vol. 36, no. 6, p. 721, jun 1996. [Online]. Available: https://dx.doi.org/10.1088/0029-5515/36/6/I04

[25] L. M. Reusch, M. D. Nornberg, J. A. Goetz, and D. J. Den Hartog, "Using integrated data analysis to extend measurement capability (invited)," *Review of Scientific Instruments*, vol. 89, no. 10, p. 10K103, 2018. [Online]. Available: https://doi.org/10.1063/1.5039349

[26] M. Galante, L. Reusch, D. D. Hartog, P. Franz, J. Johnson, M. McGarry, M. Nornberg, and H. Stephens, “Determination ofiz/isubeff/subby integrating measurements from x-ray tomography and charge exchange recombination spectroscopy,” *Nuclear Fusion*, vol. 55, no. 12, p. 123016, nov 2015. [Online]. Available: https://doi.org/10.1088/0029-5515/55/12/123016

[27] P. D. VanMeter, L. F. Delgado-Aparicio, L. M. Reusch, and D. J. Den Hartog, “Robust analysis of space-, time-, and energy-resolved soft x-ray measurements of magnetically confined fusion plasmas (invited),” *Review of Scientific Instruments*, vol. 92, no. 5, p. 053549, 2021. [Online]. Available: https://doi.org/10.1063/5.0043787

[28] B. B. ”S.P. Hirshman, R.J. Hawryluk, *”Neoclassical Conductivity of a Tokamak Plasma”*, ”Princeton Plasma Physics Laboratory”, 1977.

[29] J. Sarff, “Discussion of viscosity scaling and trapped particle fraction.” personal communication.

[30] C. Jacobson, “’lundquist number scaling in reversed field pinch’,” ’APS DPP Conference 2017 Milwaukee, WI’ Poster Presentation, 2017.

[31] L. Morton, “Turbulence and transport in magnetic islands in mst and diii-d,” Ph.D. dissertation, University of Wisconsin at Madison, 2016.

[32] L. A. Morton, W. C. Young, C. C. Hegna, E. Parke, J. A. Reusch, and D. J. Den Hartog, “Electron thermal confinement in a partially stochastic magnetic structure,” *Physics of Plasmas*, vol. 25, no. 4, p. 042306, 2018. [Online]. Available: https://doi.org/10.1063/1.5021893

[33] J. Boguski, “Local ion velocity measurements in the mst saturated single helical axis state,” Ph.D. dissertation, University of Wisconsin at Madison, 2019.

[34] D. Schnack, D. Barnes, Z. Mikic, D. S. Harned, and E. Caramana, “Semi-implicit magnetohydrodynamic calculations,” *Journal of Computational Physics*, vol. 70, no. 2, pp. 330–354, 1987. [Online]. Available: https://www.sciencedirect.com/science/article/pii/0021999187901860

[35] C. Sovinec, A. Glasser, T. Gianakon, D. Barnes, R. Nebel, S. Kruger, D. Schnack, S. Plimpton, A. Tarditi, and M. Chu, “Nonlinear magnetohydrodynamics simulation using high-order finite elements,” *Journal of Computational Physics*, vol. 195, no. 1, pp. 355–386, 2004. [Online]. Available: https://www.sciencedirect.com/science/article/pii/S0021999103005369

[36] M. Greenwald, “Verification and validation for magnetic fusion,” *Physics of Plasmas*, vol. 17, no. 5, p. 058101, 2010. [Online]. Available: https://doi.org/10.1063/1.3298884

[37] J. Sarff, personal communication, 2022.

[38] ——, “Island overlap estimation email and rester for standard plasmas,” personal communication.

[39] C. Sovinec, “Magnetohydrodynamic simulations of noninducitve helicity injection in the reversed-field pinch and tokamak,” Ph.D. dissertation, University of Wisconsin at Madison, 1995.

[40] J. Sauppe, "Extended magnetohydrodynamic modeling of plasma relaxation dynamics in the reversed-field pinch," Ph.D. dissertation, University of Wisconsin at Madison, 2015.

[41] K. Werley, J. DiMarco, R. Krakowski, and C. Bathke, "Energy confinement and future reversed field pinches," *Nuclear Fusion*, vol. 36, no. 5, p. 629, may 1996. [Online]. Available: https://dx.doi.org/10.1088/0029-5515/36/5/I09

[42] F. Najmabadi and R. Conn, "The titan reversed-field-pinch fusion reactor study the final report," *UCLA-PPG-1200*, 1990. [Online]. Available: https://inis.iaea.org/collection/NCLCollectionStore/_Pub-lic/24/017/24017831.pdf

[43] F. Najmabadi, C. P. Wong, S. P. Grotz, K. R. Schultz, E. T. Cheng, P. I. Cooke, R. L. Creedon, N. M. Ghoniem, R. A. Krakowski, M. Z. Hasan, R. C. Martin, J. P. Blanchard, S. Sharafat, D. Steiner, D.-K. Sze, W. P. Duggan, and G. O. Orient, "The titan-i reversed-field-pinch fusion-power-core design," *Fusion Engineering and Design*, vol. 23, no. 2, pp. 81–98, 1993. [Online]. Available: https://www.sciencedirect.com/science/article/pii/0920379693901252

[44] F. Najmabadi, R. W. Conn, R. A. Krakowski, K. R. Schultz, D. Steiner, J. R. Bartlit, C. G. Bathke, J. P. Blanchard, E. T. Cheng, Y.-Y. Chu, P. I. Cooke, R. L. Creedon, W. P. Duggan, P. J. Gierszewski, N. M. Ghoniem, S. P. Grotz, M. Z. Hasan, C. G. Hoot, W. P. Kelleher, C. E. Kessel, O. K. Kevton, R. C. Martin, R. L. Miller, A. K. Prinja, G. O. Orient, S. Sharafat, E. L. Vold, K. A. Werley, C. P. Wong, and D.-K. Sze, "Introduction and synopsis of the titan reversed-field-pinch fusion-reactor study," *Fusion Engineering and Design*, vol. 23, no. 2, pp. 69–80, 1993. [Online]. Available: https://www.sciencedirect.com/science/article/pii/092037969390124Z

[45] F. Najmabadi, A. Abdou, L. Bromberg, T. Brown, V. Chan, M. Chu, F. Dahlgren, L. El-Guebaly, P. Heitzenroeder, D. Henderson, H. St. John, C. Kessel, L. Lao, G. Longhurst, S. Malang, T. Mau, B. Merrill, R. Miller, E. Mogahed, R. Moore, T. Petrie, D. Petti, P. Politzer, A. Raffray, D. Steiner, I. Sviatoslavsky, P. Synder, G. Syaebler, A. Turnbull, M. Tillack, L. Waganer, X. Wang, P. West, and P. Wilson, "The aries-at advanced tokamak, advanced technology fusion power plant," *Fusion Engineering and Design*, vol. 80, no. 1, pp. 3–23, 2006, aries - AT Special Issue. [Online]. Available: https://www.sciencedirect.com/science/article/pii/S0920379605007210

[46] K. McCollam, "'notes on rfp scaling'," internal memo, 2019.

[47] J. Sarff, "'operational parameters of a rfp reactor'," personal communication, 2023.

Chapter 6

The Transition from Quasicontinuous to Bursty Reconnection Activity

While exploring the parameter space to which the PPS system upgrade allowed access, a change in the nature of sawtoothing behavior was observed at relatively low Lundquist numbers. There, reconnection activity appears to be more quasi-continuous relative to the more bursty, discrete behavior observed at higher values of Lundquist number. This chapter presents these observations and a few insights gathered from various spectral analyses applied to the data. However, the dynamics at play that lead to these different reconnection activity behaviors are still largely an open question. In this chapter, we'll first present the phenomena observed. We will then go over some spectral analysis techniques that were applied. We will end with conclusions drawn from these analyses.

6.1 Demonstrating the Transition from Quasicontinuous to Bursty Reconnection Activity

While collecting data for the Lundquist number scaling, a change was observed in the magnetic reconnection activity as the Lundquist number was lowered to ranges made accessible by the PPS system. Prior to this upgrade, MST could achieve Lundquist numbers roughly in the range $S \sim 3 \times 10^5 - 8 \times 10^7$. The PPS system extended the lower bound of this range to $S \sim 10^4$. A change in the reconnection activity was noticed in MST signals from shots below $S \sim 10^5$. Fig. 6.1 visualizes this transition. Each row shows the toroidal gap voltage signal from an example shot of each ensemble taken. This signal is representative of the reconnection activity as it is proportional to the change in toroidal magnetic flux that results from reconnection activity. Each row is labeled on the y-axis with the approximate Lundquist number of that shot. The transition between the two types of reconnection activity takes place moving through the fourth, fifth, and sixth rows.

This behavior has been seen in some simulated plasmas as well as in other RFP devices, namely RFX [1, 2, 3]. However, it has not before been observed in MST.

Following the observation of this phenomena while conducting the S-scaling study described in the previous chapter, runtime was dedicated to probing scanning Lundquist number space spanning the boundary between the two types reconnection behavior with the aim of observing this transition with greater resolution. During this runtime, a variety of plasma currents for which $S \sim 10^5$ were feasibly attainable, were selected at which to focus plasma operation, with $I_p \sim 100$ kA proving to be the approximate current at which this transition is easiest to observe operationally. For each of these currents, the Lundquist number was varied by changing the electron density. The shots collected during this

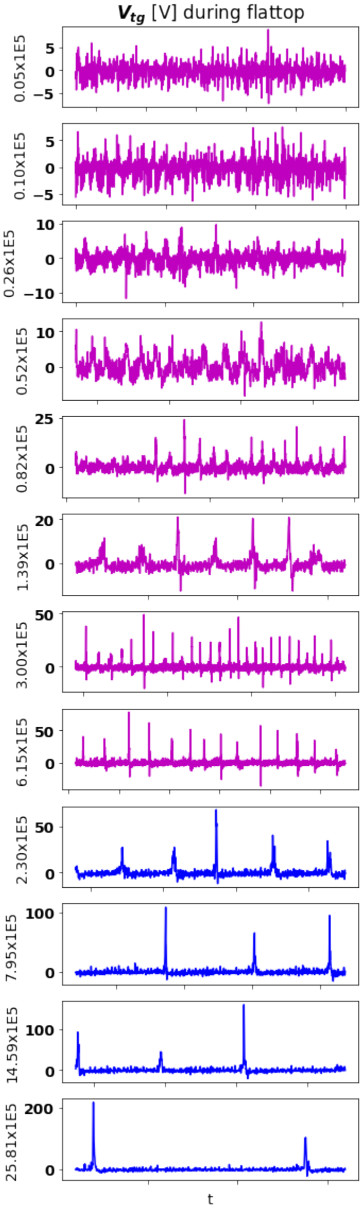

FIGURE 6.1: This figure visualizes the transition under discussion in this chapter using the toroidal gap voltage scope, which as a scope enables visualizing the variation in reconnection activity. The toroidal gap voltage scope is plotted (in Volts) versus ~ 20 ms of the flattop period. Each row is the signal from an example shot from the ensembles created for the previous chapter, plus from additional data collected outside of that framework. Each row is also labeled on the y-axis by the approximate Lundquist number of the shot. The magentic signals represent data generated via the PPS system and the blue signals represent data generated via the Legacy system. The Lundquist number for each shot increases as the rows go downward.

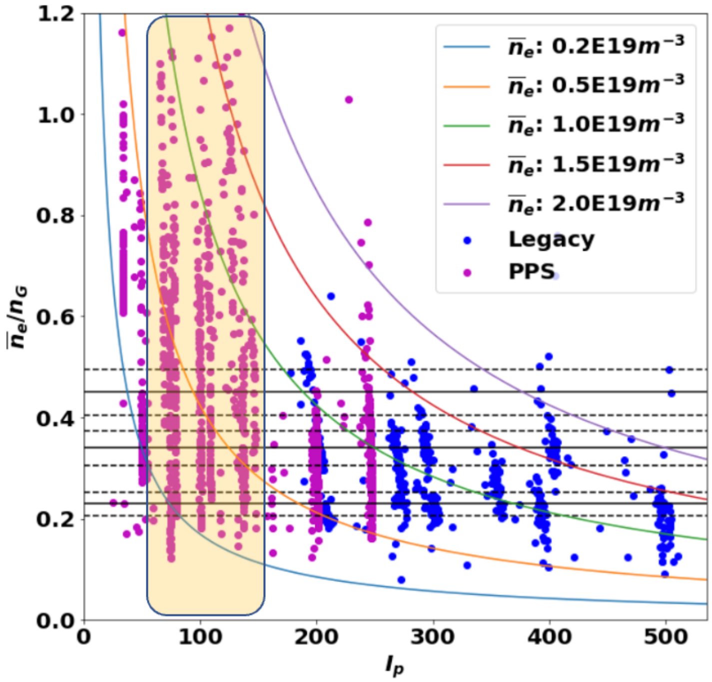

FIGURE 6.2: This reproduces Fig. 5.2, highlighted the relevant range of data for this chapter. Here, the yellow box highlights the portion of data collected that spans the transition from quasicontinuous to bursty/discrete reconnection activity.

specific campaign are highlighted by the yellow box in Fig. 6.2.

Figs. 6.3 and 6.4 show some sample results from this effort for 80 kA and 100 kA plasmas respectively. Each row features a set of traces from a 25 ms window during the flattop period of an example shot. As you move down the rows, the Lundquist number of the shot increases. The left column shows the toroidal gap voltage; it is a scope that visualizes the reconnection behavior relatively evidently. The central column shows the average toroidal magnetic field amplitude and the right column shows the toroidal magnetic field amplitude at the edge of the device.

Using this technique, plasmas exhibiting three types of behavior were observed. The

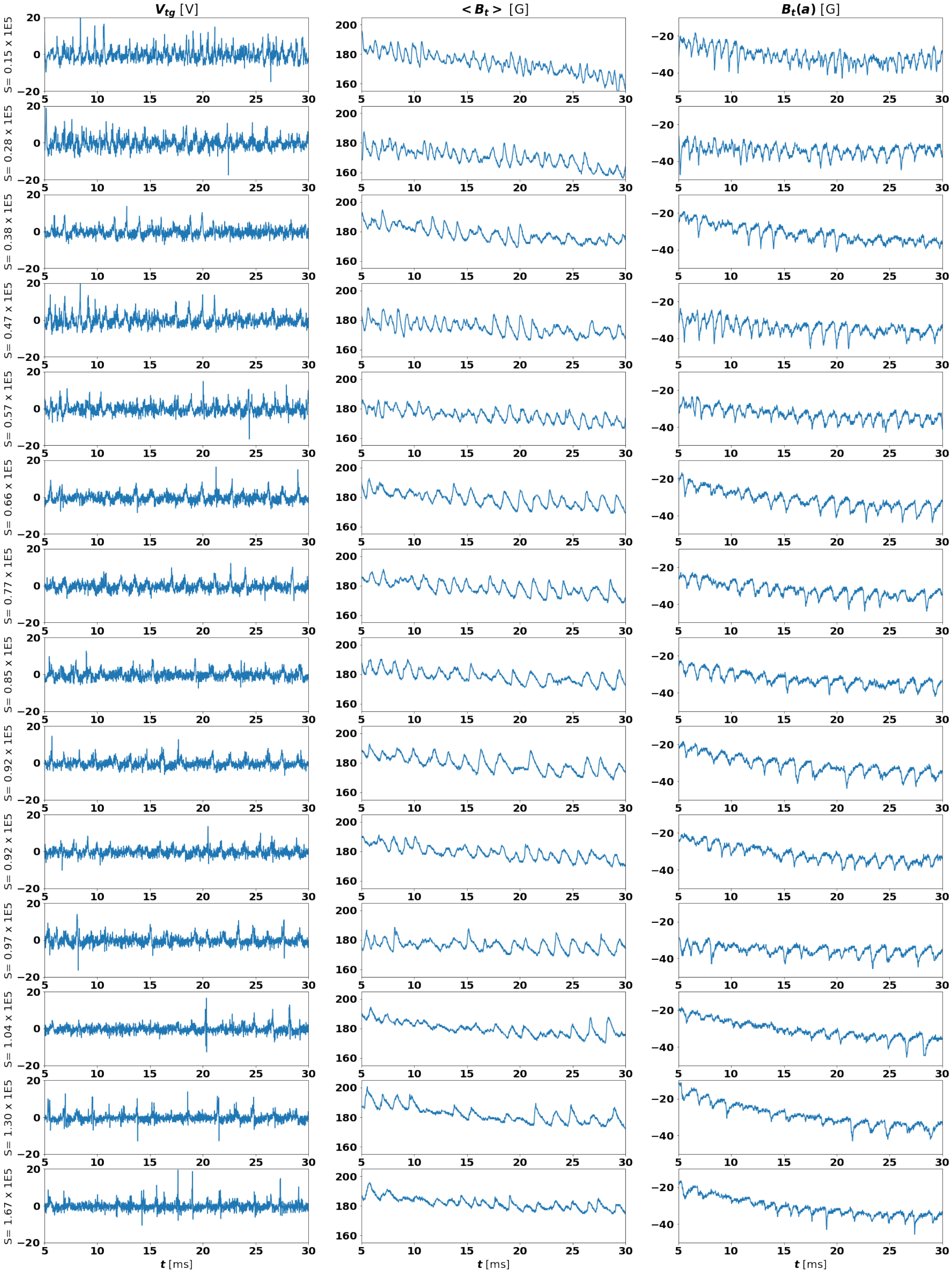

FIGURE 6.3: This figure shows the progression moving from low to high Lundquist number showing the transition from continuous to discrete for shots where the plasma current is 80 kA.

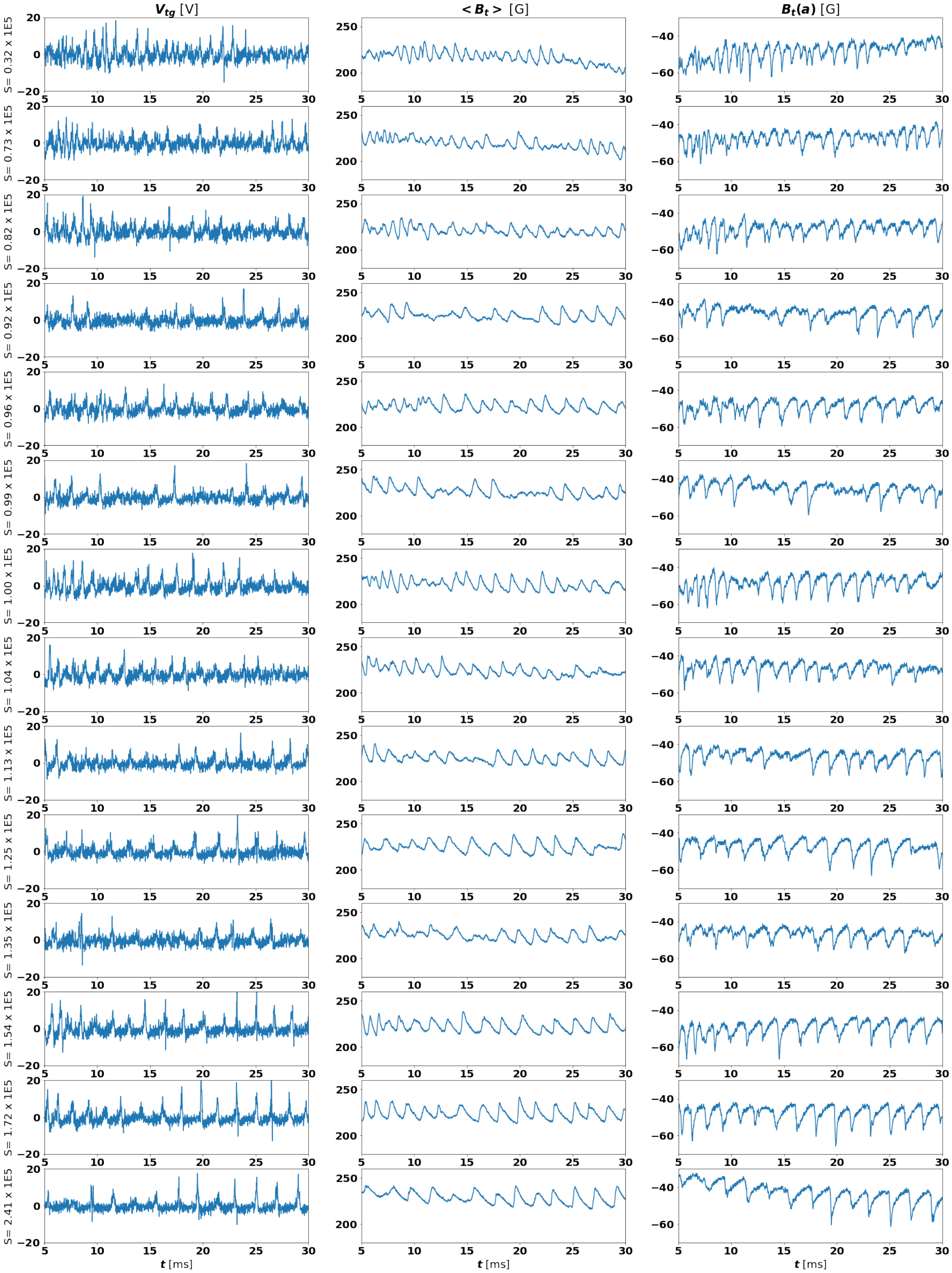

FIGURE 6.4: This figure shows the progression moving from low to high Lundquist number showing the transition from continuous to discrete for shots where plasma current is 100 kA.

"quasi-continuous" behavior at low Lundquist numbers is characterized by relatively frequent, moderately large reconnection events compared to the "bursty behavior" at high Lundquist numbers which is characterized by less frequent, large magnitude reconnection events. A "transition zone" exists for plasmas at Lundquist numbers between the two boundary cases described in the previous sentence. With this behavior, reconnection activity is a mix between the two, with more frequent but lower amplitude reconnection activity being observed. The transition region exists around $S \sim 10^5$ for the variety of plasma currents that were scanned ($I_p = 70, 80, 100, 110, 130, 140$ kA).

6.2 Spectral Analyses

Spectral analysis techniques were applied to the data to pick out relevant phenomena that may be at play. For most of the analyses presented here, the pickup-coil signals were not analog integrated so as to maximize the high frequency resolution of the signals. Additionally, while these techniques could be applied to the data generated with the Legacy power supply system, the PPS system allowed for data with less noise and more constant operational waveforms that lended themselves well to this analysis given that it proved difficult to isolate distinct characteristics of the different reconnection behaviors.

6.2.1 Fast Fourier Transform Analysis

Fast Fourier Transforms were performed on ensembles of several Lundquist numbers. These ensembles have Lundquist numbers below, at, and above the transition from quasi-continuous reconnection activity to bursty, discrete activity. The transform was performed on the numerically integrated signal of the $\dot{b}$-coils in MST taken from the dense array. The results are shown in Fig. 6.5. In this figure, each row represents an ensemble at a certain plasma current and Greenwald density fraction (i.e. Lundquist number). As you move down the rows, the Lundquist number of a given ensemble increases. The columns show results from two different $\dot{b}$-coils in MST. For this set of ensembles the transition is observed at approximately $I_p = 100$ kA and $n_e/n_G = 0.34$, such that the first two rows in the figure represent the quasi-continuous cases and the last three rows represent ensembles that exhibit increasingly bursty behavior. No significant difference in the features of the spectra are observed between the quasi-continuous and bursty cases. However, during the transition between the two cases, at $I_p = 100$ kA, $n_e/n_G = 0.34$, we see that the peak normally located at $\sim$ 10 kHz, downshifts in frequency. This frequency value indicates that the feature may correspond to the tearing mode phase velocity. It would follow, therefore, that the tearing mode phase velocity slows at Lundquist numbers in the boundary region between quasi-continuous and bursty regions.

6.2.2 Laplace-Type Analysis

A Laplace-type transform was also applied to the data. This can be done, in particular, to look for the appearance of self-similarity, or lack of it, in fluctuations at various temporal and spatial scales. A quantity, x, is self-similar in time if distributions of the function $\delta_\tau x = x(t+\tau) - x(t)$ collapse to a single distribution. In phenomonological Kolmogorov theory, for example, these functions collapse to Gaussian distributions, indicating the randomness of the turbulent interactions [2, 4].

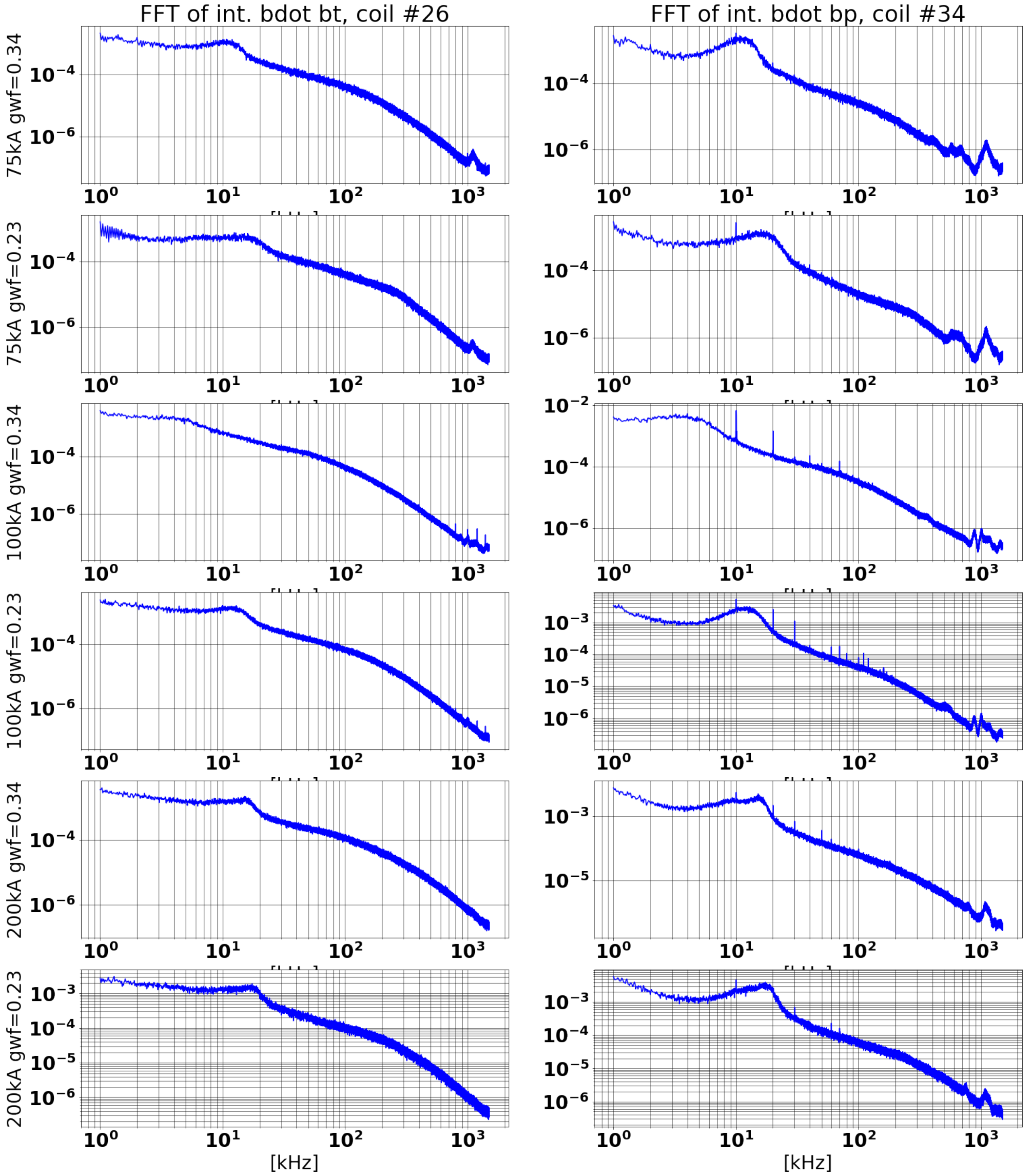

FIGURE 6.5: Fast Fourier transforms of integrated b-dot signals. The left column represents signals from the toroidal coil of coil set number 26 and the right column represents signals from the poloidal coil of coil set 34.

Applying this concept to the data gathered here, for a range of time delays, τ, the time delay function, S_τ, was calculated. This equation was defined as,

$$S_\tau = \delta_\tau \dot{b} = \dot{b}_\phi(t) - \dot{b}_\phi(t+\tau), \tag{6.1}$$

where once again we are looking at the b-dot time derivative of the magnetics signal with $\dot{b}_\phi = \dot{B}/\sigma_B$ representing the time derivative of the magnetic amplitude with unit variance and zero mean. Then probability distribution functions, or PDFS, were created from each of these signal difference functions by binning the amplitudes of the function. These distributions were then fit to the following function,

$$F(\delta b) = Ke^{-b|\delta b|^\alpha}, \tag{6.2}$$

where K, α, and b are fit parameters. This process follows that outlined by Marelli et. al in their work looking at the difference between standard and enhanced confinement plasmas [2]. As we will see below, the results from Marrelli were replicated for standard plasmas to benchmark this process. However, we also used this procedure to try to tease out other features in addition to assessing the self-similarity of the plasmas. In particular, the procedure was modified to fit the shoulder and wings of the distribution. After looking at S functions for synthetic data, it was observed that for specific τ values that line up with reconnection activity periods, this is where in the distribution the most significant change can be found.

Fig. 6.6 shows example plots for each step of the process outlined above for a single shot. The top plot shows the signal being analyzed for an example shot. The middle plot shows the time delay function for this plot for an example τ. The bottom plot shows the

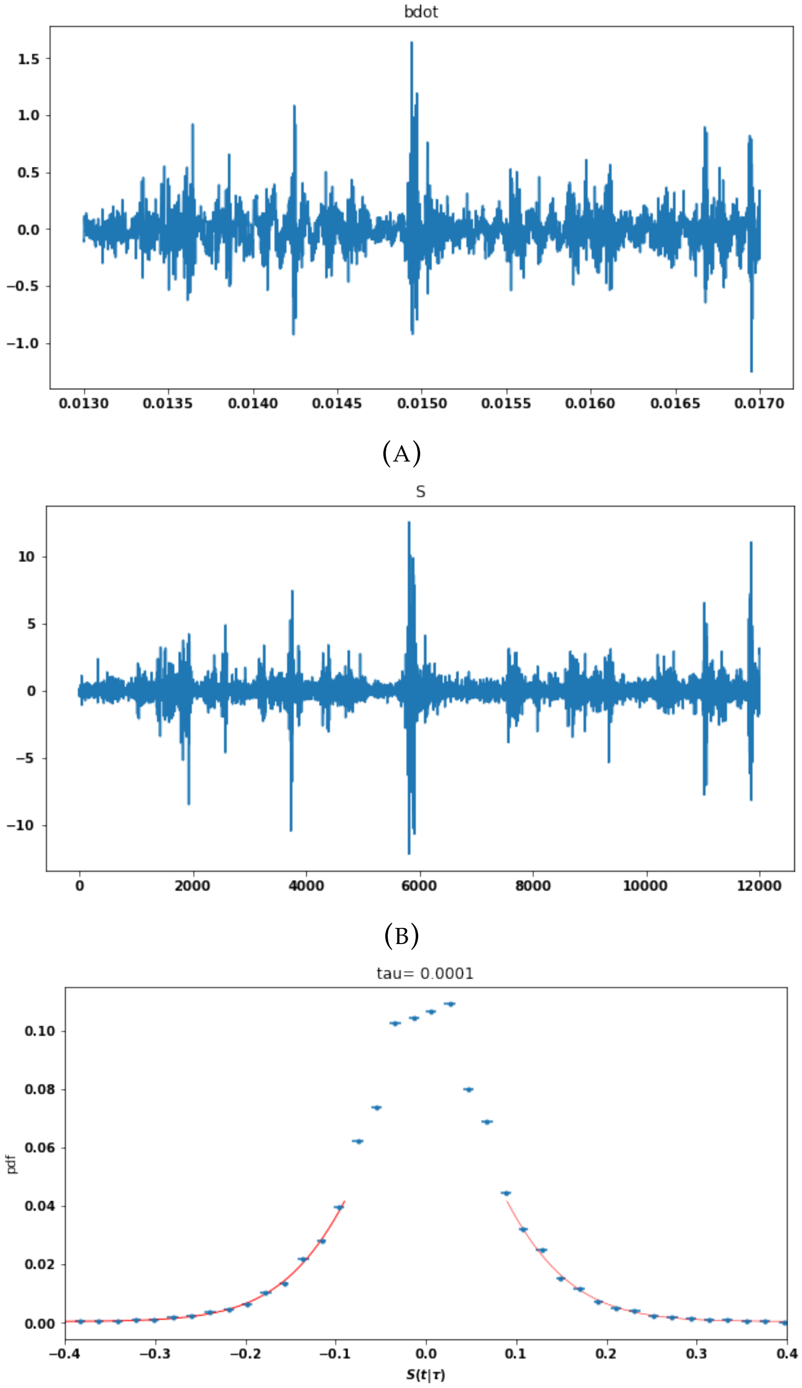

(A)

(B)

(C)

FIGURE 6.6: This series of figures show an example of the process outlined to analyze the time delay of the signal. This process is modeled off of that described by Marrelli et. al [2].

result of binning the amplitude of S to generate a PDF. The wings of this PDF were then fit to Eqn. 6.2.

Synthetic Data and Benchmarking Results

Again, these analyses follow a process laid out by Marrelli et. al, who looked at this intermittancy behavior in MST [2]. In this section, the results of benchmarking the data here to the results presented by Marrelli et. al are shown. Fig. 6.7 compares the results obtained using the data gathered for this work and the results presented by Marrelli et. al. Fig. 6.7a shows a comparison between PDFs generated at $\tau = 0.3$ μs and $\tau = 171$ μs. The top row show the results from Marrelli and the bottom row shows the benchmarked results. The α values from the fit match relatively well and the shapes of the distributions appear qualitatively consistent. Fig. 6.7b shows the α values for fitting various S_τ distributions, varying τ. Once again the top row replicates a figure from Marrelli and the bottom row presents the benchmarked result. In the Marrelli figure the black diamonds correspond to standard plasmas. We see that because they do not collapse to a single α value, it does not follow that the turbulence in MST standard plasmas is self-similar in nature. This result is replicated by the benchmarked data as well. The red and blue data represent different halves of the distribution for positive or negative S amplitudes. In the following sections, we combine these data we performing these fits. The benchmarked results replicate the conclusion drawn by Marrelli et. al.

Results Comparing Quasi-Continuous and Bursty Cases

This analysis technique was applied to ensembles of plasmas displaying quasi-continuous, boundary and bursty reconnection activity. Self-similarity was not observed in any of

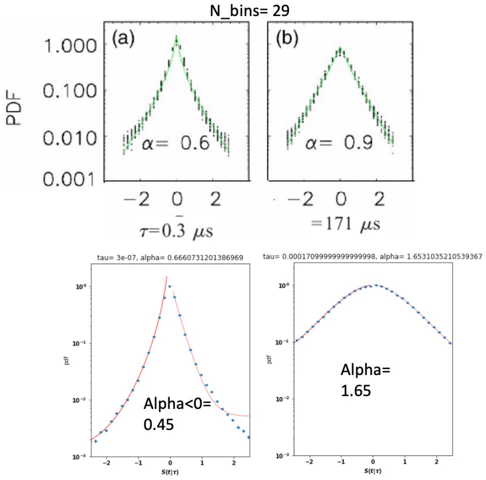

(A)

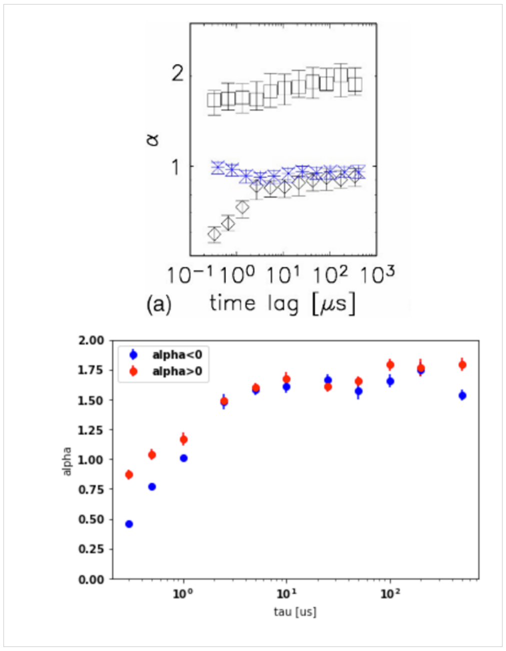

(B)

FIGURE 6.7: Comparing self-similarity analysis of S-scaling data with those found by Marrelli et. al [2]. In both (A) and (B) The top row shows the results from Marrelli et. al and the bottom row shows the benchmarked data. The results agree relatively well and are qualitatively consistent. In (B) the relevant Marrelli results that represent standard MST plasmas are plotted with the black diamond symbols.

these cases. However, looking at longer times scales of τ, and focusing the fitting to the shoulder and wings of the distributions, it was hoped that some other frequency difference could be picked out of the data to distinguish any difference between the cases. The results of these analyses are shown in Fig. 6.8. The left column shows the α parameter results from fitting the distribution while varying τ, the middle column shows the b parameter results from fitting the distribution and the right column shows an example V_{tg} signal from the ensemble as a reference for the reconnection behavior displayed. Each row represents an ensemble of data. The top row would be characterized as exhibiting quasi-continuous reconnection activity, the second row would be a boundary case and the bottom two rows are ensembles of bursty plasmas.

A small oscillation in the α values at low τ is observed in lowest three Lundquist number ensembles. These align with the period of the moderately sized reconnection events. Bursty reconnection events are narrower in time, and therefore it is to be expected that they would be more difficult to visualize with this time-difference technique. An interesting bifurcation of the α values appears for the boundary ensemble in the second row, indicating that moderately large reconnection activity is starting to appear. These events last longer than more bursty reconnection events but as the events become more bursty, they also occur more quickly so that the bifurcation disappears as Lundquist number continues to increase.

6.3 Conclusions and Future Directions

While conducting the Lundquist number scaling study at the low Lundquist number range, the upgraded PPS system was used to access lower Lundquist number shots than

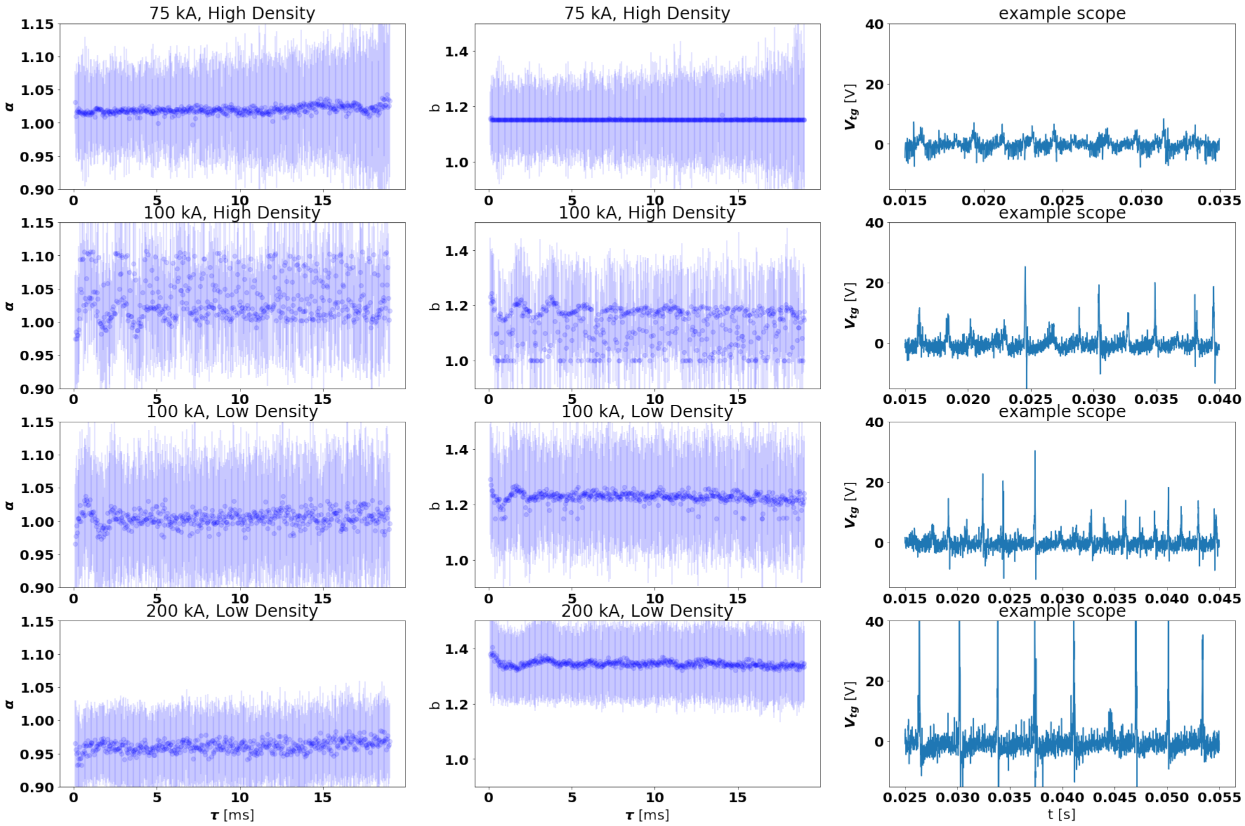

FIGURE 6.8: This figure shows a summary of the results from applying the signal difference analysis below, at and above the threshold between quasi-continuous and discrete magnetic reconnection activity.

had been previously possible to generate on the MST. While probing this space for the first time, a distinct type of reconnection activity was observed. The boundary between bursty and quasi-continuous reconnection behavior was found to be at approximately at Lundquist number, $S = 10^5$. At this boundary, distinct dynamics appear to be at play. Fast Fourier transforms of ensembles in this range show a feature that likely corresponds to the phase velocity slowing only in the boundary region. Additionally, fits of PDFs the time delay distributions in this boundary region show a larger degree to which the plasma is not self-similar relative to either bursty or quasi-continuous plasmas. This is still largely an open question but the database generated during this study will provide a great resource for any future investigations into this topic.

Bibliography

[1] C. Sovinec, "Magnetohydrodynamic simulations of noninducitve helicity injection in the reversed-field pinch and tokamak," Ph.D. dissertation, University of Wisconsin at Madison, 1995.

[2] L. Marrelli, L. Frassinetti, P. Martin, D. Craig, and J. S. Sarff, "Reduced intermittency in the magnetic turbulence of reversed field pinch plasmas," *Physics of Plasmas*, vol. 12, no. 3, p. 030701, 2005. [Online]. Available: https://doi.org/10.1063/1.1850475

[3] V. Antoni, V. Carbone, R. Cavazzana, G. Regnoli, N. Vianello, E. Spada, L. Fattorini, E. Martines, G. Serianni, M. Spolaore, L. Tramontin, and P. Veltri, "Transport processes in reversed-field-pinch plasmas: Inconsistency with the self-organized-criticality paradigm," *Phys. Rev. Lett.*, vol. 87, p. 045001, Jul 2001. [Online]. Available: https://link.aps.org/doi/10.1103/PhysRevLett.87.045001

[4] A. Kolmogorov, "The local structure of turbulence in incompressible viscous fluid for very large reynolds numbers," *Proceedings of the Royal Society A*, vol. 434, pp. 9–13, 1991. [Online]. Available: https://doi.org/10.1098/rspa.1991.0075

Chapter 7

Conclusion

7.1 Summary

A large cache of data across the range of Lundquist numbers accessible to MST was produced. These data were ensembled at points across this expanse to obtain a relationship for how the magnetic field fluctuation amplitudes measured at the edge of MST scaled with Lundquist number. A summary of these results is below in the replicated Fig. 7.1.

In the scaling fit results, we observe stronger scaling for the higher density scenario. The $n = 6$ modes exhibits unique behavior where its magnetic field fluctuation amplitudes seem to level off and not vary strongly with Lundquist number. This effect is less obvious in the high density case but may still be present when considering extenuating factors of the data collection constraints. For a chunk of modes $n = 7, 8, 9, 10$ we see highly favorable scaling terms, implying that should we extrapolate conditions to reactor-relevant scales, we have reason to suspect that stochastic transport would cease to be a dominant transport mechanism for the RFP. This suspicion is further supported by the estimation for $\chi_{RR}(r)$, which estimates that stochasticity will be low enough to be the dominant loss mechanism. In all, having an average $\alpha_{n,gwf=0.34} \sim 0.38$ for the core most modes is a very encouraging result for the RFP magnetic confinement fusion concept, especially given that a reactor will be more interested in high density cases to optimize the fusion triple product.

There are a few caveats to these estimations. The ensembling averaged over the flattop of the plasma discharges, ignoring that the sawtoothing behavior varied with Lundquist number. Taking into account the transition from quasi-continuous the bursty reconnection activity that occurs as Lundquist number is increased from below $S \sim 10^5$ to above that threshold, the activity goes from being low magnitude but persistent to having long periods of quiescent plasmas with large, intermittent bursts of activity. This could mean that as an experiment is scaled to higher Lundquist numbers, these transport is concentrated during these large reconnection events and is sufficiently large during these times that stochasticity still continues to be a significant transport mechanism. These analyses did not do a sawtooth based analysis.

Some preliminary analyses were also done to compare these data to simulations performed in DEBS and NIMROD. These data have a large range of Lundquist number value overlap with simulated data. Metrics indicate that both α_n and c_n values align well between the experimental results in the constant Greenwald fraction framework and the preliminary simulations. This is somewhat expected given that the choice of parameters used to determine Lundquist number was chosen for experimental convenience as opposed to being selected for easy comparisons with simulation results. In general, simulations and choice of experimental parameter definitions could be iterated upon to better match each other. A more thorough and extensive validation effort using these experimental data would be a future project of great interest.

Extrapolating results to high Lundquist number values argues for the promise of expanding the RFP fusion research program to larger scales. When looking at the magnetic field fluctuation amplitude and electron thermal diffusion extrapolations, we see these quantities that are most closely tied to direct measurements are expected to scale very favorably at $S_{reactor} \sim 10^9 - 10^{10}$.

Finally, τ_E did not scale with density as is predicted by the stochastic diffusion model, however, the current scaling dependence matched closely with what is expected from the stochastic model, with $\tau_E \sim I_p^{2/3}$ assuming $\alpha \sim 0.333$. This indicates that there may be physics at play that is not captured by the stochastic model.

A large database of data were created that will be accessible for future use. Perhaps the most valuable of which is the set of Thomson temperature profiles given that the diagnostic will be difficult to use without more personnel devoted to its upkeep.

A transition from quasi-continuous to discrete reconnection activity was observed at $S \sim 10^5$ for a variety of plasma currents. During this transition, but not below or above it, a feature in the FFTs of the magnetics slows. This feature most likely corresponds to the phase velocity.

7.2 Future Directions

This project could have been taken in many directions and many interesting avenues of exploration were not pursued. Namely, now that data directly overlaps in Lundquist number space with computational codes, a more thorough validation effort would be interesting and valuable in our understanding of the physics of the RFP. The Lundquist number definition as used herein could be changed to provide a better comparison with

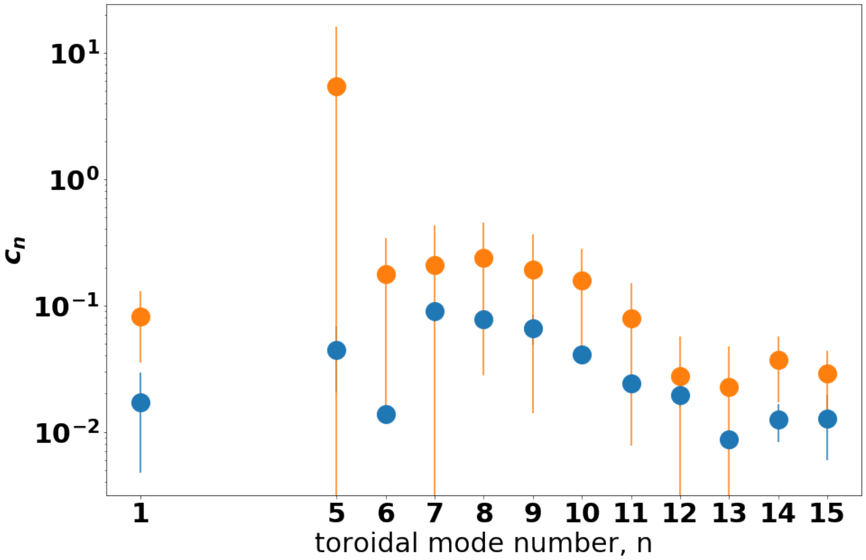

(A)

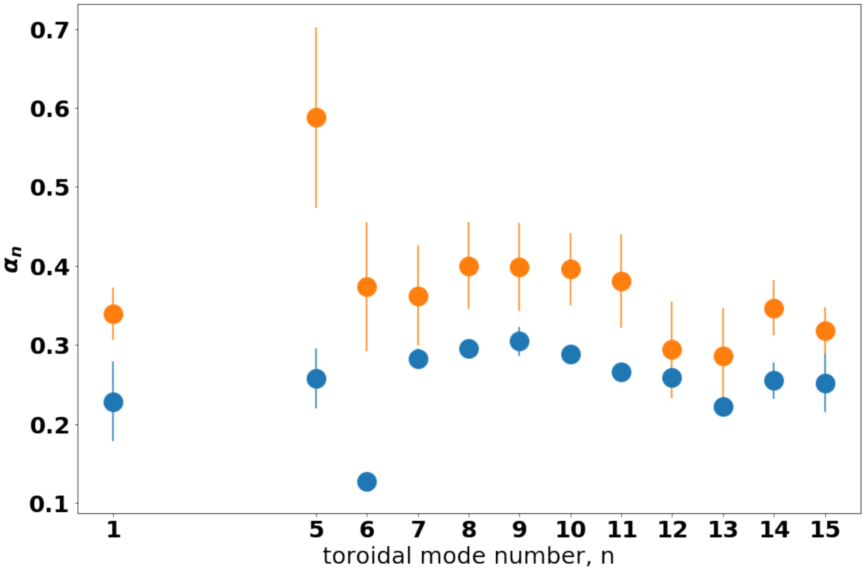

(B)

FIGURE 7.1: This set of figures summarizes the results of fitting the magnetic field fluctuation amplitude scaling data to Eqn. 5.21. The top figure shows the results of the coefficient of the scaling fit on a semilog plot against the toroidal number. The bottom figure shows the scaling parameter, α, on a linear plot against the toroidal mode number. In keeping with the convention of all data presented herein, the low density Greenwald fraction data is shown in blue while the high density Greenwald fraction data is shown in orange.

simulation. Additionally, simulations that incorporate two fluid effects and performed with an eye of more closely matching the experimental data collection framework would provide a better basis for comparison.

The change in sawtooth activity with Lundquist number was largely ignored with this scaling. However, given the possibility that transport is concentrated during the large, bursty reconnection event at higher Lundquist numbers, it would be worth considering how magnetic field fluctuations scale during different times through out the sawtooth period as compared to the quiescent period of the flattop. Josh Reusch performed ensembling to detail the electron temperature behavior over the sawtooth period in his thesis [1]. Jeff Becksted also performed a detailed analysis of the sawtooth scaling of the sawtooth activity characteristics in his thesis and Stoneking briefly covers sawtooth period scaling in his Lundquist number scaling studies [2, 3]. These data could be used to investigate the scaling during and away from sawtoothing, at least for higher Lundquist number cases. Additionally, the database contains information about when sawteeth occur for many of the higher Lundquist number shots collected for this project.

The energy confinement times did not scale as expected according to stochastic theory with regard to the electron density (or, equivalently, the Greenwald fraction) and with an exponential scaling parameter obtained by this study. This implies that there is some physics missing in the understanding of this quantity.

Finally, the transition from quasi-continuous to discrete reconnection is mostly an open question still. Contributions from theorists to direct the effort for understanding that phenomenon would be a good next step to better understanding the underlying physics.

Bibliography

[1] J. Reusch, "Measured and simulated electron thermal transport in the madison symmetric torus reversed field pinch," Ph.D. dissertation, University of Wisconsin at Madison, 2011.

[2] J. Becksted, "Sawteeth in the mst reversed field pinch," Ph.D. dissertation, University of Wisconsin at Madison, 1990.

[3] M. R. Stoneking, J. T. Chapman, D. J. Den Hartog, S. C. Prager, and J. S. Sarff, "Experimental scaling of fluctuations and confinement with lundquist number in the reversed-field pinch," *Physics of Plasmas*, vol. 5, no. 4, pp. 1004–1014, 1998. [Online]. Available: https://doi.org/10.1063/1.872670

Appendix A

Lundquist Number Scaling Database

One of the major outcomes of this study was a database spanning a wide range of Lundquist numbers of well diagnosed plasma shots often including data from soft x-ray tomography, Thomson scattering, FIR, magnetic field coils, Ross Filter, CHERS, and the multi-energy xray diagnostic. At a minimum, each shot includes high quality Thomson, magnetics, and FIR data. Before this study, FIR measurements were not included by default and instead a less reliable CO_2 interferometer was used to measure the density.

The goal of this appendix is to refer future users to resources that were created to help navigate the database and as well as to files that include shot lists. These resources can be found in the author′s dave directory (″skubala″) in the subdirectory called ″Lundquist number scaling database″. At the onset of this project, efforts were made to organize and ″clean″ the data that, though ultimately not used for the data analysis performed herein, is still included in the directory. These efforts included as noting sawtooth times for the relatively high Lundquist number shots. Basic lists of MST shot numbers used for the analyses performed herein are also included in text files located in that directory. There is also a spreadsheet that summarizes all the run days that were used to generate the data, such as which diagnostics were used, the purpose of the run day, the desired currents and densities, and a few other notes. These data can also be found in the MST logbook but the spreadsheet summarizes the logbook input so that these data can be easily parsed.

Additionally, template Jupyter notebooks for Python 3.6 are included that allow one to use the functions to visualize the data in the ensemble. Jupyter notebooks are also stored there for looking at magnetics data, Thomson data, and CHERs data. The MST Thomson Scattering wiki includes a page called ”How to ensemble/sum low temperature, density Thomson data” that summarizes the workflow that the author employed when using these notebooks. As was mentioned in the Thomson section, the Thomson ensembling technique can be performed using the Jupyter notebook template on ”tsfit” according to the instructions on this page as well.

I do not claim that all the code included is the most elegant, and I would obviously make some changes to the structure now that I have more experience working with the database. However, the time spent creating these shot lists and parsing these data should still save any future users a lot of time. The text files can be easily read by most programming languages should Python 3.6 and/or Jupyter notebook become antiquated.

Appendix B

RESTER Plots for Standard Plasmas

Included here for future reference are the RESTER plots that were used to estimate $\tilde{b}_r$, given $\tilde{b}_n(r = a)$, which in turn was used to estimate island width scaling (see Ch. 5). They were generated by John Sarff based on Standard, $\beta = 0$, F=-0.2 RFP plasmas in MST. RESTER is a numerical tool for calculating stability of cylindrical force-free profiles. First, are plots that summarize the results of the RESTER plots. These were also generated by John Sarff.

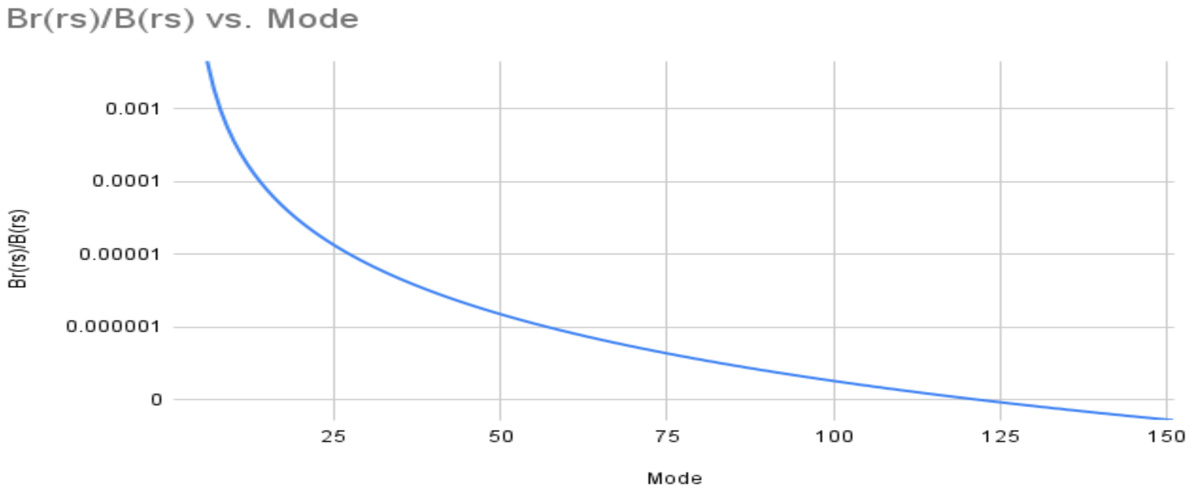
Br(rs)/B(rs) vs. Mode
Br(rs)/B(rs)
0.001
0.0001
0.00001
0.000001
0
25
50
75
100
125
150
Mode

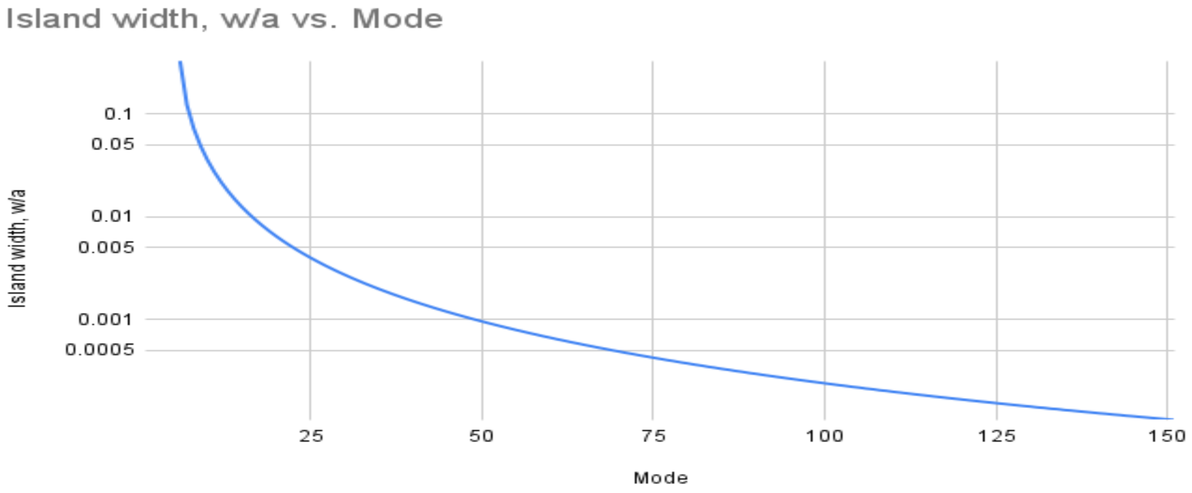
Island width, w/a vs. Mode
Island width, w/a
0.1
0.05
0.01
0.005
0.001
0.0005
25
50
75
100
125
150
Mode

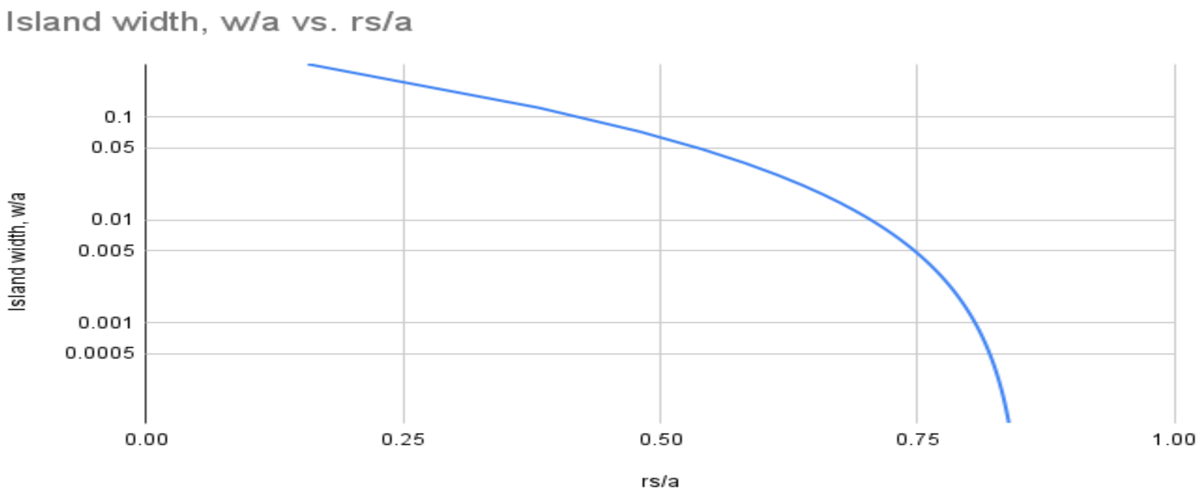
Island width, w/a vs. rs/a
Island width, w/a
0.1
0.05
0.01
0.005
0.001
0.0005
0.00
0.25
0.50
0.75
1.00
rs/a

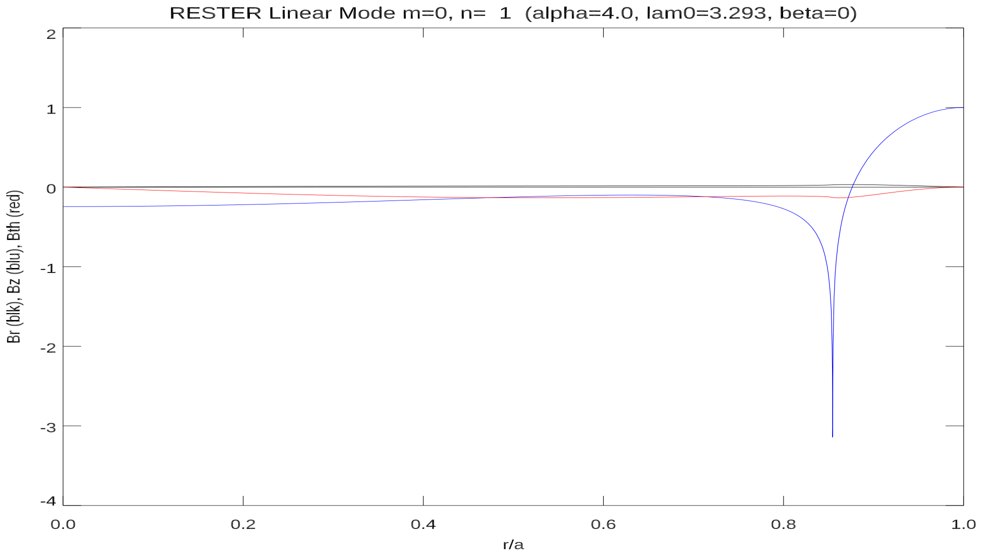
RESTER Linear Mode m=0, n= 1 (alpha=4.0, lam0=3.293, beta=0)
Br (blk), Bz (blu), Bth (red)
2
1
0
-1
-2
-3
-4
0.0
0.2
0.4
0.6
0.8
1.0
r/a

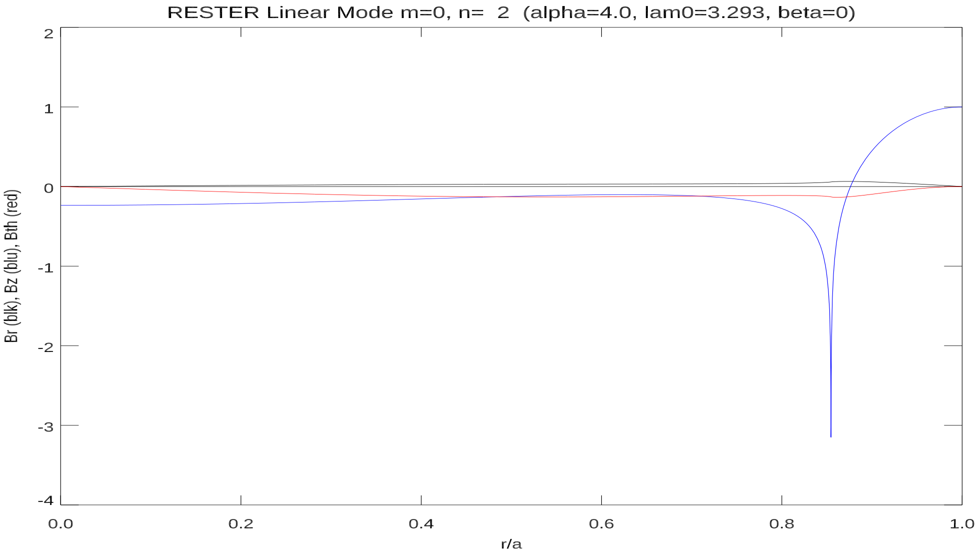
RESTER Linear Mode m=0, n= 2 (alpha=4.0, lam0=3.293, beta=0)
Br (blk), Bz (blu), Bth (red)
2
1
0
-1
-2
-3
-4
0.0
0.2
0.4
0.6
0.8
1.0
r/a

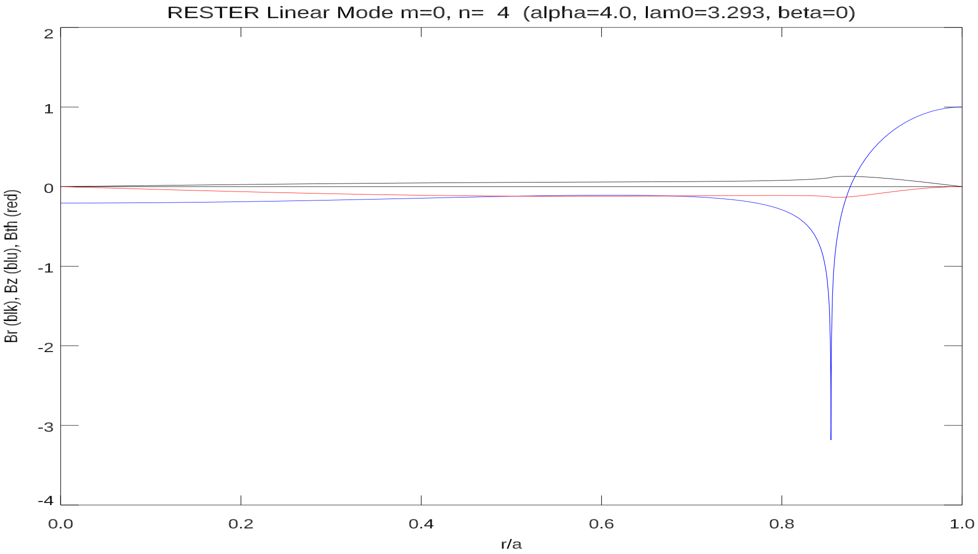
RESTER Linear Mode m=0, n= 4 (alpha=4.0, lam0=3.293, beta=0)
Br (blk), Bz (blu), Bth (red)
2
1
0
-1
-2
-3
-4
0.0
0.2
0.4
0.6
0.8
1.0
r/a

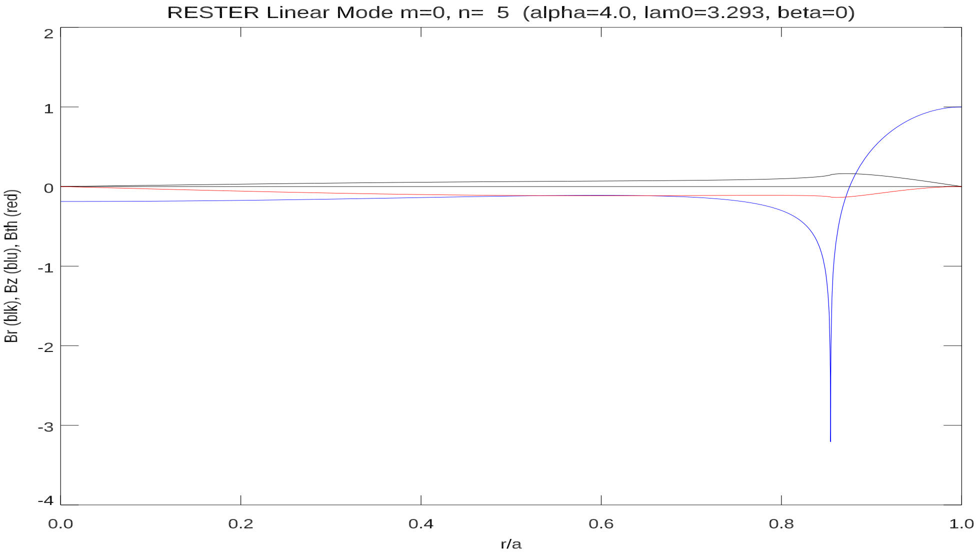
RESTER Linear Mode m=0, n= 5 (alpha=4.0, lam0=3.293, beta=0)
Br (blk), Bz (blu), Bth (red)
r/a
2
1
0
-1
-2
-3
-4
0.0
0.2
0.4
0.6
0.8
1.0

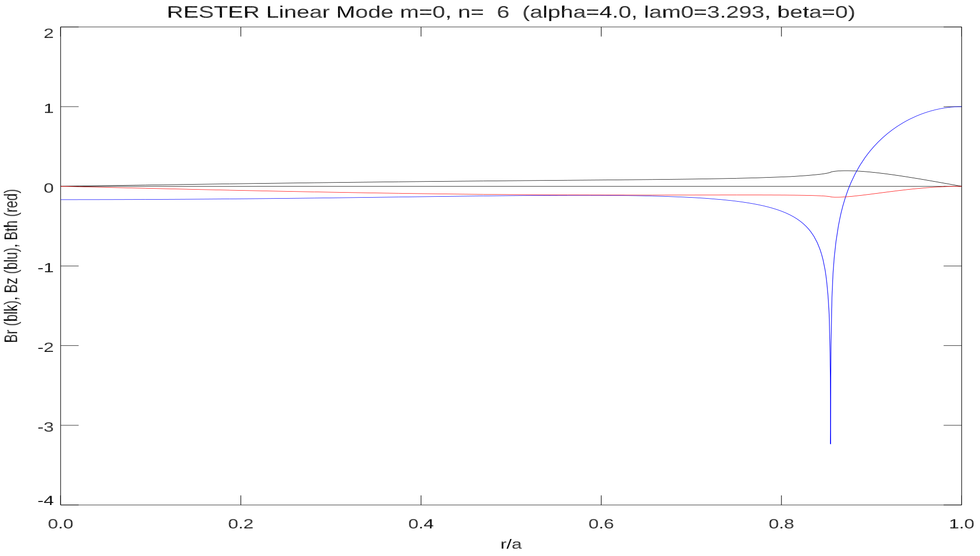
RESTER Linear Mode m=0, n= 6 (alpha=4.0, lam0=3.293, beta=0)
Br (blk), Bz (blu), Bth (red)
r/a
2
1
0
-1
-2
-3
-4
0.0
0.2
0.4
0.6
0.8
1.0

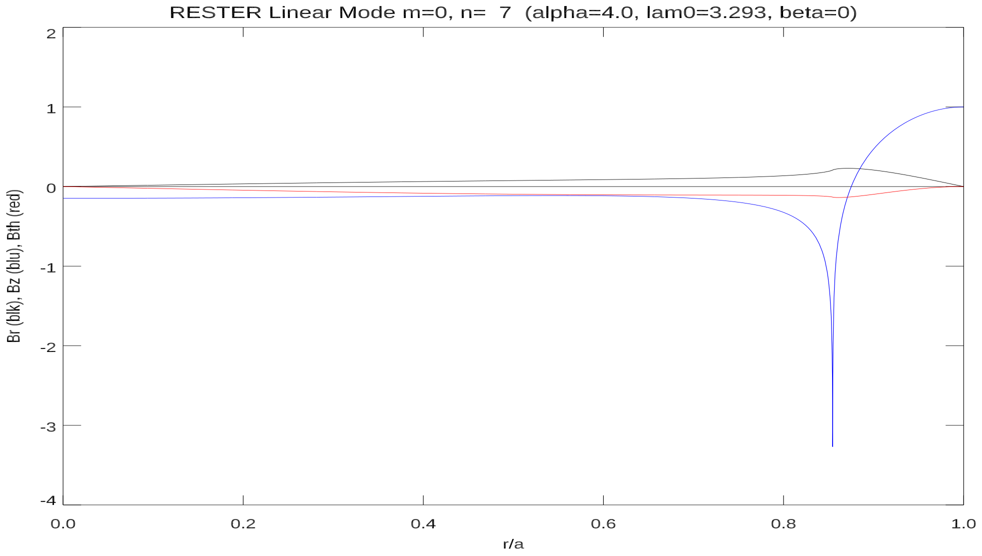
RESTER Linear Mode m=0, n= 7 (alpha=4.0, lam0=3.293, beta=0)
Br (blk), Bz (blu), Bth (red)
2
1
0
-1
-2
-3
-4
0.0
0.2
0.4
0.6
0.8
1.0
r/a

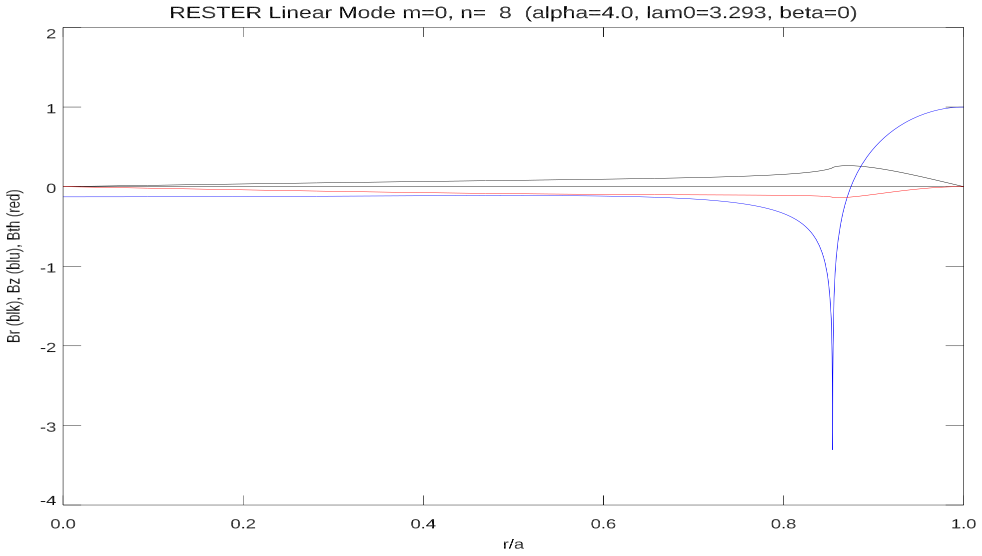
RESTER Linear Mode m=0, n= 8 (alpha=4.0, lam0=3.293, beta=0)
Br (blk), Bz (blu), Bth (red)
2
1
0
-1
-2
-3
-4
0.0
0.2
0.4
0.6
0.8
1.0
r/a

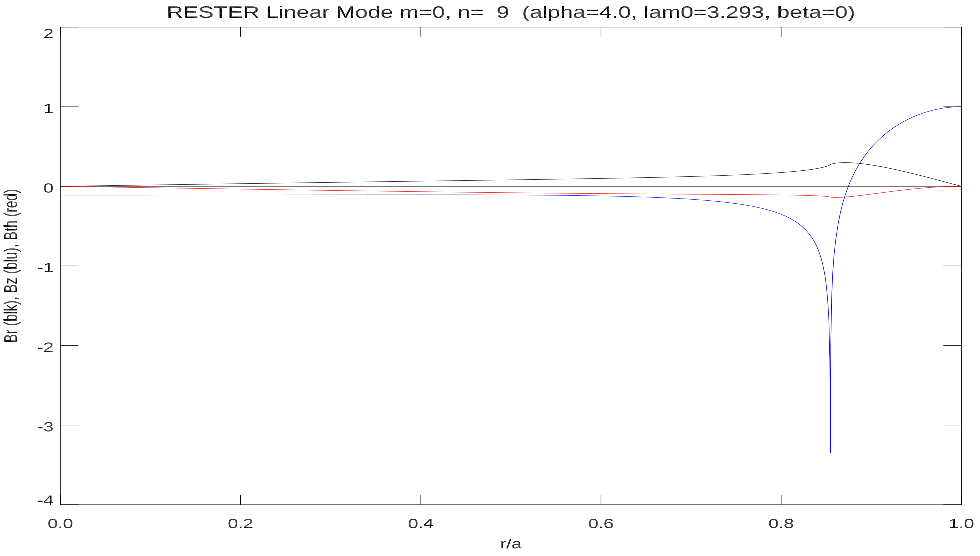
RESTER Linear Mode m=0, n= 9 (alpha=4.0, lam0=3.293, beta=0)
Br (blk), Bz (blu), Bth (red)
2
1
0
-1
-2
-3
-4
0.0
0.2
0.4
0.6
0.8
1.0
r/a

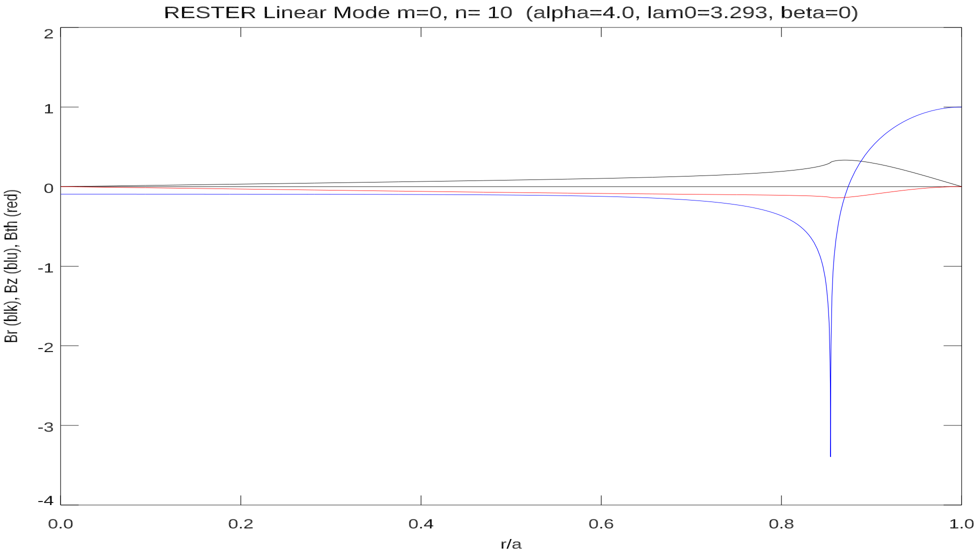
RESTER Linear Mode m=0, n= 10 (alpha=4.0, lam0=3.293, beta=0)
Br (blk), Bz (blu), Bth (red)
2
1
0
-1
-2
-3
-4
0.0
0.2
0.4
0.6
0.8
1.0
r/a

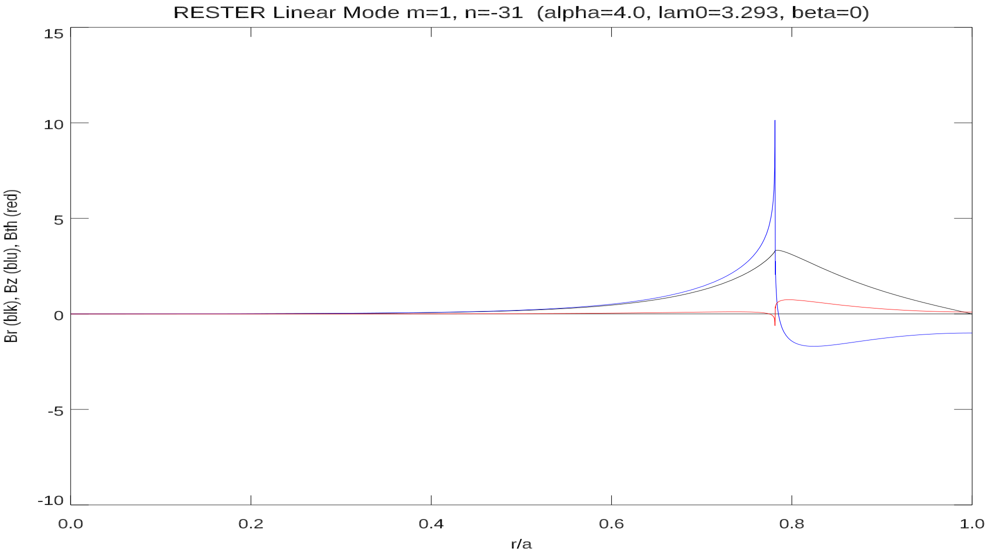
RESTER Linear Mode m=1, n=-31 (alpha=4.0, lam0=3.293, beta=0)
Br (blk), Bz (blu), Bth (red)
15
10
5
0
-5
-10
0.0
0.2
0.4
0.6
0.8
1.0
r/a

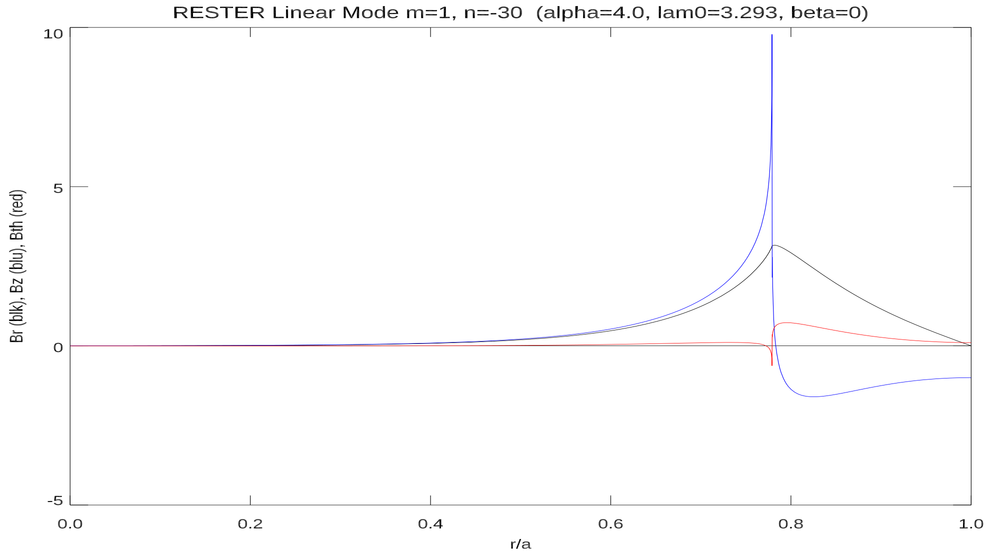
RESTER Linear Mode m=1, n=-30 (alpha=4.0, lam0=3.293, beta=0)
Br (blk), Bz (blu), Bth (red)
10
5
0
-5
0.0
0.2
0.4
0.6
0.8
1.0
r/a

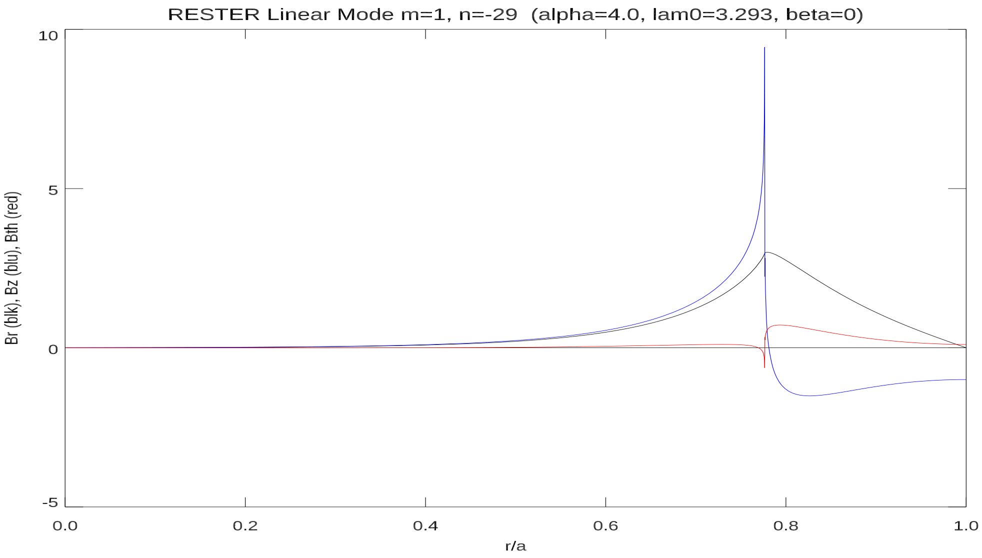
RESTER Linear Mode m=1, n=-29 (alpha=4.0, lam0=3.293, beta=0)
Br (blk), Bz (blu), Bth (red)
10
5
0
-5
0.0
0.2
0.4
0.6
0.8
1.0
r/a

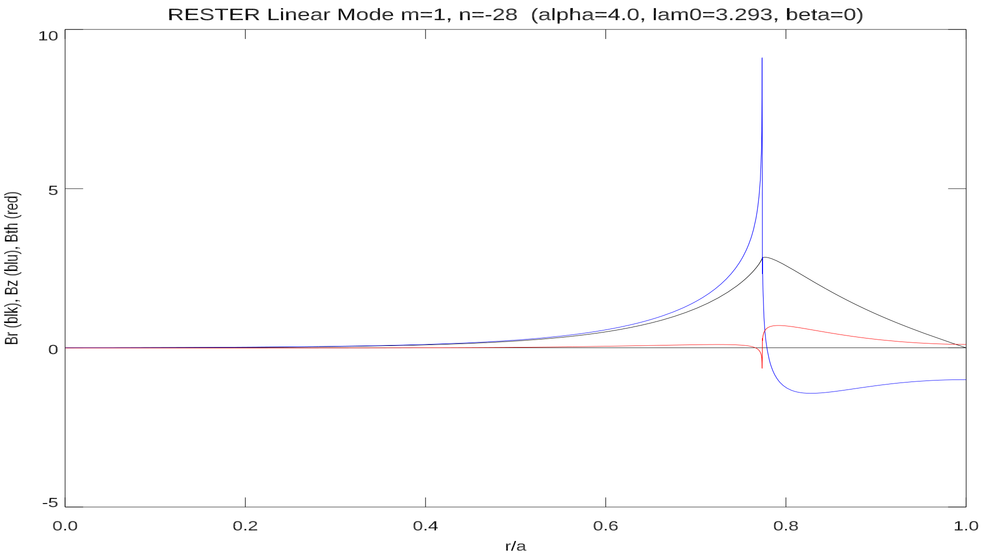
RESTER Linear Mode m=1, n=-28 (alpha=4.0, lam0=3.293, beta=0)
Br (blk), Bz (blu), Bth (red)
10
5
0
-5
0.0
0.2
0.4
0.6
0.8
1.0
r/a

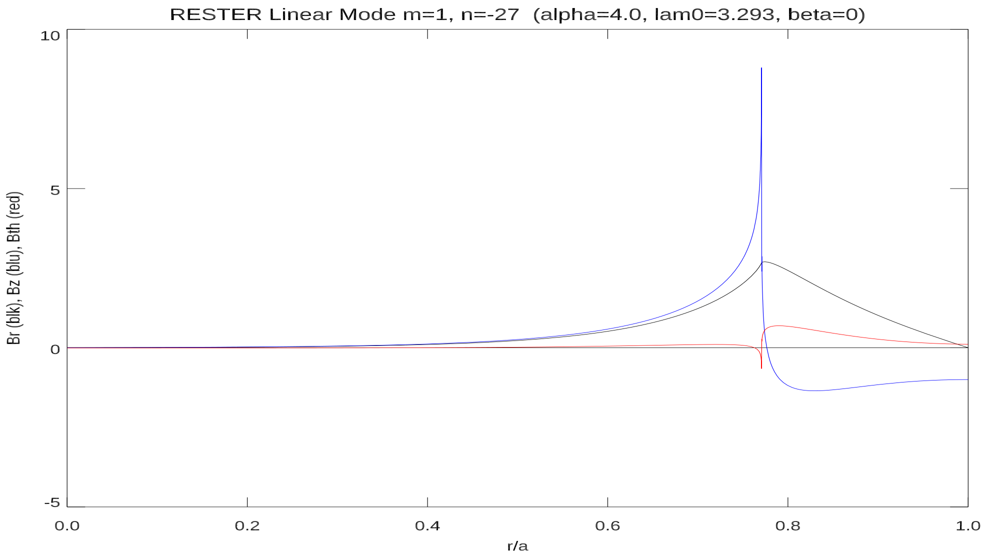
RESTER Linear Mode m=1, n=-27 (alpha=4.0, lam0=3.293, beta=0)

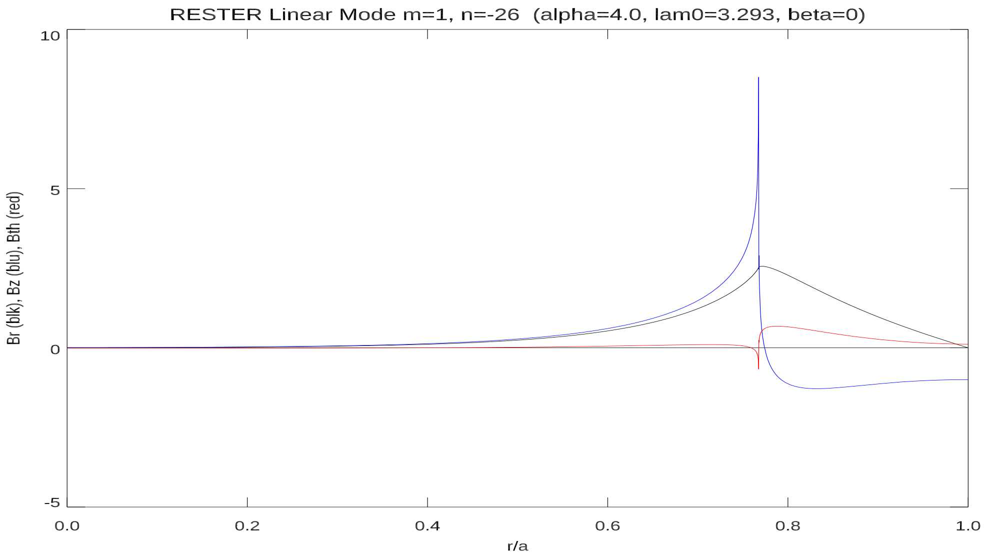
RESTER Linear Mode m=1, n=-26 (alpha=4.0, lam0=3.293, beta=0)

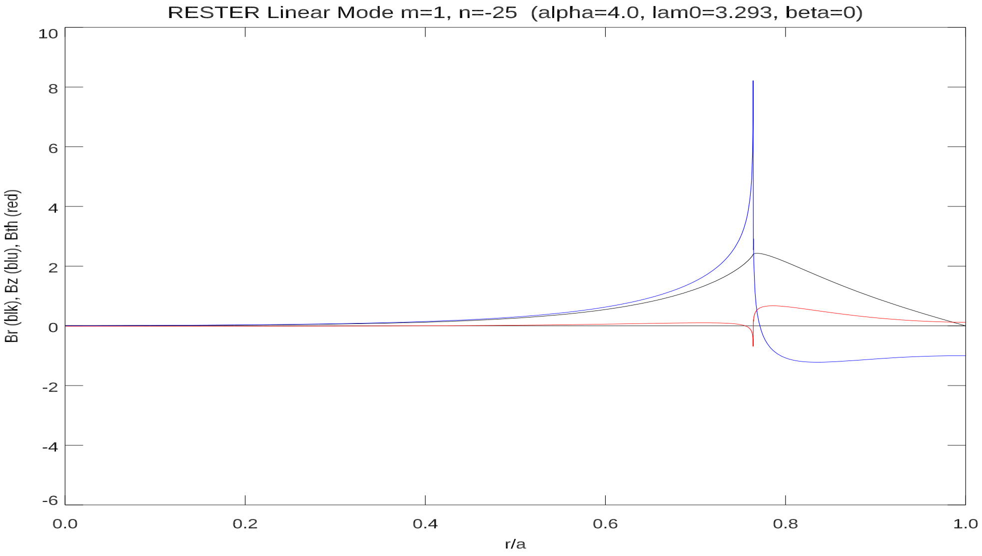
RESTER Linear Mode m=1, n=-25 (alpha=4.0, lam0=3.293, beta=0)
Br (blk), Bz (blu), Bth (red)
10
8
6
4
2
0
-2
-4
-6
0.0
0.2
0.4
0.6
0.8
1.0
r/a

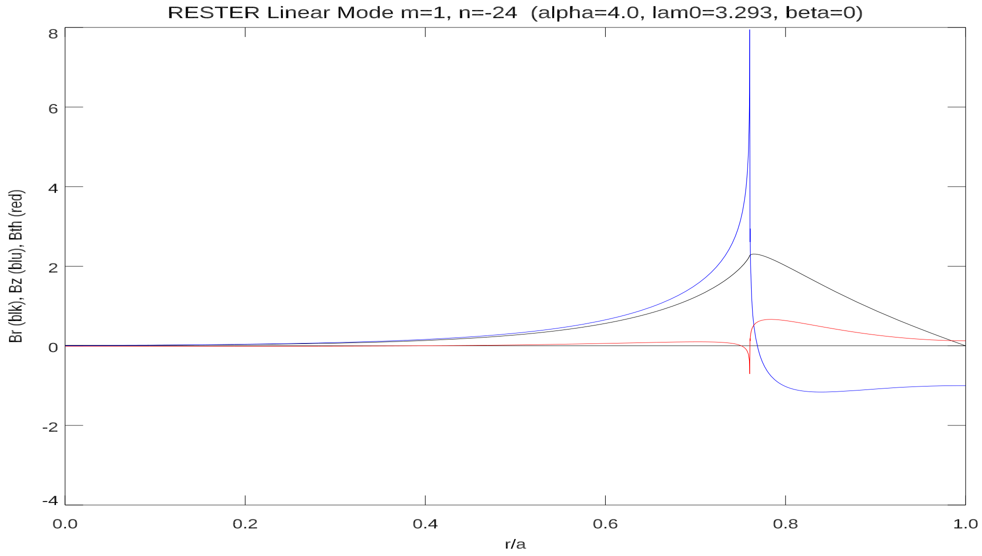
RESTER Linear Mode m=1, n=-24 (alpha=4.0, lam0=3.293, beta=0)
Br (blk), Bz (blu), Bth (red)
8
6
4
2
0
-2
-4
0.0
0.2
0.4
0.6
0.8
1.0
r/a

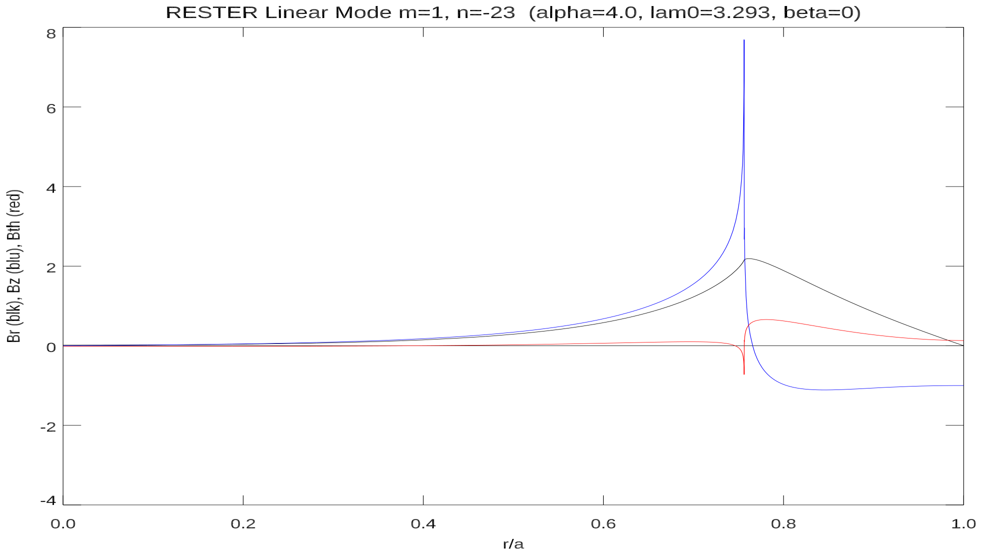
RESTER Linear Mode m=1, n=-23 (alpha=4.0, lam0=3.293, beta=0)
Br (blk), Bz (blu), Bth (red)
8
6
4
2
0
-2
-4
0.0
0.2
0.4
0.6
0.8
1.0
r/a

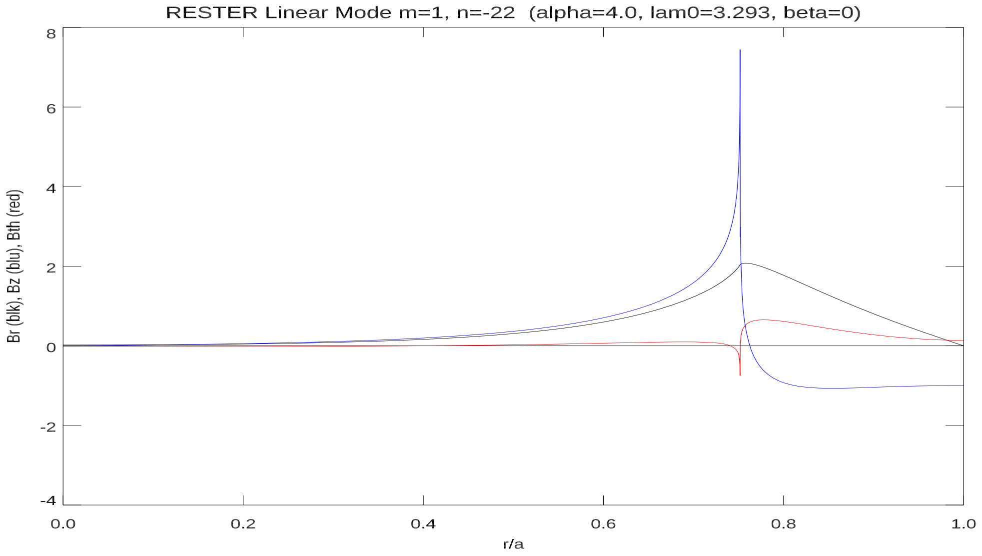
RESTER Linear Mode m=1, n=-22 (alpha=4.0, lam0=3.293, beta=0)
Br (blk), Bz (blu), Bth (red)
8
6
4
2
0
-2
-4
0.0
0.2
0.4
0.6
0.8
1.0
r/a

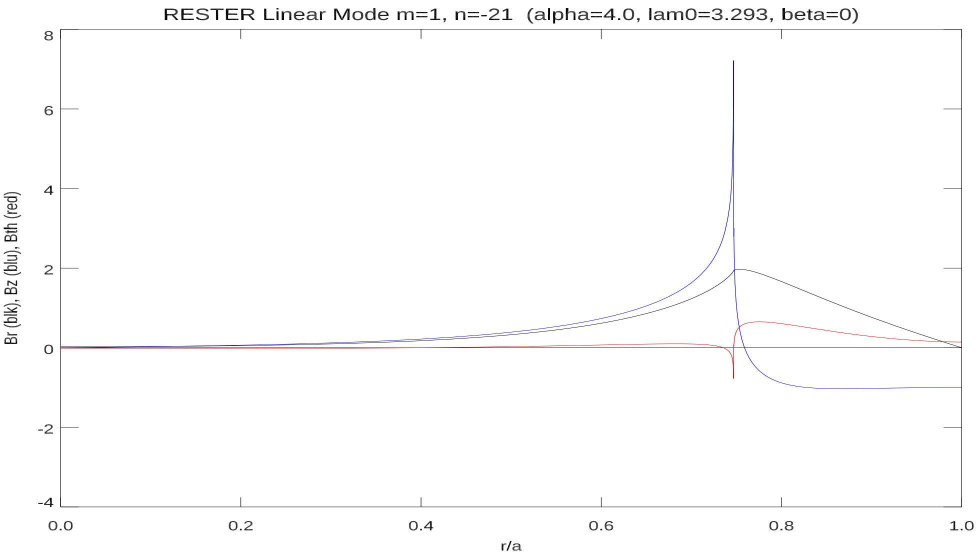

RESTER Linear Mode m=1, n=-21 (alpha=4.0, lam0=3.293, beta=0)
Br (blk), Bz (blu), Bth (red)
8
6
4
2
0
-2
-4
0.0
0.2
0.4
0.6
0.8
1.0
r/a

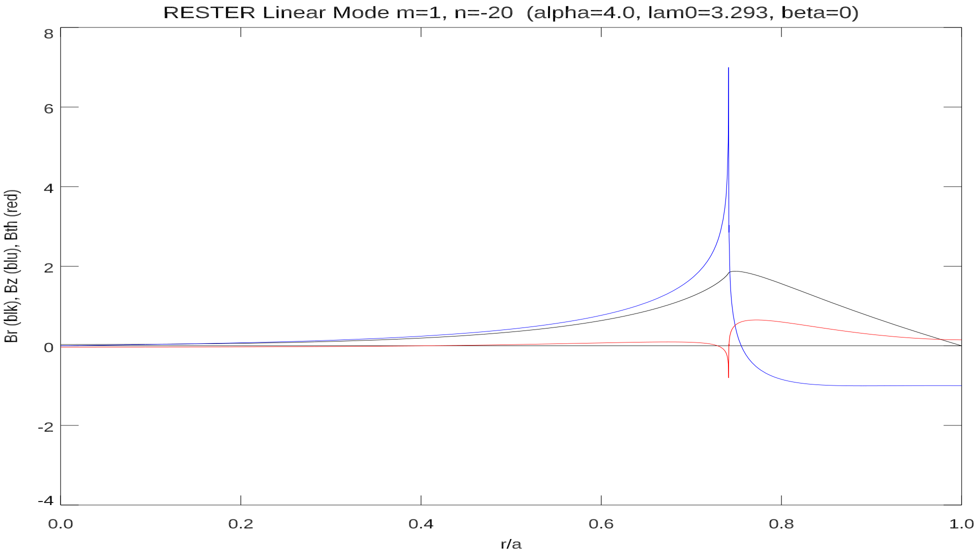

RESTER Linear Mode m=1, n=-20 (alpha=4.0, lam0=3.293, beta=0)
Br (blk), Bz (blu), Bth (red)
8
6
4
2
0
-2
-4
0.0
0.2
0.4
0.6
0.8
1.0
r/a

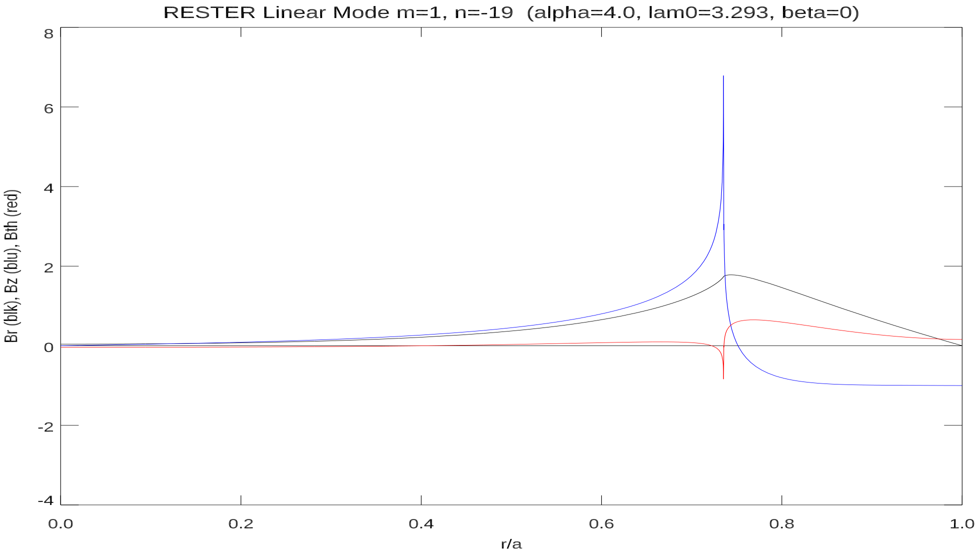
RESTER Linear Mode m=1, n=-19 (alpha=4.0, lam0=3.293, beta=0)
Br (blk), Bz (blu), Bth (red)
8
6
4
2
0
-2
-4
0.0
0.2
0.4
0.6
0.8
1.0
r/a

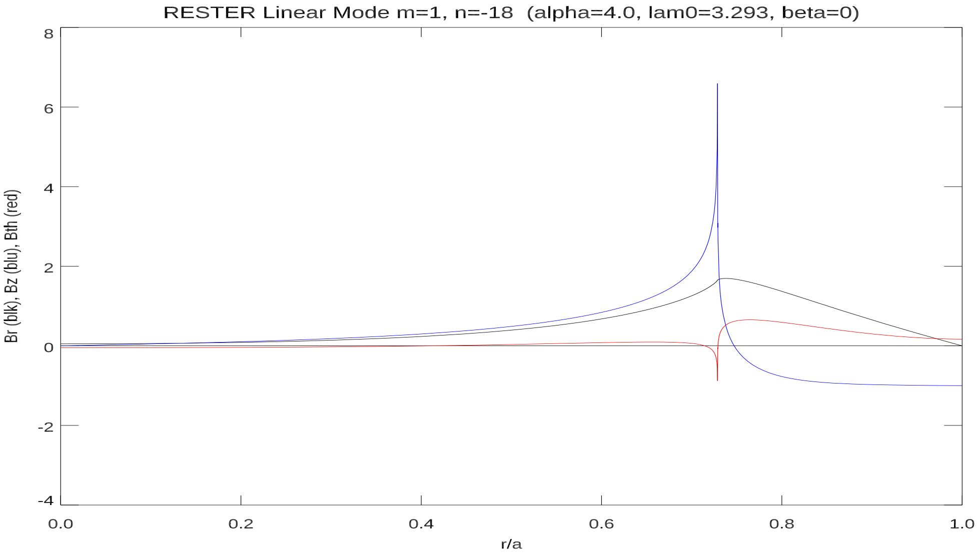
RESTER Linear Mode m=1, n=-18 (alpha=4.0, lam0=3.293, beta=0)
Br (blk), Bz (blu), Bth (red)
8
6
4
2
0
-2
-4
0.0
0.2
0.4
0.6
0.8
1.0
r/a

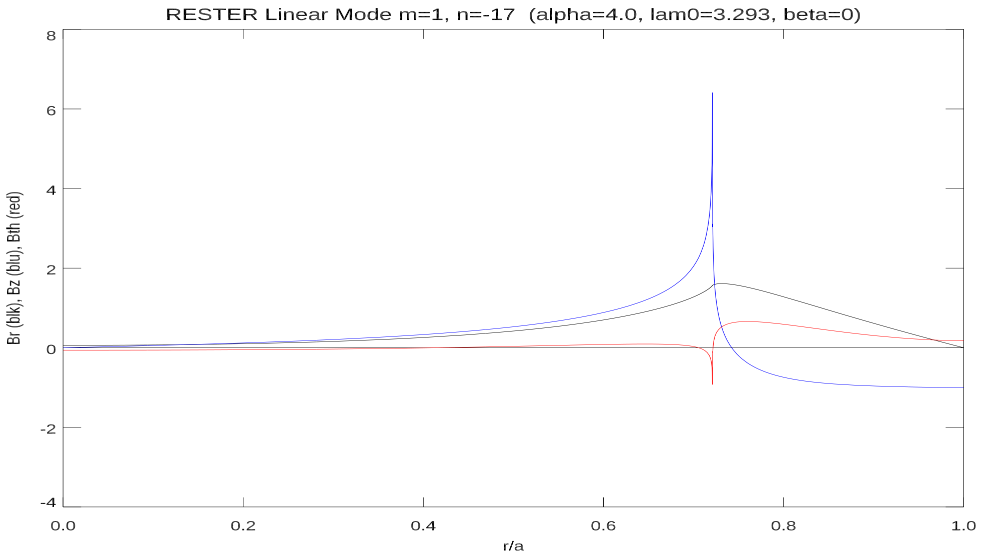
RESTER Linear Mode m=1, n=-17 (alpha=4.0, lam0=3.293, beta=0)
Br (blk), Bz (blu), Bth (red)
8
6
4
2
0
-2
-4
0.0
0.2
0.4
0.6
0.8
1.0
r/a

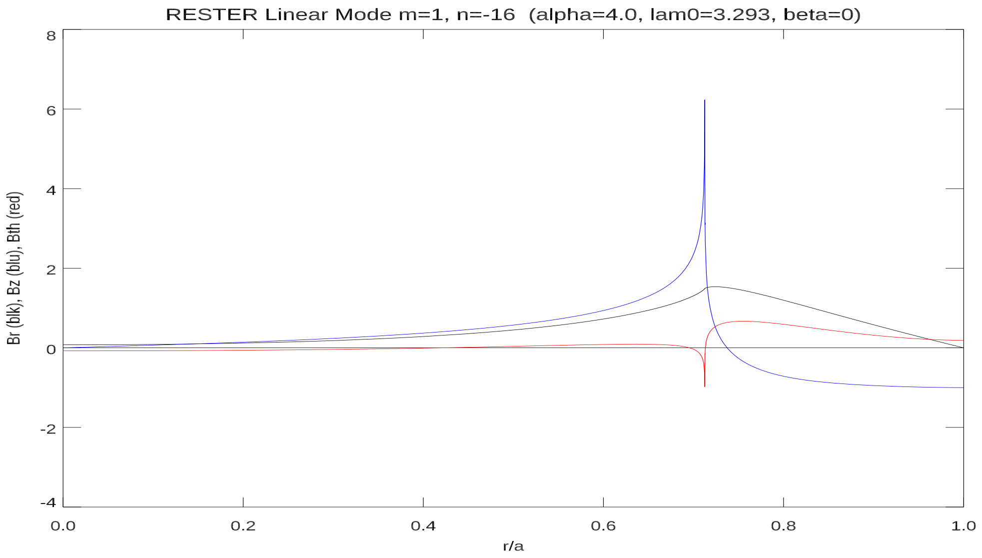
RESTER Linear Mode m=1, n=-16 (alpha=4.0, lam0=3.293, beta=0)
Br (blk), Bz (blu), Bth (red)
8
6
4
2
0
-2
-4
0.0
0.2
0.4
0.6
0.8
1.0
r/a

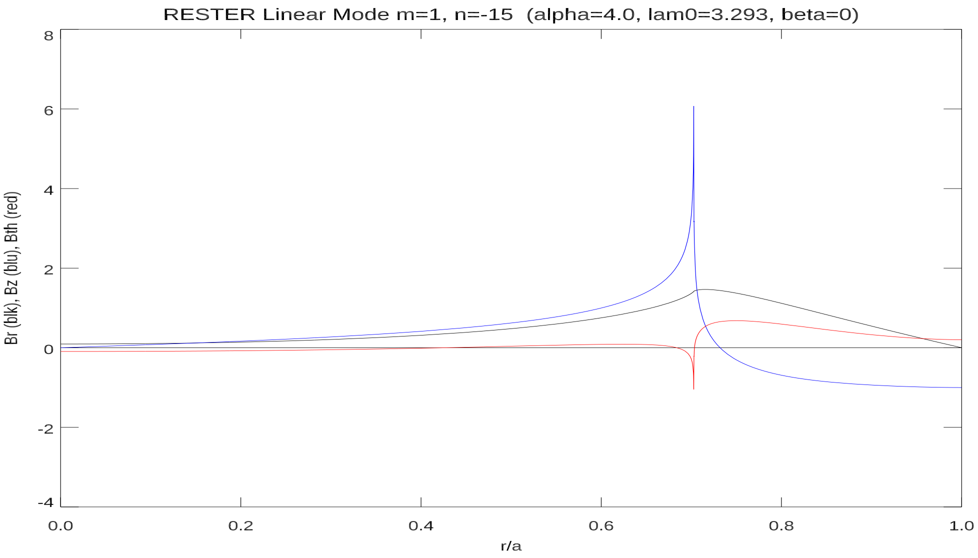
RESTER Linear Mode m=1, n=-15 (alpha=4.0, lam0=3.293, beta=0)

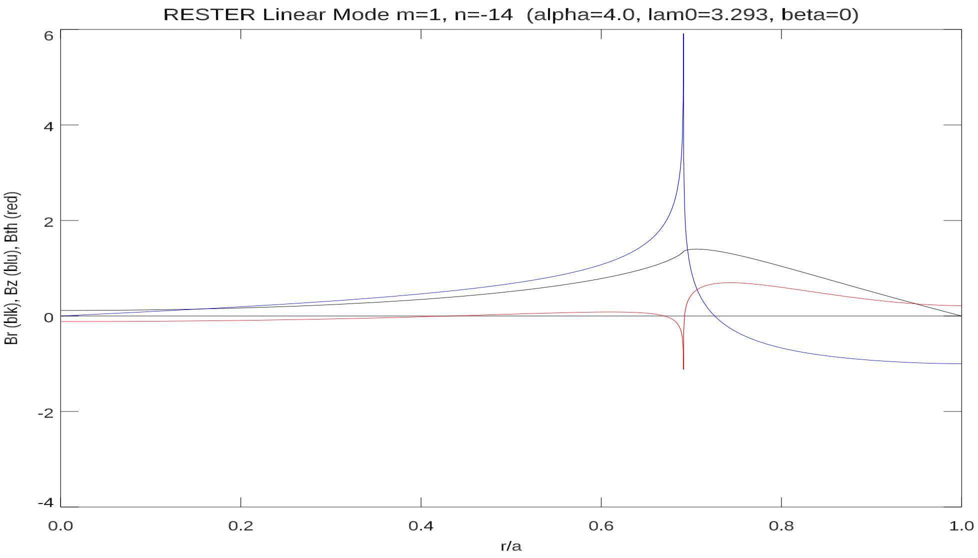
RESTER Linear Mode m=1, n=-14 (alpha=4.0, lam0=3.293, beta=0)

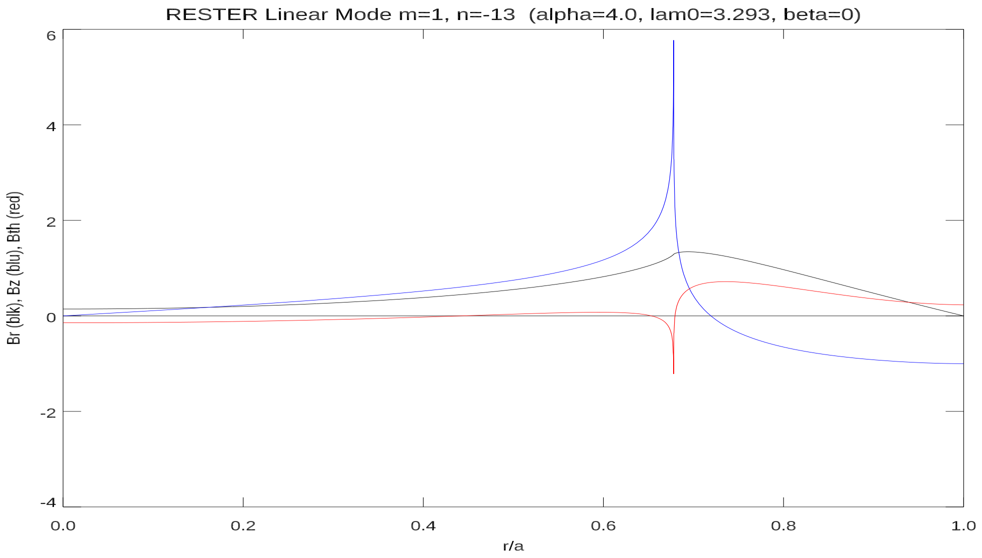
RESTER Linear Mode m=1, n=-13 (alpha=4.0, lam0=3.293, beta=0)
Br (blk), Bz (blu), Bth (red)
6
4
2
0
-2
-4
0.0
0.2
0.4
0.6
0.8
1.0
r/a

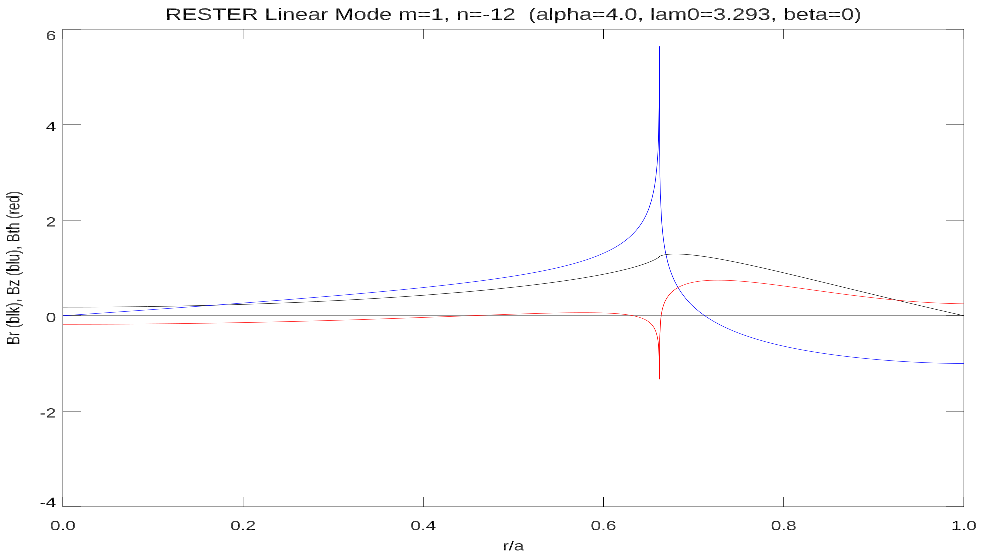
RESTER Linear Mode m=1, n=-12 (alpha=4.0, lam0=3.293, beta=0)
Br (blk), Bz (blu), Bth (red)
6
4
2
0
-2
-4
0.0
0.2
0.4
0.6
0.8
1.0
r/a

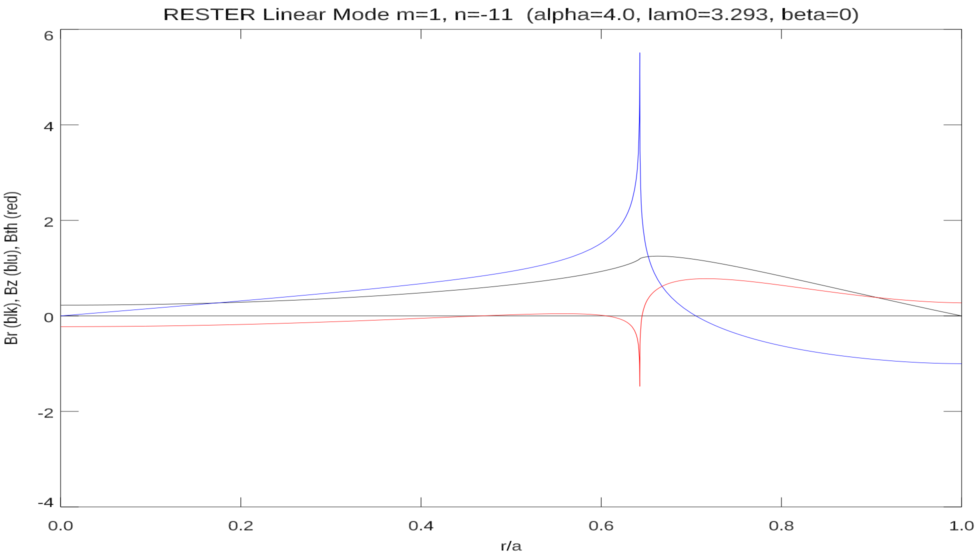
RESTER Linear Mode m=1, n=-11 (alpha=4.0, lam0=3.293, beta=0)
Br (blk), Bz (blu), Bth (red)
r/a
6
4
2
0
-2
-4
0.0
0.2
0.4
0.6
0.8
1.0

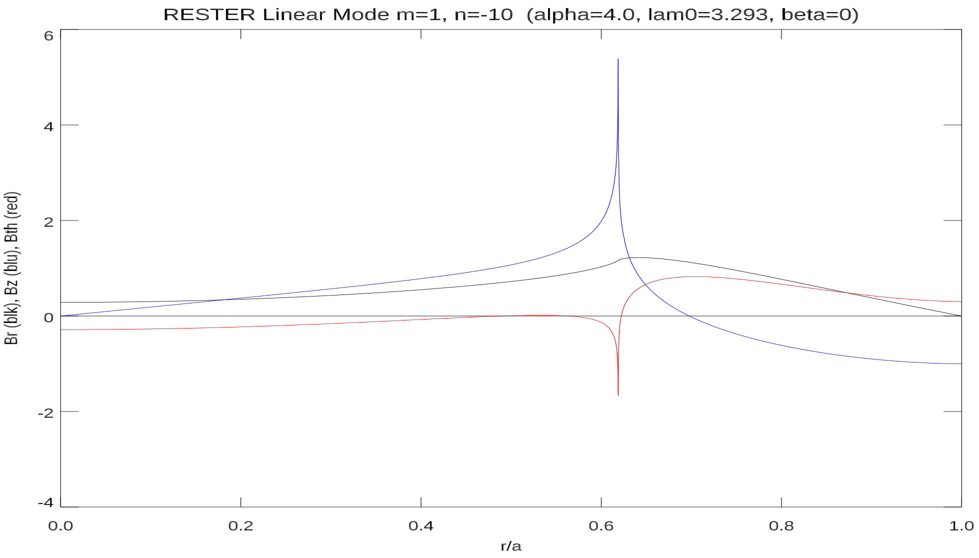
RESTER Linear Mode m=1, n=-10 (alpha=4.0, lam0=3.293, beta=0)
Br (blk), Bz (blu), Bth (red)
r/a
6
4
2
0
-2
-4
0.0
0.2
0.4
0.6
0.8
1.0

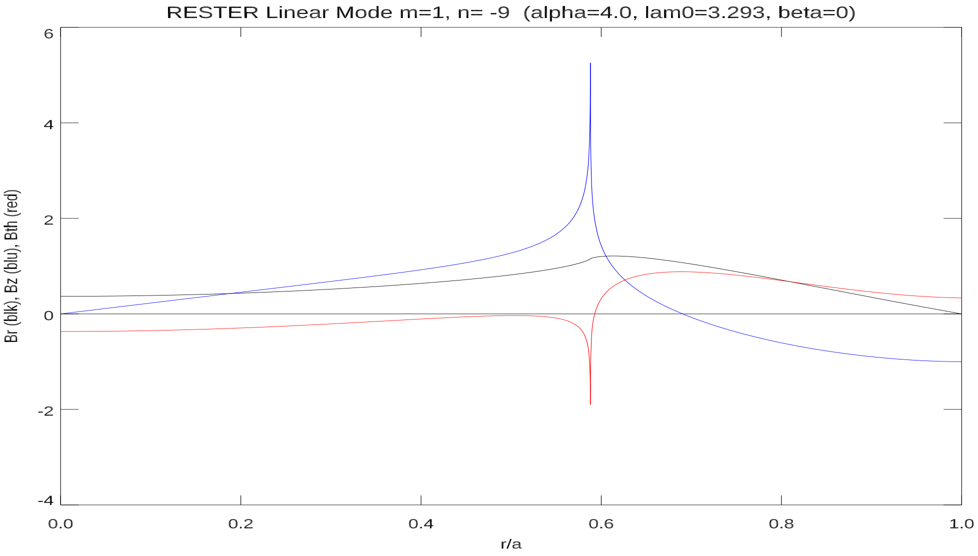
RESTER Linear Mode m=1, n= -9 (alpha=4.0, lam0=3.293, beta=0)
Br (blk), Bz (blu), Bth (red)
6
4
2
0
-2
-4
0.0
0.2
0.4
0.6
0.8
1.0
r/a

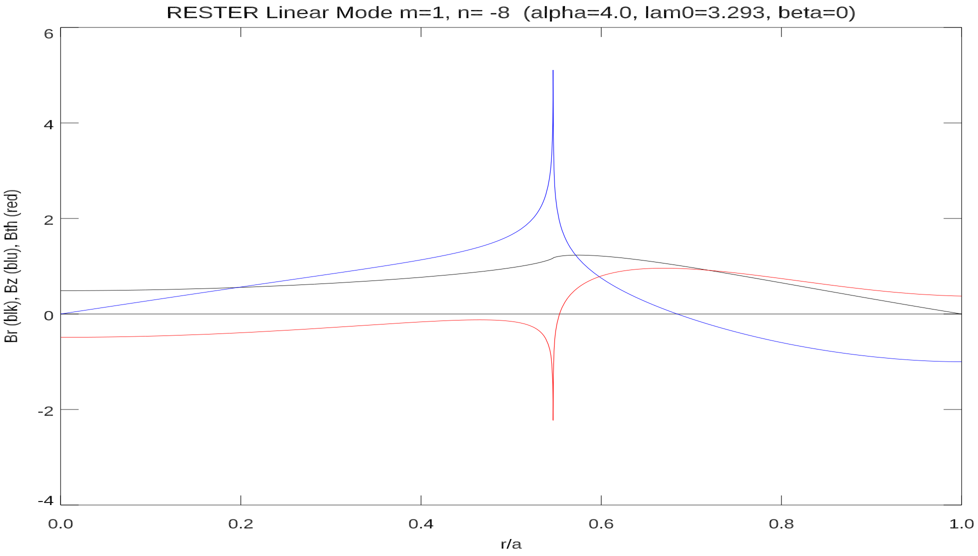
RESTER Linear Mode m=1, n= -8 (alpha=4.0, lam0=3.293, beta=0)
Br (blk), Bz (blu), Bth (red)
6
4
2
0
-2
-4
0.0
0.2
0.4
0.6
0.8
1.0
r/a

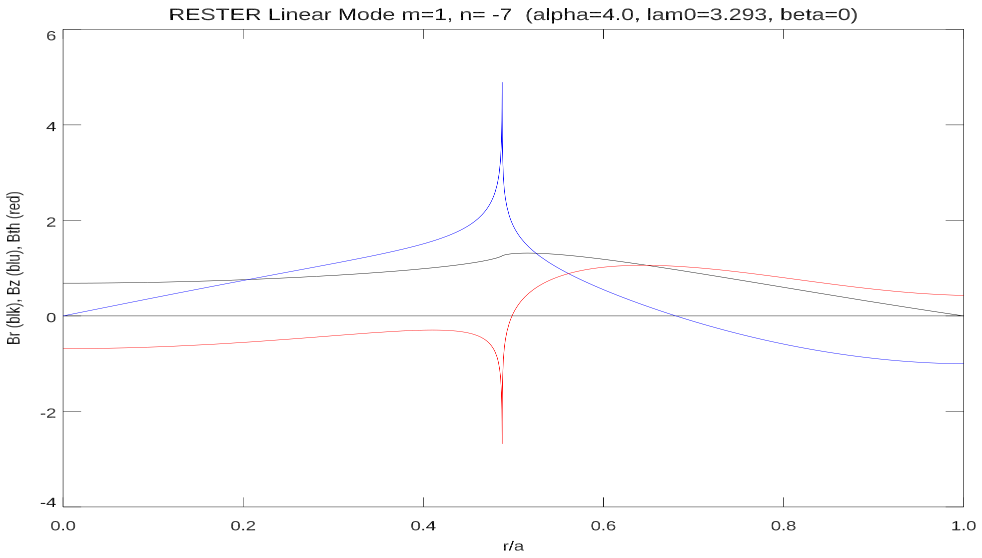
RESTER Linear Mode m=1, n= -7 (alpha=4.0, lam0=3.293, beta=0)

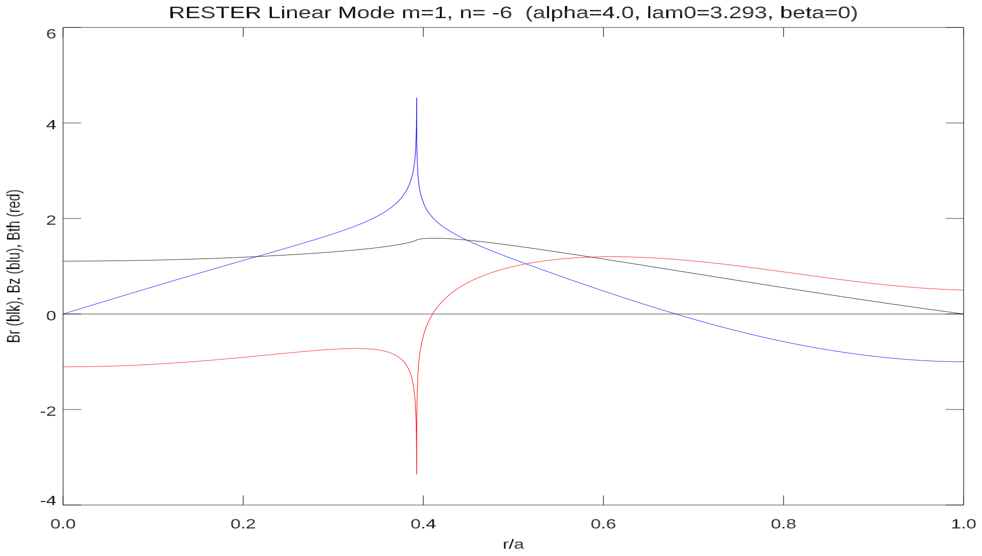
RESTER Linear Mode m=1, n= -6 (alpha=4.0, lam0=3.293, beta=0)

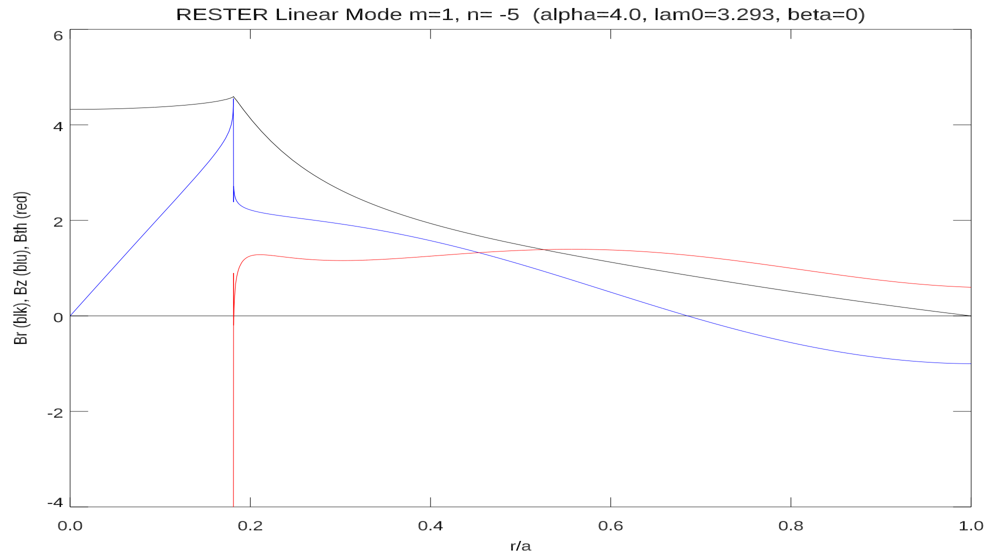
RESTER Linear Mode m=1, n= -5 (alpha=4.0, lam0=3.293, beta=0)
6
4
2
0
-2
-4
Br (blk), Bz (blu), Bth (red)
0.0
0.2
0.4
0.6
0.8
1.0
r/a

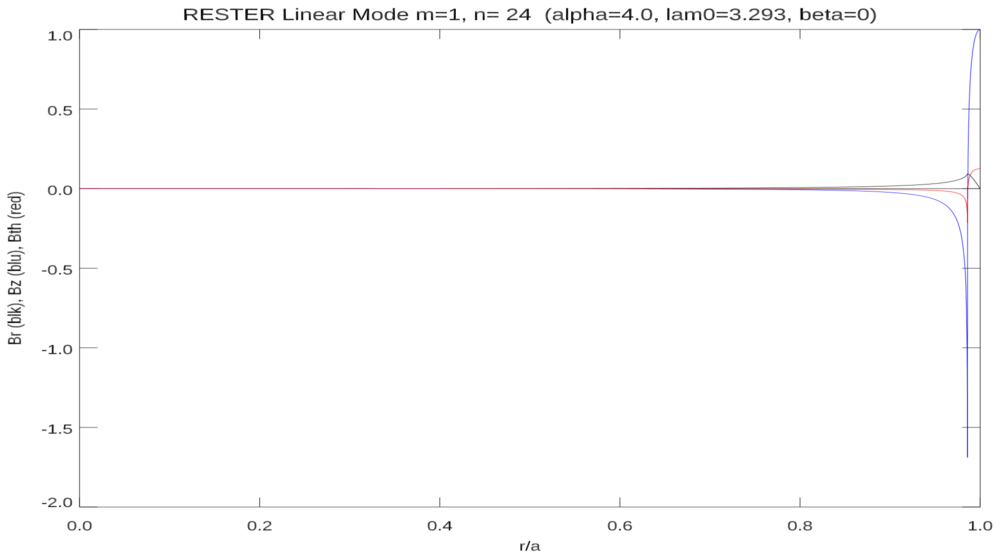
RESTER Linear Mode m=1, n= 24 (alpha=4.0, lam0=3.293, beta=0)
1.0
0.5
0.0
-0.5
-1.0
-1.5
-2.0
Br (blk), Bz (blu), Bth (red)
0.0
0.2
0.4
0.6
0.8
1.0
r/a

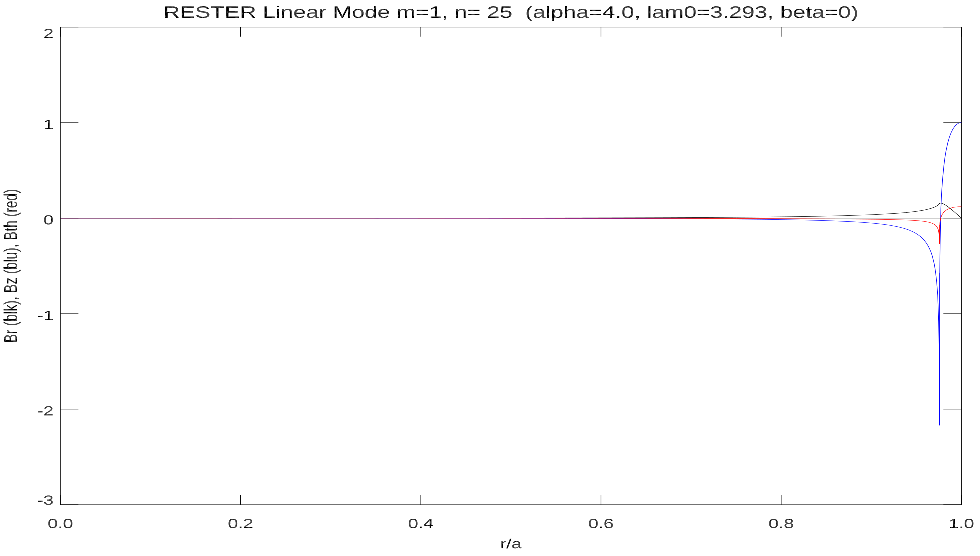
RESTER Linear Mode m=1, n= 25 (alpha=4.0, lam0=3.293, beta=0)
Br (blk), Bz (blu), Bth (red)
r/a
2
1
0
-1
-2
-3
0.0
0.2
0.4
0.6
0.8
1.0

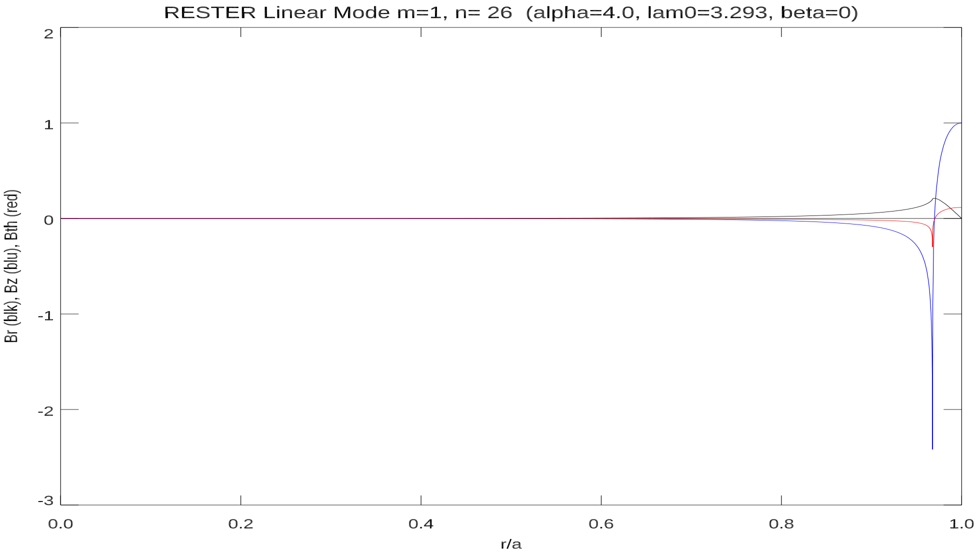
RESTER Linear Mode m=1, n= 26 (alpha=4.0, lam0=3.293, beta=0)
Br (blk), Bz (blu), Bth (red)
r/a
2
1
0
-1
-2
-3
0.0
0.2
0.4
0.6
0.8
1.0

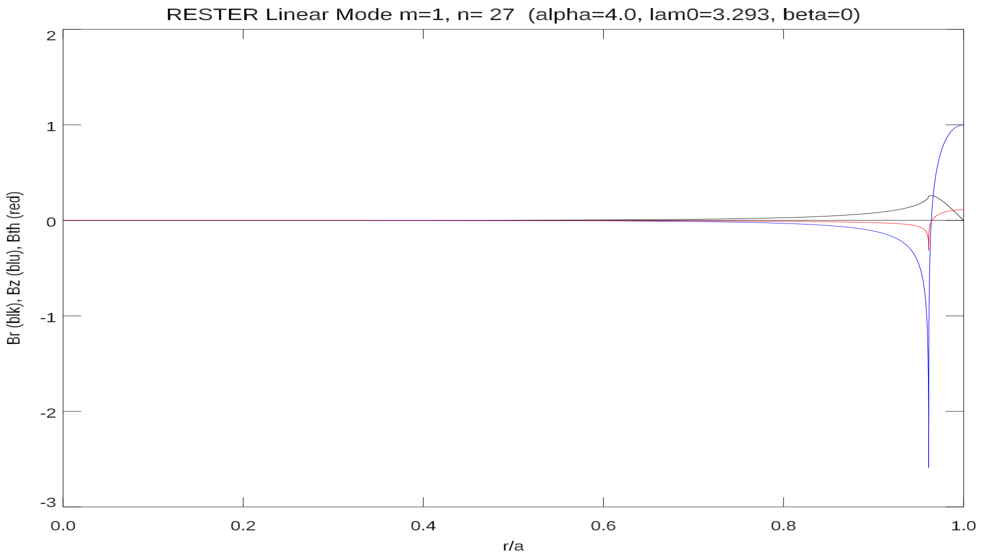
RESTER Linear Mode m=1, n= 27 (alpha=4.0, lam0=3.293, beta=0)
Br (blk), Bz (blu), Bth (red)
r/a
0.0
0.2
0.4
0.6
0.8
1.0
2
1
0
-1
-2
-3

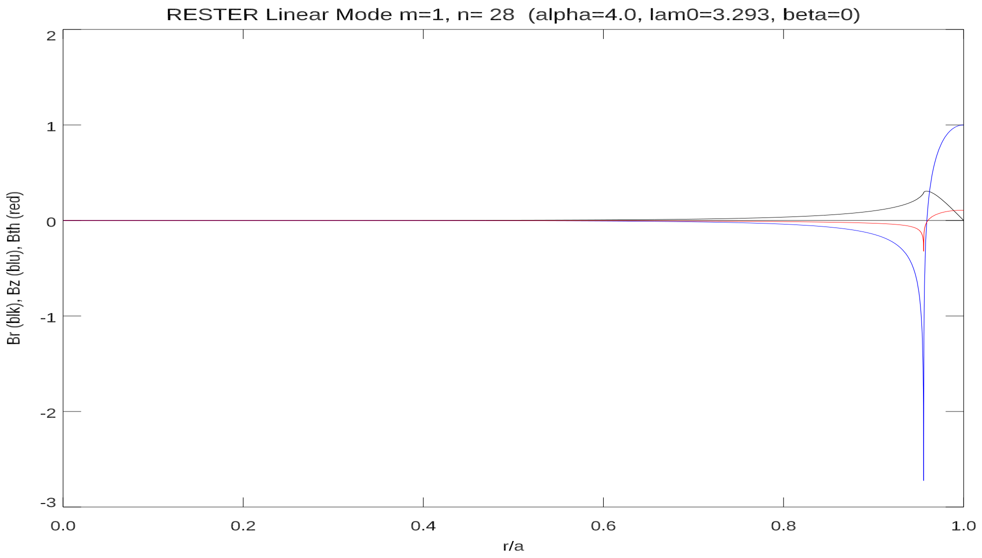
RESTER Linear Mode m=1, n= 28 (alpha=4.0, lam0=3.293, beta=0)
Br (blk), Bz (blu), Bth (red)
r/a
0.0
0.2
0.4
0.6
0.8
1.0
2
1
0
-1
-2
-3

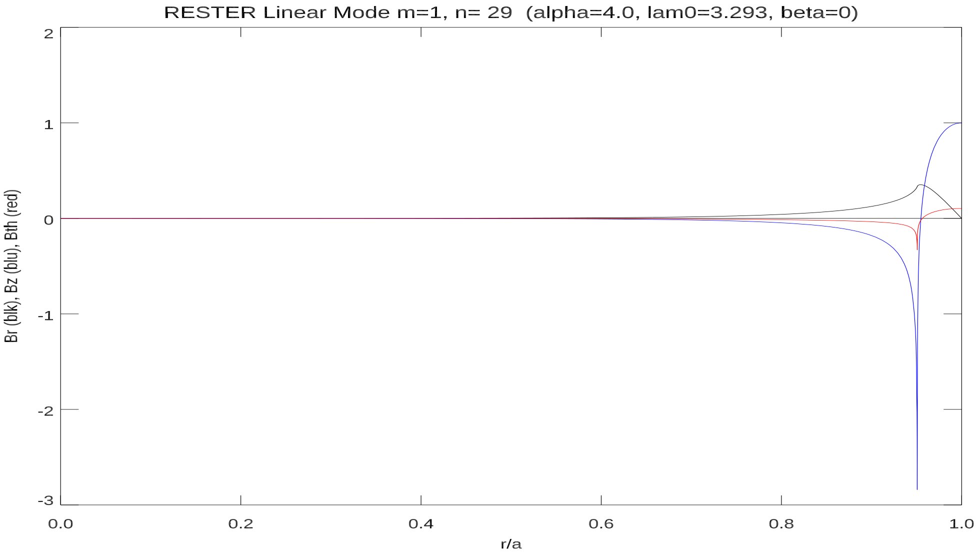

RESTER Linear Mode m=1, n= 29 (alpha=4.0, lam0=3.293, beta=0)

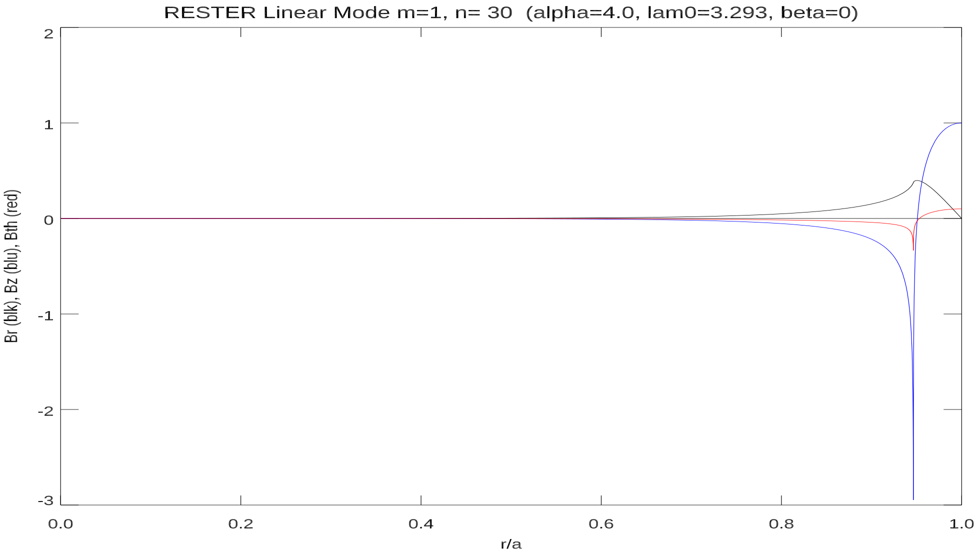

RESTER Linear Mode m=1, n= 30 (alpha=4.0, lam0=3.293, beta=0)

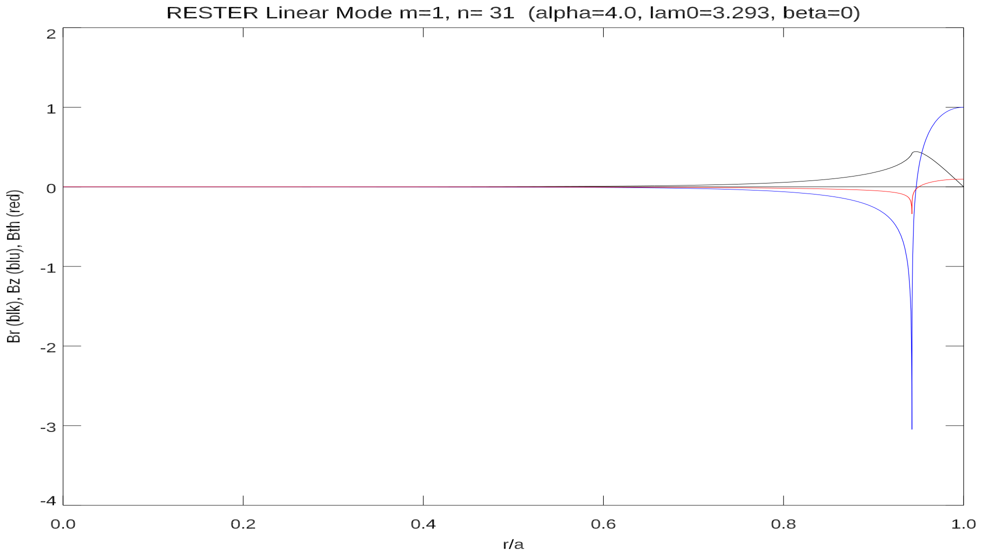
RESTER Linear Mode m=1, n= 31 (alpha=4.0, lam0=3.293, beta=0)
Br (blk), Bz (blu), Bth (red)
2
1
0
-1
-2
-3
-4
0.0
0.2
0.4
0.6
0.8
1.0
r/a